1. Introduction

Shape control of smart structure using piezoelectric material is one of the most interesting topics in smart structure fields. Shape control can be categorised as either static or dynamic. Whether it is transient or gradual change, both static and dynamic shape controls aim to find the optimal shape, size, location and voltage configuration of piezoelectric actuator patches to minimise the error between calculated and desired structural shapes. However, most of the research on static shape control focuses on finding the optimum values of the applied electric fields applied to rectangular-shaped piezoelectric actuators for achieving the desired structural shape. The voltage configurations are treated as design variables. Therefore, to study and improve on the shape control of a smart plate with complicated shapes, this research work will develop finite element software that is capable of handling structural modelling with non-rectangular elements. From this point onwards, the work will focus on piezoelectric actuator design optimisation. Some existing optimisation schemes are also employed to develop new algorithms in order to optimise the applied voltage to piezoelectric actuators and piezoelectric actuator configurations for achieving of the desired structural shapes. Following this, the finite element formulation is also extended and developed for dynamic control applications such as modal shape control and controlled resonant vibration. This chapter presents some background on smart materials, smart structures and their applications. It also provides an overview on existing mathematical models and design optimisation algorithms.

1.1 Smart Materials

The world of materials is an exciting and challenging field of research. The knowledge of materials and their uses have been around for centuries. They have been existent in the last centuries, yet there were some new types of materials, which have only been discovered in the past few decades. The search for new technologies has resulted in advanced composites materials that are light in weight and high in strength and stiffness compared to more conventional material systems. These materials are used extensively in the aerospace industry as an alternative to traditional metal alloys. During the last few decades, people have discovered some new materials, which can intelligently perform remarkable jobs. For example, the optical fibres are embedded into composite materials, which act as sensors to measure the mechanical changes, based on the interaction between mechanical motion and light properties. One new type of the materials is called smart or intelligent material. Since the time it was discovered, there have been great interests in smart material/structure applications. They have been used to investigate and control structure as in the fields of dynamic control, shape control and buckling control.

Most smart or intelligent structure systems have three basic active functions, which are sensing, actuating and processing (controlling). Sensors are used to measure changes in stress, strain, displacement, velocity, acceleration, electrical, thermal or other mechanical change of the structure. They provide this information to the processor. Actuators behave in reverse to sensors. Their actuation capabilities to change structural stiffness, geometrical configuration or else are directly controlled by receiving feedback from the controller to change electric potential, temperature, magnetic field or light. Sensors and actuators can be bonded on or embedded in controllable smart structures. Controllers (processors) are dependent on the type-functional relation or control algorithm of smart structures corresponding to different actuator/sensor types. For example, the structure is controlled and observed with collocated and distributed actuators/sensors (Loewy, 1997). Smart materials can be broadly categorised into five types. They are categorised in term of energy transformation such as *light–mechanical*, *chemo–mechanical*, *thermo–mechanical*, *magneto–mechanical* and *electro–mechanical* including *high performance actuators*.

For *light–mechanical* technique, the material can only be used as sensor because fibre optic material is embedded in structure. Its affect is based on the interaction between mechanical movement and light properties. C*hemo–mechanical* technique uses polyelectrolyte gels, which undergo with a huge active contraction of 50% strain due to electromechanical conversion. *Thermo–mechanical* uses the property of thermal expansion. The structure can change in shape by increasing (heating-up) or decreasing (cooling-down) the temperature. The *magneto–mechanical* technique is based on the conversion between magnetic field (current) and mechanical strain. As actuators, the strain is change due to magnetic field. It produces current when material is stressed. There are two different types in this category as *Magnetostrictive* materials and *Magneto-Rheological Fluid*. Similarly, the *electro-mechanical* technique considers electrical charge instead of magnetic field. It generates electrical charge due to applied mechanical loading. It is called direct piezoelectric effect and is used as sensors. In contrast, the material, which deforms due to applied electric voltage, is known as converse piezoelectric effect and is used as actuators. This category has three types of materials, which are *Piezoelectric* materials, *Electrostrictive* materials and *Electro-Rheological Fluid*.

1.2 Smart Structures

Once smart materials are bonded to or embedded in traditional structures (as host structures, adaptive structures or parent structures), those structures now have sensing, actuating and processing or controlling capabilities. They are known as intelligent structures or smart structures. These structures have high performance along with high level of energy efficiency and autonomy. They are used widely in structural engineering (Loewy, 1997). Smart structures are classified into four groups as self-sensing, self-adaptive, active and intelligent. They all have three basic functions as sensor, actuators and processor. They are all differently implemented in smart structure technology of several applications. Table 1.1 shows the properties of each group. At the current stage, there are several applications and structures such as fibres optic sensor, shape memory alloy, piezoelectric actuators/sensors, magnetostrictive actuators/sensors, electro or

magneto rheological fluid and polyelectrolyte gels, which describes the great detail of introduced materials in previous section.

Table 1.1: Summary of Smart Structure Subsets (Loewy, 1997)

Subset Classification	Function	Implementation
Self-adaptive	Sensor	Non-structural
	Processor	Non-structural, external
	Actuator	Embedded, integrated
Self-sensing	Sensor	Load carrying, embedded, integrated
	Processor	Non-structural, external
	Actuator	Traditional, concentrated, external to structure
Active	Sensor	Embedded, integrated
	Processor	Non-structural, external
	Actuator	Load carrying, embedded, integrated
Intelligent	Sensor	Load carrying, embedded, integrated
	Processor	Embedded, integrated
	Actuator	Embedded, integrated

Fibre optic sensors are used to measure variables such as crack; strain etc… (Gandhi and Thompson, 1992) and is based on the light-mechanical effect, which involves the interaction between mechanical motion and light properties (polarization, wavelength, frequency, intensity or else other). It means that the mechanical change in structure is defined in term of difference between the initial and final light pulses. The advantages of fibre optics are their small size compared to the host structure and involve small energy loss during the transmission of light as well as free of electromagnetic interference. Also fibre optics can be embedded into a host structure.

Conducting polymers undergo a geometric change due to chemo-mechanical doping and de-doping of the polymer. Their elongations and contractions depend on the current flow between the conducting polymer and a counter-electrode separated by either a liquid or solid electrolyte. With a low applied voltage, it can produce reasonable

strains and high stresses. However the response time is slow because the chemo-mechanical conversion is diffusion regulated. So the diffusion time can be decreased to improve the time of response. Della Santa et. al (1997) used conducting polymers to produce a linear muscle-like actuator.

Shape memory alloy is a type of smart structure, based on the thermo-mechanical effect. It can memorise its original shape. The change in structural shape relies on the transformation between martensite to austenite phase and the lattice structure of the material due to applied heat energy. Hodgson et. al (1996) demonstrated the deformation and the ability to return to initial shape of the shape memory alloy by either cooling or heating. It can be used as sensor and actuator and is capable of producing large strains. This material has disadvantages of response time, large thermal energy loss and applied temperature range. And permanent structural deformation occurs if applied temperature is out of phase. Shape memory alloys have several forms such as wire or composite forms. With composite form, wire form can be embedded into composite material. At present there are only two commercial smart metal alloys, which are Nikel-Titatium (NiTi) alloys and copper-based alloys ($CuZnA_1$).

Magnetostrictive and Magneto-Rheological Fluid (MRF) are known as smart materials based on conversion of strain subjected magnetic field for actuators and conversion of current due to change in stress for sensors. Magnetostrictive materials are capable of producing great strains at moderate magnetic field strengths and display excellent response time. There is the restriction of high frequency response due to eddy current in the material. Hall and Flatau (1998) used magnetostrictive materials in vibration control systems. Unlike magnetostrictive materials, MRF contains dielectric particles, which are distributed randomly in fluid. These materials work based on the changes of fluid properties such as viscosity and solubility. These properties are changed due to the change in magnetic field. These particles form a chain structure under applied electric field. It is hard to describe the fluid properties accurately in theory and mathematical modelling. Therefore, they are not widely used. Nava et. al (1997) have found that the response time constant of MRF depends on the direction of current. The time constant is increased with alternating current.

Electro-Rheological Fluid (ERF), Electrostrictive and Piezoelectric materials undergo electro-mechanical deformation. ERF mostly works like MRF. Electrostrictive materials are not effective as sensor due to the extension of strain under applied electric field and the non-linear relation between strain and electric field. While piezoelectric materials are two ways effect between stress/strain and electric field/voltage. They can be used as sensors and actuators. Piezoelectric materials are subdivided into two groups of piezoceramics and piezopolymers, which have high stiffness and low stiffness, respectively. Piezoceramics (example Lead Zirconate Titanate-PZT) are good to design for actuating applications and its maximum actuation strain is about 1000 micro strain; whilst piezopolymers (e.g. Polyvinylidene Fluoride, PVDF) are desirable for sensing applications and its maximum actuation strain is about 700 micro strains. They have been widely used in many areas and applications. Piezoelectric materials are the most interesting materials and many researchers try to improve their capabilities to enhance its usefulness.

1.3 Piezoelectric Materials Modelling

Piezoelectric materials are the most common smart materials, which undergo electro-mechanical effects. They undergo deformation in strain when an electric potential is applied across them and reversely generate voltage when strain is applied. Curie brothers, Pierre and Jacques in 1880, have discovered the effects of this material due to development of stress and electric charge. A while later, they also discovered the reverse effect, which localised strain is generated in response to an applied voltage on the material. The main property of the piezoelectric effect that differentiates it from the electrostriction effect (change of geometry due to applied electric fields) is that the geometry will change in the opposite direction if the electric field is reversed. The widely accepted mathematical model for piezoelectric effect is linear model in which the electrical and mechanical effects contributed independently to strain/stress and electric displacement. This section will be introducing the linear effect and modelling of piezoelectric materials.

Equation (1.1) shows the general theory of linear elasticity of mechanical behaviour by Hook's law, which is defined in term of second rank tensor of mechanical stress (σ_{ij}), strain (ε_{kl}) and stiffness (c_{ijkl}), where i, j, k, l *= 1, 2, 3*.

$$\sigma_{ij} = c_{ijkl}\varepsilon_{kl} \tag{1.1}$$

By Cauchy's infinitesimal strain tensor, strains in Equation (1.1) are:

$$\begin{aligned}
\varepsilon_{xx} &= \frac{\partial U}{\partial x} \quad ; \quad \gamma_{yz} = \left(\frac{\partial V}{\partial z} + \frac{\partial W}{\partial y}\right) \\
\varepsilon_{yy} &= \frac{\partial V}{\partial y} \quad ; \quad \gamma_{zx} = \left(\frac{\partial W}{\partial x} + \frac{\partial U}{\partial z}\right) \\
\varepsilon_{zz} &= \frac{\partial W}{\partial z} \quad ; \quad \gamma_{xy} = \left(\frac{\partial U}{\partial y} + \frac{\partial V}{\partial x}\right)
\end{aligned} \tag{1.2}$$

Where: ε_{xx}, ε_{yy} and ε_{zz} are normal strains. γ_{xy}, γ_{yz} and γ_{zx} are shear strains. U, V, W are displacements in x, y, z directions, respectively.

Equation (1.3) shows the Hook's law in term of two-dimensional stiffness tensor matrix.

$$\sigma_i = c_{ij}\varepsilon_j ; \quad \text{Where: i, j = } 1,\ldots,6 \tag{1.3}$$

The dielectric materials (known as insulators) are used in development of piezoelectric materials. Although they do not conduct current, they may be polarised under influence of applied electrical fields. The aim of polarisation is to align the electric dipoles to produce an equivalent volume charge density (ρ_p). The electric displacement (D) is defined by using Gauss's Divergence theorem to incorporate ρ_p. Equation (1.4) shows the electric displacement in term of the third rank tensor of stress, strain and electric field (E) for the piezoelectric effect.

$$\begin{aligned}
D_i &= d_{ijk}\sigma_{jk} \\
\varepsilon_{jk} &= d_{ijk}E_i
\end{aligned} \qquad \text{Where: i, j, k = } 1, 2, 3 \tag{1.4}$$

Equation (1.4) can be rewritten in term of two-dimensional matrix of piezoelectric stress and strain constant as shown in Equation (1.5):

$$\begin{aligned} D_i &= d_{il}\sigma_l \\ \varepsilon_l &= d_{il}E_i \end{aligned} \qquad \text{Where: } i = 1,...,3;\ l = 1,\ldots,6 \qquad (1.5)$$

Finally, the general equation for piezoelectric materials in term of total internal energy density ($\mathbf{U}(\varepsilon,D)$) due to mechanical and electrical work done is stated in Equation (1.6).

$$d\mathbf{U}(\varepsilon, D) = \mathbf{E}dD + \boldsymbol{\sigma}d\varepsilon \qquad (1.6)$$

Equation (1.6) shows that the mechanical and electrical behaviours are independent from each other for piezoelectric materials. They are coupled, where piezoelectric materials are considered as relation between mechanical variables of stress and strain as well as relation between electrical variables of electric field and displacement. Readers who are interest in fully derived formulation of piezoelectric materials should refer to Chee (2000c) in Chapter 2. More details on of piezoelectric materials can also be found in Chopra (2002). For the linear constitutive equations, piezoelectric materials can only be maintained for low strain, where the electric field and voltages are low. For example, the piezoelectric fibre composites are capable of both orthotropic and anisotropic actuation.

The total derivatives of the stress and the electric displacements in function of the natural variables of strain and electric field can be expressed as Equation (1.7), which is in fact of the differential form of the electro-mechanically coupled piezoelectric constitutive equation.

$$\begin{bmatrix} d\boldsymbol{\sigma} \\ d\mathbf{D} \end{bmatrix} = \begin{bmatrix} \dfrac{\partial\boldsymbol{\sigma}}{\partial\varepsilon} & \dfrac{\partial\boldsymbol{\sigma}}{\partial E} \\ \dfrac{\partial\mathbf{D}}{\partial\varepsilon} & \dfrac{\partial\mathbf{D}}{\partial E} \end{bmatrix} \begin{bmatrix} d\varepsilon \\ dE \end{bmatrix} \qquad (1.7)$$

Equation (1.8) shows the electro-mechanically coupled piezoelectric constitutive equation of piezoelectric stress formulation in term of materials properties.

$$\begin{bmatrix} \boldsymbol{\sigma} \\ \mathbf{D} \end{bmatrix} = \begin{bmatrix} \mathbf{c} & \mathbf{e}^{T} \\ \mathbf{e} & \boldsymbol{\chi} \end{bmatrix} \begin{bmatrix} \boldsymbol{\varepsilon} \\ \mathbf{E} \end{bmatrix} \tag{1.8}$$

For laminated composite structure modelling, each layer can be rotated about transverse z-axis. The change in material properties will give the smart structure additional actuation authority due to rotation of the materials. Equation (1.9) shows the relation of electric displacement and electric field between the local coordinate system (σ_l, ε_l, D_l, and E_l) and global coordinate system (σ, ε, D, and E) using the standard transformation tensor (see Figure 1.1 and Appendix C).

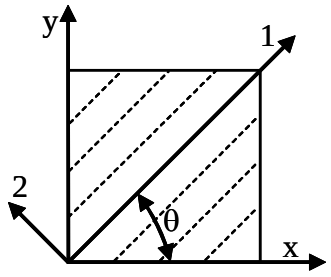

1, 2: Local coordinate system

x, y: Global coordinate system

θ: Angle between local and global coordinate system

Figure 1.1: Lamina Orientation

$$\begin{aligned} \boldsymbol{\sigma} &= \mathbf{T}^{-1}\boldsymbol{\sigma}_1 \\ \boldsymbol{\varepsilon} &= \mathbf{R}\mathbf{T}^{-1}\mathbf{R}\boldsymbol{\varepsilon}_1 \end{aligned} \quad ; \quad \begin{aligned} \mathbf{D} &= \mathbf{Q}^{-1}\mathbf{D}_1 \\ \mathbf{E} &= \mathbf{Q}^{-1}\mathbf{E}_1 \end{aligned} \tag{1.9}$$

Where: **T** = 2nd rank transformation tensor (contracted notation)

Q = 1st rank transformation tensor

R = Engineering strain transformation matrix

1.4 Mathematical Modelling

In general, the smart structural behaviours can be investigated by several methods such as analytical analysis or finite element analysis. The structures can be simulated via developed formulation to reduce time and cost. Several research groups focus on development of formulation for beam, plate and shell structures. Whether analytical or finite element modelling is better depends on particular objectives of modelling and application. Each method has its own advantages and disadvantages.

1.4.1 Analytical Solutions

The analytical formulation can have accurate solution and consume less time in computation. On the other hand, they are limited to some particular problems such as geometries and physical assumptions. Many researchers try to develop new formulation or improve existent formulation to achieve better analytical solutions.

Crawley and Deluis (1987) and Crawley et. al (1988) modelled piezoelectric actuators embedded in cantilever beams. This is a one-dimensional problem, which investigated bending and extension of the beam. The derivation led to the generic dynamic equation of motion due to the existence of electrical potential and piezoelectric constants. The theoretical models of using piezoelectric in control of intelligent structures have been further developed for Bernoulli-Euler beam (Chaudhry and Rogers, 1994), laminated composite plates (Crawley and Lazarus, 1991) with the assumption that plane sections normal to the mid-surface before deformation rotate such that they remain plane and normal after deformation. In addition, an electrical model was also formulated to allow calculation of damping and tuning of the electrical system. Im and Atluri (1989) improved Crawley's model by considering shear stress and axial force in the formulation.

Richard and Cudney (1993) developed analytical solution for a model with multiple layers of piezoelectric actuators. They developed equation of motion including rotary inertia and shear deformation effect. Wang et. al (1996) derived analytical solution for the case of actuators bonded on both sides of a beam to investigate dynamic behaviours of piezoelectric coupled actuators. The formulation considered simple one-dimensional constitutive relation. The formulation highlighted the electro-mechanical coupling effect between the longitudinal motion of the actuator and transverse vibration. Karczmarzyk (1996) studied the vibration problems of composite structure using analytical elastodynamic solution. The formulation was dealing with problem in plane stress state. Wang and Meguid (2000) developed an analytical solution for smart structure using PZT. The structures can have a fully embedded or haft plane boned with a PZT rod.

Luo and Tong (2002a and 2002b) developed the analytical model for a PZT composite beam including adhesive layers based on the classic theory in bonded joints for static and dynamic analysis (Tong and Steven, 1999). Piezoelectric patches and the host beam are considered as Euler-Bernoulli beams, and the adhesive layer is modelled as a system of continuous springs with shear and peel stiffness. The formulation is capable analysing structure with de-bonding and delamination effect. Edge de-bonding is also studied by simply considering a shortened PZT length. The formulation is capable of actuating internal forces and displacements of the host beam as well as sensing the electric charge of the PZT material.

Crawley and Lazarus (1991) developed analytical formulation to find induced strain and curvature for isotropic and anisotropic plate structure under bending and twisting. The formulation can only solve for the case of isotropic in-plane actuation strain and no actuation shear strain. The analysis to determine induced strain actuation for laminated composite plate was developed by Wang and Rogers (1991) using Classical Laminated Plate theory. The analysis allows the piezoelectric actuator to be distributed anywhere within the structure. The Heaviside-Step function is used for the contribution of these discrete actuator patches. The general formulation was then simplified to illustrate the solutions for two special cases and their effects such as bending, extension and bending-twist.

Heyliger (1994) developed analytical solution for rectangular plate, where applied sinusoidal loading or potential is considered. Heyliger and Saravanos (1995) derived formulation to solve for vibration of laminated plate in which the piezoelectric can be modelled as laminated layers. Heliger and Brook (1996) developed the solution of piezoelectric laminated plates in cylindrical bending. Heyliger (1997) developed exact solutions for simply supported laminated piezoelectric plates. In Pan and Heyliger (2003), analytical solutions are derived for the cylindrical bending of multilayered, linear and anisotropic magneto-electro-elastic plate under simply-supported edge conditions. The formulation is derived for a homogeneous plate in terms of the Stroh-type formalism. Multilayered solution has an elegant and simple expression using the propagator matrix method.

One of the applications of smart structure is control of the shape of the structure. Koconis et. al (1994) developed analytical methods for determining the optimum values of the applied electrical fields of fixed-shape actuators for achieving overall specified shapes for sandwich plates and shells. Unlike other analytical model, this formulation seems to have a general applicability, which can solve for structure with different shapes, different boundary conditions, and various composition or laminar arrangements where layers can be isotropic or orthotropic.

Another general methodology for piezoelectric laminated shells was developed by Pletner and Abrmovich (1997) but this analysis involved shells rather than plates. The laminates can be substrate, actuator or sensor. The displacement field was assumed to be first order using the Mindlin-Reissner theory only. The resultant forces and moment are expressed in terms of induced strains. The general formulation was then reduced to a simplified case where a single layer substrate is bonded on both sides by piezoelectric material. The sensor voltage was expressed as an integral. The author suggested the technique of using equivalent loading and induced strains being more advantage than using finite element formulation. Miller and Abrmovich (1995) presented an analytical formulation based on shell theory including piezoelectric effects. The formulation is first order displacement and allows piezolaminated actuator model to be self-sensing. The modelled material was transversely anisotropic. It was also limited to the applied electric field in transverse direction only. A three-dimensional analytical solution has been developed for shape control application (Kapuria et. al, 1997). The cross-ply orthotropic laminated cylindrical panel was considered in the formulation. Double Fourier series was used to satisfy the boundary condition. Stam et. al (1995) presented an analytical solution for cylindrical piezoelectric system including thermal loads. Thermo-electric-elastic was used so that the modelling can function at various ranges of temperatures. The theory was based on cylindrical coordinates. The relationship between thermal and electrical effects (Pyroelectric coefficient) was assumed negligible. Piezoelectric strain coefficients were found to be temperature dependent.

1.4.2 Finite Element Formulation

Although analytical technique presents a mathematical base but it is not easy to formulate and solve problem except in some very simple cases. The development of finite element technique provides opportunities to solve various complex problems. Many researchers have developed specialised finite element in-house codes to deal with smart structures. Allik and Hughes (1970) developed the finite element (FE) formulation including piezoelectric effects. Tzou (since1988) developed FE formulation, which is capable to solve for complex problems. The Hamilton's Energy Variational Principle was used to derive the FE formulation. The Hamilton's Energy Variational Principle is stated in Equation (1.10), where K, P, W is kinetic energy, potential energy and work done, respectively.

$$\int_{t_0}^{t_1} \delta K \times dt - \int_{t_0}^{t_1} \delta P \times dt + \int_{t_0}^{t_1} \delta W \times dt = 0 \tag{1.10}$$

Equation (1.11) shows the final FE system, which is expressed in terms of the nodal variables including both mechanical and electric quantities.

$$\begin{bmatrix} \mathbf{M}_{uu} & 0 \\ 0 & 0 \end{bmatrix} \begin{bmatrix} \ddot{\mathbf{u}}_g \\ \ddot{\boldsymbol{\phi}}_g \end{bmatrix} + \begin{bmatrix} \mathbf{C}_{uu} & 0 \\ 0 & 0 \end{bmatrix} \begin{bmatrix} \dot{\mathbf{u}}_g \\ \dot{\boldsymbol{\phi}}_g \end{bmatrix} + \begin{bmatrix} \mathbf{K}_{uu} & \mathbf{K}_{u\phi} \\ \mathbf{K}_{\phi u} & \mathbf{K}_{\phi\phi} \end{bmatrix} \begin{bmatrix} \mathbf{u}_g \\ \boldsymbol{\phi}_g \end{bmatrix} = \begin{bmatrix} \mathbf{F}_g \\ -\mathbf{Q}_g \end{bmatrix} \tag{1.11}$$

In the FE formulation, strain and electric field can be expressed in terms of displacement u, and electric potential ϕ. Shape interpolation function is employed to define displacement and electric potential in terms of nodal variable of displacement and electric potential.

In Allik and Hughes (1970), the FE formulation is capable to analyse smart plate and smart shell structure in one and two dimensional. The damping term was not considered in this formulation. The development of FE model from distributed sensing and actuation is given by Tzou and Tseng (1990). The derivation was similar to Allik and Hughes (1970). The physical model is a two-dimensional structure with the piezoelectric sensor layer at the bottom and piezoelectric actuator layer on top. It can

simulate two types of active control for vibration suppression such as constant gain and constant amplitude feedback. A slight variation of the FE method was developed by Ha et. al (1992). This method is general in the sense that it can be applied to composite laminate substrates bonded with distributed piezoelectric actuators and sensors. Saravanos (1996) developed a finite element formulation for the mixed fields laminate theory in curvilinear coordinates. The main assumptions were linear displacement though the thicknesses of the laminate for displacement on curved surface, while transverse displacement are constant through thickness; and layer-wise electric potential is assumed through laminate. Saravanos et. al (1997) developed layer-wise models and finite element for dynamics analysis of piezoelectric composite plates. Lin and Hsu (1996) employed first order shear deformation with correction factor of 5/6 to develop FE formulation. The structures consist of 3 types of elements and they are modelled differently such as 8-node isoparametric quadratic plate element for substrate, 16-node adhesive interface element and 8-node isoparametric element for actuator. The works illustrate deflection of beam structures and the deformed shape of plate structures.

Chee et. al (2000a) developed new electro-mechanical coupled mathematical model for the analysis of beam and plate. The mechanical deformation was modelled based on the third order displacement field, whilst layer-wise electric potential was used to model the electrical effects. He also developed finite element formulation based on the theory for the analysis of smart beam and smart plate structures. The feature of developed FE software is that uses symbolic integration of the electro-mechanical stiffness matrix. Only eight-node rectangular element is considered to model plate structures. Nguyen and Tong (2002a) developed finite element formulation for smart composite plates based on the third order plate theory and linear layerwise theory to study the effect of the varying actuator shape on the resulting of error function. Luo and Tong (2002c) developed finite element formulation for piezoelectric smart plates based on the *Reissner-Mindlin* plate theory. It is also used to study piezoelectric de-bonding in smart plates. Gornandt and Gabbert (2002) developed FE analysis for thermopiezoelectric smart structures including the thermal effects. Both the static and the dynamic responses of combined thermal, electric and mechanical excitations are considered. Ray and Mallik (2004) developed FE formulation static analysis of laminated smart composite plates integrated with a piezoelectric fiber-reinforced composite layer acting as distributed actuators. A simple first-order shear deformation

theory based on a generalised-energy-based finite element model is used for deriving the model. Eight-node isoparametric serendipity elements are used for discretising the domain. Lage et. al (2004) developed a partial mixed layer-wise finite element model for adaptive plate structures. They also presented static analysis of magneto-electro-elastic laminated plate structures. The mixed FE formulation is obtained by considering a Reissner mixed variational principle. The FE formulation is derived using transverse stresses, displacement components and electric and magnetic potentials as primary variables.

1.5 Applications

The shape control has been applied to various systems such as adaptive mirror (Paradies et. al 1996), aerospace antenna (Balas, 1985), and flexible wing (Austin et. al, 1994). The applications of smart structures using piezoelectric material are widely used in the field of shape control. Shape control can be categorised as either static or dynamic shape control. Whether it is transient or gradual change, both static and dynamic shape controls aim to determine the size of piezoelectric actuators, their applied electrical fields and loci, such that the desired shape is achieved effectively.

1.5.1 Static Shape control

Shape control of a structure can be achieved through optimally selecting the loci, shapes and sizes of the piezoelectric actuators attached to the structure and also choosing the electric fields applied to the actuators. For quasi-static shape control, the shapes of piezoelectric actuators and electrical field are the important design variables for achieving the desired structural shape. However, most of the researches on static shape control focus on finding the optimum values of the electric fields applied to rectangular-shaped piezoelectric actuators for obtaining the desired shape. In this case, the electric fields in the actuators are the design variables and their optimum values are determined by minimising the difference between the calculated and desired structural shapes. Koconis et. al (1994) developed analytical methods for determining the optimum values of the applied electrical fields to fixed rectangular-shaped actuators for achieving the specified shapes for sandwich plates and shells. The determination of voltage required

for a specified shape is actually an inverse problem. In other words, there is no direct analytical solution. The procedure involved minimising error function between calculated and desired shape and producing voltage distribution. Chandrashekhara and Varadarajan (1997) presented a shape control technique for composite beams using third order displacement theory in FE formulation. The technique is the precursor of the later work by Varadarajan and Chandrashekhara (1998) on the composite plate using first order displacement theory in FE formulation. The Principle of Stationary Potential Energy was employed to develop FE formulation. The aim is to minimise the error function based on the same manner. Wang et. al (1997) developed a FEA technique for static shape control of plate structures using piezoelectric materials and claimed their method saved memory and computational cost. The FE method using the standard technique based on Lagrangian Energy integrals. The electro-mechanical coupling was not considered. The 4-node and 12 degrees of freedom isoparametric thin plate element and the classical Kirchoff displacement theory were used in the formulation. The shape control technique uses the relation between applied voltage and electric charge. The charge is then expressed as the surface density and then inserted into electric force vector. The electric force vector represents the actuator force responsible for actuation. The voltages are calculated using condensed sensor equation. The voltages are multiplied by a gain and used in feedback control law actuator. It is then iterated until the calculated displacements match the desired structural shape.

Chee et. al (2000a and 2000b) employed the 3rd order plate theory for mechanical deformation and the layer-wise theory for modelling the electric field in the finite element formulation for shape control of smart composite plate structures with rectangular actuators. They developed the Build-up Voltage Distribution (BVD) algorithm to search voltage distribution for specific desired shape, known as Displacement Based Shape Control (DBSC). Displacement is used as criterion in the objective function, which is defined in terms of normalisation of least square error between the calculated and desired nodal transverse displacements. They also extended the concept of Displacement Based Shape Control to using higher order attributes of shape such as Slope-Displacement Based Shape Control (SDSC) (Chee, Tong and Steven, 2002) and Curvature-Displacement Based Shape Control (CDSC) (Chee, Tong and Steven, 2001). They also developed the Perturbation Build-up Voltage Distribution

(PBVD) algorithm for SDSC and CDSC. The advantage of this algorithm is that the results reduced the bumpiness that occurred in DBSC.

An iterative structural shape control approach for improving the smoothness of the controlled surface needs to employ many different criteria. The angle/orientation of a piezoelectric actuator was also considered as a design variable to minimise the error function (Chee, Tong and Steven, 2002). The technique of piezoelectric actuator orientation optimisation is based on a similar concept of BVD algorithm. Chen et. al (2004) employed displacement-stress dual criteria. This approach is based on normal displacement control where stress modification is considered in the entire optimisation process to control high stress in the local domain.

In the majority of research available on static structural shape control, the energy consumption is not mentioned. Sometimes, the required energy consumption is very high to achieve the desired structural shape. Energy consumption is a very important issue in shape control problems. Sun and Tong (2003) used Lagrangian multiplier method to develop an algorithm to minimise the difference between the calculated and desired shapes under constrained energy consumption. They also presented the method that minimised the energy consumption with displacement constraint handling. Mukherjee and Joshi (2001) developed the algorithm to minimise the power consumption based on the actuator layout for achieving the specified displacement in plates.

1.5.2 Dynamic Control

The use of piezoelectric actuators to control the vibration of structure is widely used in development of high performance structures such as adjustment of structural damping. A lot of research works have been carried out on development of techniques to control structure responses. Tzou and Tseng (1991) presented technique of structural identification and vibration control in conjunction with FE method. It is particularly applied to distributed actuators and sensors. Lim et. al (1996) illustrated the transient response of smart structure using finite element incorporated with a modified time integration technique. Redmond and Barney (1997) proposed a vibration control technique for plates with integrated PZT stack actuators. The application is in damping

vibration-manufacturing platens. It was noted that actuators should be placed in region of high strain or curvature.

Akella et. al (1994) noted that the location, distribution and number of piezoelectric actuators and sensors affects the stability, controllability, observability and enhances robustness in vibration control of smart structure. Mackiewicz et. al (1996) and Kang et. al (1996) searched the sizes, number and locations of the piezoelectric sensors/actuator to control vibration of smart composite beams. Irschik et. al (2003) designed the piezoelectric actuation to obtain a displacement field that coincides with a selected dynamic displacement field induced by external forces. Librescu et. al (1997) integrated structural tailoring and piezoelectric materials to control the dynamic response of cantilever beams subject to external excitations. Kang et. al (1998) presented a gradient-based numerical scheme based on the damping characteristics to optimise the sensor and actuator placement for vibration control of plates. Sloss et. al (2001) developed an integral equation approach for the closed loop displacement feedback control for smart beams. The accuracy of approximation eigenvalues can be easily determined when the kernel of the integral equation is expanded in terms of the characteristic functions. Rizet et. al (2000) developed an algorithm to control the flexural vibrations of a beam with a modal filtering for first five modes. The control algorithm was implemented on a Digital Signal Processing (DSP) board and the input and output signals were filtered using high order low pass filters

In current researches, there are two available control algorithms such as multiple inputs - multiple outputs (MIMO) and single input - single output (SISO). MIMO control algorithm with full state feedback is the most effective control method. The advantage of this algorithm is to control multiple modes instantaneously. Zhang et. al (2000) employed genetic algorithm technique to optimise the piezoelectric actuator and sensor locations and feedback gain simultaneously. Tong et. al (2001); and Sun and Tong (2002) developed an integration approach for the closed-loop displacement feedback control. (Sun et. al, 2001) investigated the effects of piezoelectric sensor/actuator debonding on vibration control of smart beams. More detail on shape control of structures can be found in Irschik (2002).

1.6 Design Optimisation

Design optimisation problems have drawn much attention from mathematicians, scientists, and engineers. The unconstrained and constrained optimal problems are the two types in engineering design. Both aim to minimise or maximise the objective function. Constrained optimal problem is very much interested in real engineering design. For a general engineering design problem, the optimisation can be mathematically expressed as

$$\text{Minimise} \quad F(x) \tag{1.12}$$

$$\text{Subject to} \quad g_j(x) \leq 0 \qquad (j=1,...,N_c) \tag{1.13}$$

Where $x \in R$ denotes the vector of design variables, $F(x)$ is the objective function and $g_j(x)$ is the constraints. N_c is the number of constraints

In Section (1.5) the use of piezoelectric actuator to perform shape control has been shown to be very promising by many authors but this can involve many variables. There is a need to optimise the use of piezoelectric actuators in terms of their various objectives and constraints of the design problem. The objective function, in general is a function of the electric field, actuator thickness, adhesive thickness, location, size and shape of actuators.

1.6.1 Mathematical Optimisation

Mathematical optimisations were the first search technique for structure optimisation. In 17^{th} and 18^{th} centuries, the Lagrangian function was used to formulate the constrained optimisation problem. The objective function was extended by adding the product of multiplier λ and sum of constraints (g_j) and slack variables (s_j) as shown in Equation (1.14). It is then converted into an unconstrained extremum problem, and the optimal solution can be obtained by solving system of Equation (1.15).

$$\begin{aligned} L(x,s,\lambda) &= F(x) + \lambda^T \hat{g} \\ \hat{g}_j &= g_j(x) + s_j \end{aligned} \tag{1.14}$$

$$\begin{cases} \dfrac{\partial L}{\partial x} = 0 \\ \dfrac{\partial L}{\partial \lambda} = 0 \\ \dfrac{\partial L}{\partial s} = 0 \end{cases} \tag{1.15}$$

Venkayya (1993) noted that the solution restricts the range of application, for which the problem is non linear and has differential equation system, except in some very simple cases.

Due to lack of Langrangian function, Sequential Linear Programming has been adopted to deal with non-linear constrained optimisation problem (Kelley, 1960). The method was based on and extended from the idea of Linear Programming, which has been developed in the middle of last century (Dantzig, 1948 and 1963). The first order Taylor's expansion was employed to linearise the non-linear objective function and constraints about design point. This linear equation system can be solved using simplex algorithm. It can be expressed as

$$\begin{aligned} \hat{F}(\delta x) &= F(x_{p-1}) + \nabla F(x_{p-1})\delta x \\ \hat{g}(\delta x) &= g(x_{p-1}) + \nabla g(x_{p-1})\delta x \end{aligned} \tag{1.16}$$

Where: $\delta x = x_p - x_{p-1}$ and $\delta x_L \le \delta x \le \delta x_u$

δx is defined in terms of x in the present (x_p) and previous (x_{p-1}) iterations. δx with subscripts of U and L are the side constraints, known as moving limit. ∇F and ∇g are gradients of objective function constraints in the present and previous iteration.

Following simplex algorithm, Hadley (1964) developed Quadratic Programming using Kuln-Tucker condition, slack variables and extension of simplex algorithm to deal with quadratic objective function and linear constraints. Sequential Quadratic Programming was also developed by Powell (1978) based on Quadratic Programming formulation. In general, mathematical methods can be applied to a problem with a large

number of design variables, constraints and objective function. It is easily emerged to various numerical analysis techniques as finite element analysis. Venkayya (1993) found that there were too much local optimum solutions for complex problem, and the global optimum solution cannot be reachable. However, mathematical optimisations are applied in various fields of design optimisation. Kristensen and Madsen (1976) used SLP to optimise shape of fillets in plate structures. Lamberti and Pappalettere (2000) compared the numerical efficiency of different SLP based algorithms for structural optimisation. Tong and Sun (2002) used the SLP to optimise the shape of the bonded patch to minimise the adhesive stresses in curved thin-walled structures. Sun and Tong (2003) optimised the control voltage constrained using an algebraic equation in terms of the Lagrangian multiplier for static shape control of mart structures.

1.6.2 Optimality Criteria

Optimality criteria methods were developed in the late 1960s as an alternative approach to mathematical programming methods for solving structural optimisation. The fundamental ideas of these methods were based on the works of Michell (1904) on the least weight plane trusses. Prager and Sield (1967) initially developed optimal layout theory. The continuum based optimality criteria method is then developed based on the variational methods. Rozvany and Zhou (1994) took the advantage of development in both school of analytical and numerical optimisation to develop the optimality criteria (OC) methods, which are capably applied to both discrete and continuum structures. In the OC method, the objective functions are indirectly optimised instead of directly optimised in the mathematical programming methods. OC can be used to deal with the optimisation problems, which have a large number of the desired variables (Rozvany, 1989). It has been shown that the OC methods are more computationally efficient and also more significantly powerful than mathematical programming method. Optimality criteria are derived based on Kuhn-Tucher condition as an integral part of the method formulation to satisfy a set of criteria related to the behaviour of the structure based on Hassani and Hinton (1998). Equations (1.12) and (1.13) can be rewritten in general form as shown in Equation (1.17).

$$\begin{cases} \dfrac{\partial F}{\partial x_i} + \sum_{j=1}^{N_c} \lambda_j \dfrac{\partial g_j}{\partial x_i} = 0 \\ g_j \le 0 \\ g_j \lambda_j = 0 \\ \lambda_j \ge 0 \end{cases}$$ Where: i is the number of design variables (1.17)

The convergence of the OC method depends on the resizing or scaling scheme of the design variables and type of optimisation problem. The aim of resizing or scaling is to reduce number of steps required by leading to design variable to constrained boundaries. In examples of Khot et. al (1979) and Venkaya (1993), the recursive resizing of the design variables for next iteration can be defined in terms of design variables of current iteration (k^{th}) as shown Equation (1.18) and (1.19), respectively.

$$x_i^{k+1} = \left[\alpha - (1-\alpha) \left(\frac{\sum_{j=1}^{N_c} \lambda_j \dfrac{\partial g_j}{\partial x_i}}{\dfrac{\partial F}{\partial x_i}} \right)^k \right] x_i^k \qquad (1.18)$$

$$x_i^{k+1} = \left[\left(\frac{-\sum_{j=1}^{N_c} \lambda_j \dfrac{\partial g_j}{\partial x_i}}{\dfrac{\partial F}{\partial x_i}} \right)^k \right]^{\left(\frac{1}{\alpha}\right)} x_i^k \qquad (1.19)$$

Where α is a relaxation factor controlling the step size.

1.6.3 Stochastic Optimisation Methods

Genetic Algorithm (GA) and Simulated Annealing (SA) are the two algorithms of stochastic optimisation methods. GA is capable of handling parameters and constraints that may be changed during the optimisation process. It involves optimising an objective function. GA is a search technique based on population genetics, which is introduced by Holland (1975) and extended by Goldberg (1989). GA is characterised by bit string presentations of a possible solution to a given problem, known as population. Each

population has an objective function. Procedures are based on the crossover and the mutation operator. Crossover involves cutting bit string in one population and joining it to other cut bits. Mutation changes one bit in the population. SA is motivated from the principles of statical mechanics. GA and SA have been widely used in control of smart structure. Odetayo and McGregor (1989) presented a simple dynamic system using GA. Onada and Hanawa (1992) compared different approaches of finding optimal actuators location for static shape control. The methods included Exhaustive Single Point Substitution, Worst Out Best In, SA and GA. In addition, SA and GA were combined to produce Improved Simulated Annealing. The optimisation of actuators location can be achieved by GA and can be even improved by combining this with deterministic algorithm (Furuya and Haftka, 1996). The problem of optimum placement of piezoelectric actuator and sensor for vibration control of a composite plate was attempted by Han and Lee (1999). Nagaya and Ryu (1996) employed GA to investigate shape control of a flexible beam with actuators that consist of shape memory alloy wires and are governed by a linear constitutive equation.

1.6.4 Shape Optimisation

In the optimisation problem, when the geometries of an existing boundary are chosen as design variables to optimise then it will be known as Shape Optimisation (SO), where the finite element analysis, sensitivity analysis and mathematical programming algorithms are combined in one optimisation algorithm. It has been developed by Zienkiewicz and Campbell (1973) using sequential linear programming to optimise the boundary node of FEA model for a dam. It also can be found in Haftka and Grandhi (1986) and Ding (1986). Unlike the optimisation of discrete design variables, shape optimisation must be continuum problem and the design variables alter in order to improve the structural performance. The optimisation of continuum problem is more expensive in computational cost and sensitivity analysis. Botkin and Bennett (1985) mentions that the mesh generation occupied about 30% computer processing time. It is also very difficult to maintain adequacy in finite element analysis. Therefore in shape optimisation, three important issues (desired variable boundaries, structural analysis and finite element mesh) are considered to define the number of desired variables and to avoid the boundary meshing distortion or the crashing of elements or the general deterioration of finite element results due to changes in boundary. Bhavikatti and

Ramakrishnan (1977) and Ding (1986) used the polynomial constants as design variables to reduce the number of design variables. Imam et. al (1982) used elements as design variables, which are controlled by selected nodes in those elements. Braibant and Fleury (1984) used B-spline function as boundary representation. The FE mesh has been manually regenerated after a certain number of iterations of optimisation process by Oda and Yamazaki (1981). Botkin and Bennett (1985) used automated mesh generation in advance.

1.6.5 Topology Optimisation

Topology optimisation is a much more generalised problem that supplies greater improvement in structural performance. The basic concept is that the perturbations of design variables in the design structure are based on deleting and adding material. This method can be applied for problems that have either continuum or discrete design variables. The design variables are relaxation instead of alteration in order in the shape optimisation method. Lurie and Cherkaev (1984) and Bendsøe (1995) noted that topology optimisation cannot always achieve true optimal solution. Topology optimisation approaches the optimal solution based on variable material density function (ρ). Kohn and Strang (1983); and Lurie and Cherkaev (1984) mentioned that the solution may be yielded in three possible regions such as solid ($\rho=1$), empty ($\rho=0$) and porous ($0\langle\rho\langle 1$) when using a microstructure model. Yin and Wang (2001) noted that there are mainly two types of problems in the literature on topology optimisation. One is on minimisation of the material resource, subjected to equilibrium condition and structural performance. The other is focused on the optimisation of structure performance, subjected to equilibrium condition and material resources. The topology method is classified into three groups known as homogenisation method, material distribution without homogenisation and optimisation method without material model.

Firstly, Homogenisation method has been developed by Bendsøe and Kikuchi (1988) and is based on mathematical optimisation including theory of homogenisation. The concepts of homogenisation method are the use of a microstructure model and the theory of the homogenisation to aggregate the micro material properties. Rozvany et. al (1992 and 1995) noted that the structure is optimised based on an optimal

microstructure, which produces topologies with large porous region, and is not practical in the most engineering applications.

In the second group, Yang and Chuang (1994); and Maute and Ramm (1994) considered the continuous artificial density function ($0 \leq \eta \leq 1$) instead of theory of homogenisation to determine the distribution of material in the structure. Artificial density function (η) is used as design variables to define the material volumes, which are known as artificial materials. The material volume is linearly proportional to η, where η is penalised by setting the exponential $n>1$ to ensure a solid void solution for topology optimisation (Zhou and Rozvany, 1991; and Rozvany et. al, 1992), as shown in Equation (1.20).

$$E_i = \eta_i^n E_0 \tag{1.20}$$

For optimisation without material model, Xie and Steven (1997) introduced the Evolutionary Structural Optimisation (ESO) with the goal of obtaining solid-void topologies. In traditional ESO algorithms, the initial design domain of structure is set to be greater than the optimal design with a dense finite element mesh. The elements are gradually removed in accordance with a given elemental criterion during the optimisation process to achieve a performance function. Xie and Steven (1992); and Steven and Xie (1993) considered a stress criterion to decide the efficiency of the material usage and slowly remove it from structure. Following that, Querin (1997); Querin et. al (1998); and Young et. al (1999) developed bi-directional evolutionary structural optimisation (BESO), which is an extension of ESO, where material is allowed to be removed from low-stressed areas or added to high-stressed regions in the structure during the evolution process in order to achieve the best structural performance. The ESO has been progressively developed into more reliable and practical design tool including stiffness (Chu et. al, 1996), frequency (Xie and Steven, 1994; and Zhao et. al, 1996) and thermal conductivity (Li et. al, 1999). The application of ESO to multiple criteria optimisation has been developed by Proos et. al (2000). The displacement and thermo-elastic sensitivities that were respectively derived by Chu et. al (1996) and Li et. al (1999) are chosen as criteria to deal with stiffness and thermo-elastic optimisation problem.

1.7 Thesis Scope

The development of the TODL-finite element formulation of smart composite plate structures using third order plate theory and linear layer-wise formulation for modelling the mechanical deformation and electric field has been developed in 1999 (Chee et. al, 1999). The TODL-FE software was written for and thus limited to the 8 nodes serendipity rectangular element using symbolic integration. The first idea behind this thesis is the extension of TODL-FE software to TOF-FE software that uses 8 nodes isoparametric element and the addition of numerical time integration scheme and dynamic analysis capability. Secondly, the research will be concentrated on the piezoelectric actuator design optimisation (PADO) for static shape control problem in terms of achieving the desired structural shape. This will utilise the TOF-FE software to allow greater generality of the structure, to be controlled with non-rectangular actuators. The research also investigates controlled resonant vibrations. The objectives of the research include following major points.

1.7.1 FE Formulation for Laminated Composite Plate Structures with Non-Rectangular Element

The TODL-FE software can only be applied to a shape control problem with rectangular elements as well as rectangular actuators. However, it is not practically easy to strictly/closely generate good/accurate rectangular shape when small actuator elements are actually manufactured. Therefore, to study and improve on the shape control of a smart plate with complicated shapes, TOFL-FE software is developed further to deal with non-rectangular elements as well as non- rectangular actuators. Eight-node isoparametric element is used to transform the global coordinates to local coordinates. The volume integral has been transformed into the sum of the elemental volume integrals using the *3x3* Gaussian Quadrature numerical integration methods. This finite element formulation of smart composite plate structures also incorporates third order plate theory and linear layer-wise formulation for modelling the mechanical deformation and electric field. The TOF-FE software in static analysis is numerically compared with the TODL-FE software and commercial FE software Strand7 solutions to show its convergence and accuracy. Experimental facility is developed to test the structural behaviour under the presence of electric field in piezoelectric materials in

order to verify the TOF-FE formulation. From this point onwards, the TOF-FE formulation is incorporated into control algorithms based on voltage and piezoelectric actuator design optimisation.

1.7.2 Static Shape Control

The shape control problem aims at achieving the final shape that is as close as possible to desired structural shape by optimising the piezoelectric actuator configuration and applied voltage to piezoelectric actuator patches. Koconis et. al (1994) and (Chee et. al (2000a) developed analytical and numerical solution, respectively, to determine the optimum values of the applied electrical fields to given shaped actuators for achieving the specified desired structural shapes. Nguyen and Tong (2002a) showed the effects of varying actuator shapes on the error function and the applied voltage, where the optimal actuator shape has the potential to give better controllability with reduced energy consumption. For this reason, this research attempts to develop shape control algorithms to optimise piezoelectric actuator configurations and required applied voltage for achieving the desired structural shape. Two groups of algorithms are developed to solve this problem. One is Piezoelectric Actuators Design Optimisation group, where geometrical dimensions of actuators are chosen as design variables for piezoelectric actuator shape optimisation. The other is Evolutionary Piezoelectric Actuators Design Optimisation group, which optimises the piezoelectric actuator shape based on removing of piezoelectric material elements. These methods are applied to previously known test examples and the results are compared to show the improvement in the error function

1.7.2.1 Piezoelectric Actuators Design Optimisation

Generally, Linear Least Square (LLS) (Rorres and Anton, 1979) and GA are employed to develop algorithms for finding/optimising the shape and applied electric fields of piezoelectric actuators.

- For a known applied voltage: GA method was used.

- To optimise shape and voltage simultaneously, the following methods were introduced:
    - Only GA method was used.
    - By alternatively uniting of LLS and GA methods, known as Coupled-Alternating Algorithm (CAA).
    - Combination of LLS and GA methods, where LLS is mapped into GA to compute the fitness function, known as Coupled-Concurrent Algorithm (CCA).

1.7.2.2 Evolutionary Piezoelectric Actuators Design Optimisation

The Linear Least Square (LLS) and the feature of evolutionary strategies (Xie and Steven, 1997) are employed to find the applied voltages and configuration for the active piezoelectric actuators, respectively, to achieve the desired structural shapes subjected to the removal of active piezoelectric material based on the error function sensitivity number. On the basis of the FE analysis, an error function sensitivity number including electro-mechanical effect is derived to compute the change in error function, which is defined in terms of the least square difference between calculated and desired structural shape, due to removing active piezoelectric materials. The Evolutionary Piezoelectric Actuator Design Optimisation (EPADO) is proposed here. It has been developed further to include applied voltage optimisation, which is named as Alternative Voltage and Evolutionary Piezoelectric Actuator Design Optimisation (AVEPADO); and Voltage and Evolutionary Piezoelectric Actuator Design Optimisation (VEPADO). Both algorithms aim to optimise the active piezoelectric actuator configuration and the applied voltages to such multi-criteria design problem.

1.7.3 Static Shape Control with constraints handling

The literature reviews noted that the applied voltage requirement is usually very high in order to achieve the desired structural shape. In the current state of technology, there are many limitations on piezoelectric materials including the applied electric field requirements. Such limitations include: 1) high voltage leading to depolarisation; 2) in the high voltage range, the relationship of strain and applied voltage is nonlinear (the

current analysis may not be applicable); 3) there may be a limit on available energy. Due to these problems, the topic of shape control with energy constraint is now interesting in engineering practice. Sun and Tong (2003) used Lagrangian multiplier method to develop an algorithm to minimise the difference between the calculated shape and desired shape under constrained energy consumption for voltage optimisation only. They also presented the method that minimises the energy consumption with displacement constraint handling. The results note that it is hard to achieve the desired structural shape when control energy considered is below the optimal value, which is obtained without considering constraint. For this reason, this dissertation attempts to investigate the effect of voltage and piezoelectric shape optimisation on the error function for shape control problem with energy constraint. Genetic Algorithm (GA) is employed to optimise the applied voltage and the configuration of piezoelectric actuators to achieve the desired structural shapes subjected to a given energy consumption limits. In addition, the algorithm is modified to minimise the total energy consumption subject to error function constraint including voltage and piezoelectric actuator configuration optimisation.

1.7.4 Controlled resonant vibration

As an extension of static shape control problem, the modal analysis and LLS techniques are also employed to optimise the applied electric fields in actuators in order to achieve the desired modal shapes. The Newmark direct time integration method is used to study harmonic excitation of smart structures. The formulation for harmonic vibration of structure with controlled magnitude via adjusting the damping is introduced.

2. Finite Element Formulation and Verifications

In this chapter, the finite element formulation for the general laminate composite plate structures is extended to analyse static and dynamic deformations of the smart structures with non-rectangular elements. Its mechanical deformation is modelled using a third order plate theory, while the electric field is simulated based on a layer-wise theory. For both static and dynamic cases, the finite element formulation is verified by comparing with available numerical results. Experimental facilities have been set up to test structure deformations induced by applying electric field to piezoelectric actuators to validate the finite element formulation for static deformation. The numerical results demonstrate the influence of the shapes of actuators to the error function for static shape control. The results are obtained for the optimum values of the electric field in the actuators to achieve the desired shape using the Linear Least Square (LLS) method.

2.1 Introduction

The shape control problem aims to achieve the optimal shape, as close as possible to the desired structural shape by optimising the configuration and applied voltages to piezoelectric actuator patches. It can be solved by an iterative procedure consisting of finite element analysis. For piezoelectric actuator design optimisation, the incorporation of non-rectangular shaped element into FE software is very important. It effectively helps to analyse the problems with complicated piezoelectric actuator configurations, as well as to study its improvement on the shape control of smart plate structure. First thing of this research work aims to develop finite element software, which is capable to solve shape control problem with non-rectangular actuators. Most of the research on static shape control focus on finding the optimum values of the applied electric fields applied to rectangular-shaped piezoelectric actuators for achieving the desired structural shape. For example, Koconis et. al (1994) developed analytical methods for determining the optimum values of the applied electrical fields to fixed rectangular-shaped actuators for achieving the specified shapes for sandwich plates and shells. Chee et. al (2000a) employed the 3rd order plate theory (Lo et. al, 1977) for modelling mechanical

deformation and the layer-wise theory (Saravanos and Heyliger, 1995) to model the electric field in the finite element formulation for shape control of smart composite plate structures with rectangular actuators.

Composite structures have drawn considerable interest for structure performance in the transverse direction by using in-plane elements to avoid three dimensional finite element modelling. Past research developed and employed several theories to model displacement field. The first theory is classical displacement theory where the transverse shear effect and transverse normal strain are not included. The classical Kirchoff's thin plate bending theory was used by Crawley and Lazarus (1991), whereas the Bernoulli-Euler thin beam theory was employed by Chaudhry and Roger (1994). Wang and Roger (1991) expanded classical bending theory to classical laminated plate theory to deal with the coupling of extension, bending and twisting in plate structure. From theoretical prediction of experimental results, Reddy and Phan (1985) noted that there is under-prediction of displacement and over-prediction of natural frequencies and buckling load for thick composite model. Another group of formulations, which includes transverse shear effect, is known as the first order shear deformation theory or the Reissner-Mindlin theory for plate and has presented the shear-locking phenomenon (Prahbu and Dhanaraj, 1994). Whitney and Pagano (1970) developed an analytical formulation for heterogeneous anisotropic plates. Pryor and Parker (1971) developed FE formulation for laminated composite plate. Prabhu and Dhanaraj (1994) discussed shear locking in thermal buckling of laminated composite plate. Kabir (1995) developed triangular FE for thick and thin laminate composite plate. In first order shear deformation theory; the shear correction factor (SCF) is required due to the inaccuracies in the solution. SCF were estimated based on the comparison with exact elasticity solution, which is used to correct surface condition. The SCF does not arise naturally out of the formulation and thus has no physical foundation. Its value is taken as *5/6* (Kabir, 1995). Whitney and Pagano (1970) noted that shear deformation was quite significant for thick anisotropy laminated composite plate (h/a=*20*%). Another type of displacement theory is known as higher order displacement theory. For example, Lo et. al (1977) determined interlaminar stresses using a third order displacement theory for laminated plates. Reddy and Phan (1985) derived analytical formulation for laminated composite plate based on Reddy's higher order shear deformation, and Phan and Reddy (1985) pointed out that the SCF is not needed when using Reddy's higher order shear deformation. Chee (2000c)

mentioned that the third order plate theory has many advantages as it can be used to model both thick and thin laminate structures, transverse shear strains in different directions, shear correction factor is not required and the displacement field is independent of material properties, boundary conditions and derivatives. Lo et. al (1977) used the cubic displacement function relative to transverse dimension, whereas the displacement function is simplified within certain boundary condition (Putcha and Reddy, 1986a and 1986b; Reddy, 1984, 1987, 1989a, 1989b, 1989c). Gu et. al (2000) employed a higher order theory to model the coupled thermo-piezoelectric-mechanical behaviours. Chee (2000c) employed the Hamilton's variational principle to develop the finite element formulation for smart laminate composite plate structure based the 3rd order plate theory and the layer-wise theory that uses 8-nodes rectangular element and Maple software to integrate the electrical and mechanical stiffness matrix. The layer-wise formulation has been developed by Reddy (1989a), and was shown to be better used for modelling a structure with multiple types of material. This formulation also has been applied to smart structure using piezoelectric materials (Robbins and Reddy, 1991; Heyliger et. al, 1994; Saravanos and Heyliger, 1995; and Saravanos, 1997). Heyliger noted that this formulation has more accuracies and lower computational cost than higher order displacement theory. That was the reason why the mechanical variables were modelled using 3rd order plate theory and only the layerwise formulation is considered for electrical variables in this FE formulation (Chee, 2000c).

In this chapter, based on the finite element formulation for smart laminate composite plate structure (Chee et. al, 2000a), a finite element formulation using non-rectangular element is developed to analyse in order to then optimise the piezoelectric actuator configuration. The dynamic analysis is also included as modal analysis and free vibration analysis. It was built and developed on the same displacement, electrical field theories and variational principle (Nguyen and Tong, 2002 and 2004). The real displacements can be interpolated using the shape functions and nodal variables for an 8 nodes isoparametric element. The entire mechanical, electrical and electro-mechanical stiffness matrices are calculated by using numerical integration method. Finally several numerical examples was presented in order to verify the finite element formulation for static and dynamic analyses by comparing with numerical results available and numerical results obtained from commercial software Strand7. The developed software (called TOF) uses linear layer-wise electric potential theory whilst Strand7 uses thermal

expansion theory. Strand7 is not applied for problem under electrical loading. Several experiments have also been conducted to measure the structural deformation under influence of electric current and verified the finite element formulation by correlating with experimental results for static analysis. In addition, some numerical examples are present to study the influence of the shapes of piezoelectric actuators variations on the resulting error function and applied voltage for quasi-static shape control problem. Numerical results are obtained for the optimum values of the electric field in the fixed piezoelectric actuators shape to achieve the desired structural shape using the Linear Least Square (LLS) method (Rorres and Anton, 1979).

2.2 Analytical Formulation

This section describes in detail the 3rd order plate theory and layer-wise concept, which are respectively used to model the mechanical deformation and electric field for smart laminated composite plate structure in FE formulation (Chee, 2000c).

2.2.1 Displacement Field

The displacement field theory of laminated composite plate based on the 3rd order plate theory, proposed by Lo et. al (1977), is used to model the mechanical deformation of the structure as shown in Equation (2.1) and refer to Figure (2.1) for global coordinate systems.

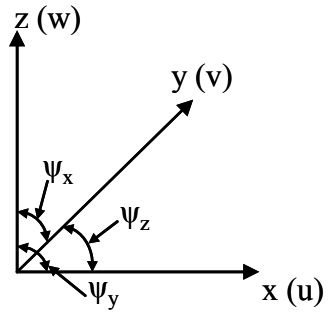

Figure 2.1: Global coordinate systems

$$
\begin{aligned}
U(x,y,z) &= u_o(x,y) + z\psi_x(x,y) + z^2\zeta_x(x,y) + z^3\phi_x(x,y) \\
V(x,y,z) &= v_o(x,y) + z\psi_y(x,y) + z^2\zeta_y(x,y) + z^3\phi_y(x,y) \\
W(x,y,z) &= w_o(x,y) + z\psi_z(x,y) + z^2\zeta_z(x,y)
\end{aligned}
\tag{2.1}
$$

Where $U(x, y, z)$, $V(x, y, z)$ and $W(x, y, z)$ are the total displacements at any point in the laminate plate in the direction of x, y, z coordinates, respectively. For any point on the mid-plane with x & y coordinates, $u_o(x,y)$, $v_o(x,y)$ are the two in-plane displacements and $w_o(x,y)$ is the out-of-plane displacement; ψ_x, ψ_y and ψ_z are the rotations about the x, y and z axes of the reference mid-plane. And ζ_x, ζ_y, ζ_z, ϕ_x and ϕ_y are the higher order terms in the Taylor's series expansions of the total displacements.

Chee et. al (1999) noted that Equation (2.1) can be used due to its generality. It can be used to model both thick and thin laminate structures including the effects of transverse shear and transverse normal strain without shear correction factor. Also the displacement field is independent of material properties, boundary condition and derivative.

2.2.2 Strain-Displacement Relation

Mechanical strains are defined as Cauchy's infinitesimal strain tensor (Chee, 2000c) as shown in Equation (2.2).

$$\begin{aligned} \varepsilon_{xx} &= \frac{\partial U}{\partial x} \quad ; \quad \gamma_{yz} = \left(\frac{\partial V}{\partial z} + \frac{\partial W}{\partial y} \right) \\ \varepsilon_{yy} &= \frac{\partial V}{\partial y} \quad ; \quad \gamma_{zx} = \left(\frac{\partial W}{\partial x} + \frac{\partial U}{\partial z} \right) \\ \varepsilon_{zz} &= \frac{\partial W}{\partial z} \quad ; \quad \gamma_{xy} = \left(\frac{\partial U}{\partial y} + \frac{\partial V}{\partial x} \right) \end{aligned} \tag{2.2}$$

Where: ε_{xx}, ε_{yy} and ε_{zz} are normal strains. γ_{xy}, γ_{yz} and γ_{zx} are shear strains.

2.2.3 Electrical Field

As discussed in the literature review (Section 2.1), Robbins and Reddy (1991); Saravanos and Heyliger (1995) used layer-wise concept to developed formulation for thick and thin laminated composite structures. It is suitable to demonstrate the electric potential in the layers of laminated composite structure. Chee et. al (1999) applied this

concept to model electrical variables only due to computational cost when layer-wise is applied for entire structure including electro-mechanical variables. The basic concept of this formulation is similar to "Separation of Variables' technique (Chee, 2000c), where z variable (thickness) is decoupled from x and y variables. Equation (2.3) shows the electric potential in laminated composite structure based on layer-wise concept.

$$\phi(x,y,z) = \sum_{l=1}^{nlayer+1} L_l(z)\phi_l(x,y) \tag{2.3}$$

Where *nlayer* is number of layer in a structure. $L_l(z)$ and $\phi_l(x,y)$ respectively are layer-wise function and electric potential function in xy plane of l^{th} interface. The total electric potential in layer is the sum of electric potential on top and at bottom interface of that layer. Therefore, the total electric potential of "*nlayer*" layers is the sum of "*nlayer+1*" interfaces electric potential.

The voltage distribution between two interfaces of j^{th} (j=*1*, …, nlayer) layer is a linear function. Therefore, the electric potential within the j^{th} layer can be defined by linearising the electric potential of top and bottom interface in z direction (See Appendix A). So it can be written as Equation (2.4). Figure (2.2) shows the configuration of j^{th} layer.

$$\phi_j(x,y,z) = \frac{z - z_{j+1}}{z_j - z_{j+1}}\phi_j(x,y) + \frac{z - z_j}{z_{j+1} - z_j}\phi_{j+1}(x,y) \tag{2.4}$$

Where z_{j+1} and z_j are top and bottom interfaces coordinates of j^{th} layer, respectively.

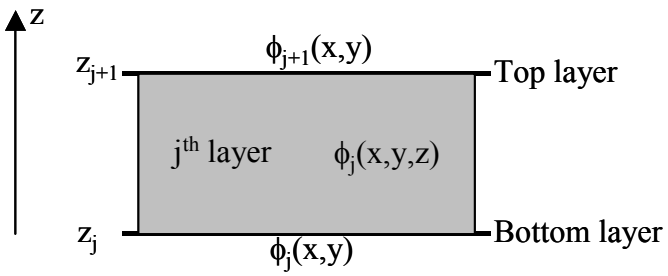

Figure 2.2: Electric potential of j^{th} layer

The electric field is defined in term of the first order derivative of the electric potential with respect to the displacement as shown in Equation (2.5).

$$E_{xx} = -\frac{\partial \phi(x,y,z)}{\partial x} \quad ; \quad E_{yy} = -\frac{\partial \phi(x,y,z)}{\partial y} \quad ; \quad E_{zz} = -\frac{\partial \phi(x,y,z)}{\partial z} \tag{2.5}$$

By substituting Equation (2.4) into Equation (2.5) and taking partial derivative with respect to x,y and z variables, the electric field within the j^{th} layer can be rewritten in form as Equation (2.6).

$$\begin{aligned}
E^{j}_{xx}(x,y,z) &= -\left[\left(\frac{z-z_{j+1}}{z_j - z_{j+1}}\right)\left(\frac{\partial \phi_j(x,y)}{\partial x}\right) + \left(\frac{z-z_j}{z_{j+1}-z_j}\right)\left(\frac{\partial \phi_{j+1}(x,y)}{\partial x}\right)\right] \\
E^{j}_{yy}(x,y,z) &= -\left[\left(\frac{z-z_{j+1}}{z_j - z_{j+1}}\right)\left(\frac{\partial \phi_j(x,y)}{\partial y}\right) + \left(\frac{z-z_j}{z_{j+1}-z_j}\right)\left(\frac{\partial \phi_{j+1}(x,y)}{\partial y}\right)\right] \\
E^{j}_{zz}(x,y,z) &= -\left[\left(\frac{\partial \phi_j(x,y)}{z_j - z_{j+1}}\right) + \left(\frac{\partial \phi_{j+1}(x,y)}{z_{j+1}-z_j}\right)\right]
\end{aligned} \tag{2.6}$$

2.2.4 Hamilton's Variational Principle

In structural analysis, sometimes it becomes a complex problem for solving analytical solutions. In the development of FE formulation, researchers tried to solve more complicated problems with acceptable accuracy and robustness compared to analytical solution. In all existing publications, it can be seen that the FE formulation has been developed based on Hamilton's variational principle. In this technique, the physics of the entire structure has been fully accounted in the variational energy integral and there is no need to derive equations based on force and moment. In the fields of smart/intelligent structure, the earliest FE formulation including piezoelectric effect has been developed by Allik and Hughes (1970) and followed by Tzou and his colleagues as discussed in more details in Chapter 1. The main difference in potential variational including piezoelectric effects is the electrical contribution in the potential energy. The constitutive equation does not only consist of stress (σ) and strain (ε) but also has

electric fields (E) and displacement (D). Also there are additional variables or degrees of freedom for electric potential (ϕ) besides the displacement (U) in virtual work.

The general equation of Hamilton's variational principle is stated in Equation (2.7)

$$\int_{t_0}^{t_1} \delta K \times dt - \int_{t_0}^{t_1} \delta P \times dt + \int_{t_0}^{t_1} \delta W \times dt = 0 \tag{2.7}$$

Where K, P, W are kinetic energy, potential energy and work done, respectively.

The kinetic energy variation is defined in term of a function of acceleration and variation of displacement and volume (V).

$$\int_{t_0}^{t_1} \delta \mathbf{K} \times dt = \int_{t_0}^{t_1} \left(\int_V \rho \delta \mathbf{U}_T^T \ddot{\mathbf{U}}_T \times dV \right) \times dt \tag{2.8}$$

Where:

$$\mathbf{U}_T = [U(x,y,z),\ V(x,y,z),\ W(x,y,z)]$$

Equation (2.9) shows the potential variation in terms of the relationship between σ, ε, D, and E in the global system via the piezoelectric constitutive equation (refer to Equation (1.6)).

$$\int_{t_0}^{t_1} \delta \mathbf{P} \times dt = \int_{t_0}^{t_1} \left(\int_V \left(\boldsymbol{\sigma} \times d\varepsilon - \mathbf{D} \times dE \right) \times dV \right) \times dt \tag{2.9}$$

Due to laminated composite structure modelling, each layer can be rotated about transverse z-axis as shown in Figure 1.1. The change in material properties will give the smart structure additional actuation authority due to rotation of the materials. Equation (1.9) shows the relation of electric displacement and electric field between the local coordinate system (σ_l, ε_l, D_l, and E_l) and global coordinate system (σ, ε, D, and E). By substituting a set of equations, which are introduced in Section 1.3, into form of Equation (1.8), Equation (2.10) then shows the general piezoelectric stress formulation

of coupled constitutive equation, which expresses in term of global material properties including rotation angle about lateral x-y plane.

$$\begin{bmatrix}\boldsymbol{\sigma}\\ \mathbf{D}\end{bmatrix}=\begin{bmatrix}\mathbf{T}^{-1}\mathbf{c}_{\text{local}}\mathbf{R}\mathbf{T}\mathbf{R}^{-1} & -\mathbf{T}^{-1}\mathbf{e}_{\text{local}}^{\text{T}}\mathbf{Q}\\ \mathbf{Q}^{-1}\mathbf{e}_{\text{local}}\mathbf{R}\mathbf{T}\mathbf{R}^{-1} & \mathbf{Q}^{-1}\boldsymbol{\chi}_{\text{local}}\mathbf{Q}\end{bmatrix}\begin{bmatrix}\boldsymbol{\varepsilon}\\ \mathbf{E}\end{bmatrix}=\begin{bmatrix}\mathbf{c}_{\text{global}} & -\mathbf{e}_{\text{global}}^{\text{T}}\\ \mathbf{e}_{\text{global}} & \boldsymbol{\chi}_{\text{global}}\end{bmatrix}\begin{bmatrix}\boldsymbol{\varepsilon}\\ \mathbf{E}\end{bmatrix} \tag{2.10}$$

The transformation matrices and local and global material properties matrices can respectively be found in Appendices C and D.

Equation (2.9) can now be rewritten in term of strain, electric field and material property variables including rotation angle about lateral x-y plane as shown in Equation (2.11).

$$\int_{t_0}^{t_1}\delta\mathbf{P}\times dt=\int_{t_0}^{t_1}\left(\int_V\left(\delta\boldsymbol{\varepsilon}_b^{\text{T}}(\mathbf{c}_b\boldsymbol{\varepsilon}_b-\mathbf{e}_b^{\text{T}}\mathbf{E}_o)+\delta\boldsymbol{\varepsilon}_s^{\text{T}}(\mathbf{c}_s\boldsymbol{\varepsilon}_s-\mathbf{e}_s^{\text{T}}\mathbf{E}_i)\right)\times dV\right)\times dt$$

$$-\int_{t_0}^{t_1}\left(\int_V\left(\delta\mathbf{E}_o^{\text{T}}(\mathbf{e}_b\boldsymbol{\varepsilon}_b+\boldsymbol{\chi}_o\mathbf{E}_o)+\delta\mathbf{E}_i^{\text{T}}(\mathbf{e}_s\boldsymbol{\varepsilon}_s+\boldsymbol{\chi}_i\mathbf{E}_i)\right)\times dV\right)\times dt \tag{2.11}$$

Where:

$$\boldsymbol{\varepsilon}_b=\begin{bmatrix}\varepsilon_{xx} & \varepsilon_{yy} & \varepsilon_{zz} & \gamma_{xy}\end{bmatrix}^{\text{T}};\quad \boldsymbol{\varepsilon}_s=\begin{bmatrix}\gamma_{yz} & \gamma_{zx}\end{bmatrix}^{\text{T}}$$

$$\mathbf{c}_b=\begin{bmatrix}c_{11} & c_{12} & c_{13} & c_{16}\\ c_{12} & c_{22} & c_{23} & c_{26}\\ c_{13} & c_{23} & c_{33} & c_{36}\\ c_{16} & c_{26} & c_{36} & c_{66}\end{bmatrix};\quad \mathbf{c}_s=\begin{bmatrix}c_{44} & c_{45}\\ c_{45} & c_{55}\end{bmatrix}$$

$$\mathbf{e}_b=\begin{bmatrix}e_{31} & e_{32} & e_{33} & e_{36}\end{bmatrix};\quad \mathbf{e}_s=\begin{bmatrix}e_{14} & e_{24}\\ e_{15} & e_{14}\end{bmatrix}$$

$$\boldsymbol{\chi}_i=\begin{bmatrix}\chi_{11} & \chi_{12}\\ \chi_{12} & \chi_{22}\end{bmatrix}\qquad \boldsymbol{\chi}_o=\begin{bmatrix}\chi_{33}\end{bmatrix}$$

$$\mathbf{E}_i=\begin{bmatrix}E_x & E_y\end{bmatrix}^{\text{T}};\qquad \mathbf{E}_o=\begin{bmatrix}E_z\end{bmatrix}$$

For convenience, strain is subdivided into bending strain $\boldsymbol{\varepsilon}_b$ and transverse shear strain $\boldsymbol{\varepsilon}_s$. It is also similarly done for mechanical stiffness constant, piezoelectric constant, electric permittivity and electric field.

For this formulation, there are two groups of virtual work, which are mechanical and electrical work. Mechanical work consists of volume load ($\mathbf{F}_V$), surface load ($\mathbf{F}_S$) and point load ($\mathbf{F}_P$). The electrical work consist only surface charge ($\mathbf{Q}_S$). The total work including both mechanical and electrical is shown in Equation (2.12).

$$\int_{t_0}^{t_1} \delta \mathbf{W} \times dt = \int_{t_0}^{t_1} \left(\int_V \delta \mathbf{U}_T^T \mathbf{F}_V \times dV + \int_S \delta \mathbf{U}_T^T \mathbf{F}_S \times dS + \delta \mathbf{U}_T^T \mathbf{F}_P - \int_S \delta \boldsymbol{\phi} \mathbf{Q}_S \times dS \right) \times dt \qquad (2.12)$$

2.3 Finite Element Formulation for Static and Dynamics Analysis

This section describes in detail the FE formulation based on the 3rd order plate theory and the layer-wise theory using Hamilton's variational principle, which were introduced from last section. The technique in FE formulation including piezoelectric effects is that all physical variables, such as σ, ε, E and D, are transformed into nodal variables including both mechanical (u) and electric (ϕ) quantities.

2.3.1 Element Representation

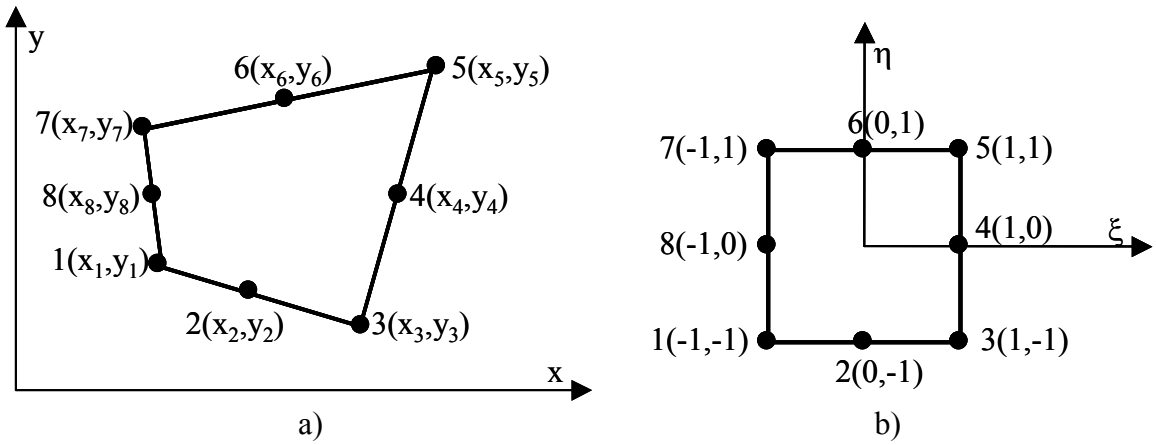

Figure 2.3: a) 8-node non-rectangular element in global coordinates.
b) 8-node square element in local coordinates.

A two-dimensional 8 nodes isoparametric element (Cook et. al, 1989) has been used for mechanical element. Its global and local coordinates are shown in Figure 2.3a and Figure 2.3b, respectively. The shape functions and their derivatives with respect to ξ and η are defined in Equation B.1, B.2 and B.3, respectively. For the change of variable during integration, the differential relationship is stated in Equation (B.4) in Appendix B.

2.3.2 Degrees of Freedom

2.3.2.1 Mechanical

Equation (2.1) is rewritten in matrix form as shown in Equation (2.13). Matrix **A**(z) consists of z variable and **u**(x,y) is composed of the in plane function as shown in Equation (2.14) and (Equation 2.15), respectively (Chee, 2000c).

$$\begin{bmatrix} U(x,y,z) & V(x,y,z) & W(x,y,z) \end{bmatrix}^T = \begin{bmatrix} \mathbf{A}(z) \end{bmatrix} \begin{bmatrix} \mathbf{u}(x,y) \end{bmatrix} \tag{2.13}$$

$$[\mathbf{A}(z)] = \begin{bmatrix} 1 & 0 & 0 & z & 0 & 0 & z^2 & 0 & 0 & z^3 & 0 \\ 0 & 1 & 0 & 0 & z & 0 & 0 & z^2 & 0 & 0 & z^3 \\ 0 & 0 & 1 & 0 & 0 & z & 0 & 0 & z^2 & 0 & 0 \end{bmatrix} \tag{2.14}$$

$$\begin{aligned} \mathbf{u}(x,y) = [\, & u_o(x,y) \quad v_o(x,y) \quad w_o(x,y) \quad \psi_x(x,y) \quad \psi_y(x,y) \quad \psi_z(x,y) \\ & \zeta_x(x,y) \quad \zeta_y(x,y) \quad \zeta_z(x,y) \quad \phi_x(x,y) \quad \phi_y(x,y)]^T \end{aligned} \tag{2.15}$$

$$\mathbf{u}(x,y) = \begin{bmatrix} \mathbf{N}_u(\xi,\eta) \end{bmatrix} \begin{bmatrix} \mathbf{u}_e \end{bmatrix} \tag{2.16}$$

Equation (2.16) shows that the in-plane function is expressed in term of mechanical nodal variables. Hence the Equation (2.13) becomes:

$$\begin{bmatrix} U(x,y,z) & V(x,y,z) & W(x,y,z) \end{bmatrix}_e^T = \begin{bmatrix} \mathbf{A}(z) \end{bmatrix} \begin{bmatrix} \mathbf{N}_u(\xi,\eta) \end{bmatrix} \begin{bmatrix} \mathbf{u}_e \end{bmatrix} \tag{2.17}$$

Where:

$$[\mathbf{N}_u(\xi,\eta)] = \begin{bmatrix} N_1 & . & . & N_2 & . & . & . & . & N_8 & . & . \\ . & * & . & . & * & . & . & . & . & * & . \\ . & . & N_1 & . & . & N_2 & . & . & . & . & N_8 \end{bmatrix}$$

$$\mathbf{u}_e = [u_1 \quad v_1 \quad w_1 \quad \ldots \quad \phi_{x1} \quad \phi_{y1} \quad \ldots \quad \ldots \quad u_8 \quad \ldots \quad \phi_{y8}]^T$$

With 8-node element and each node has 11 degrees of freedom. The interpolation function $[\mathbf{N}_u(\xi,\eta)]$ matrix has dimension of [*11x88*]. Star(*) represents the shape functions N_i (i = *1,…,8*) and Dot (.) in the above matrix represents zeros. u_e is displacement vector of [*1x88*] in dimension. u_i, v_i, w_i, ψ_{xi}, ψ_{yi}, ψ_{zi}, ζ_{xi}, ζ_{yi}, ζ_{zi}, ϕ_{xi} and ϕ_{yi} are the nodal displacement of node i inside element as per definition of Equation (2.1). Equation (2.6) is rewritten to express Strain-Displacement relation in term of mechanical nodal variables as shown in equations (2.18) and (2.19) for bending train and transverse shear strain.

$$\boldsymbol{\varepsilon}_b = \begin{bmatrix} \frac{\partial}{\partial x} & 0 & 0 & \frac{\partial}{\partial x} & 0 & 0 & \frac{\partial}{\partial x} & 0 & 0 & \frac{\partial}{\partial x} & 0 \\ 0 & \frac{\partial}{\partial y} & 0 & 0 & \frac{\partial}{\partial y} & 0 & 0 & \frac{\partial}{\partial y} & 0 & 0 & \frac{\partial}{\partial y} \\ 0 & 0 & 0 & 0 & 0 & 1 & 0 & 0 & 2z & 0 & 0 \\ \frac{\partial}{\partial y} & \frac{\partial}{\partial x} & 0 & \frac{\partial}{\partial y} & \frac{\partial}{\partial x} & 0 & \frac{\partial}{\partial y} & \frac{\partial}{\partial x} & 0 & \frac{\partial}{\partial y} & \frac{\partial}{\partial x} \end{bmatrix} [\mathbf{u}(x,y)] = [\mathbf{D}_b][\mathbf{u}(x,y)]$$

$$\boldsymbol{\varepsilon}_s = \begin{bmatrix} 0 & 0 & \frac{\partial}{\partial y} & 0 & 1 & \frac{\partial}{\partial y} & 0 & 2z & \frac{\partial}{\partial y} & 0 & 3z^2 \\ 0 & 0 & \frac{\partial}{\partial x} & 1 & 0 & \frac{\partial}{\partial x} & 2z & 0 & \frac{\partial}{\partial x} & 3z^2 & 0 \end{bmatrix} [\mathbf{u}(x,y)] = [\mathbf{D}_s][\mathbf{u}(x,y)]$$

or

$$\boldsymbol{\varepsilon}_b = [\mathbf{D}_b][\mathbf{N}_u(\xi,\eta)][\mathbf{u}_e] = [\mathbf{B}_{bu}][\mathbf{u}_e] \tag{2.18}$$

$$\boldsymbol{\varepsilon}_s = [\mathbf{D}_s][\mathbf{N}_u(\xi,\eta)][\mathbf{u}_e] = [\mathbf{B}_{su}][\mathbf{u}_e] \tag{2.19}$$

2.3.2.2 Electrical

In the finite element formulation, the electric potential in each interface is considered. Similarly to mechanical modelling, the Equation (2.20) shows that the interface functions in 2-dimentional can be expressed in term of the electrical nodal variables.

$$\begin{bmatrix} \phi_1(x,y) \\ \vdots \\ \phi_{j+1}(x,y) \end{bmatrix} = [\mathbf{N}_\phi(\xi,\eta)][\boldsymbol{\phi}_e] \tag{2.20}$$

Where:

$$\mathbf{N}_\phi(\xi,\eta) = \begin{bmatrix} \mathbf{N}_{\phi,1}(\xi,\eta) \\ \vdots \\ \mathbf{N}_{\phi,j+1}(\xi,\eta) \end{bmatrix} = \begin{bmatrix} N_1 & . & . & N_2 & . & . & . & . & N_8 & . & . \\ . & * & . & . & * & . & . & . & . & * & . \\ . & . & N_1 & . & . & N_2 & . & . & . & . & N_8 \end{bmatrix}$$

$$\boldsymbol{\phi}_e = [\phi_{11} \quad \cdots \quad \phi_{(j+1)1} \quad \cdots \quad \phi_{18} \quad \cdots \quad \phi_{(j+1)8}]^T$$

$[\mathbf{N}_\phi(\xi,\eta)]$ is an interpolation function matrix of [(nlayer+1) x ((nlayer+1)x8)] and ϕ_{ji} are the nodal electric potential of node i inside element as per definition of Equation (2.3).

For electric potential, the simplified equation of electric potential of j^{th} layer and e^{th} element in term interface (z-coordinate) and layer-wise functions can be expressed as shown in Equation (2.21).

$$[\boldsymbol{\phi}_e^j(x,y,z)] = \begin{bmatrix} \cdots & \dfrac{z-z_{j+1}}{z_j-z_{j+1}} & \dfrac{z-z_j}{z_{j+1}-z_j} & \cdots \end{bmatrix} [\mathbf{N}_\phi(\xi,\eta)][\boldsymbol{\phi}_e] \tag{2.21}$$

or

$$[\boldsymbol{\phi}_e^k(x,y,z)] = [\mathbf{N}_\phi(\xi,\eta,z)][\boldsymbol{\phi}_e]$$

Equation (2.4) is rewritten to express electrical fields in term of electrical nodal variables as mentioned from last section which are shown in Equation (2.22) and (2.23).

$$\mathbf{E}_x(x,y,z)_e^k = -\left[\left(\frac{z-z_{j+1}}{z_j-z_{j+1}}\right)\left[\frac{\partial N_1}{\partial\xi} \quad \cdots \quad \frac{\partial N_8}{\partial\xi}\right]\frac{\partial\xi}{\partial x}+\left(\frac{z-z_j}{z_{j+1}-z_j}\right)\left[\frac{\partial N_1}{\partial\xi} \quad \cdots \quad \frac{\partial N_8}{\partial\xi}\right]\frac{\partial\xi}{\partial x}\right]\left[\phi_e\right]$$

$$\mathbf{E}_y(x,y,z)_e^k = -\left[\left(\frac{z-z_{j+1}}{z_j-z_{j+1}}\right)\left[\frac{\partial N_1}{\partial\eta} \quad \cdots \quad \frac{\partial N_8}{\partial\eta}\right]\frac{\partial\eta}{\partial y}+\left(\frac{z-z_j}{z_{j+1}-z_j}\right)\left[\frac{\partial N_1}{\partial\eta} \quad \cdots \quad \frac{\partial N_8}{\partial\eta}\right]\frac{\partial\eta}{\partial y}\right]\left[\phi_e\right]$$

$$\mathbf{E}_z(x,y,z)_e^k = -\left[\left(\frac{1}{z_j-z_{j+1}}\right)\left[N_1 \quad \cdots \quad N_8\right]+\left(\frac{1}{z_{j+1}-z_j}\right)\left[N_1 \quad \cdots \quad N_8\right]\right]\left[\phi_e\right]$$

or

$$\mathbf{E}_i = \begin{bmatrix}\mathbf{E}_x & \mathbf{E}_y\end{bmatrix}^T = \left[\mathbf{B}_{\phi i}(\xi,\eta,z)\right]\left[\phi_e\right] \tag{2.22}$$

$$\mathbf{E}_o = \left[\mathbf{E}_z\right] = \left[\mathbf{B}_{\phi o}(\xi,\eta,z)\right]\left[\phi_e\right] \tag{2.23}$$

2.3.3 Finite Element Solution

The derived FE formulation, as in Sections 2.2.4, now can be expressed in terms of the nodal variables including both mechanical and electric quantities by substituting the displacement strain relation and electric field into equations (2.8), (2.11) and (2.12), yielding equations (2.24), (2.25) and (2.26), respectively.

$$\int_{t_0}^{t_1}\delta\mathbf{K}\times dt = -\int_{t_0}^{t_1}\left(\sum_{e=1}^{n_element}\delta\mathbf{u}_e^T\mathbf{M}_{uu}^e\ddot{\mathbf{u}}_e\right)\times dt \tag{2.24}$$

$$\int_{t_0}^{t_1}\delta\mathbf{P}\times dt = \int_{t_0}^{t_1}\left(\sum_{e=1}^{n_element}\left(\delta\mathbf{u}_e^T\mathbf{K}_{uu}^e\mathbf{u}_e-\delta\mathbf{u}_e^T\mathbf{K}_{u\phi}^e\phi_e-\delta\phi_e^T\mathbf{K}_{\phi u}^e\mathbf{u}_e-\delta\phi_e^T\mathbf{K}_{\phi\phi}^e\phi_e\right)\right)\times dt \tag{2.25}$$

$$\int_{t_0}^{t_1}\delta\mathbf{K}\times dt = -\int_{t_0}^{t_1}\left(\sum_{e=1}^{n_element}\left(\delta\mathbf{u}_e^T\mathbf{F}^e-\delta\phi_e^T\mathbf{Q}^e\right)\right)\times dt \tag{2.26}$$

Where n_element is the number of element in the structure and

$$\mathbf{M}_{uu}^{e} = \sum_{j=1}^{nlayer} \int_{\xi=-1}^{1} \int_{\eta=-1}^{1} \int_{z=z_j}^{z_{j+1}} \mathbf{N}_u^T \rho \mathbf{N}_u \left| \frac{\partial(x,y)}{\partial(\xi,\eta)} \right| dz d\eta d\xi \tag{2.27}$$

$$\mathbf{K}_{uu}^{e} = \sum_{j=1}^{nlayer} \int_{\xi=-1}^{1} \int_{\eta=-1}^{1} \int_{z=z_j}^{z_{j+1}} (\mathbf{B}_{bu}^T \mathbf{c}_b \mathbf{B}_{bu} + \mathbf{B}_{su}^T \mathbf{c}_s \mathbf{B}_{su}) \left| \frac{\partial(x,y)}{\partial(\xi,\eta)} \right| dz d\eta d\xi \tag{2.28}$$

$$\mathbf{K}_{u\phi}^{e} = \sum_{j=1}^{nlayer} \int_{\xi=-1}^{1} \int_{\eta=-1}^{1} \int_{z=z_j}^{z_{j+1}} (\mathbf{B}_{bu}^T \mathbf{e}_b \mathbf{B}_{\phi o} + \mathbf{B}_{su}^T \mathbf{e}_s \mathbf{B}_{\phi i}) \left| \frac{\partial(x,y)}{\partial(\xi,\eta)} \right| dz d\eta d\xi \tag{2.29}$$

$$\mathbf{K}_{\phi u}^{e} = \sum_{j=1}^{nlayer} \int_{\xi=-1}^{1} \int_{\eta=-1}^{1} \int_{z=z_j}^{z_{j+1}} (\mathbf{B}_{\phi o}^T \mathbf{e}_b \mathbf{B}_{bu} + \mathbf{B}_{\phi i}^T \mathbf{e}_s \mathbf{B}_{su}) \left| \frac{\partial(x,y)}{\partial(\xi,\eta)} \right| dz d\eta d\xi \tag{2.30}$$

$$\mathbf{K}_{\phi\phi}^{e} = \sum_{j=1}^{nlayer} \int_{\xi=-1}^{1} \int_{\eta=-1}^{1} \int_{z=z_j}^{z_{j+1}} -(\mathbf{B}_{\phi i}^T \boldsymbol{\chi}_i \mathbf{B}_{\phi i} + \mathbf{B}_{\phi o}^T \boldsymbol{\chi}_o \mathbf{B}_{\phi o}) \left| \frac{\partial(x,y)}{\partial(\xi,\eta)} \right| dz d\eta d\xi \tag{2.31}$$

$$\begin{aligned} \mathbf{F}^{e} = & \sum_{j=1}^{nlayer} \int_{\xi=-1}^{1} \int_{\eta=-1}^{1} \int_{z=z_j}^{z_{j+1}} \mathbf{N}_u^T \mathbf{A}_u^T \mathbf{F}_V^e \left| \frac{\partial(x,y)}{\partial(\xi,\eta)} \right| dz d\eta d\xi \\ & + \int_{\xi=-1}^{1} \int_{\eta=-1}^{1} \mathbf{N}_u^T \mathbf{A}_u^T \mathbf{F}_S^e \left| \frac{\partial(x,y)}{\partial(\xi,\eta)} \right| d\eta d\xi + \mathbf{N}_u^T \mathbf{A}_u^T \mathbf{F}_P^e \end{aligned} \tag{2.32}$$

$$\mathbf{Q}^{e} = \int_{\xi=-1}^{1} \int_{\eta=-1}^{1} \mathbf{N}_\phi^T \mathbf{Q}_S^e \left| \frac{\partial(x,y)}{\partial(\xi,\eta)} \right| d\eta d\xi \tag{2.33}$$

The volume integral has been transformed into the sum of the elemental volume integrals using the *3x3* Gaussian Quadrature numerical integration methods (See Appendix E). By Hamilton's variational principle, the sum of variational is zero. Therefore, the expression associated with each type of variation is also zero. For static and dynamic analysis of laminate composite structures, the final system of equations, in terms of the nodal variables including both mechanical and electrical quantities, is given by

$$\begin{bmatrix} \mathbf{M}_{uu} & 0 \\ 0 & 0 \end{bmatrix} \begin{bmatrix} \ddot{\mathbf{u}}_g \\ \ddot{\boldsymbol{\phi}}_g \end{bmatrix} + \begin{bmatrix} \mathbf{K}_{uu} & \mathbf{K}_{u\phi} \\ \mathbf{K}_{\phi u} & \mathbf{K}_{\phi\phi} \end{bmatrix} \begin{bmatrix} \mathbf{u}_g \\ \boldsymbol{\phi}_g \end{bmatrix} = \begin{bmatrix} \mathbf{F}_g \\ -\mathbf{Q}_g \end{bmatrix} \tag{2.34}$$

Equation (2.34) is the general dynamic equation of the system without damping. When dealing with static analysis, it can be simplified by ignoring the first term in equation as mass matrix. When damping is considered, it becomes

$$\begin{bmatrix} \mathbf{M}_{uu} & 0 \\ 0 & 0 \end{bmatrix} \begin{bmatrix} \ddot{\mathbf{u}}_g \\ \ddot{\boldsymbol{\phi}}_g \end{bmatrix} + \begin{bmatrix} \mathbf{C}_{uu} & 0 \\ 0 & 0 \end{bmatrix} \begin{bmatrix} \dot{\mathbf{u}}_g \\ \dot{\boldsymbol{\phi}}_g \end{bmatrix} + \begin{bmatrix} \mathbf{K}_{uu} & \mathbf{K}_{u\phi} \\ \mathbf{K}_{\phi u} & \mathbf{K}_{\phi\phi} \end{bmatrix} \begin{bmatrix} \mathbf{u}_g \\ \boldsymbol{\phi}_g \end{bmatrix} = \begin{bmatrix} \mathbf{F}_g \\ -\mathbf{Q}_g \end{bmatrix} \tag{2.35}$$

Where: $\mathbf{C}_{uu}$ is proportional damping in the form of $[\mathbf{C}_{uu}] = \alpha[\mathbf{M}_{uu}] + \beta[\mathbf{K}_{uu}]$ and α & β are Rayleigh's damping coefficients. $\ddot{\mathbf{u}}_g$, $\dot{\mathbf{u}}_g$, $\mathbf{u}_g$ and $\boldsymbol{\phi}_g$ are the vectors of the global nodal acceleration, velocity, displacements and voltages, respectively. $\mathbf{F}_g$ and $\mathbf{Q}_g$ are the vectors of the applied mechanical loading and electrical charges respectively. $\mathbf{K}_{uu}$, $\mathbf{K}_{u\phi}$, $\mathbf{K}_{\phi u}$, $\mathbf{K}_{\phi\phi}$ and $\mathbf{M}_{uu}$ are matrices representing the total strain potential and mass contribution of the element irrespective of whether it is piezoelectric or otherwise.

2.3.4 Capabilities of TOF Software

The TOF software was built based on the developed FE formulation in previous section, which is applicable for a laminated composite plate structure using piezoelectric materials.

2.3.4.1 Static Analysis

1. It can model plate structures with single layer or multiple layers with flat structural configuration. It can also be applied for beam models by using plate elements.
2. Able to analyse structural performance under influence of external forces (mechanical force and electrical charge) under general boundary conditions (displacement and applied voltage). In the FE model, each layer of each element can be specified to consist of piezoelectric materials and non-piezoelectric materials. In the TOF software, it is easy to set piezoelectric stress constants (e_b,

e_s) to be zero for non-piezoelectric materials. Hence the adaptive material can be located anywhere in the structures. The structure can have empty spaces or holes.

3. The element can be modeled as non-rectangular (arbitrary) shape with different possibility of fibre orientation with respect to the xy plane.
4. The general piezoelectric materials and non-piezoelectric materials that are almost widely used are orthotropic materials. It means that any material can be used up to orthotropic, including isotropic and transversely isotropic. Piezo-polymers-PVF, and Poly-crystalline-$Pb(Zr,Ti)_3$ are two types material, which are widely used in smart structure application. Readers who are interested in internal structure of piezoelectric materials should refer to Chee (2000c) in Chapter 2.
5. It can be applied for thick and thin structures with good accuracy.
6. Adaptive material can be treated as either actuator or sensors based on the appropriate boundary conditions.
7. The stress status of the structures subjected to external forces together with the control inputs on the patches has not been included. Therefore, this research works was assumed that there is no failure in the structure.

2.3.4.2 Dynamic Analysis

1. It is able to solve natural frequency corresponding to eigenvector (modal shape) of the i^{th} mode using inverse iteration method.
2. It is capable to analyse structural responses for vibration with and without damping using Newmark direct time integration method, where proportional damping with Rayleigh's damping coefficients is considered in the present thesis.

2.4 Numerical Verification

As in section 2.3, the finite element formulation including static and dynamic analysis was developed for the laminate composite plate with non-rectangular element. In this section, the numerical results are presented to verify finite element formulation by comparing these with results obtained from a commercial software package, Strand7. These demonstrated the structural deformation under electric field (TOF) and thermal expansion (Strand7).

2.4.1 Static Analysis

This section aims to verify results from the computer algorithm on the non-rectangular element software against results obtained from existent studies on the laminated smart composite structures for static analysis. For such structures with non-rectangular elements, the numerical results provide accurate results.

Consider a square cantilever aluminium T2024-T6 plate clamped at the left end without any applied mechanical load. The plate has a length of 0.20 m, a width of 0.20m and consists of a single layer of thickness 0.0005m. The plate material stiffness constants are as follows: $c_{11}=c_{22}=c_{33}=104GPa$, $c_{12}=c_{13}=c_{23}=51.1GPa$, $c_{44}=c_{55}=c_{66}=26.3GPa$. With reference to Figure 2.4(a), two active patches are bonded to the plate. The piezoelectric actuators are of PZT-5-1 of rectangular shape and are 0.02m high, 0.03m wide and 0.0005m thick. The patches are modelled in Strand7 using a Quad8 isoparametric element. The shape and number of elements comprising the patch can be altered as long as the connectivity between the actuating patch and host plate remains consistent. Both patches have identical stiffness constants, these are as follows: $c_{11}=c_{33}=c_{22}=128GPa$, $c_{12}=c_{13}=c_{23}=71.8GPa$. The values for electrical permittivity for patch 1 and 2 are $d_{31}= d_{32}= 131pm/V$, $d_{33}= 600pm/V$, $d_{24}= d_{15}= 0pm/V$ and $d_{31}= d_{32}= 148pm/V$, $d_{33}= 600pm/V$, $d_{24}= d_{15}= 0pm/V$ respectively. Three hundred voltages are applied to each patch in the structure.

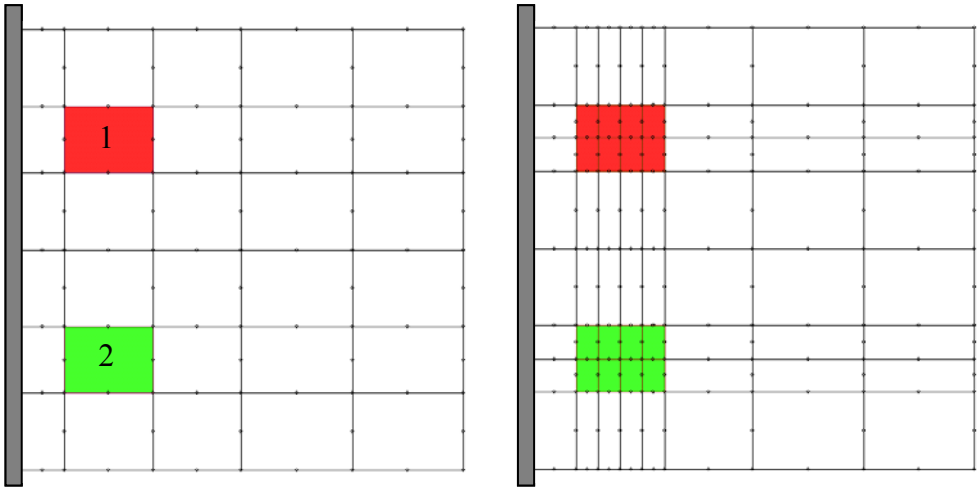

Figure 2.4: Cantilever plate with a) single-element patch; b) eight-element patch

The first part of this test considered model with a single-element patch and an eight-element patch as shown in Figure 2.4(a) & 2.4(b). Figures 2.5 and 2.6 show the deflection at the center of the plate (in the xz plan) and the tip defection (in the yz plan) in z direction and compares the results of the 8 node non-rectangular FEA (hereafter TOF refers to the general program) to the 8 node rectangular FEA (Pz2 developed by Chee et. al. 2000a) as well as the Strand7 Software results. The errors between the non-rectangular and rectangular FEA are very small (<1%) with a slight difference (~ 4%) between non-rectangular FE and Strand7 results. This is attributed to the differences in the formulation and calculation techniques. For example, the rectangular FE program uses symbolic integration via Maple software, while the non-rectangular FE program uses 3x3 Gaussian Quadrature numerical integration method and both use linear layer-wise electric potential theory whilst Strand7 uses thermal expansion theory. Thus the above results validate the present formulation for a non-rectangular element piezoelectric composite plate structure. From now on, all testing will be performed with non- rectangular FEA.

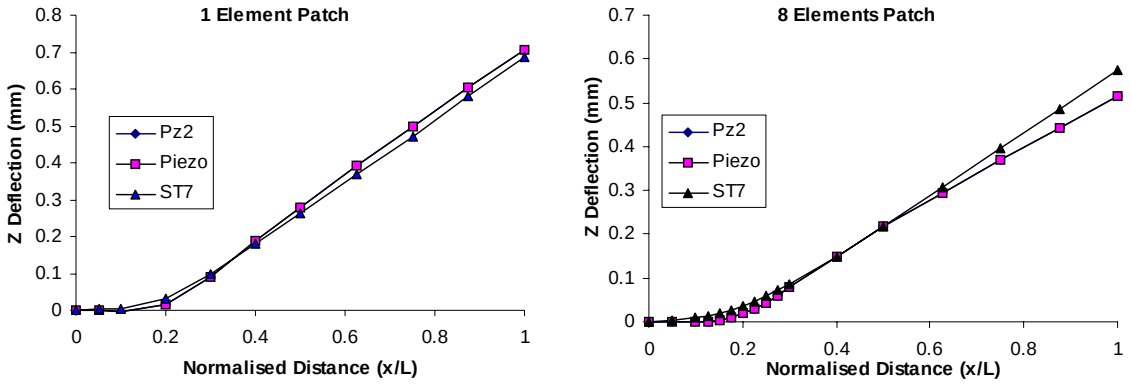

Figure 2.5: Deflection at the centre of the plate along x-axis.

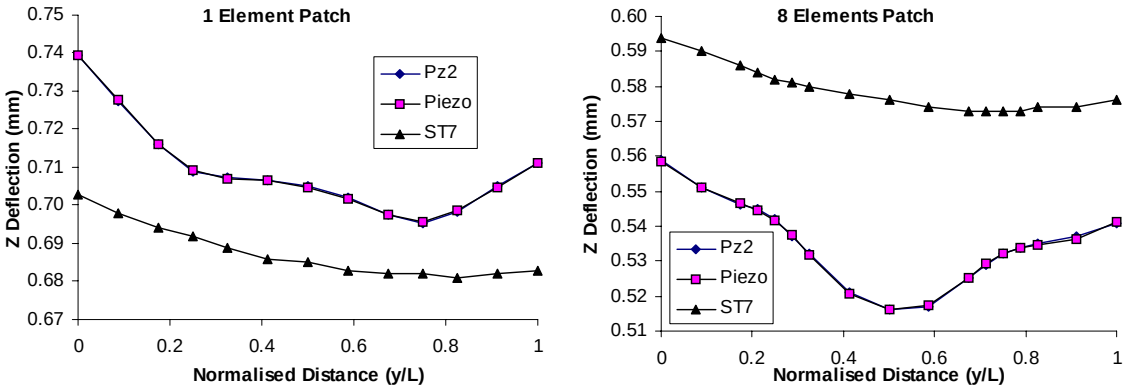

Figure 2.6: Tip deflection of the plate along y-axis.

In the second part, the investigation is completed using a different mesh. Whilst maintaining the actuator patch area, the patches are now modelled using one, two, four and eight finite elements as shown in figures 2.4(a & b) and 2.7(a & b) respectively. The results in Figure 2.8 show that the deflections slightly decrease as the number of elements in the patches increase. So if the structure is subdivided further into a greater number of elements then result will converge to the exact solution.

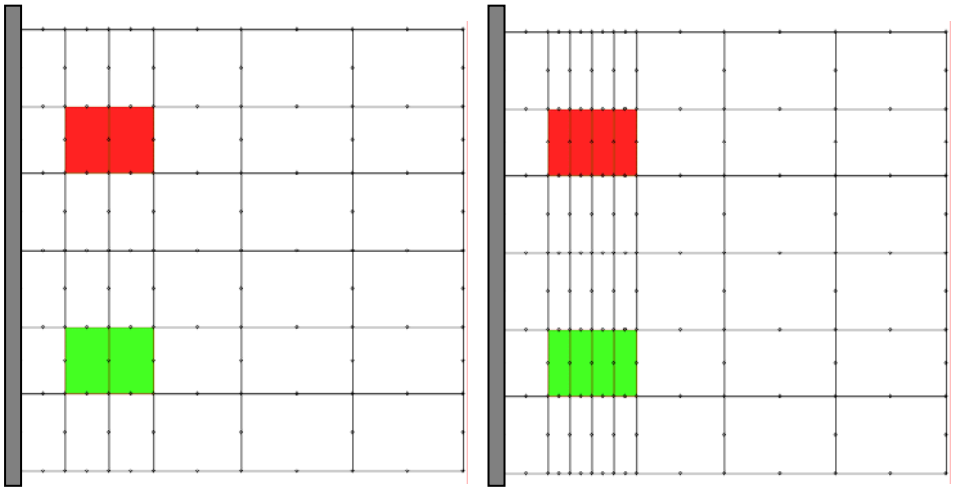

a) b)

Figure 2.7: Cantilever plate with a) two-elements patch; b) four-elements patch.

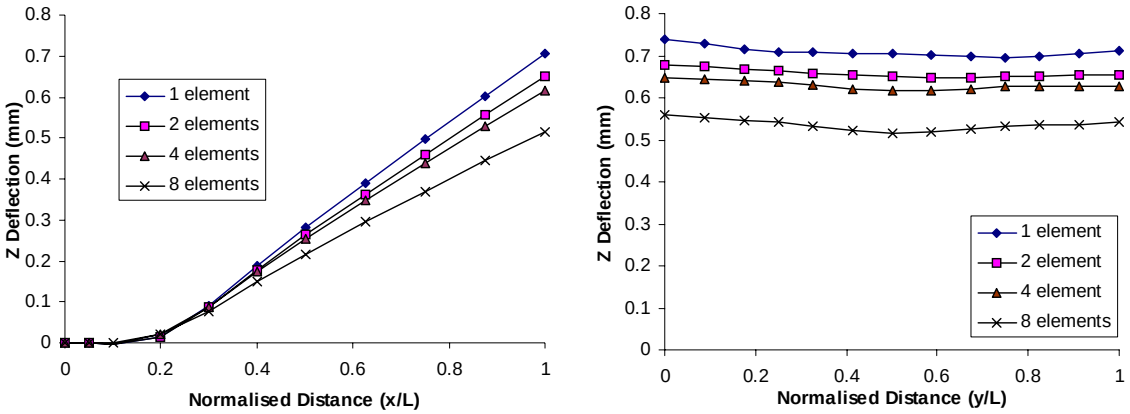

a) b)

Figure 2.8: Deflection of plate along a) center line b) tip

2.4.2 Dynamic Analysis

For dynamic analysis, the present finite element software included modal analysis and linear transient dynamics for smart plate. It determines the eigenvalue, eigenvector as natural frequency and mode shape for i^{th} mode. As well as linear transient dynamics, the Newmark direct time integration method is used to simulate excitation of smart structure. In this part, the typical example is present to verify modal analysis of present finite element software only. The verification of transient dynamic can be seen in Chapter 6 of this thesis.

Consider a long cantilever plate clamped at left end and subject to without any applied load, which has a length of 0.15 m, width of W and consists of 4 layers of thickness of 0.0005m. The material of the plate has the following stiffness constants: $c_{11}=c_{22}=c_{33}=92.9$GPa, $c_{12}=c_{13}=c_{23}=39.8$GPa, $c_{44}=c_{55}=c_{66}=26.5$GPa; density $\rho=2780$kg/m^3. Three active patches are bonded to plate, which are modelled using six elements. Patch #1 and #3 are bonded at both ends and patch #2 is bonded at middle of the plate as numbered in Figure 2.9. The properties of patches include the stiffness constant: $c_{11}= c_{22}=c_{33}=112.6$GPa, $c_{12}=c_{13}=c_{23}=55.5$GPa, $c_{44}=c_{55}=c_{66}=28.6$GPa, density $\rho=8000$kg/m^3; the electric permittivity: $\chi_{11}=\chi_{22}=15.3\text{x}10^{-9}$F/M, $\chi_{33}=15.0\text{x}10^{-9}$F/M; and piezoelectric strain constants $d_{31}=254$pm/V, $d_{32}=-204$pm/V, $d_{33}=374$pm/V, $d_{24}=584$pm/V, $d_{15}=584$pm/V.

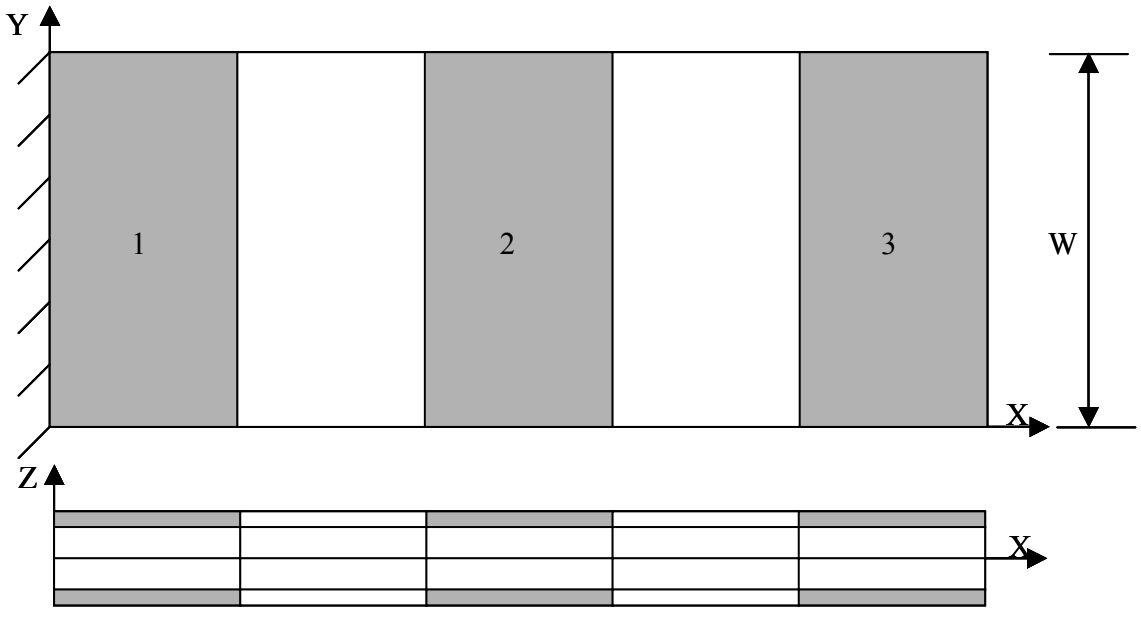

Figure 2.9: Cantilever plate in XY and XZ plane

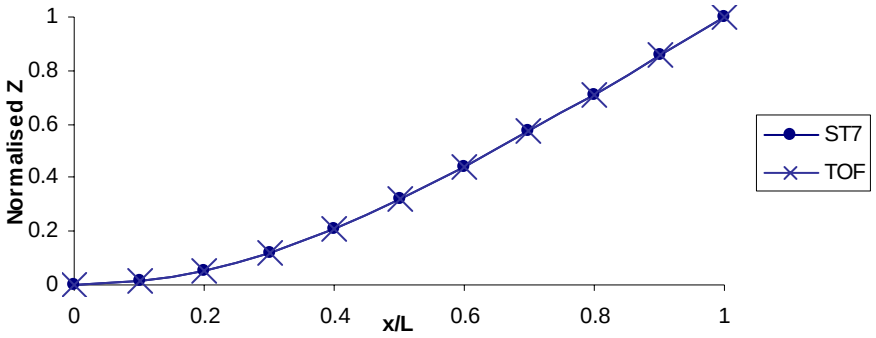

a) Mode 1

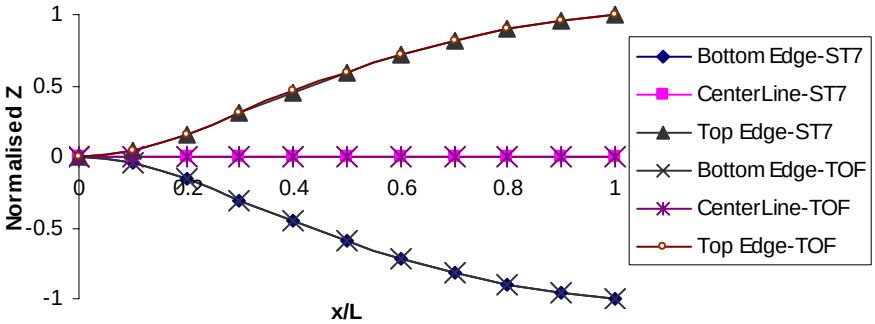

b) Mode 2

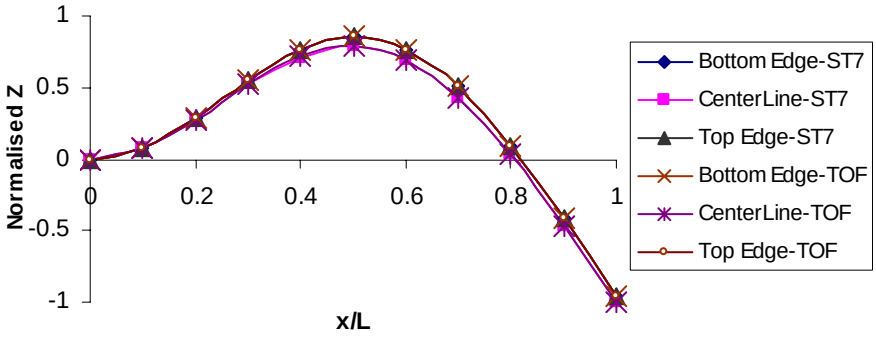

c) Mode 3

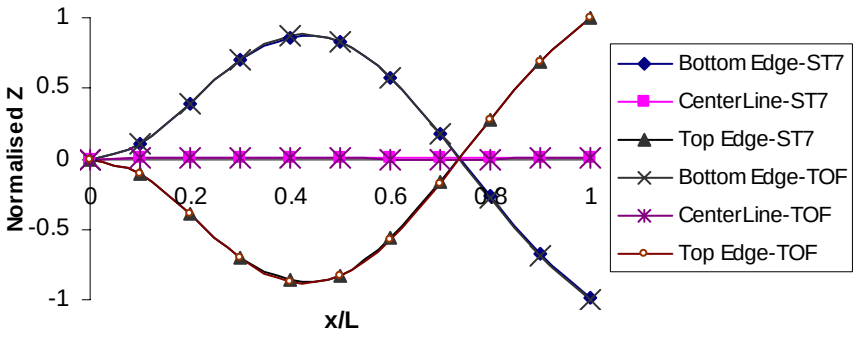

d) Mode 4

Figure 2.10: First 4 modes shape of the cantilever plate

Table 2.1: Comparison of natural frequencies

Width (W)	0.006 m			0.06 m		
Mode/FEA	**ST7 (Hz)**	**TOF (Hz)**	**Error (%)**	**ST7 (Hz)**	**TOF (Hz)**	**Error (%)**
1	58.75	58.71	-0.068	60.39	60.33	0.099
2	173.07	173.10	0.017	316.28	316.10	0.057
3	389.10	388.70	-0.103	396.62	396.10	0.131
4	1120.40	1121.00	0.054	1015.00	1014.00	0.099

To demonstrate the applicability and performance of the present model in free vibration analysis, Table 2.1 shows the first four frequencies of the cantilever plate (W=0.06m) and cantilever beam (W=0.006m), which is using 8 nodes plate element to modelling and compares the results of TOF (current program) to Strand 7 FEA results. The errors between them are very small (<0.02%) with a slight difference (~0.1%). This is attributed to the difference in formulation and calculation technique. For example, the current program models as 11 degrees of freedom in each node instead of 6 degrees freedom in Strand 7. In Figure 2.10, it can be observed the predictions of the first 4 modal shape of top, bottom edge and centerline of the cantilever plate (W=0.06m), respectively. In mode 1, the top, bottom edge and centerline have the same modal shape. Therefore, Figure 2.10a presents only the results of the bottom edge, which obtain from Strand 7 and TOF FEA. Mode 2 and 4 generated twist in the plate. In Mode 3, the amplitude of centerline is off from the top and bottom edge of plate. Thus the above results validate current program. From now on, all the testing will perform with TOF FEA.

2.5 Experimental Verification

This section aims to provide a comparison between the prediction of the present FEA formulation and experimental results. The electrical load and transverse displacement data extracted from the TOF output was compared to these results obtained from measured experimental data.

2.5.1 Specimen Preparation and Material Properties

The test specimen is square cantilever aluminium T2024-T6 plate of 0.2m long and 0.0005m thick. The plate constants are $c_{11}=c_{22}=c_{33}=104$GPa, $c_{12}=c_{13}=c_{23}=51.1$GPa, $c_{44}=c_{55}=c_{66}=26.3$GPa. The piezoelectric actuators are of PZT-5-1 of rectangular shape and are 0.02m high, 0.03m wide and 0.0005m thick. The actuators have the same stiffness constants: $c_{11}=c_{33}=c_{22}=128$GPa, $c_{12}=c_{13}=c_{23}=71.8$GPa, $c_{44}=c_{55}=c_{66}=27.9$GPa. The first specimen has two bonded actuator patches and the second one has a single bonded actuator patch as show in Figure 2.4 and 2.11, respectively. In the first specimen, the values for electrical permittivity for patch #1 and #2 are $d_{31}= d_{32}=$ 131pm/V, $d_{33}=$ 600pm/V, $d_{24}= d_{15}=$ 0pm/V and $d_{31}= d_{32}=$ 148pm/V, $d_{33}=$ 600pm/V, $d_{24}= d_{15}=$ 0pm/V respectively. And the specimen #2 has electrical permittivity as $d_{31}=d_{32}=153$pm/V, $d_{33}=600$pm/V, $d_{24}=d_{15}=0$pm/V. The piezoelectric actuator patches are bonded to host plates by a thin layer of conductive glue and super glue, which are treated as thin adhesive layer in this test. The adhesive properties are not given here because adhesive layer is not considered in the FE formulation. Six points, as shown in Figure 2.11, are taken into count for measurement of their deflection. Their coordinates are 1(10cm, 15cm), 2(10cm, 10cm), 3(10cm, 5cm), 4(15cm, 15cm), 5(15cm, 10cm) and 6(15cm, 5cm), respectively.

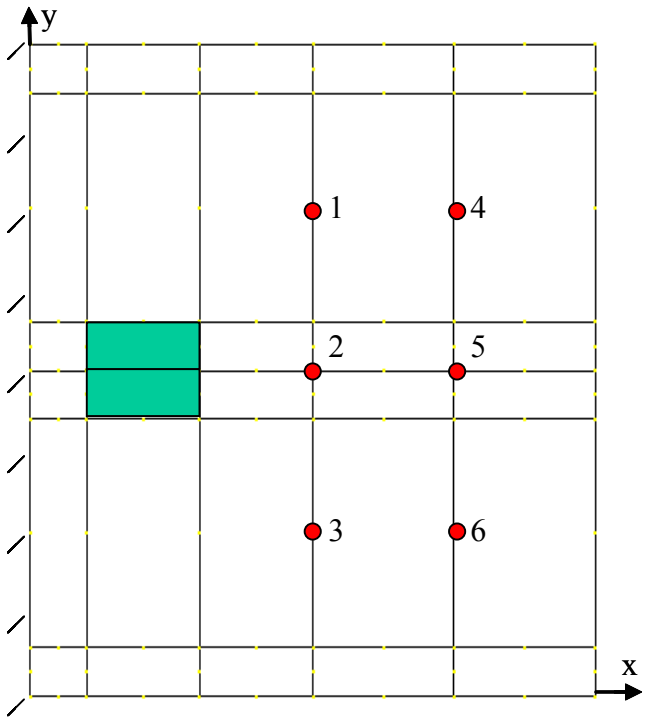

Figure 2.11: Plate panel with one piezoelectric patch (specimen #2).

2.5.2 Test Set-up and Procedures

Figure 2.12 shows a photograph of the experimental setting for a cantilever plate and Figure 2.13 depicts the block diagram, which illustrates how the experiment system works. The sensor contains in its tip an inductance element, which responds the presence of the target on the plate when inductance element excited by alternating current. The output is voltage, which appears on shape control interface via signal conditioner and lab view data acquisition system. The target deflection is measured based on the difference of initial and final output voltage. The testing set-up consists of the following electrical equipment and some of them are numbered as shown in Figure 2.12.

1. Indikon AP1300-7 Integrated proximity probe (non-contact sensor), sensitivity for steel 4140 type: 2 mV/μm; Linearity range of standing distance: 1mm-9.1mm, frequency range: 0-10 KHz, reading error: 1%.
2. National instruments SCXI-1327 Signal conditioner (8 Channels) (not in the picture).
3. PI E-500 HVPZT Amplifier 3 channels, providing up to 500 volts.
4. PI E-500K012 LVPZT Amplifier (6 Channels).
5. Dual Power supplies (2 Channel) (not in the picture).
6. Shape control interface based on Lab View Data Acquisition System.

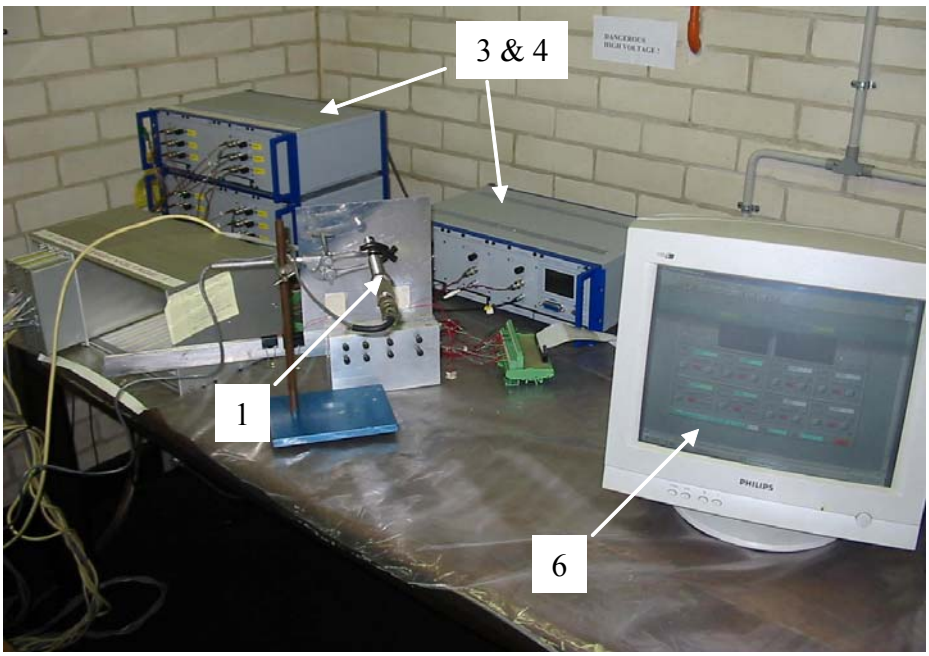

Figure 2.12: Laboratory facility and experimental setting

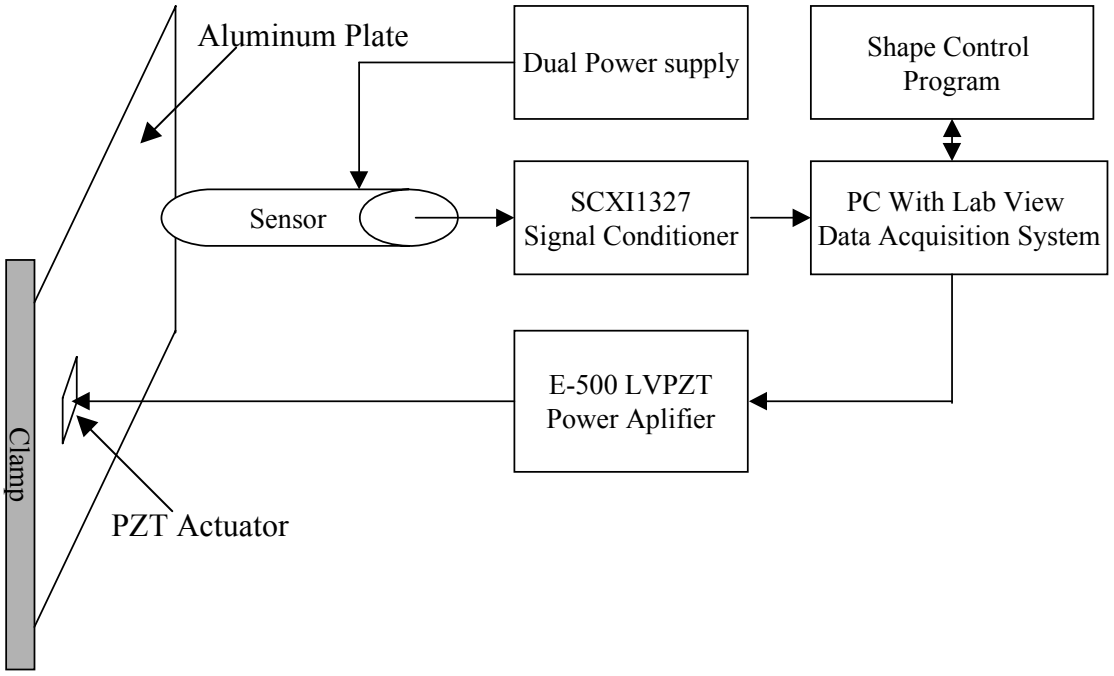

Figure 2.13: Block diagram for the experiment

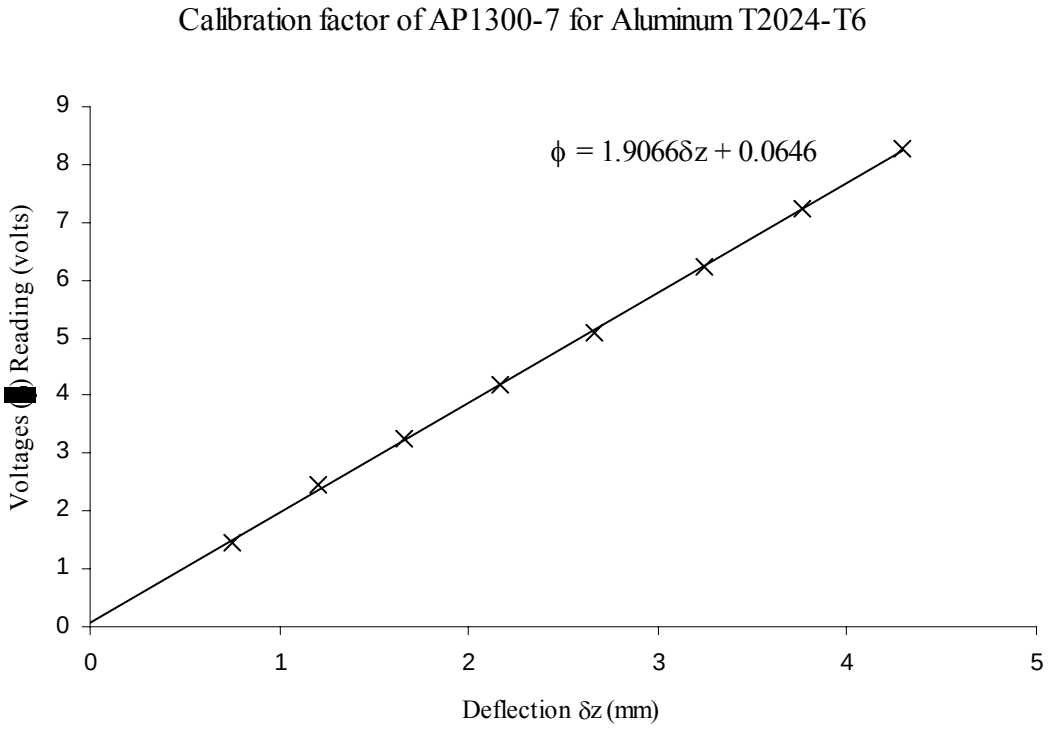

Figure 2.14: Calibration factor of AP1300-7 for Aluminum T2024-T76

Calibration factor of the AP1300-7 probe for Aluminium T2024-T6 plate is 1.90V/mm, which is calculated based on the linear relationship between the movement of the plate and the reading voltage (see Figure 2.14). A travelling microscope has also been used to calibrate the sensor. The travelling microscope measures the gap between sensor and the plate with accuracy of 0.01mm.

The deflection of the plate through the thickness direction needs to be measured with no mechanical loads and only by applying electrical fields to actuators. To avoid the effect of self-weight, the plate was set up so that the gravity has been aligned with the local y axis.

2.5.3 Results and Discussions

The smart plates are modelled with 5x5 finite element (FE) mesh by using the developed 8-node isoparametric element. All nodes on the clamped side of the plates are fixed, while all nodes on the other sides are set to be free. The shaded elements are piezoelectric actuator patches as shown in figures 2.4 and 2.11.

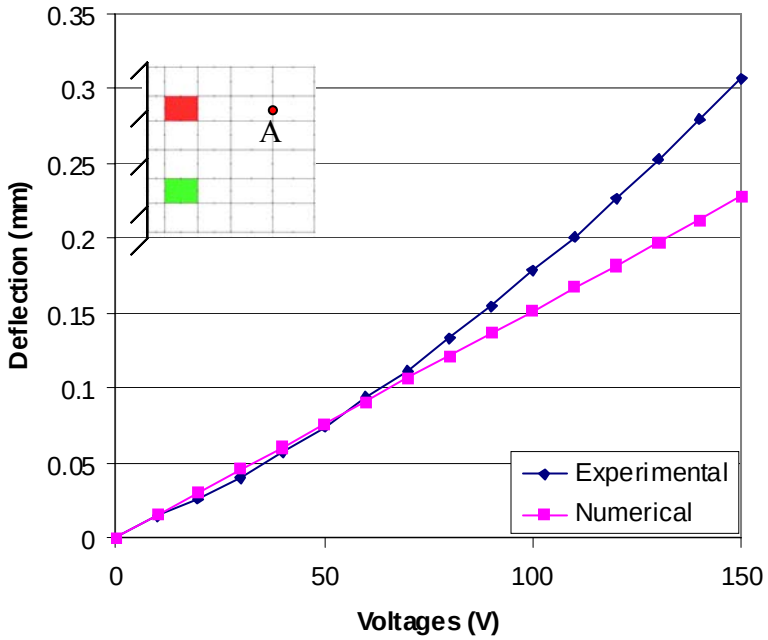

Figure 2.15: Deflection of point A versus voltages

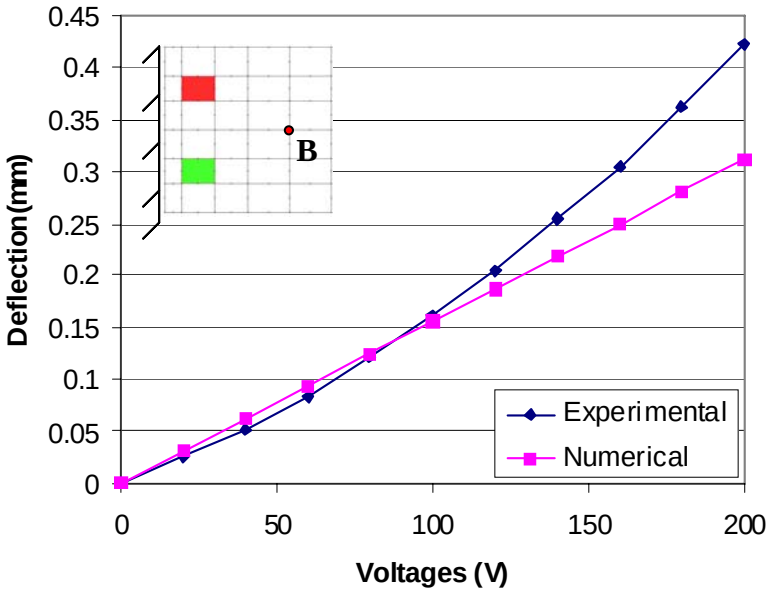

Figure 2.16: Deflection of point B versus voltages

Figures 2.15 and 2.16 plot the measured and predicted deflections of points A and B of specimen #1 versus electrical voltage, the two points have the coordinates of (15cm, 15cm) and (15cm, 10cm), respectively. In the numerical results, the deflection increases linearly as increasing of electrical fields, whilst a non-linear curve is observed in the experimental results, whereas there is the presence of non-linear behaviour in properties of piezoelectric materials. The difference between the predicted and measured displacements is small when the actuating voltage is less than 100 volts, which is equivalent to electric field of 200KV/m. The difference becomes larger when the voltage is greater then 100 volts. For example, a 30% difference is noted when the applied voltage is a 150 volts.

Table 2.2: Deflection of panel with one piezoelectric patch

Node	Location	Exp	FEA	% Error
1	(10,15)	0.123666	0.16671	25.82
2	(10,10)	0.126668	0.12886	1.70
3	(10,5)	0.128899	0.16671	22.68
4	(15,15)	0.255325	0.29365	13.05
5	(15,10)	0.269597	0.27950	3.54
6	(15,5)	0.256345	0.29365	12.70

Table 2.2 shows the testing results and comparison between experimental and numerical results of specimen #2 (see Figure 2.11). This test investigates the deflection at node 1, 2, 3, 4, 5 & 6, with an applied electrical field of 300 voltages. Nodes 1, 2 and 3 lie on the same vertical line (same x-coordinate as shown in Figure 2.11) and have the same z-deflection. Similar results are observed for node 4, 5 and 6.

The above results demonstrate that there is a good correlation between the measured and predicted result in the low electric field range (less than 100 volts). The result indicates that a non-linear strain-electric field relationship should be used when high electric field is applied to a PZT actuator. In addition, it's observed that permanent deformation occurs during the test when an extremely high electric field is applied. This may take place in the host structure or piezoelectric material, which may lead to de-bonding between the host structures and piezoelectric actuator patches.

2.6 Investigation of Error Function Effects

This section is to demonstrate the effect of the piezoelectric actuator shape on the resulting of error function (Lnm), which is a weighted sum of all square differences in displacements at selected nodes between the desired and calculated structural shapes (refer to chapter 3 for more details of the Lnm calculation). To find the optimum values of electric fields for a given actuator patch shape, (Chee et al 200b) proposed the Buildup Voltage Distribution (BVD), (Anton & Rorres, 1979) Linear Least Square (LLS) and Simplex algorithms for finding the optimum voltages applied to actuators. In this section, the LLS method is used to investigate the effect of non-rectangular shape on the optimum voltage values in term of achieving the desired structural shape.

2.6.1 Example 1: Bending Shape

Consider a long thick cantilever plate, which has a length of 0.15 m, a width of 0.06m and consists of 2 layers of thickness 0.01m, clamped at the left end and subject to no applied mechanical load (see Figure 2.17). The desired shape is defined as $w^d(x,y)=10^{-5}\text{Cos}(10x-1)$. The plate material has the following stiffness constants: $c_{11}=c_{22}=c_{33}=82.68\text{GPa}$, $c_{12}=c_{13}=c_{23}=27.56\text{GPa}$, $c_{44}=c_{55}=c_{66}=26.5\text{GPa}$. Three active

patches are bonded to the plate; these are modelled using six finite elements. Patches 1 and 3 are bonded at both ends and patch 2 is bonded at the middle of the plate as numbered in Figure 2.17 (Model A). The patch properties are: stiffness constants: $c_{11}=c_{33}=84.8GPa$, $c_{22}=29.68Gpa$, $c_{12}=c_{13}=c_{23}=36.35GPa$, $c_{44}=c_{55}=c_{66}=24.2Gpa$; electric permittivity: $\chi_{11}=\chi_{22}=15.3x10^{-9}F/M$, $\chi_{33}=15.0x10^{-9}F/M$; and piezoelectric strain constants $d_{31}=254pm/V$, $d_{32}=-204pm/V$, $d_{33}=374pm/V$, $d_{24}=484pm/V$, $d_{15}=584pm/V$.

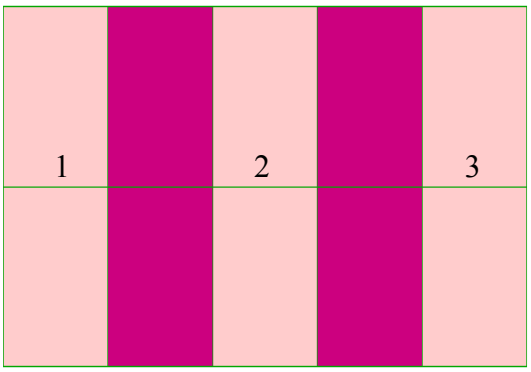

Figure 2.17: Model A

The FE model of this structure is comprised of 10 elements. Model A has rectangular patches with different element shapes. In Model B, the patches are rotated backward by 14 degrees. The top and bottom elements of the patches in model C & D have been shifted back and forward by 14 degrees respectively as shown in Figure 2.18. The total area of the patches is kept constant.

The approach of this test is to investigate the effect of different patch pattern on the bending shape control of the cantilever plate. The voltages required for each patch to achieve the desired bending shape were obtained using the LLS algorithm and are listed in Table 2.3. Comparison with model B, C and D to model A showed that model B has come closest to achieving the desired shape, i.e. error function Lnm is reduced 16%. However the applied voltage in the patches is high with patch 1, 2 and 3 increasing by 13%, 4% and 16% respectively. In model C, the applied voltage in patch 1, 2 and 3 is decreased by 4%, 2% and 13% respectively with a slight increase of 1.5% in the shape match factor.

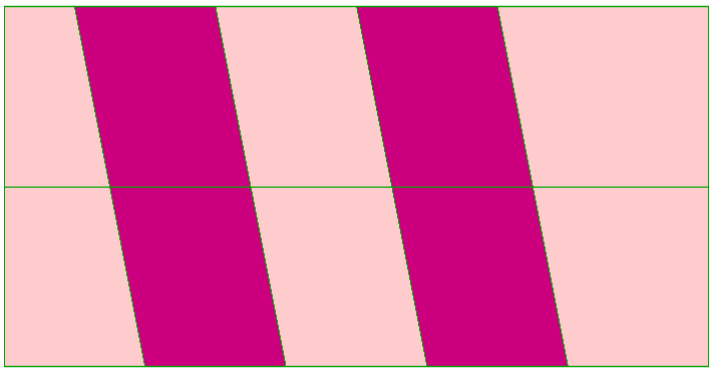

Model B

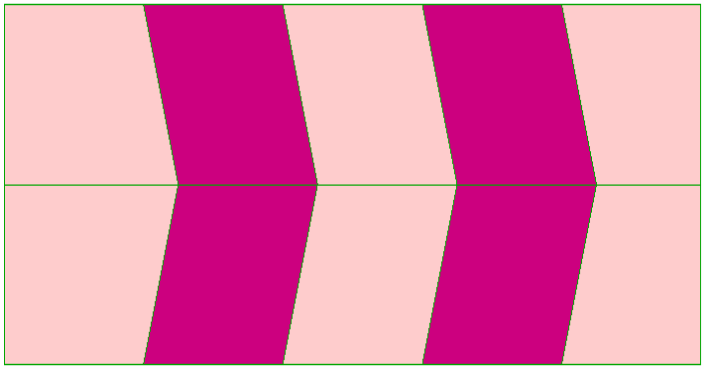

Model C

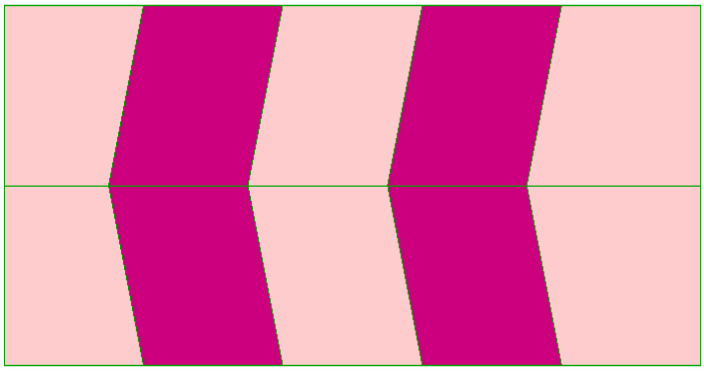

Model D

Figure 2.18: Cantilever plate with different patch pattern

Table 2.3: Voltage Distribution values for bending control cantilever plate with different patches pattern

Model	**A**	**B**	**C**	**D**
Patch/Voltages (Volts)				
1	393.2	444.2	377.6	414.3
2	477.7	495.7	466.8	487.3
3	135.7	157.6	117.9	147.9
Lnm ($1e^{-5}$)	**2.1172**	**1.7778**	**2.1497**	**1.9551**

2.6.2 Example 2: Twisting Shape

Consider a cantilevered of 0.292 m long, 0.152 m wide and 0.83 mm thick. There is no applied mechanical load on the structure. The plate has the following material constants: $c_{11}=c_{22}=c_{33}=82.68$GPa, $c_{12}=c_{13}=c_{23}=27.56$GPa, $c_{44}=c_{55}=c_{66}=27.6$GPa. Fifteen piezoelectric ceramic patches of 0.25 mm in thickness are attached to the top and bottom of the structure, which have been indicated in Figure 2.19 (model F). Patch 1, 6 and 11 each consist of two elements. The properties of the patches include the elastic constants: $c_{11}=c_{22}=c_{33}=84.8$GPa, $c_{12}=c_{13}=c_{23}=36.35$GPa, $c_{44}=c_{55}=c_{66}=24.2$GPa; electric permittivity: $\chi_{11}=\chi_{22}=15.3\text{x}10^{-9}$F/M, $\chi_{33}=15.0\text{x}10^{-9}$F/M; and piezoelectric strain constant $d_{31}=-254$pm/V, $d_{32}=-204$pm/V, $d_{33}=374$pm/V, $d_{15}=584$pm/V, $d_{24}=484$pm/V. The piezoelectric patches 1, 2, 3, 4, 5, 11, 12, 13, 14 and 15 have an area of 1950.75mm^2. Patch 6 has an area of 637.5mm^2 and patches 7, 8, 9 and 10 have area of 1275mm^2. The finite element mesh has 84 elements and total of 3 layers. This example focuses on the effect of the patch pattern for the twist problem. Consider 3 rows of patches along the plate; the middle row will be unchanged, while the patches on the top and bottom row can rotate. For model G, H and I, the top and bottom row patches can be rotated in plane by ±14 degrees as shown in Figure 2.19. The left ends of all models have been clamped. The desired shape is described as $w^d(x,y) = 10^{-3}(cosh(x)\text{-}1)sin(y)$. By using the LLS method, the optimum applied voltages values of each patch are obtained and listed in Table 2.4.

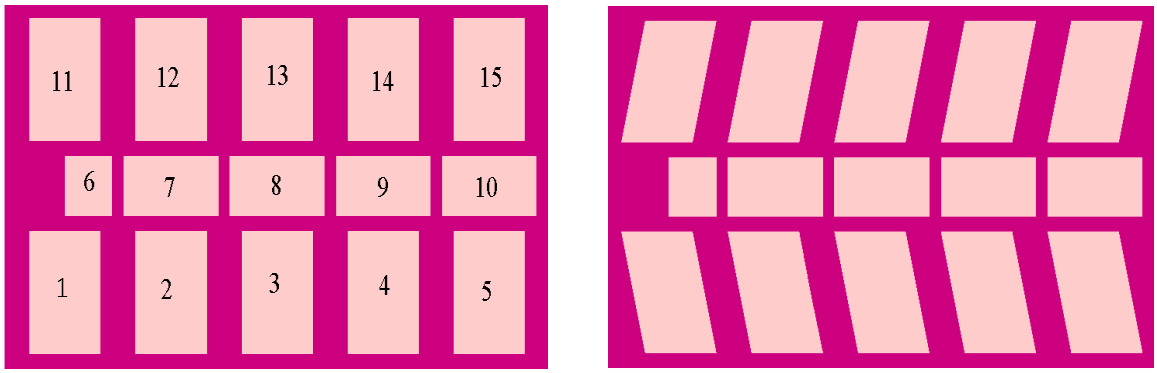

Model F Model G

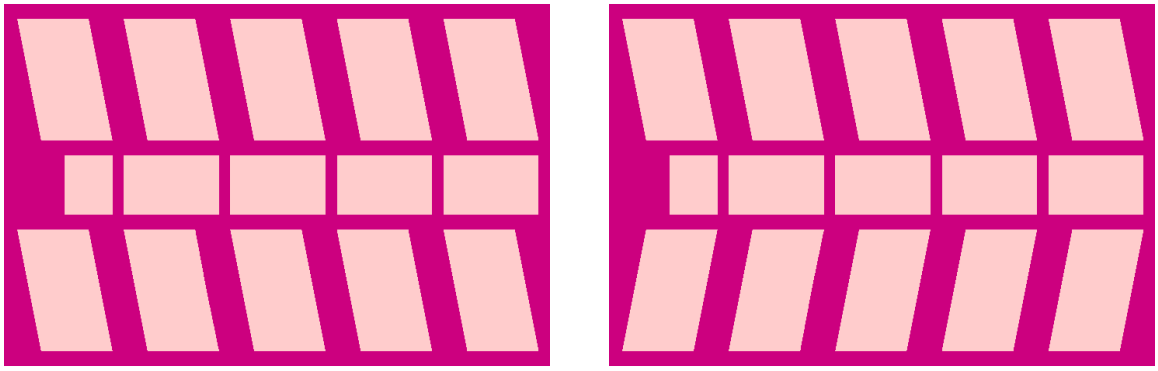

Model H Model I

Figure 2.19: Twisted Cantilever plate with different patch pattern

Results in Table 2.4 show that Models F, G, H and I have the highest magnitude of voltage and equal to 4.2V, 5.5V, 6.5V, 3.2V, respectively. The total magnitude of the voltage is 21.2V, 21.1V, 30.0V, 18.9 V and shape match factor, Lnm, is 2.744×10^{-3}, 4.388×10^{-3}, 2.285×10^{-3} and 2.089×10^{-3}, respectively. Hence the comparison between models I to model F, Table 2.5 shows that the maximum magnitude of voltage, total voltage and shape match factor are reduced by 25.5%, 10.5% and 23.9%, respectively. Figure 2.20 & 2.21 show the actuated and desired shape of the plate with different patch pattern. The results show that there exists three major advantages in twisted shape control with different patch patterns: (1) the reduction in magnitude of the maximum applied voltage to a single actuator patch, (2) reduction in total voltage applied to all actuators and (3) a better fit to the desired shape.

Table 2.4: Voltage distribution for cantilever plates with different patch pattern

Model / **Patch/Voltages**	**F**	**G**	**H**	**I**
1	4.2	5.5	2.9	1.8
2	1.8	0.8	1.5	3.2
3	2.0	2.4	2.2	1.6
4	1.0	0.8	1.0	1.1
5	-1.6	-0.8	0.4	-1.8
6	0.0	0.2	6.5	0.0
7	0.0	-0.2	-0.4	0.0
8	0.0	0.1	0.7	0.0
9	0.0	0.0	-1.7	0.0
10	0.0	0.0	-1.1	0.0
11	-4.2	-5.5	-3.5	-1.8
12	-1.8	-0.8	-3.1	-3.1
13	-2.0	-2.4	-1.7	-1.6
14	-1.0	-0.8	-1.0	-1.1
15	1.6	0.8	2.3	1.8
Total Voltage	**21.2**	**21.1**	**30.0**	**18.9**
Lnm ($1e^{-3}$)	**2.7440**	**4.3880**	**2.2285**	**2.0890**

Table 2.5: Comparison for cantilever plates with different patch pattern

Error	G	H	I
Voltage (%)	0.90	42.62	-10.52
Lnm (%)	59.91	-16.73	-23.87

Figure 2.20: Desired Shape

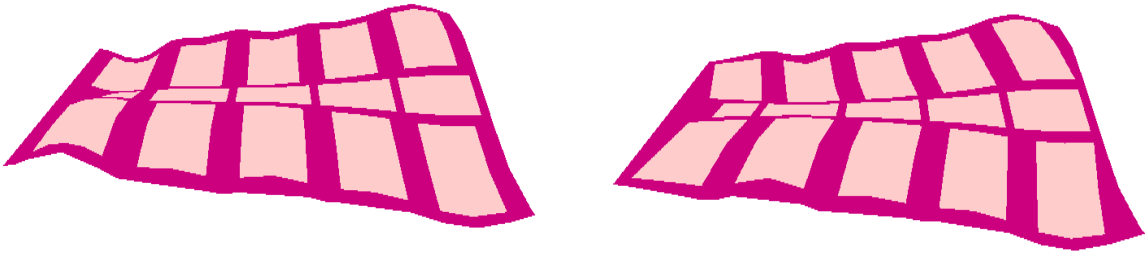

Model F Model I

Figure 2.21: Calculated Shape

2.7 Summary

This chapter presented a finite element formulation with non-rectangular shaped actuators for laminated smart composite structure based on the 3rd order displacement theory and layer-wise concept. Computer code to implement the finite element formulation for static and dynamic analysis and control of smart composite plate structures has been developed. Actuated deflections are measured from experimental and numerical results obtained from different software packages for smart cantilever plates and are used to validate the present formulation, which shows good correlation compared to measured and predicted results. The FE formulation developed in this chapter constitutes the main research tool for later shape control work including static and dynamic analysis. In addition, an investigation into the effect of actuator pattern on the optimum values of the applied voltages and the shape match factors (error function) in shape control of smart plate structures has also been presented. Numerical results show that the actuator patterns may have an important influence on the values of the optimum voltages applied to each individual actuator and the final shape match factor. It is shown that by adequately designing the actuator pattern, the total voltage and the maximum voltage in all actuators may be reduced while also achieving an improved desired shape match factor.

3. Piezoelectric Actuator Design Optimisation for Static Shape Control of Smart Plate Structures.

This chapter presents several coupled algorithms for piezoelectric actuator design optimisation (PADO) for shape control of structures with both the applied voltages and the shapes of actuators being treated as design variables. The optimum values for the applied voltages to actuators can be determined using the Linear Least Square (LLS) method, whereas the shapes of actuators can be optimized using the Genetic Algorithm (GA). These algorithms are combined together to develop a GA+LLS coupled algorithm (GALLS), for design optimisation of both actuators' shapes and voltages in either an alternating or a concurrent manner. In the alternating approach, LLS is utilised to determine the optimum voltages with a given actuator geometry, and then GA is used to determine the optimal actuator shapes with given voltages; the alternating calculations continue until the selected convergence condition is met. In the concurrent approach, (GALLS) the LLS is embedded in GA to determine optimum voltages and then to modify the associated strings for each individual population. Numerical results are presented to validate the proposed algorithms. It is found that the concurrent GALLS algorithm appears to be the most efficient and effective one.

3.1 Introduction

Shape control of a structure with distributed piezoelectric actuators can be achieved through optimally selecting the loci, shapes and sizes of the actuators and choosing the electric fields applied to the actuators or even optimally designing host structure's topology to best match the desired structural shape. It is an optimisation problem that can be formulated by integrating the following three aspects: objective function(s), design variables and constraints. This optimisation problem has been addressed by many researchers through selecting different combination of objective function(s), design variables and constraints and using different numerical algorithms. One option is to employ the square difference between the desired and actuated

displacements as the objective function as a measure of matching desired and actuated structural shapes, and the voltages applied to actuators as design variables, and it has been widely addressed in Koconis et. al (1994); Agrawal et. al, (1994); and Ghosh and Batra (1995). In the definition of the objective function, other physical quantities, such as slopes and curvatures, have been introduced in addition to the displacements (Chee et. al, 2001 and 2002b; Sun and Tong, 2003). For design variables, the location and size of an actuator as well as distribution pattern of rectangular-shaped actuators have been employed in addition to the voltage applied to an actuator (Bruch et. al, 2000; Donthireddy and Chandrashekhara, 1996; Eisenberger and Abramovich, 1997; Onoda and Hanawa, 1998). In addition, the influence of the shape of an actuator on shape control of structures has been parametrically studied (Nguyen and Tong, 2002b and 2004). The shape control problem has been attempted by using analytical methods and various numerical algorithms, including linear least square (LLS) method (Chee et. al, 2001 and 2002b), sequential linear programming (SLP) method (Nguyen and Tong, 2002b), genetic algorithm (GA) and simulated annealing method (Onoda and Hanawa, 1998). To further improve shape control of structures with piezoelectric actuators using minimum energy consumption, it is important to investigate the piezoelectric actuator design optimisation (PADO) problem by considering the loci, shapes and sizes of actuators and the applied voltages.

The present chapter introduces several coupled numerical algorithms for solving piezoelectric actuator design optimisation for static shape control of a structure. Combined usage of LLS and GA is proposed to optimally determine the voltages applied to actuators and actuator geometries in an alternating or concurrent approach. The proposed algorithms are implemented for static shape control of smart composite plate structures, whose finite element formulation is developed by using a 3rd order plate theory to model the mechanical deformations and a layer-wise theory to model the electric fields (Lo et. al, 1977; Saravanos and Heyliger, 1995; and Chapter 2). Numerical results are presented to illustrate the capacity of the proposed combined algorithms. It is noted that the coupled-concurrent GALLS algorithm, in which LLS is embedded in GA, is capable of yielding the best match to the selected desired structural shapes with minimum overall electrical energy consumption

3.2 Problem Formulation

The shape control problem considered in this chapter focuses on piezoelectric actuator design optimisation (PADO) in terms of finding optimum values for applied voltages and actuator geometries. When the geometrical parameter vector of piezoelectric actuators **X** and the applied voltage vector $\boldsymbol{\phi}$ are considered as design variables, the quasi-static shape control problem can be defined, in the context of optimisation formulation (Gallagher and Zienkiewicz, 1973), as follows:

Find $\mathbf{V}=[\mathbf{X}, \boldsymbol{\phi}]^T$ to

$$\text{Minimise } f(\mathbf{V}) = \text{Lnm}(\mathbf{X},\boldsymbol{\phi}) = \frac{\sum_{i=1}^{N} \frac{\left(w_i^d - w_i^c(X,\boldsymbol{\phi})\right)^2}{(w_{max}^d)^2}}{4 \times N} \tag{3.1}$$

$$\text{Subject to } g(\mathbf{V}) = 0 \Rightarrow [\mathbf{K}_{uu}(\mathbf{X})][\mathbf{u}_g(\mathbf{X},\boldsymbol{\phi})] + [\mathbf{K}_{u\phi}(\mathbf{X})][\boldsymbol{\phi}_g] = [\mathbf{0}] \tag{3.2}$$

$$\mathbf{V}_L \le \mathbf{V} \le \mathbf{V}_U \Rightarrow \mathbf{X}_L \le \mathbf{X} \le \mathbf{X}_U \text{ and } \boldsymbol{\phi}_L \le \boldsymbol{\phi} \le \boldsymbol{\phi}_U \tag{3.3}$$

Where, in the context of general optimisation formulation, **V** is the design variable vector; f(**V**) is the objective function; g(**V**) is the performance constraint; and $\mathbf{V}_L$ and $\mathbf{V}_U$ is the lower and upper bounds of the design variable vectors. The subscripts L and U denote lower and upper bounds respectively. In the context of the PADO problem, the design variable vector V has two components, namely, the geometric variable vector **X** and the applied voltage variable vector $\boldsymbol{\phi}$. In this chapter, the geometric variables in vector **X** are chosen to be the coordinates of selected design nodes, whereas the voltage variables in vector ϕ are the electrical potentials applied across the thickness direction of each actuator. The objective function f(**V**) in Equation (3.1) is defined as the estimated error function Lnm($\mathbf{X},\boldsymbol{\phi}$), which is a weighted sum of all square differences in displacements at selected nodes between the desired and calculated structural shapes. Where w_i^d and $w_i^c(\mathbf{X},\boldsymbol{\phi})$ are the desired and actuated (or calculated) displacements of the i^{th} node respectively, and w_{max}^d is the maximum displacement in the desired structural shape and N is the total number of nodes considered. For the case of plates considered in this chapter, w_i^d and $w_i^c(\mathbf{X},\boldsymbol{\phi})$ are the transverse displacements which is the $[(i-1)*11+3]^{th}$ displacement component in the global displacement vector $u_g(\mathbf{X},\boldsymbol{\phi})$. The

constraint equations in Equation (3.2) are the equilibrium equations that govern the structural behaviour when the structure is only subjected to electrical loading and are formulated using the finite element method. $[\phi_g]$ is global vector of nodal voltages. $[\mathbf{K}_{uu}(\mathbf{X})]$ and $[\mathbf{K}_{u\phi}(\mathbf{X})]$ are the global stiffness matrix and the global piezoelectric linearly coupling matrix respectively as described in detail in Chapter 2. As described by Equations (3.1-3.3), the PADO is an inverse problem and the optimum applied voltages and geometry parameters of piezoelectric actuators can be obtained simultaneously.

3.3 Optimisation Schemes

This section firstly describes two existing optimisation algorithms, namely, Linear Least Square (LLS) method and Genetic Algorithm (GA) method and their applications to static shape control of smart structures. By combining these two algorithms, several coupled new optimisation schemes are proposed.

3.3.1 Linear Least Square (LLS) Method

When the actuator configurations are known, the LLS method (Rorres and Anton, 1979) can be used to determine optimum voltage distribution to achieve the desired structural shape. In this case, Equations 3.1 and 3.2 become

Find ϕ to

$$\text{Minimise } \text{Lnm}(\phi) = \frac{\sum_{i=1}^{N} \frac{\left(w_i^d - w_i^c(\phi)\right)^2}{(w_{max}^d)^2}}{4 \times N} \tag{3.4}$$

$$\text{Subject to } [\mathbf{K}_{uu}][\mathbf{u}_g(\phi)] + [\mathbf{K}_{u\phi}][\phi_g] = [\mathbf{0}] \tag{3.5}$$

By minimising the least square error function between the actuated and the desired structural shapes, defined by the transverse nodal displacements for the case of plate structures. Equation (3.4) can then be simplified as follows:

$$\mathrm{Lnm}(\boldsymbol{\phi}) = \left([\mathbf{w}^{d}] - [\mathbf{w}^{c}(\boldsymbol{\phi})]\right)^{2} = 0 \tag{3.6}$$

Equation (3.5) indicates that there exists a linear relationship between the voltage and displacement variables. The linear relationship between the displacements and the voltages allows the former to be expressed as a linear combination of the latter. Equation (3.5) can be used to calculate the influence coefficient matrix $[\mathbf{C}^{w}]$. The k^{th} column $[\mathbf{C}^{w}]_k$ of $[\mathbf{C}^{w}]$ can be determined as the displacement vector $[\mathbf{w}^{c}]_k$ obtained by applying a unit voltage to the k^{th} patch, with ϕ_k =1.0Volts and 0.0Volts on all other patches. The entire influence coefficient matrix $[\mathbf{C}^{w}]$ can be constructed by applying a unit voltage to one patch at a time namely:

$$[\mathbf{w}^{c}(\boldsymbol{\phi})] = \sum_{i=1}^{N} \mathbf{w}_{i}^{c}(\boldsymbol{\phi}) = \sum_{i=1}^{N} \left(\mathbf{C}_{i1}^{w}\boldsymbol{\phi}_{1} + \mathbf{C}_{i2}^{w}\boldsymbol{\phi}_{2} + \ldots + \mathbf{C}_{iN_p}^{w}\boldsymbol{\phi}_{N_p} \right) = \sum_{i=1}^{N}\sum_{k=1}^{N_p} \mathbf{C}_{ik}^{w}\boldsymbol{\phi}_{k}$$

or
$$[\mathbf{w}^{c}(\boldsymbol{\phi})] = \sum_{k=1}^{N_p} [\mathbf{C}^{w}]_k \boldsymbol{\phi}_k = \left[\mathbf{C}^{w}\right][\boldsymbol{\phi}] \tag{3.7}$$

By substituting Equation (3.7) into Equation (3.6), the solution of optimum voltage can be expressed in terms of the influence coefficient matrix and the desired displacement vector $[\mathbf{w}^{d}]$ as follow:

$$[\boldsymbol{\phi}] = \left(\left[\mathbf{C}^{w}\right]^{T}\left[\mathbf{C}^{w}\right]\right)^{-1}\left[\mathbf{C}^{w}\right]^{T}[\mathbf{w}^{d}] \tag{3.8}$$

3.3.2 Genetic Algorithm (GA)

The Genetic Algorithm (GA) method is stochastic search method that was developed by (Holland, 1975) and then extended by (Goldberg, 1989). More details of history with discussion of GA and its application in practical engineering design can be found in (Woon, 2002). GA is employed to achieve piezoelectric actuator design optimisation for the structural shape control problem by treating the applied voltages and/or geometrical parameters of actuators as independent design variables. In GA, a fitness function is introduced, and then all design variables in the design space are transformed into bit string representations of possible solutions in the genetic space,

which are treated through the basic random operator of selection, crossover and mutation. Figure 3.1 depicts a flowchart of applying GA to solve the structural shape control problem.

Design variables are categorised as either discrete or continuous variables. Discrete variables can be represented as a binary or integer string, whereas continuous variables can be represented as a binary or float string. The binary string representation of the optimisation problem utilises the actual bounds of design variables. These design variables may be represented by chromosome like strings. Each design variables will be converted into its binary string equivalent and be mapped into a fixed length string of 0s and 1s. A binary value of "1" represents a stepwise movement and binary value of "0" represents no movement of a particular boundary design variable. Similarly, the integer and float string representation is an unsigned integer and floating number, respectively.

In this study, the GA is used in applications of static shape control of smart structures to find the optimal voltage distribution and optimal configuration of actuators for shape control problem. Where voltage distribution and geometry of actuators are treated as separate or simultaneous design variables. The performance criterion shown in Equation 3.1 is used as an objective function, which is used to determine the fitness function. GA requires the transformation of the design variables from design space into genetic space, which are presented in strings for each population. Then GA was characterised by bit string representation of possible solutions to a give problem through the basic random operators of selection, crossover and mutation. Design variables are categorised as either discrete or continuous variables. Discrete variables can be represented as a binary or integer string, while continuous variables can be represented as a binary or float string. The binary string representation of the optimisation problem utilises the actual boundary of design variables. These design variables may be represented by chromosome like strings. Each design variable will be converted into its binary string equivalent and be mapped into a fixed length string of 0s and 1s. A binary value of "*1*" represents a stepwise movement and binary value of "*0*" represents no movement of a particular boundary design variable. Similarly, the integer and float string representation is an unsigned integer and floating number, respectively.

Population size

The population size equals the length of the string or chromosome (L). The length of the integer and floating string is the number of discrete and continuous design variables, respectively. L of the binary string can be written as:

(a) Discrete binary string:

$$L = \text{integer}\left[\frac{\log(N_d)}{\log(2)}\right] \tag{3.9}$$

where N_d is the number of discrete variables.

(b) Continuous binary string:

$$L = \sum_{i=1}^{N_d} L_i \tag{3.10}$$

where

$$L_i = \text{integer}\left[\frac{\text{Log}\frac{v_{i,U} - v_{i,L}}{v_{i,\text{step}} + 1}}{\text{Log}(2) + 1}\right] \tag{3.11}$$

where $v_{i,U}$, $v_{i,L}$ and $v_{i,\text{Step}}$ are the lower and upper bounds as well as the stepwise increment of the i^{th} continuous design variable, respectively.

String decoding

The discrete and continuous binary string is converted into an unsigned integer. It is then mapped to the associated practical discrete value and physical value. For example, a string [A B C D] of the i^{th} design variable, where A, B, C, D can be 0 or 1, can be decoded as $T = A\ 2^3 + B\ 2^2 + C\ 2^1 + D\ 2^0$, then mapped to the $(T+1)^{th}$ discrete value in the list of design variables and the relevant physical value is then computed by

$$v_i = v_{i,L} + \frac{(v_{i,U} - v_{i,L}) \times T}{2^{L_i} + 1} \tag{3.12}$$

After decoding of the integer string, the location of the practical value in the discrete value list corresponds to the number in the string as A^{th}, B^{th}, C^{th} and D^{th} in the discrete value list. The numbers in a float string are also physical values.

Fitness function

Consider a total of N_{pop} populations. Let Lnm_i be the objective error function of the i^{th} population, thus $Lnm_{max} = \max_{1 \le i \le Npop} (Lnm_i)$ and $Lnm_{min} = \min_{1 \le i \le Npop} (Lnm_i)$. For the structural shape control problem, the fitness function f_i' for the i^{th} population can be defined as:

$$f_i' = a \times f_i + b \tag{3.13}$$

where

$$f_i = \left(\frac{Lnm_i - Lnm_{min}}{Lnm_{max} - Lnm_{min}} \right)^2 \tag{3.14}$$

and

$$\left.\begin{aligned} a &= 1 \\ b &= 0 \end{aligned}\right\} \quad \text{when} \quad f_{max} = f_{min}$$

or

$$\left.\begin{aligned} a &= \frac{f_{average}}{f_{max} - f_{average}} \\ b &= \frac{f_{average}(f_{max} - 2 \times f_{average})}{f_{max} - f_{average}} \end{aligned}\right\} \quad \text{when} \quad f_{average} < \left(\frac{f_{max} + f_{min}}{2} \right)$$

or

$$\left.\begin{aligned} a &= \frac{f_{average}}{f_{average} - f_{min}} \\ b &= -\frac{f_{min} \times f_{average}}{f_{average} - f_{min}} \end{aligned}\right\} \quad \text{when} \quad f_{average} \ge \left(\frac{f_{max} + f_{min}}{2} \right) \tag{3.15}$$

In the above equations for calculating the constants a and b, the following definitions are used:

$$f_{max} = \max_{1 \le i \le Npop} (f_i), \qquad f_{min} = \min_{1 \le i \le Npop} (f_i), \qquad f_{average} = \frac{1}{N_{pop}} \sum_{i=1}^{N_{pop}} (f_i) \quad (3.16)$$

GA operators

Once the evaluation of all individuals in a population is completed, the binary string is manipulated through the basic random operators of selection, crossover and mutation. Selection is based on a tournament selection scheme, which was used between two randomly selected binary strings (P) via relative fitness (f'_r) and fitness cumulative (f'_c). Random number generator (P^r) facilitates the random selection of strings to be included in the selection process for next the population (P^{next}) as given by

$$P_i^{next} = P_1 \quad \text{when} \quad P_i^r < f'_{c_1}$$

$$P_i^{next} = P_{j+1} \quad \text{when} \quad \begin{cases} P_i^r \ge f'_{c_1} \\ \\ f'_{c_j} \le P_i^r < f'_{c_{j+1}} \end{cases} \quad (3.17)$$

where i, j =1,…,N_{pop} and $f'_{c_i} = f'_{r_{i-1}} + f'_{r_i}$; i=2,…,$N_{pop}$ and $f'_{r_i} = \dfrac{f'_{r_i}}{\sum_{j=1}^{N_p} f'_{r_j}}$

The tournament selection is performed twice for every crossover in order to find a suitable pair of parents. Equation (3.17) is also considered to define two parents string. After these parents string are selected, the crossover is executed by randomly choosing two sites on the parent's string and swapping them between chosen sites to produce the offspring. It can be clearly seen in the following example as the **bold strings** are swapped between parent 1 and parent 2 to produce child 1 and child 2 (offspring).

Parent 1 = 111**10010100**10111→Child 1 = 111**00101010**10111

Parent 2 = 001**00101010**10101→Child 2 = 001**10010100**10101

For the integer string, the process under taken by the crossover operator is similar to that of the binary string. For the float string, two parents are selected randomly from the mating pool and an offspring is generated according to the following equation:

$$\text{Child1} = \text{Parent1} + r\ \{\text{Parent1} - (\text{Parent2})^r\} \quad (3.18)$$

where r is a random number ($0<r<1$). f(Parent1 ≥ Parent2) and f(Parent1 ≤ Parent2) for maximising and minimising objective function (f), respectively.

Mutation is the last process in GA operator. This process is simply to choose a few members from the population pool. It alters genes with a small probability on a bit-by-bit basis. These values were set to contribute to a fast convergence toward the local or global optimum point and prevent premature phenomena. For a binary string, the probability of crossover was set to 1 while the probability of mutation was set to 0 or vice versa. For an integer string, gene locus is replaced by a random integer between 1 and number of discrete values corresponding to the design variables. For a float string, non-uniform mutation and dynamic mutation are applied. It chooses randomly the gene value and searches for the minor domain near the original design. The procedures of GA are defined below:

Step 1: Obtain the structural and GA input parameters

Step 2: Select boundaries for design variables. The maximum and minimum values of the design variable mapped to the maximum and minimum of chromosome or binary string in the GA

Step 3: Generate the initial design value randomly for piezoelectric actuators and voltage distribution, knows as population string chromosomes.

Step 4: Decode one of the string chromosomes of the population to boundary movement.

Step 5: Using the FEA solver to calculate the nodal transverse displacement of the structure of designs.

Step 6: Compute fitness value of individual designs.

Step 7: Repeat step 4 through 6 until all members of the population have been evaluated.

Step 8: Perform to check the relative error of average fitness of continuous generation. If it is very small the then the population is deemed to have converged. If so, create a new set of design variable based on the fittest chromosome. Create a new random parent population.

Step 9: If a set number in Step 8 is converged then go to 12; otherwise go on to step 10.

Step 10: If the fittest chromosome has not been reproduced then randomly replace one offspring through selection, crossover and mutation. Repeat until a new population of offspring has been created.

Step 11: If the number of generation has been reached then go on to step 12, otherwise return to step 4.

Step 12: Replace design variable by movement vector of the fittest chromosome of the last population. The final set of design variable defines the optimum solution.

And the flowchart of this process is shown in Figure 3.1.

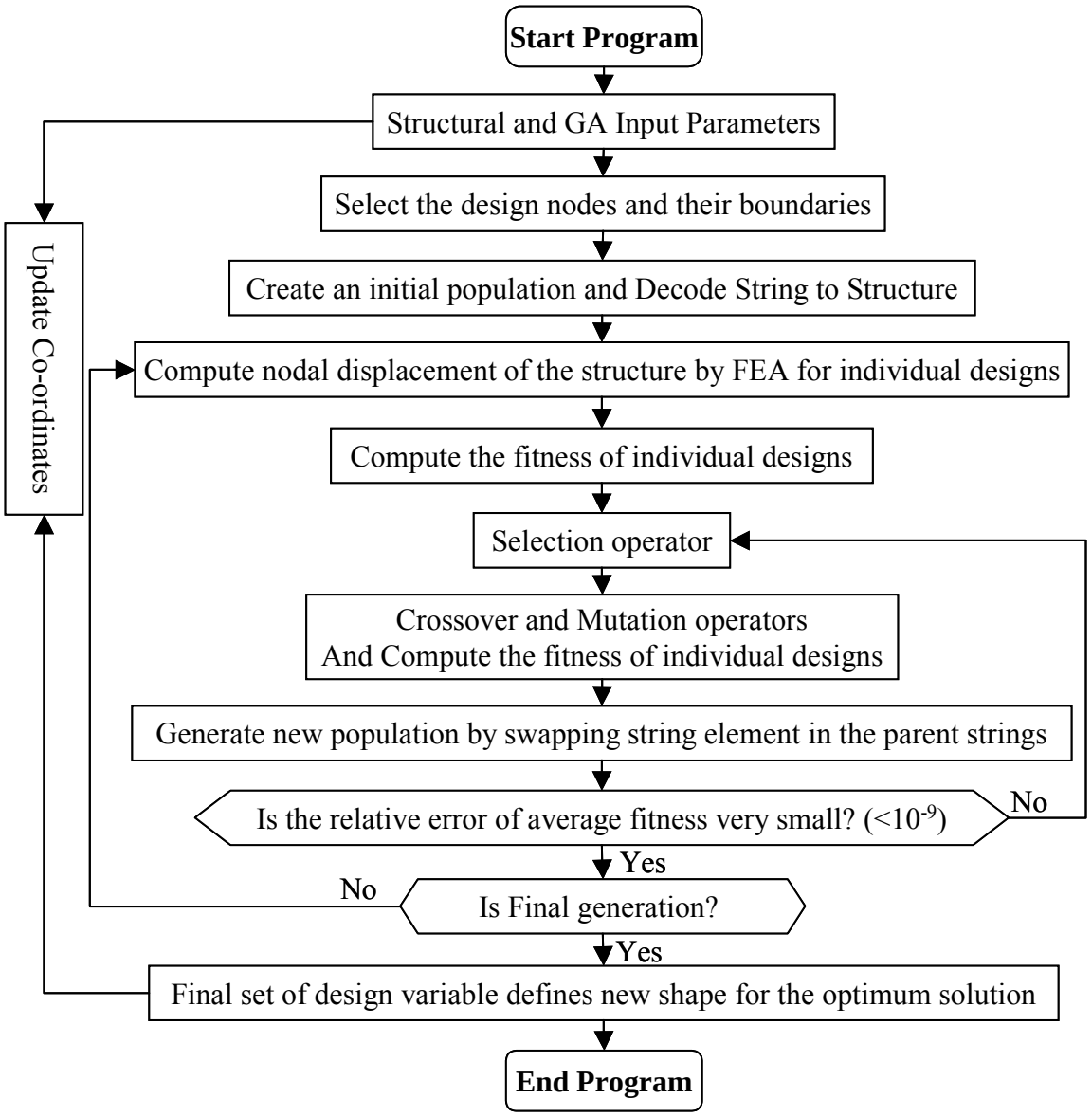

Figure 3.1: Flow chart of the GA algorithm

3.3.3 Coupled Algorithms

For the structural shape control problem defined in Equations (3.1)-(3.3), both the voltages and the geometric parameters of the actuator patches are chosen as the design variables and should be determined in a coupled fashion. In this section, we propose a coupled algorithm that determines the voltage distribution using the LLS algorithm and the geometry of the actuator patches using the GA algorithm in an alternating or concurrent fashion.

3.3.3.1 Coupled-Alternating Algorithm

Figure 3.2 depicts the flowchart of the coupled-alternating algorithm (CAA) in which each iteration loop has two stages. As shown in Figure 3.2, an initial actuator shape design $\mathbf{X}^0$ is selected. For the k^{th} iteration loop ($k \geq 1$), at stage 1, the LLS is employed to determine the optimum voltage distribution for the current iteration loop using the actuator shapes obtained in the previous iteration loop as the fixed actuator geometry; then at stage 2, GA algorithm is utilised to determine the optimum actuator shapes for the current iteration loop using the optimum voltage distribution determined at the first stage of the current iteration loop. At the end of each iteration loop, a convergence condition defined in terms of the objective error function is checked. Such iteration process continues until the selected convergence criterion is satisfied. Thus the mathematical formulation in equations (3.1)-(3.3) become: Find $\mathbf{V}=[\mathbf{X}^k, \boldsymbol{\phi}^k]^T$ ($k \geq 1$) via the following two stages in an alternating fashion until selected convergence condition is met:

Stage 1: determine the optimum voltage distribution using LLS method and the actuator geometry from previous iteration loop:

$$[\boldsymbol{\phi}^k] = \left(\left[\mathbf{C}^w(\mathbf{X}^{k-1}) \right]^T \left[\mathbf{C}^w(\mathbf{X}^{k-1}) \right] \right)^{-1} \left[\mathbf{C}^w(\mathbf{X}^{k-1}) \right]^T [\mathbf{w}^d] \tag{3.19}$$

Stage 2: determine the optimum actuator geometry using GA method and the optimum voltage distribution obtained at stage 1:

$$\text{Minimise } f(\mathbf{V}) = \text{Lnm}(\mathbf{X}^k, \boldsymbol{\phi}^k) = \frac{\sum_{i=1}^{N} \frac{\left(w_i^d - w_i^c(\mathbf{X}^k, \boldsymbol{\phi}^k)\right)^2}{(w_{max}^d)^2}}{4 \times N}$$

$$\text{Subject to } g(\mathbf{V}) = 0 \Rightarrow [\mathbf{u}_g(\mathbf{X}^k, \boldsymbol{\phi}^k)] = -[\mathbf{K}_{uu}(\mathbf{X}^k)]^{-1}[\mathbf{K}_{u\phi}(\mathbf{X}^k)][\boldsymbol{\phi}_g^k]$$

$$\mathbf{X}_L \le \mathbf{X} \le \mathbf{X}_U \text{ and } \forall \boldsymbol{\phi} \in \mathbf{R} \qquad (3.20)$$

We refer the LLS and GA based CAA algorithm as LLS-GA algorithm.

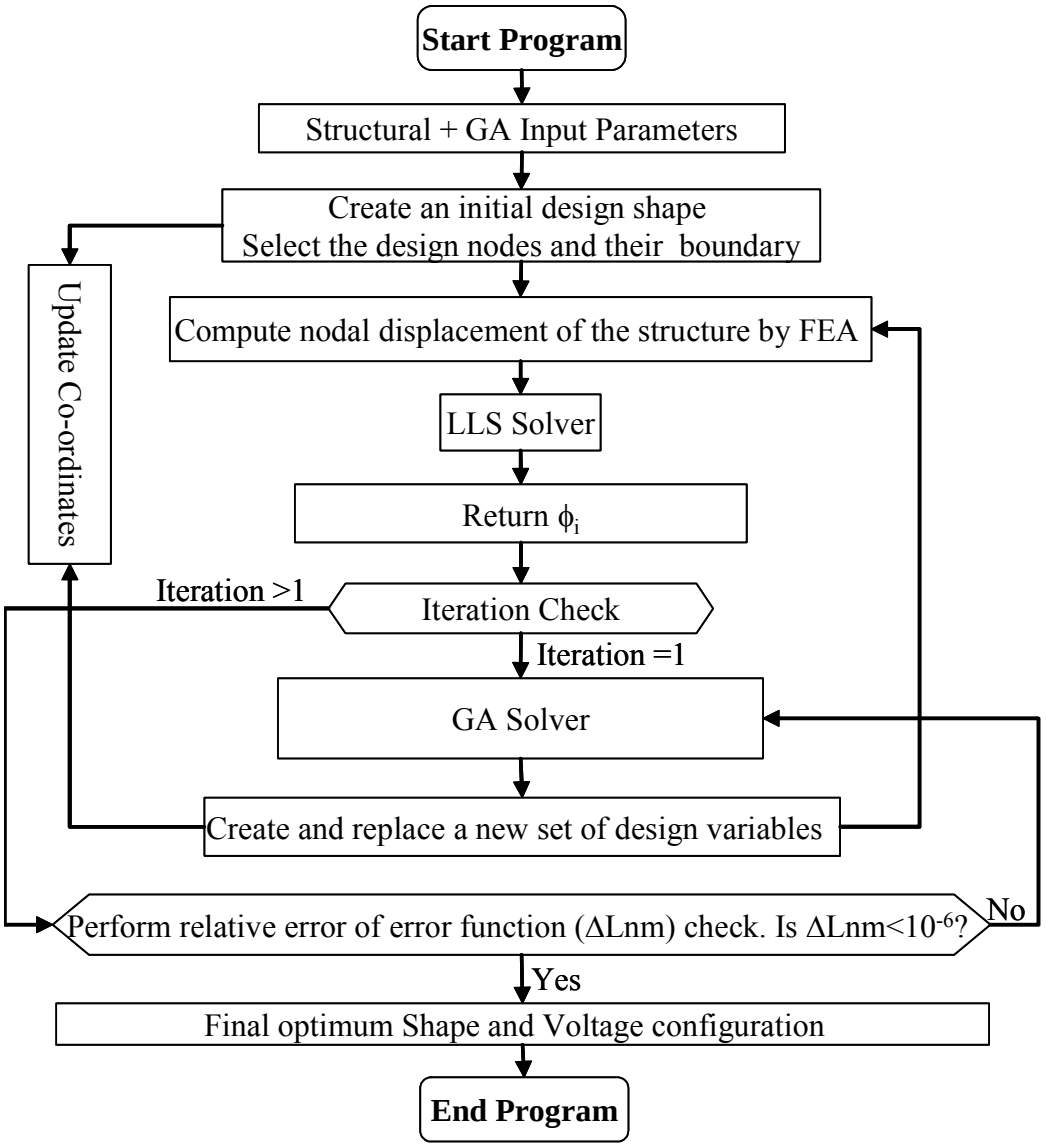

Figure 3.2: Flow chart of the coupled-alternating algorithms (LLS-GA)

3.3.3.2 Coupled-Concurrent Algorithm

Figure 3.3 depicts the flowchart of the coupled-concurrent algorithm (CCA) in which the LLS is employed to determine the optimum voltage distribution and then to update the voltage element of the string code for each individual design in the GA. This algorithm has the same procedure as the GA except that, after creating a population and its decoding string, there is an addition step in which the LLS is employed to optimise the voltage distribution for the individual design. By adding this step, the objective function of each individual design is calculated based on a random actuator configuration and its optimal voltage distribution obtained by LLS. This algorithm is referred to as GALLS, for which the mathematical formulation in Equations (3.1)-(3.3) can then be rewritten as:

$$\text{Find} \quad \mathbf{V}=[\mathbf{X}^k,\ \boldsymbol{\phi}^k]^T \text{ to}$$

$$\text{Minimise } f(\mathbf{V}) = \text{Lnm}(\mathbf{X}^k,\boldsymbol{\phi}^k) = \frac{\sum_{i=1}^{N} \frac{\left(w_i^d - w_i^c(\mathbf{X}^k,\boldsymbol{\phi}^k)\right)^2}{\left(w_{max}^d\right)^2}}{4 \times N}$$

$$\text{Subject to } g(\mathbf{V}) = 0 \Rightarrow [\mathbf{u}_g(\mathbf{X}^k,\boldsymbol{\phi}^k)] = -[\mathbf{K}_{uu}(\mathbf{X}^k)]^{-1}[\mathbf{K}_{u\phi}(\mathbf{X}^k)][\boldsymbol{\phi}_g^k] \qquad (3.21)$$

$$\mathbf{X}_L \le \mathbf{X} \le \mathbf{X}_U \text{ and } \forall \boldsymbol{\phi}^k \in \mathbf{R}$$

$$\text{where} \quad [\boldsymbol{\phi}^k] = \left(\left[\mathbf{C}^w(\mathbf{X}^k)\right]^T\left[\mathbf{C}^w(\mathbf{X}^k)\right]\right)^{-1}\left[\mathbf{C}^w(\mathbf{X}^k)\right]^T[\mathbf{w}^d] \qquad (3.22)$$

After all values of the objective function are evaluated, the selection, crossover and mutation operators are performed to check if the best individual design in the generation meets the convergence criterion as shown in the flowchart of Figure 3.3.

The coupled-concurrent algorithm is developed by replacing the voltage string elements for each randomly generated design in the GA with the optimum voltage string elements obtained by employing the LLS solver. This is a fully coupled process with the voltage related string elements being optimally determined and then embedded in each individual design in the GA. This is different from the coupled-alternating GA and LLS algorithm in which the optimisation process is a partially coupled one and it

optimises the applied voltage distribution and the actuator shapes independently by two stages to achieve desired shape.

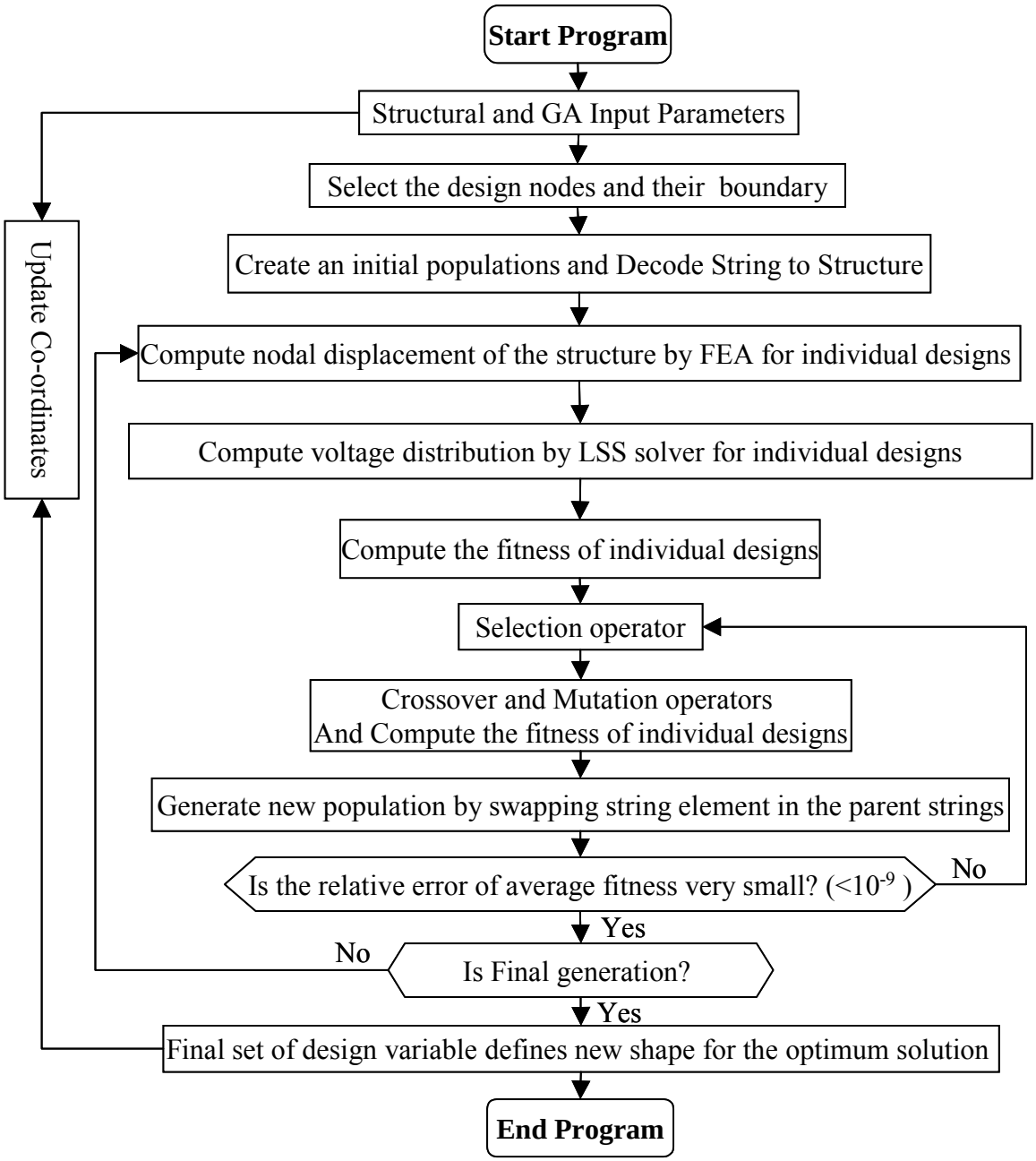

Figure 3.3: Flow chart of the GALLS algorithm

3.4 Numerical Examples

3.4.1 Bending shape control test

Consider a cantilever plate that is clamped at its left edge and subjected to no applied mechanical loading, as shown in Figure 3.4. The plate has a length of 0.15 m, width of 0.06m and consists of two orthotropic layers of 0.01m thickness each. Three pairs of collocated piezoelectric actuators of 0.001m thick each are bonded to the top and bottom surfaces of the host plate. Only the top actuator patches are activated in this case. The plate material has the following stiffness constants: $c_{11}=c_{22}=c_{33}=82.68$GPa, $c_{12}=c_{13}=c_{23}=27.56$GPa, $c_{44}=c_{55}=c_{66}=26.5$GPa. The mechanical, permittivity and piezoelectric material properties of piezoelectric actuator patches are: $c_{11}=c_{33}=84.8$GPa, $c_{22}=29.7$GPa, $c_{12}=c_{13}=c_{23}=36.35$GPa, $c_{44}=c_{55}=c_{66}=24.2$GPa; $\chi_{11}=\chi_{22}=15.3\text{x}10^{-9}$F/M, $\chi_{33}=15.0\text{x}10^{-9}$F/M and $d_{31}=-254$pm/V, $d_{32}=-254$pm/V, $d_{33}=374$pm/V, $d_{24}=584$pm/V, and $d_{15}=584$pm/V.

For the bending shape control test, the desired shape of the cantilever plate is defined as $w^d(x,y)=10^{-5}\cos(10x-1)$, which represents cylindrical bending of the plate. The finite element model of the considered smart plate is composed of 10 elements. Each piezoelectric actuator patch is modelled using two elements.

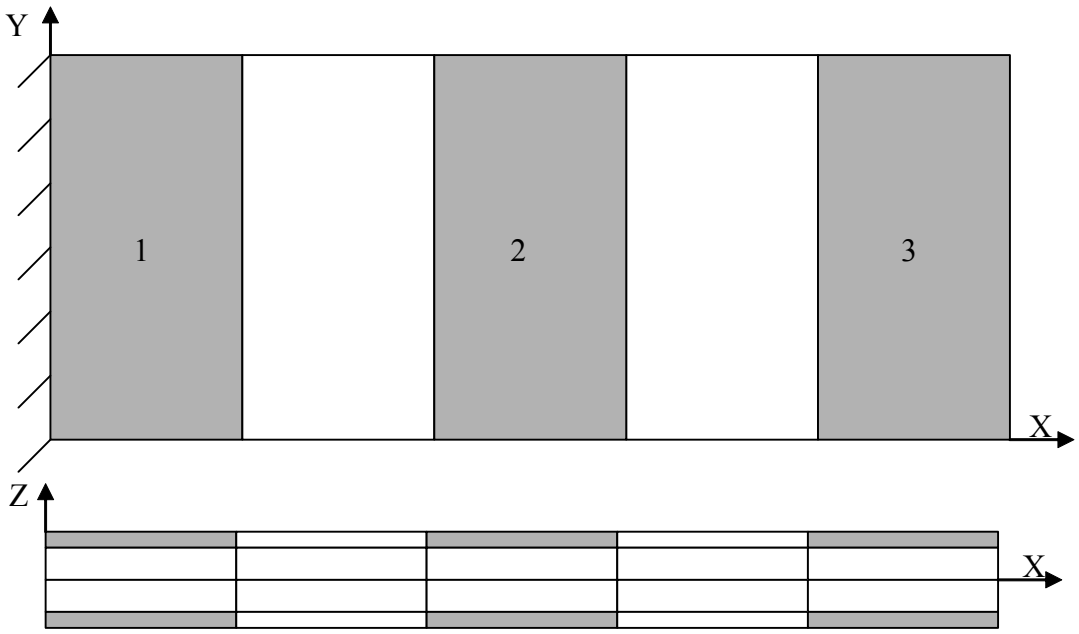

Figure 3.4: Cantilever plate in XY and XZ plane

3.4.1.1 Example 1: Optimum voltage distribution by using GA

In this example, the applied voltages applied to piezoelectric actuator patches with given geometry are the only design variables with –500 volts and 500 volts as lower and upper bounds respectively. The piezoelectric actuator patches are in rectangular shape as shown in Figure 3.4, and have the same dimensions of 0.06 m long and 0.03m wide. In the GA calculation, the population is taken as 10; the maximum number of generation is 1000; the length of binary string is 16; and the probability of crossover and mutation are 1 and 0.001, respectively. The optimum voltages for each piezoelectric actuator patch obtained by the LLS method and the GA are listed in Table 3.1. The results show that this desired shape could be best matched with the error estimation Lnm in the order of $2x10^{-5}$, and relative difference in the values of the error functions calculated using the two methods is less than 0.1%. It is noted that the LLS method yields the bending shape slightly closer to the desired bending shape than the GA method. In terms of computing efficiency, the GA results were achieved after 36 convergences over a total of 500 generations whereas the LLS method requires only one calculation. Table 3.2 lists the results predicted by the GA with different random initial values of voltages applied to the three patches. All the runs underwent 1000 generations, and they all seem to converge to voltage distributions close to those predicted by LLS. There exists a good agreement between the optimum voltages determined by the LLS and GA methods. Figure 3.5 shows the convergence histories obtained by GA.

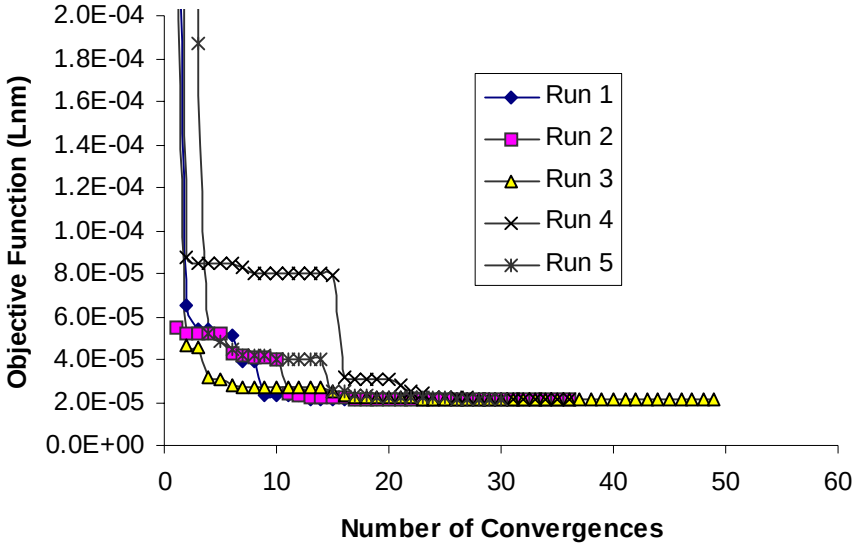

Figure 3.5: Convergence history of voltage optimization in various GA runs

Table 3.1: Optimum voltage distributions determined using LLS and GA algorithms for the shape control of the cantilever plate

Patch	LLS	GA
1	393.2	392.6
2	477.7	480.0
3	135.7	129.1
Lnm	2.117×10^{-5}	2.119×10^{-5}
Generations	-	1000

Table 3.2: Random initial voltage distributions and error estimations and their final optimum results obtained with 5 GA runs

Runs		1	2	3	4	5
Lnm	Initial	3.968×10^{-4}	5.498×10^{-5}	2.548×10^{-4}	1.109×10^{-3}	1.135×10^{-3}
	Final	2.134×10^{-5}	2.139×10^{-5}	2.134×10^{-5}	2.119×10^{-5}	2.182×10^{-5}
		Voltage (Volts)				
Initial	Patch 1	389.0	378.3	425.0	466.3	336.3
	Patch 2	394.3	489.4	487.4	176.2	393.9
	Patch 3	54.4	376.6	147.7	70.1	463.2
Final	Patch 1	390.4	390.3	396.0	392.6	388.7
	Patch 2	484.6	486.3	471.4	480.0	492.2
	Patch 3	125.4	119.4	142.4	129.1	93.3

3.4.1.2 Example 2: Shape optimisation by using GA

In this example, the geometrical parameters that define the shape of an actuator patch are treated as the only design variables whereas the applied voltages are assumed to be given. Consider the same composite plate in Example 1, and choose the x-coordinates at the 12 points in Figure 3.6 as the design variables. The physical boundaries for the design variables are: $0.001 \le x_1, x_2, x_3 \le 0.044$; $0.046 \le x_4, x_5, x_6 \le 0.074$; $0.076 \le x_7, x_8, x_9 \le 0.104$; $0.106 \le x_{10}, x_{11}, x_{12} \le 0.149$. Two voltage distribution cases are considered. In the first case, the voltage distribution predicted by the LLS method in Table 3.1 is used, namely, $\phi_1 = 393.2$ volts, $\phi_2 = 477.7$ volts and $\phi_3 = 135.7$ volts. In the second case, the optimal voltage distribution is chosen as: $\phi_1 = 301.2$ volts, $\phi_2 = 224.6$ volts and $\phi_3 = 84.1$ volts, which are from Example 5. The parameters selected in the GA runs are the same as those in Example 1 except that the maximum number of generation is chosen as 500 and 200 for first and second cases, respectively.

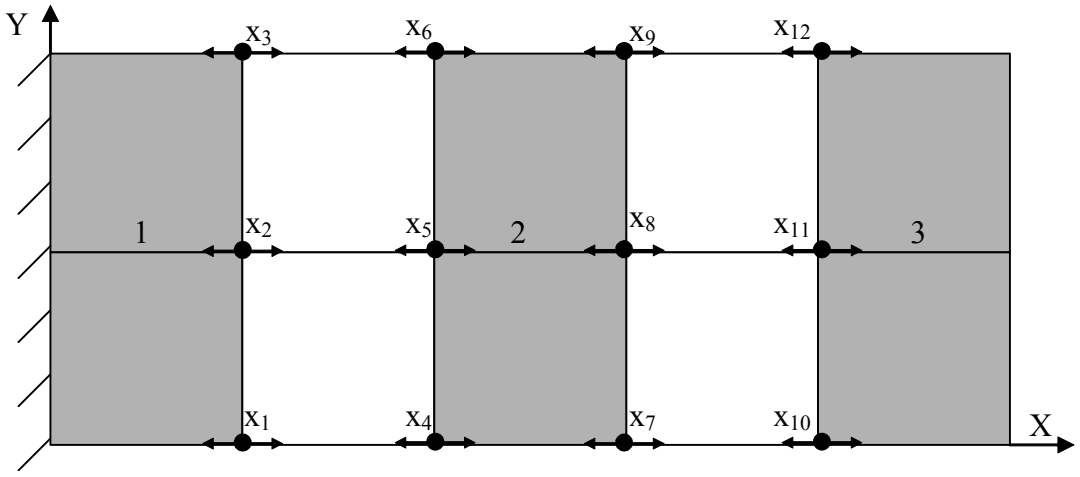

Figure 3.6: Directional of design variables

In the first case, the optimum shapes of the three actuators were obtained after 438 generations consisting of 23 convergences. Figures 3.7 and 3.8 show the actuator shapes and the convergence history, respectively. The achieved minimum error function Lnm is 9.38×10^{-6}, which is a reduction of 56% compared to that in Example 1. In the second test, the optimum actuator shapes were achieved after 65 generations consisting of 21 convergences. Figure 3.9 shows the final actuator configurations. The achieved minimum error function Lnm is 9.41×10^{-7}, which represents a 96% reduction compared to that in Example 1. Five GA runs were conducted for the second case with five different random initial piezoelectric actuator shapes. All the runs were performed with the maximum number of generation as 200 and all converged to exactly the same actuator shape configuration as shown in Figure 3.9. Tables 3.3 and 3.4 compare the initial and final values of Lnm, number of convergences and the total number of generations for the two cases and the five GA runs respectively. Figure 3.10 depicts the convergence histories of these five GA runs.

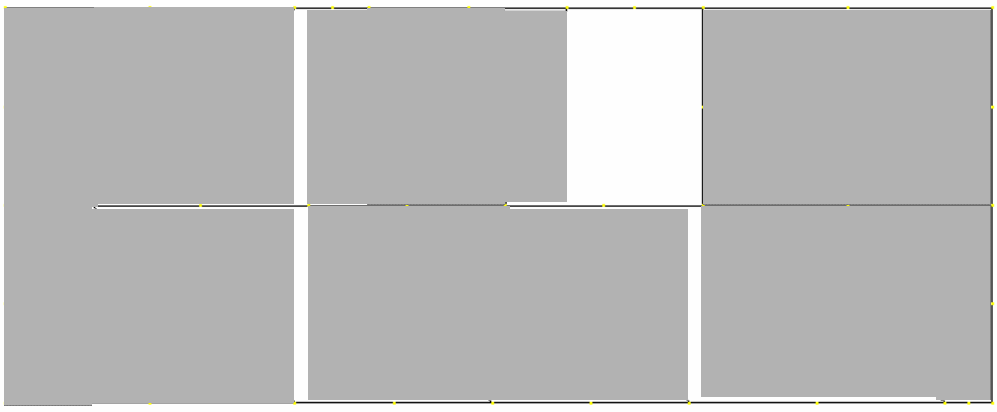

Figure 3.7: Final actuator shape with ϕ_1=393.2 volts, ϕ_2=477.7 volts and ϕ_3=135.7 volts

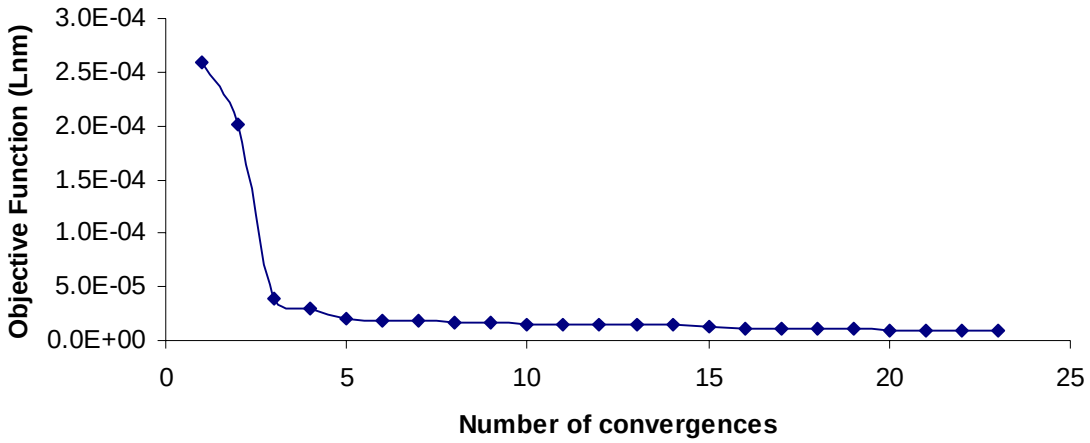

Figure 3.8: Convergence history of shape optimization by GA.

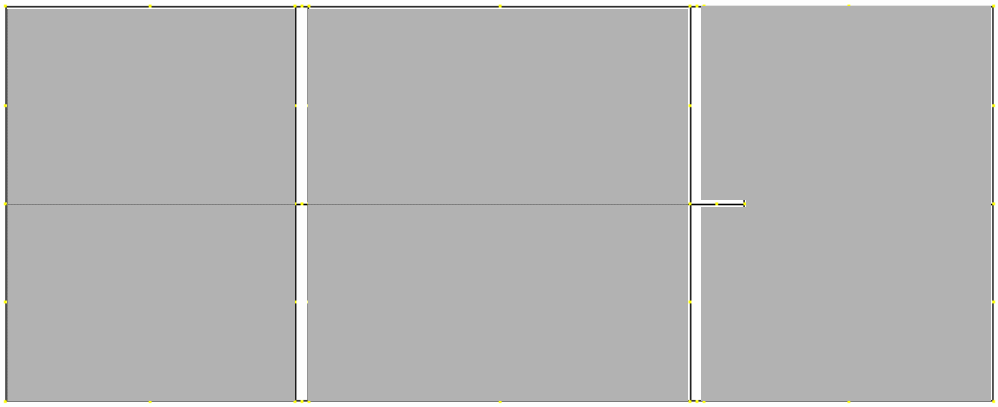

Figure 3.9: Final actuator shape with ϕ_1=301.2 volts, ϕ_2=224.6 volts and ϕ_3=84.1 volts.

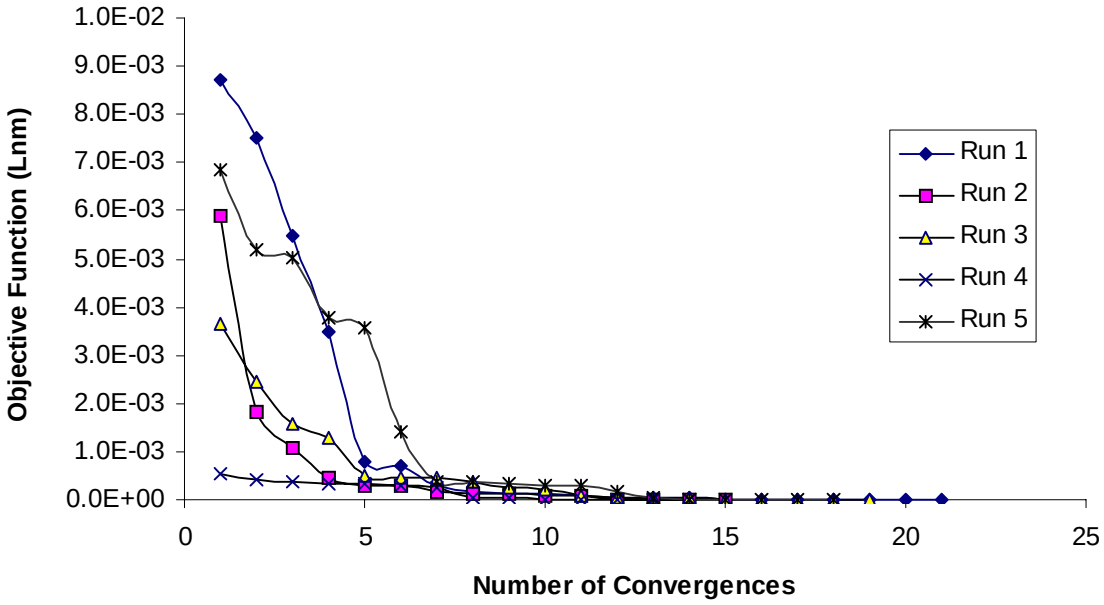

Figure 3.10: Convergence history of shape optimization with various runs by GA.

Table 3.3: Results for optimum actuator shape with different applied voltage

Test No	1	2
Maximum of generations	500	100
No of convergences	23	21
Total No of generations	438	65
Lnm	9.383×10^{-6}	9.410×10^{-7}
% change of Lnm	-56	-96

Table 3.4: Results for optimum actuator shape with random initial of design variables

Runs		1	2	3	4	5
Lnm	Initial	8.709×10^{-3}	5.909×10^{-3}	3.670×10^{-3}	5.282×10^{-4}	6.850×10^{-3}
	Final	9.410×10^{-7}	9.410×10^{-7}	9.410×10^{-7}	9.410×10^{-7}	9.410×10^{-7}
No of Convergences		21	15	19	14	18
Total No of Generation		65	147	187	71	175

These results show that the achieved minimum error functions Lnm are dependent of the voltage distribution. In the first case the optimum voltage distribution for the baseline actuator configuration shown in Figure 3.4 is employed, whereas in the second case the optimum voltage distribution for the actuator configuration shown in Figure 3.9 is used, and it is the optimal one for this problem as will be shown in Example 5. In the first case, a local minima was achieved whereas in the second case a global minima was obtained as the achieved minimum Lnm value in the second case is about 10% of that in the first case. This illustrates that the optimisation should be conducted by coupling the determination of voltages and the actuator shapes.

The results for both cases show that the final piezoelectric actuator shapes can be symmetrical or non-symmetrical about the middle line of the plate in the vertical direction. It is believed that the objective error function is calculated based on the least square difference between the calculated and desired displacements at all the nodes in the plate. There are thus three possible solutions for the actuated displacements, namely, less than, equal or greater than the desired displacement, at any node. In this particular example, if both actuated transverse displacements (in z-direction) at all nodes on the neutral plane is less than or greater than the desired displacements, then the final shapes of actuators are expected to be symmetrical as shown in Figure 3.9. Otherwise, if the actuated displacements are larger than the desired displacements at certain nodes and

less than those at remaining nodes, it is expected that the actuator shapes will be non-symmetrical solution as shown in Figure 3.7.

For the second case, each actuator element in Figure 3.6 is subdivided into 2 and 3 elements in the vertical direction, thus each patch is composed of 4 and 6 elements along the vertical direction. The total numbers of design variables then become 20 and 28, respectively. The achieved optimum actuator shapes are shown in Figures 3.11 and 3.12, respectively. Figure 3.13 compares the convergences of the three different mesh cases. Table 3.5 shows a comparison of the results obtained using three different finite element meshes. It can be seen that the number of convergences, total number of generations and the minimum error Lnm increase when finer meshes are used. It is believed that this is due to the increase in the total number of nodes at which the square differences between the desired and actuated displacements are computed while keeping the total number of actuators unchanged.

Table 3.5: Optimum actuator shape optimisation with different FE mesh

No of elements	10	20	30
Maximum of generations	100	500	1500
No of convergences	21	29	39
Total No of generations	65	143	890
Lnm	9.410×10^{-7}	10.30×10^{-7}	12.59×10^{-7}

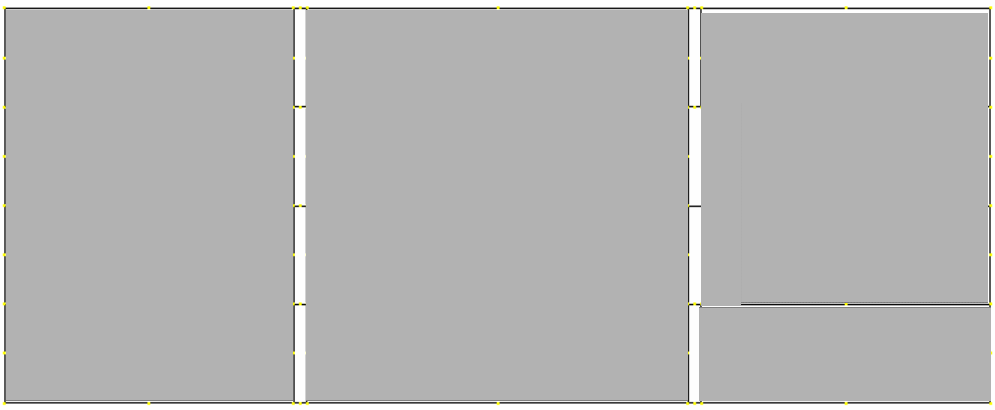

Figure 3.11: Final actuator shape of 4x5 FE model.

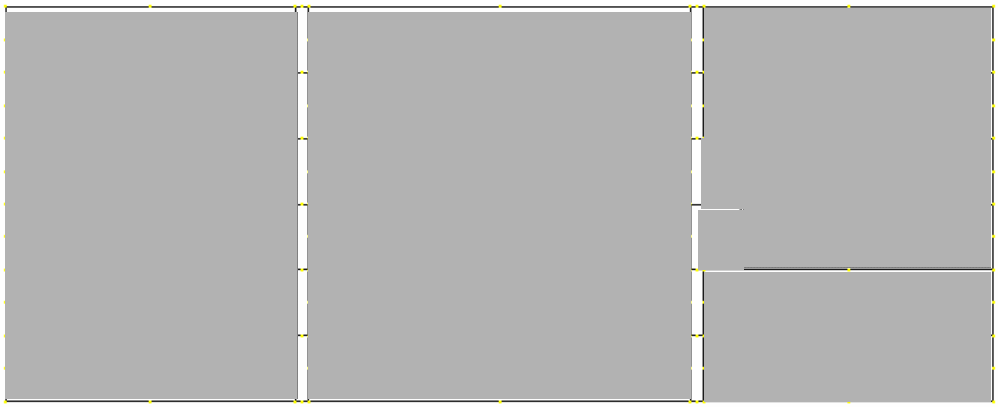

Figure 3.12: Final actuator shape of 6x5 FE model.

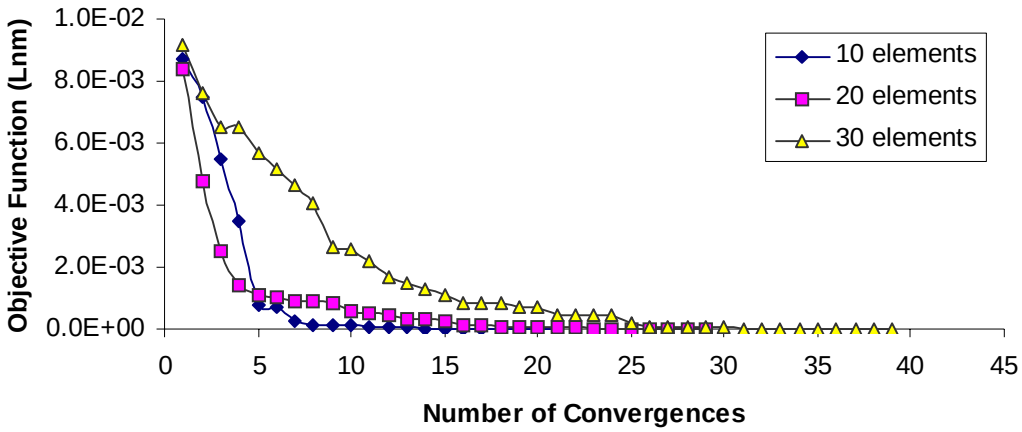

Figure 3.13: Convergence history of shape optimisation with three different FE meshes

3.4.1.3 Example 3: Shape and voltage optimisation by using GA

In this example, GA will be used to optimise the voltage distribution and the piezoelectric actuator shapes simultaneously to achieve the desired shape. The applied voltages and the selected nodal coordinates are set as design variables to minimise the error function Lnm. Consider the same model and employ the same parameters in GA for both the voltage and geometry design variables as given in examples 1 and 2. Five GA runs, each with different initial values of the design variables, were performed and the best results obtained are presented here. The optimum geometrical shape and the convergence-history are shown in Figures 3.14 and 3.15, respectively. The optimum voltages applied to the actuator patches are ϕ_1 = 317.2 volts, ϕ_2 = 307.2 volts and ϕ_3 = 125.0 volts, and the error function is 2.85×10^{-6}. It is evident that the values for the optimum applied voltages and the error function are in the associated ranges of the two

cases given in Example 2. This indicates that there exists a better solution with a voltage distribution and actuator shapes that yield lower value of the error function. In this GA run, the final solution was achieved at after 111 convergences over a total of 10,358 generations, which are significantly larger than those in Table 3.3 indicating a slow convergence and more time consuming. This can also be seen in Figure 3.15 as the objective error function reduces very slowly after several convergences. These results show that GA method can be applied to simultaneously search for the optimum voltage distribution and piezoelectric actuator shapes to minimise the objective error function. However, direct usage of the GA can be time consuming due to slow convergence.

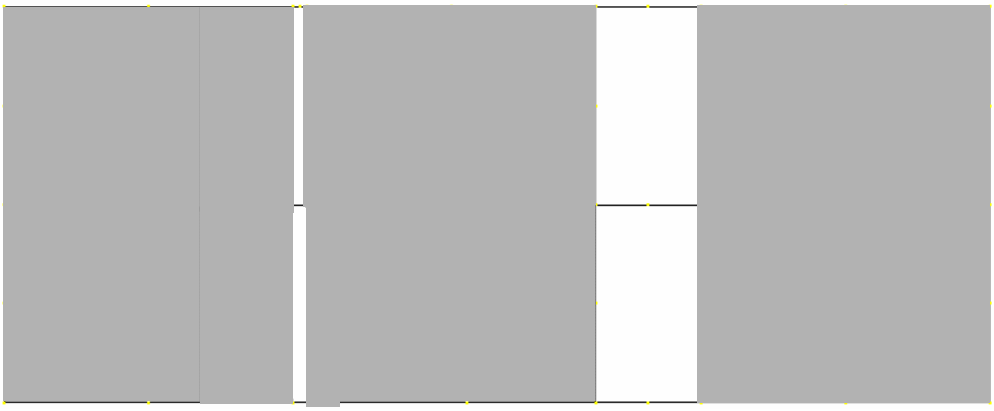

Figure 3.14: Final actuator shape considering actuator shape and voltage optimisation using GA.

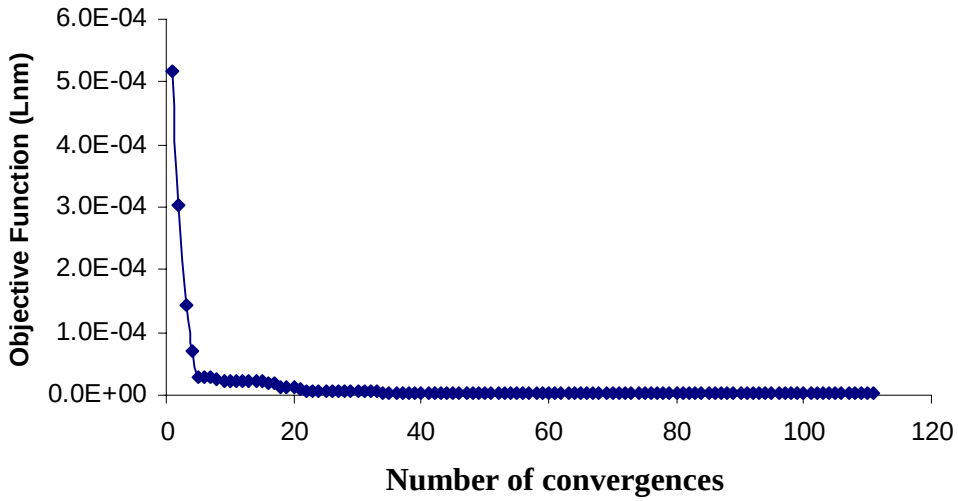

Figure 3.15: Convergence history considering actuator shape and applied voltage optimisation using GA.

3.4.1.4 Example 4: Shape and voltage optimisation by using coupled-alternating algorithms

The LLS-GA based coupled-alternating algorithm was used to solve the problem given in Example 2 using the same model and bounds of design variables. When employing the LLS-GA algorithm with an initial actuator geometry shown in Figure 3.6, the numerical results are summarised in Table 3.6. The solution converged at the 4^{th} loop. The final optimum values of the total applied voltage and the objective error function are 782.3 volts and 3.22×10^{-6}. Thus the total applied voltage and the objective error function Lnm are reduced by 22.28% and 84.81%, respectively. It is not clear whether or not the LLS-GA algorithm yields a local or global optimum solution.

Table 3.6: Results of voltages and error function at different loops in the LLS-GA

Iteration loop	1	2	3	4
Patch 1 (volts)	393.2	359.9	335.5	301.9
2 (volts)	477.7	408.0	343.0	308.4
3 (volts)	135.7	161.6	199.5	172.0
Total of Volatges	1006.6	929.5	878.0	782.3
Lnm	2.117×10^{-5}	7.071×10^{-6}	5.212×10^{-6}	3.225×10^{-6}

3.4.1.5 Example 5: Shape and voltage optimisation by using GALLS

The GALLS algorithm was utilised to solve the problem in Example 2 using the same 2x5 finite element mesh in Figure 3.6 and bounds of design variables. In total four GA runs were performed using different random initial piezoelectric actuator shapes with a maximum of 200 generations. The numerical results for these four runs are given in Table 3.7. It is evident that all the four GA runs converged to exactly the same value of error function Lmn=9.41×10^{-7}, which indicates a reduction of 96% in the minimum value of the error function compared to that in Example 1 as given in Table 3.1. The final optimum voltages applied to three actuators are the same for all four runs, namely, ϕ_1 = 301.2 volts, ϕ_2 = 224.6 volts and ϕ_3 = 84.1 volts. The optimum values of the applied voltages of patch 1, 2 and 3 reduce 23%, 53% and 38%, respectively, compared to these in Example 1 as given in Table 3.1. The shapes of each actuator patch are identical as shown in Figure 3.9. The convergence histories for the four runs are shown

in Figure 3.16. The number of convergence and the total number of generation are different for each run because of the difference in randomly selected values of the design variables in each generation.

Table 3.7: Results obtained using GALLS with random initial design variables

Runs		1	2	3	4
Lnm	Initial	8.664×10^{-6}	9.324×10^{-6}	6.667×10^{-6}	1.027×10^{-5}
	Final	9.411×10^{-7}	9.411×10^{-7}	9.411×10^{-7}	9.411×10^{-7}
	Patch (Volts)				
	1	301.2	301.2	301.2	301.2
	2	224.6	224.6	224.6	224.6
	3	84.1	84.1	84.1	84.1
No of convergences		29	16	18	15
Total No of generations		180	56	111	115

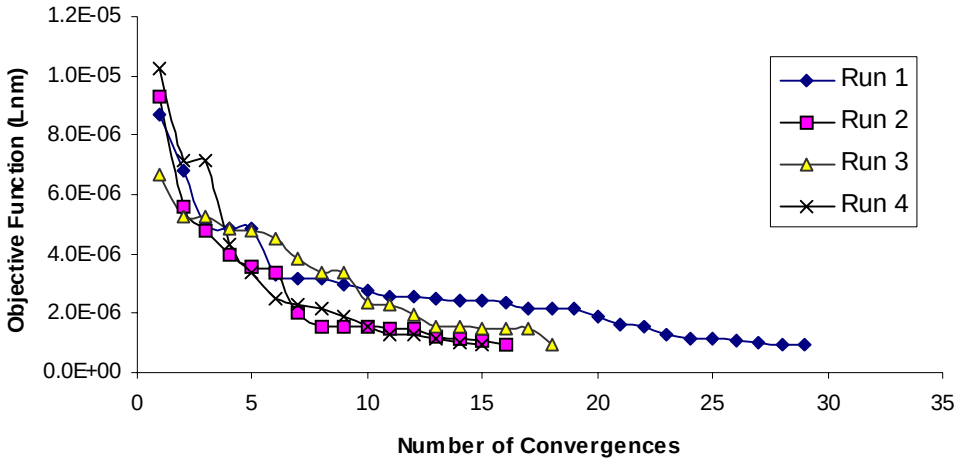

Figure 3.16: Convergence history of four actuator design optimisation runs using GALLS.

Table 3.8: Results obtained using GALLS with random initial design variables and different FE mesh.

FE Mesh		2x5	4x5	6x5	8x5	10x5
Patch(Volts)	1	301.3	303.2	305.4	304.7	304.8
	2	224.5	228.5	233.0	232.3	233.0
	3	81.5	96.4	95.8	97.6	96.7
No of convergences		10	32	51	56	74
Total No of generations		28	128	426	626	993
Lnm		9.449×10^{-7}	7.079×10^{-7}	6.440×10^{-7}	5.986×10^{-7}	5.807×10^{-7}

Table 3.8 compares the numerical results obtained using the GALLS algorithm to solve the same problem but employing different finite element meshes, i.e., 2x5, 4x5, 6x5, 8x5 and 10x5, respectively. The x coordinates of the nodes along the designable vertical sides of each patch are the design variables and their bounds are: $0.03 \leq$ along the right edge of patch $\#1 \leq 0.044$; $0.046 \leq$ along the left edge of patch $\#2 \leq 0.06$; $0.09 \leq$ along the right edge of patch $\#2 \leq 0.104$; $0.106 \leq$ along the left edge of patch $\#3 \leq 0.12$. The final shapes of the optimum actuators are depicted in Figures 3.9, 3.17, 3.18, 3.19, and 3.20. Figure 3.21 depicts the convergence histories for the GA runs with different finite element meshes. As shown in Table 3.8, it is evident that an increase in the number of elements (fine mesh) decreases the minimum value of the error function and enlarges the values of optimum voltages applied to the three actuators. The relative error of the objective error function for the 10x5 fine mesh is 38.5% smaller than that for the 2x5 coarse mesh. Another point worth noting is that the optimum voltages and the minimum value of the error function converge as the finite element mesh is refined. It is evident that the GALLS algorithm for piezoelectric actuator design optimization yields the actuator configurations with minimum applied voltage requirement to achieve best match to the desired shape.

Numerical results given in Examples 1 to 5 unveil that the GALLS algorithm is best algorithm to determine optimum voltage distribution and actuator configurations to best fit the desired shape with a least value of the error function and lowest voltages.

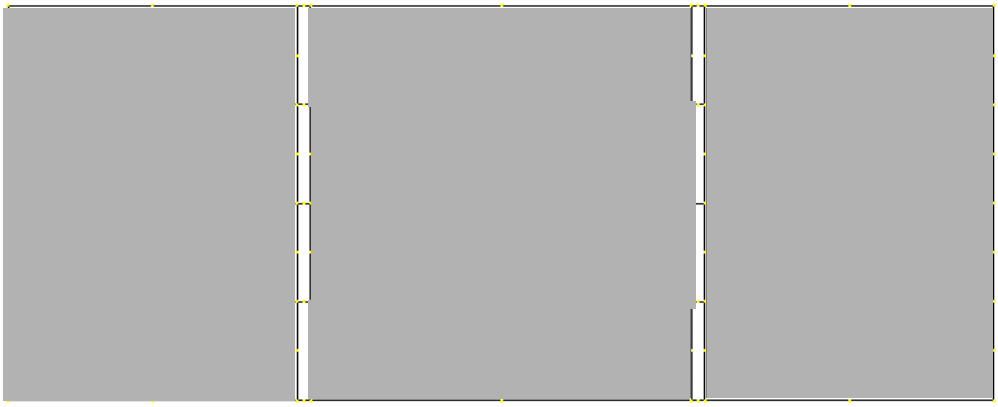

Figure 3.17: Final actuator shape of 4x5 FE model

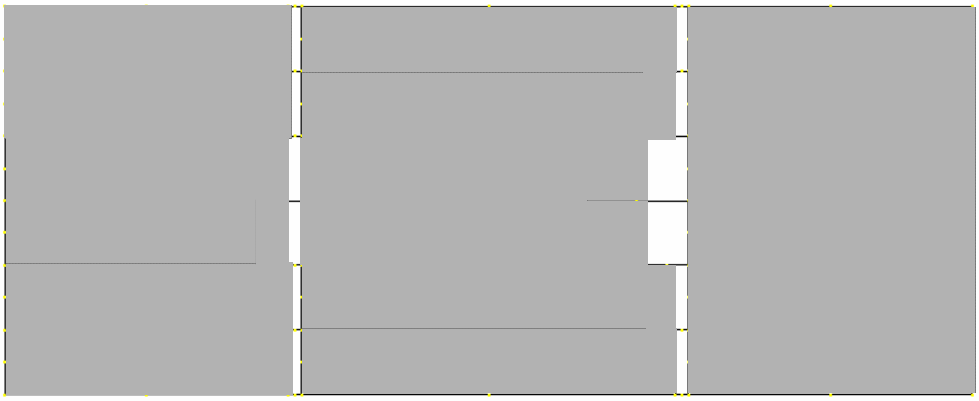

Figure 3.18: Final actuator shape of 6x5 FE model

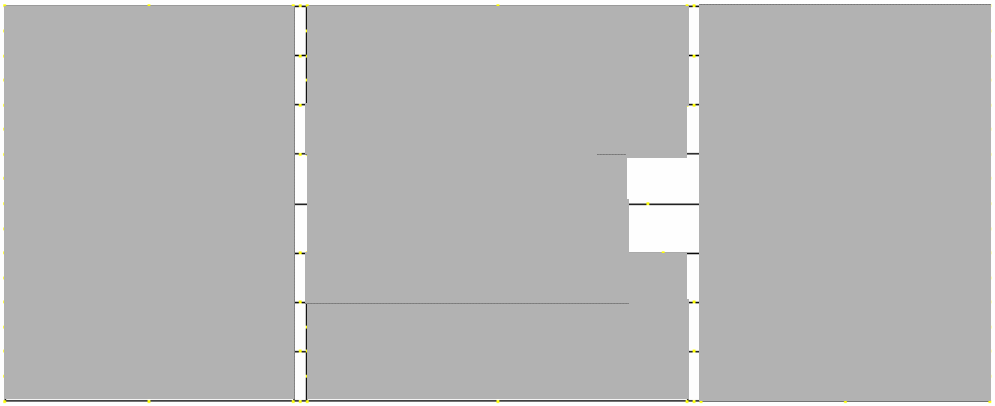

Figure 3.19: Final actuator shape of 8x5 FE model

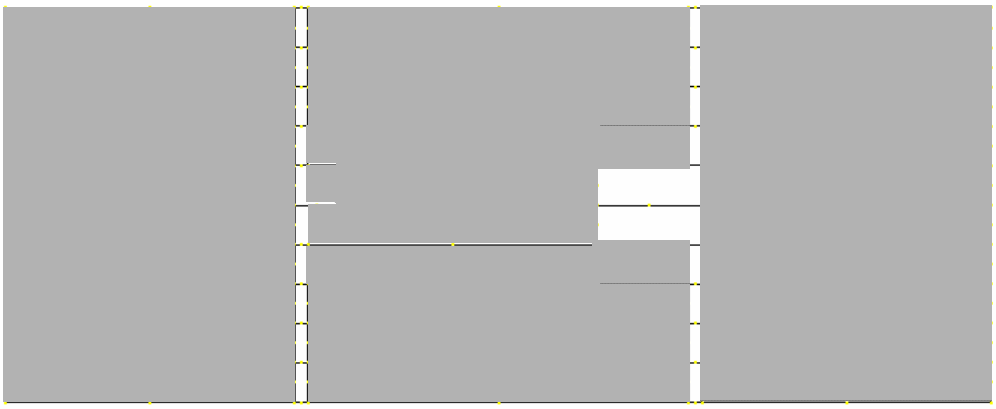

Figure 3.20: Final actuator shape of 10x5 FE model

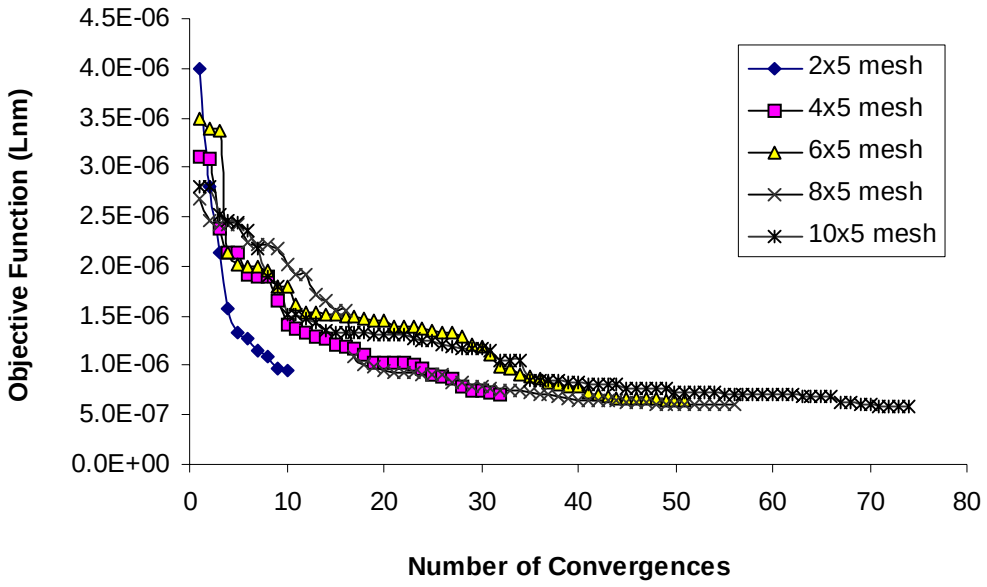

Figure 3.21: Convergence history of shape optimisation with various FE mesh

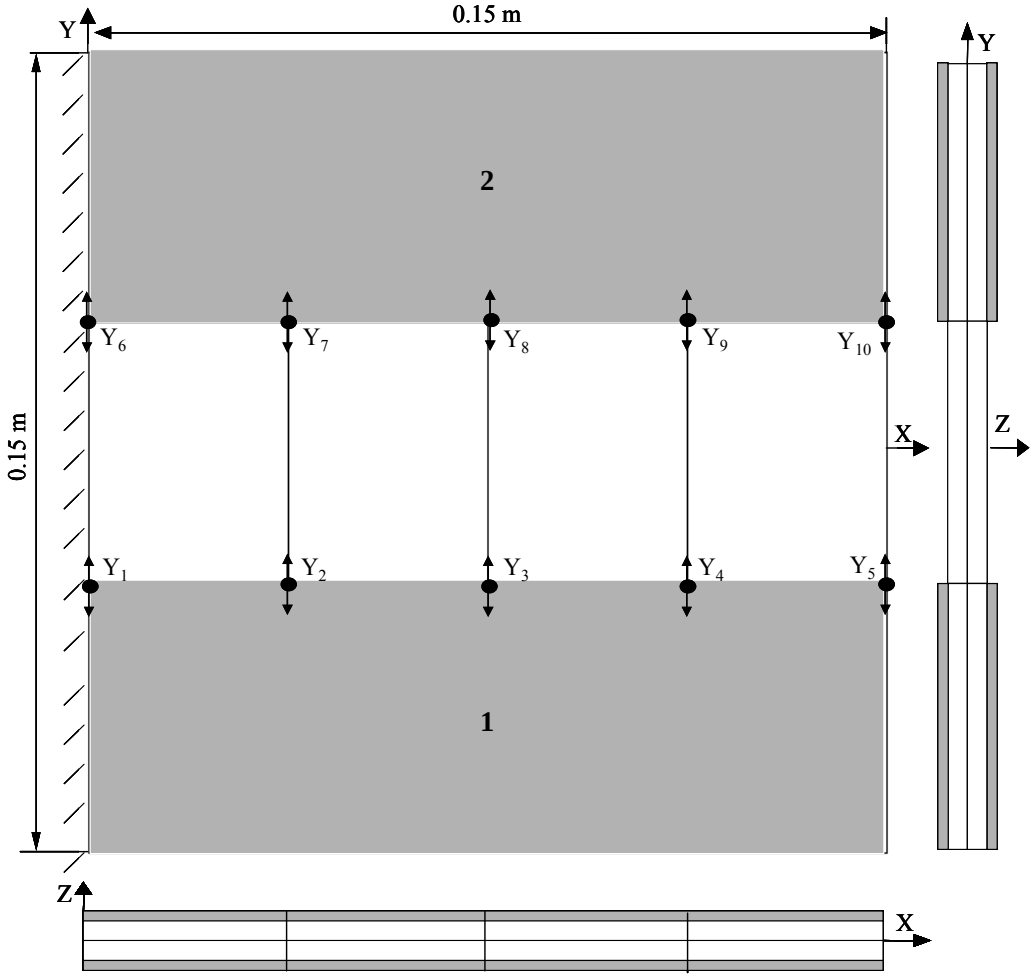

Figure 3.22: Cantilever plate in XY and XZ, ZY plane and move directions of design variables

3.4.2 Twisted structural shape control test

In this section, two numerical examples for twisting shape control of a cantilever plate clamped at its left edge and subject to non-applied mechanical loading are presented to verify the GALLS algorithm. For each example, the GA search is repeated numerous times with different initial value of design variables. Only the best results obtained are given here.

3.4.2.1 Example 6:

The plate has sides of 0.15m and consists of two layers of thickness 0.01m each. Two pairs of piezoelectric actuators of 0.001 m thick each are attached to the top and bottom surfaces of the plate shown in Figure 3.22. Only the top actuator patches are activated. For the twisting structural shape, the desired structural shape is defined as $w^d(x,y) = 10^{-5}(\cosh(x)-1)\sin(y)$, where $0 \le x \le 0.15$ and $-0.075 \le y \le 0.075$. The plate is modelled by a 3x4 finite element mesh, and each actuator is modelled using 4 elements. There are 10 points, which can move only in the y-direction as shown in Figure 3.22. The bounds for the geometrical variables are $-0.074 \le y_1, y_2, y_{3,} y_4, y_5 \le -0.001$; $0.001 \le y_6, y_7, y_8, y_9, y_{10} \le 0.074$. The plate material has the following stiffness constants: $c_{11}=c_{22}=c_{33}=82.68$GPa, $c_{12}=c_{13}=c_{23}=27.56$GPa, $c_{44}=c_{55}=c_{66}=26.50$GPa. The patch properties are: $c_{11}=c_{33}=84.8$GPa, $c_{22}=29.68$GPa $c_{12}=c_{13}=c_{23}=36.30$GPa, $c_{44}=c_{55}=c_{66}=24.20$GPa; $\chi_{11}=\chi_{22}=15.3\text{x}10^{-9}$F/M, $\chi_{33}=15.0\text{x}10^{-9}$F/M and $d_{31}=-254$pm/V, $d_{32}=-254$pm/V, $d_{33}=374$pm/V, $d_{24}=584$pm/V and $d_{15}=584$pm/V.

With the actuators configuration shown in Figure 3.22, the error function and voltage distribution obtained by the LLS method are: $Lnm = 1.416\text{x}10^{-3}$ and $\phi_1 = 1.241$ volts; $\phi_2 = -1.241$ volts. When using the GALLS, the optimal solution is obtained after 23 convergences and a total of 6129 generations. The required applied voltage for actuator patch 1 and 2 are $\phi_1 = 2.196$ volts and $\phi_2 = -2.196$ volts, respectively. The voltages predicted by the GALLS are higher than these by the LLS. This is because the size of each actuator patch is reduced. The minimum value of the error function (Lnm) is $6.228\text{x}10^{-5}$, which is 96% smaller than that obtained by the LLS. The convergence history is given in Figure 3.23. The optimal piezoelectric actuator shapes are depicted

by the shaded regions in Figure 3.24. Figure 3.25a shows the desired structural shape, whereas the calculated structural shape obtained using the LLS and the GALLS are plotted in Figure 3.25b and 3.25c, respectively. It is evident that the actuated shape by the GALLS algorithm has a better fit to the desired shape than that by the LLS.

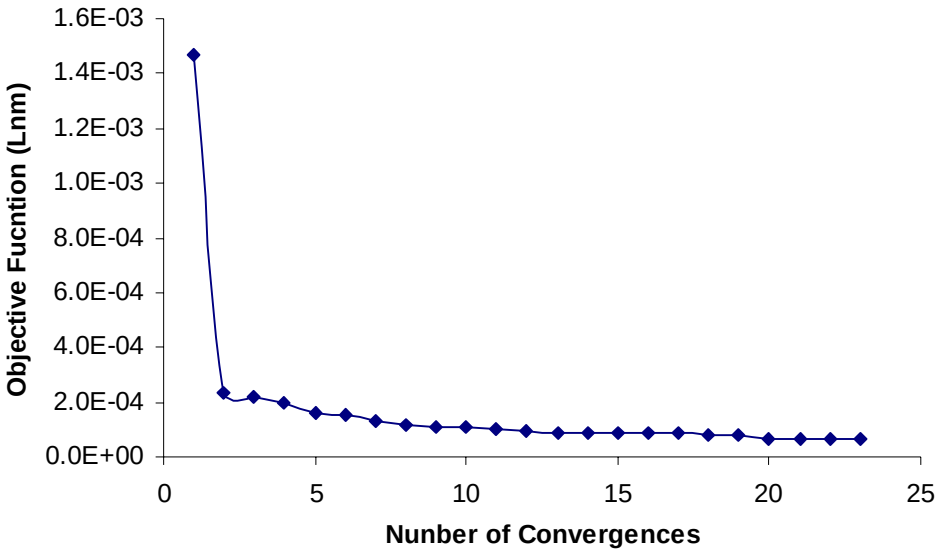

Figure 3.23: Convergence history using GALLS algorithm

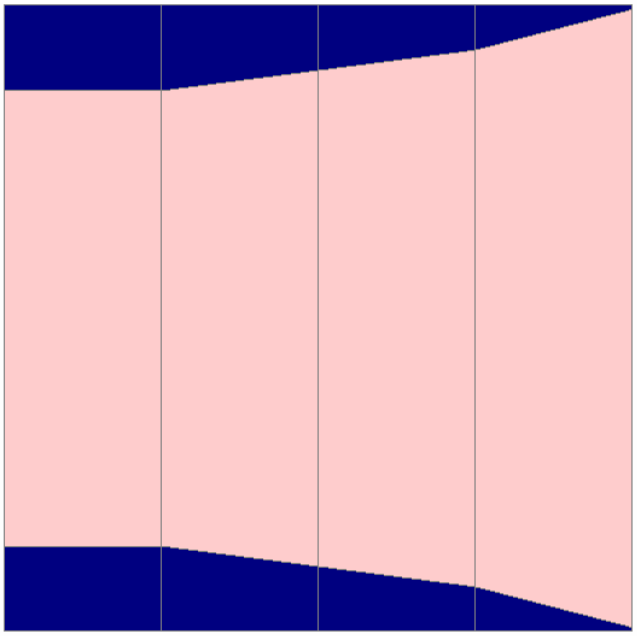

Figure 3.24: Optimal actuator shape designs using the GALLS algorithm

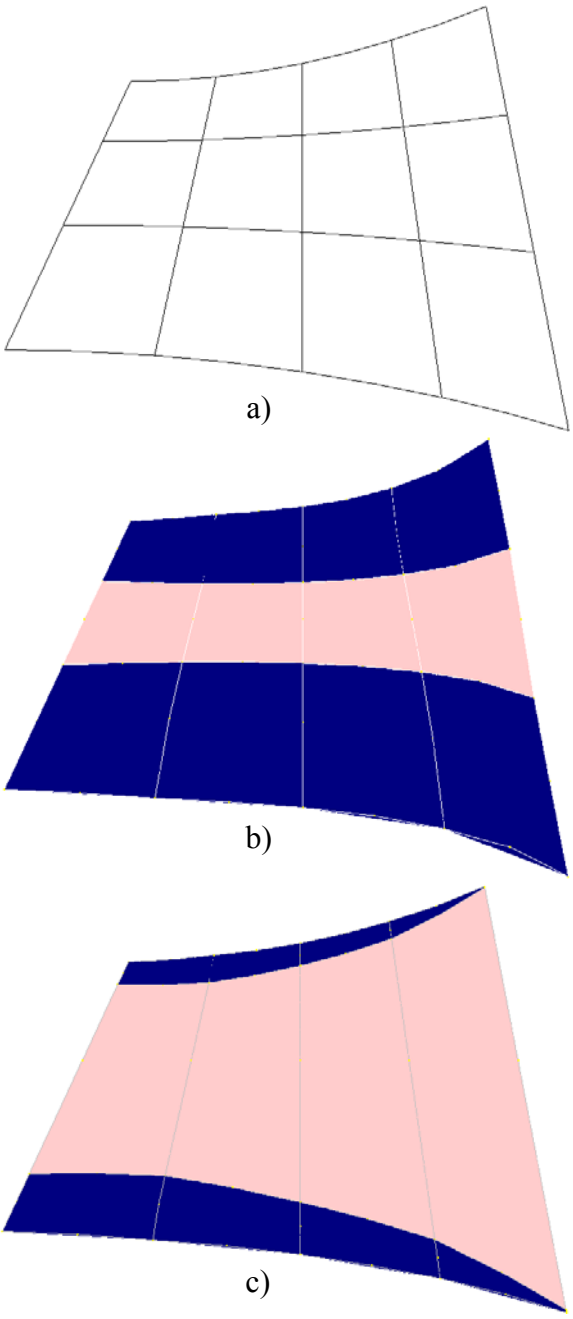

Figure 3.25: a) Desired structural shape; b) Calculated structural shape using the LLS method-voltage optimisation only; c) Calculated structural shape using the GALLS algorithm.

3.4.2.2 Example 7:

Consider a rectangular plate that has a length of 0.3m, width of 0.15m and consists of two layers of thickness 1mm each. Sixteen piezoelectric actuators are attached to the top and bottom surfaces of the plate as shown in Figure 3.26 and each actuator has a thickness of 1mm. Only the top actuator patches are activated. For the plate, the desired shape is defined as $w^d(x,y) = 10^{-3}(\cosh(x)-1)\sin(y)$, where $0 \le x \le 0.30$ and $-0.075 \le y \le 0.075$. The plate is subdivided into 3x7 finite elements as shown in Figure 3.26. There are 24 nodes that are allowed to move only in the x-direction as shown in Figure 3.26. The bounds for the design variables are: $0.022 \le x_1, x_2, x_3, x_4 \le 0.064$; $0.065 \le x_5, x_6, x_7, x_8 \le 0.1071$; $0.1072 \le x_9, x_{10}, x_{11}, x_{12} \le 0.149$; $0.151 \le x_{13}, x_{14}, x_{15}, x_{16} \le 0.192$; $0.193 \le x_{17}, x_{18}, x_{19}, x_{20} \le 0.235$; $0.236 \le x_{21}, x_{22}, x_{23}, x_{24} \le 0.278$. The plate has the following stiffness constants: $c_{11}=c_{22}=c_{33}=82.68$GPa, $c_{12}=c_{13}=c_{23}=27.56$GPa, $c_{44}=c_{55}=c_{66}=27.60$GPa. The patch properties are: $c_{11}=c_{22}=c_{33}=84.8$GPa, $c_{12}=c_{13}=c_{23}=36.35$GPa, $c_{44}=c_{55}=c_{66}=24.2$GPa; $\chi_{11}=\chi_{22}=15.3\text{x}10^{-9}$F/M, $\chi_{33}=15.0\text{x}10^{-9}$F/M and $d_{31}=-254$pm/V, $d_{32}=-204$pm/V, $d_{33}=374$pm/V, $d_{24}=484$pm/V and $d_{15}=584$pm/V.

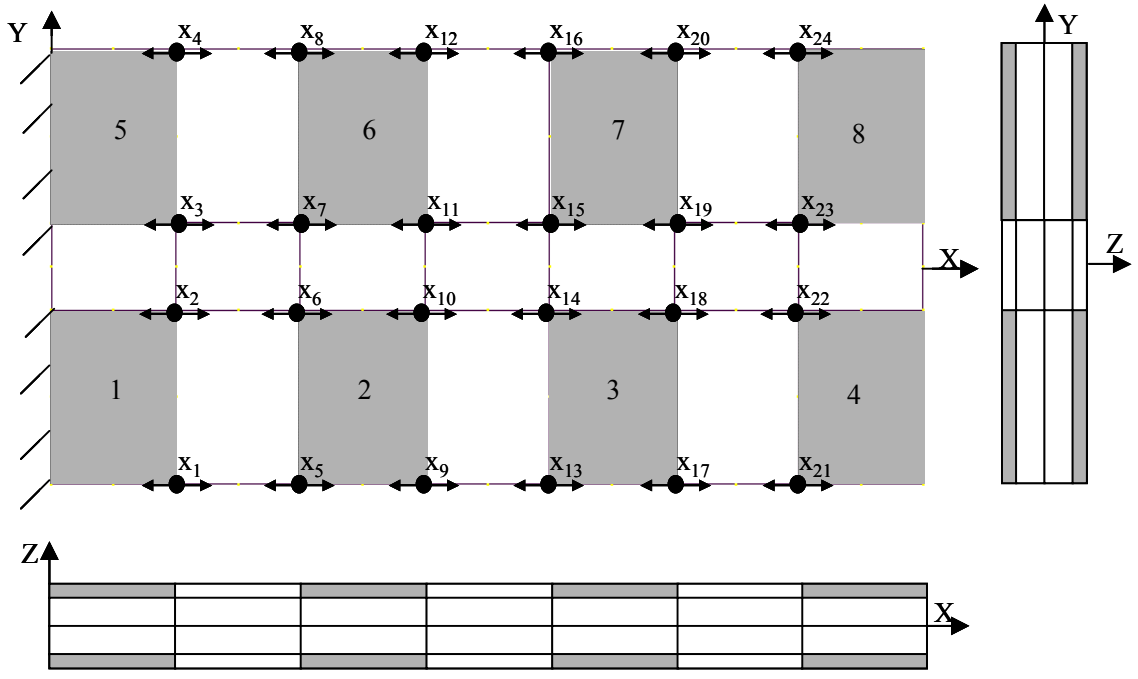

Figure 3.26: Cantilever plate in XY and XZ, ZY plane and direction of design variables

With the piezoelectric actuators configuration as shown in Figure 3.26, the error function obtained via the LLS method is Lnm = 1.892×10^{-3}. When the GALLS algorithm is used, the optimal solution is obtained after 58 convergences over total of 2246 generations. The error function (Lnm) is 3.852×10^{-4}. Table 3.9 compares the optimum values for the applied voltages and the minimum values of the error function obtained using the LLS and GALLS. It is shown that the GALLS algorithm yields a remarkable 80% reduction in the minimum value of the error function and a 32% decrease in the total energy consumption compared to the LLS solutions. The convergence history is depicted in Figure 3.27. Figure 3.28 depicts the optimal piezoelectric actuator shapes plotted as the shaded regions. It is seen that the optimally shaped piezoelectric actuators exhibit a symmetrical pattern and the applied voltages in Table 3.9 have an anti-symmetrical pattern. This is due to the desired shape exhibits an anti-symmetry feature about the x-axis. Figure 3.29a shows the desired structural shape, and the calculated structural shapes obtained via the LLS and GALLS algorithm can be seen in Figure 3.29b and 3.29c, respectively. It is evident that the actuated shape generated using the GALLS fits the desired shape better than that obtained using the LLS. This illustrates that it is important to perform a fully coupled piezoelectric actuator design optimisation.

Table 3.9: Comparison of results between LLS and GALLS methods

Patch	LLS	GALLS
1	19.30	24.83
2	31.81	18.92
3	14.96	11.17
4	-10.74	-8.93
5	-19.30	-24.83
6	-31.81	-18.92
7	-14.96	-11.17
8	10.74	8.93
Lnm	1.892×10^{-3}	3.852×10^{-4}
Total of Energy Consumption (E)	3447.97	2358.17
% Change in	Lnm	-80
	E	-32

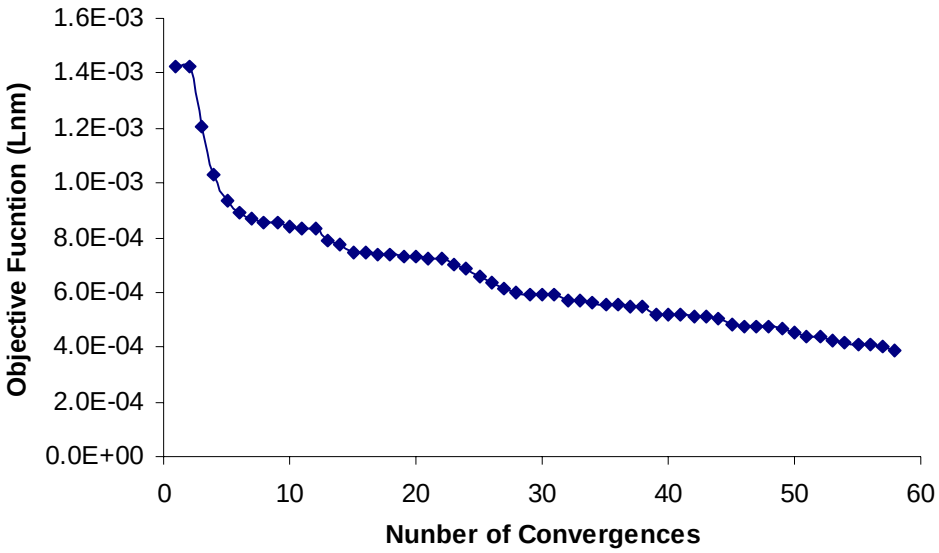

Figure 3.27: Convergence history using GALLS algorithm.

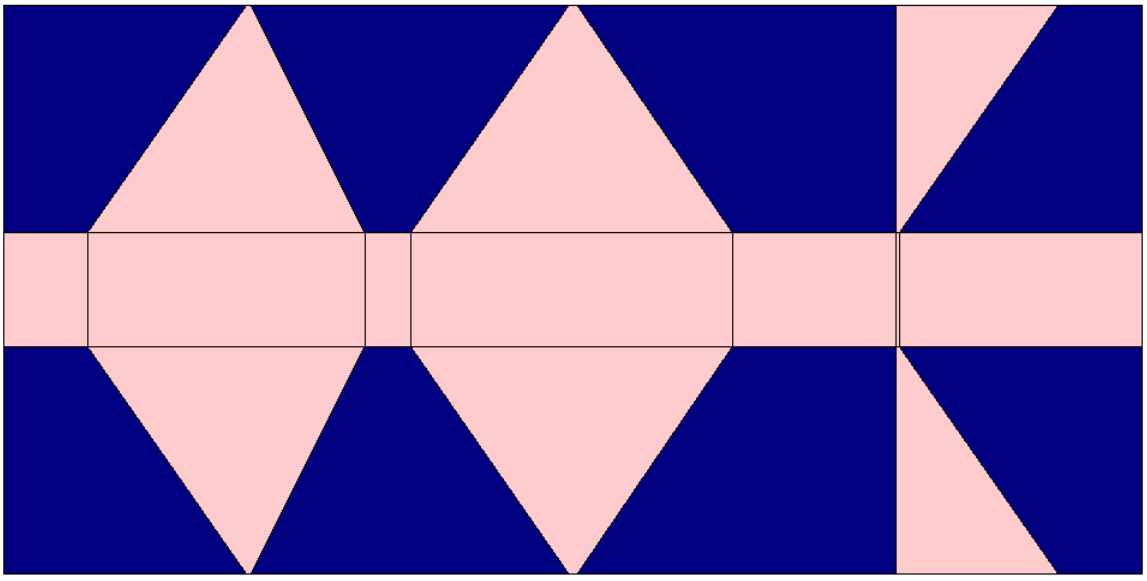

Figure 3.28: Optimal actuator shape designs using GALLS algorithm.

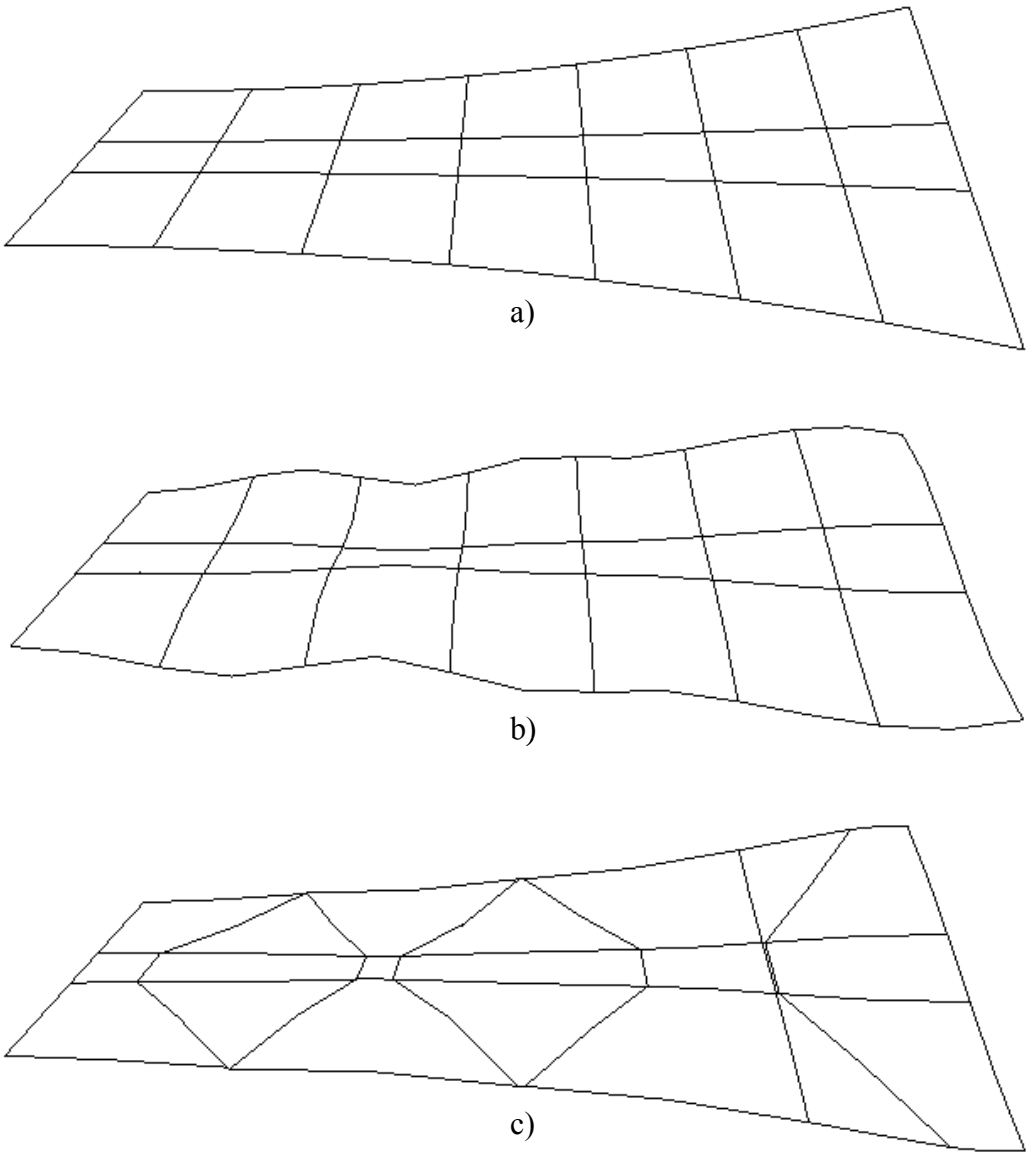

Figure 3.29: a) Desired structural shape; b) Calculated structural shape using the LLS method-voltage optimisation only; c) Calculated structural shape using the GALLS algorithm.

3.5 Summary

This chapter treats the applied voltages and actuator geometries as design variables in piezoelectric actuator design optimization (PADO) for shape control of smart structures. After reviewing currently available algorithms, such as LLS and GA, two coupled algorithms such as LLS-GA and GALLS are proposed to determine the optimum shapes of actuators and the optimum voltages applied to them. Several numerical examples for bending and twisting shape control are presented to demonstrate the capacity of each algorithm. The following salient points were observed: (a) both LLS and GA algorithms are capable of finding optimum voltage distribution for given actuator geometry; (b) GA and LLS-GA are capable of finding the voltage distribution and actuator geometry that further reduces the estimated error function between actuated and the desired shapes; and (c) GALLS algorithm is capable of determining the optimum voltage distribution and optimum actuator geometry that leads to the least estimated error function between the actuated and desired shapes. Thus the GALLS algorithm is the most capable, efficient and effective algorithm amongst all the algorithms considered in this research.

4. GA Based Algorithm for Static Shape Control of Smart Plate Structures with Constraints Handling

This chapter presents the shape control of smart composite plate structures under additional constraints beyond the structural behaviour constraint. Two main issues are investigated here. One minimises the error function (Lnm) subjected to the electrical energy consumption constraints. The other minimises the total electrical energy consumption subjected to the error function constraint. Both issues aim to control the structure close to desired structural shape within a given electrical energy consumption or error function. A Genetic Algorithm (GA) is employed to optimise the applied voltage to piezoelectric actuators and the geometry of piezoelectric actuators subject to given additional constraints. For each issue, numerical results are presented to demonstrate the effect of given additional constraints on the results of the objective function. Also, a comparison is given for the results obtained through single criterion optimisation (only voltages optimisation) method and multiple criteria optimisation (voltages and geometry of piezoelectric actuators optimisation) method.

4.1 Introduction

In recent years, piezoelectric materials have been widely used in the field of shape control. The piezoelectric actuator can be used as traditional force to prevent unexpected structural deformation or generate the shape as set. The presence of electric potential in piezoelectric actuator is needed to do so. Therefore applied voltage is an important criteria design in shape control problem. Koconis et. al (1994); and Chee et. al, (2000b) searched the optimal voltage distribution for achieving the desired structural shape. In most available researches on static shape control as referenced in Chapter 3, they did not mention about the limitation of the applied voltage. The literature reviews noted that the applied voltage requirement is usually very high in order to achieve the desired structural shape. In the current state of technology, there are many limitations on

piezoelectric materials; the applied electric field being one of them. Other such limitations include: 1) high voltage may yield depolarisation. 2) In the high voltage range, the relationship of strain and applied voltage is nonlinear (the current analysis may not be applicable). 3) There may be a limit on available energy. Due to these problems, the topic of shape control with energy constraint is now interesting in engineering practice. In recent few years, Mukherjee and Joshi (2001) developed an algorithm to search for piezoelectric actuator profile with an optimal of power consumption. Sun and Tong (2003) used a Lagrangian multiplier method to develop an algorithm to minimise the difference between the calculated shape and desired shape under constrained energy consumption. They also presented the method that minimised the energy consumption with displacement constraint handling. Sun and Tong (2003) noted that good control results can be achieved when the controlled energy is limited in a proper range around an optimal value. In other word, the desired structural shape is hard to achieve with low controlled energy.

This chapter presents the static shape control of smart composite plate structures under additional constraints beyond the structural behaviour constraint. Two main issues are investigated here. One minimises the error function (Lnm), which is defined in terms of the sum of least square errors between calculated and desired nodal transverse displacement, subjected to energy constraints, where three types of constraints are considered in this problem including the total energy consumption constraint and the single and multiple voltage constraints. The other minimises the total energy consumption subjected to the error function constraint. Both issues aim to control the structure that closes to desired structural shape within a given energy consumption or error function. Although a considerable of the interesting on voltage distribution and piezoelectric actuator design can be observed in using the Genetic Algorithm (GA) for the static of shape control of smart structures without constraints handling (see in Chapter 3). Once again GA is employed to optimise the voltage distribution in piezoelectric actuators and the geometry of piezoelectric actuators subject to a given additional constraints. For each issue, the numerical results are presented to demonstrate the effect of given additional constraint on the resulting of objective function. Also a comparison is given for the results obtained through single criterion optimisation (voltage optimisation only) method and multiple criteria optimisation (voltages and geometry of piezoelectric actuators optimisation) method.

4.2 Formulation of Static Shape Control Problem with Constraints

The shape control problem considered in this chapter focuses on piezoelectric actuator design optimization (PADO) in terms of finding optimum values for applied voltages and actuator geometries to achieve the desired structural shapes subject to a given additional constraints. When the geometrical parameter vector of piezoelectric actuators (**X**) and the applied voltage vector ($\boldsymbol{\phi}$), are considered as design variables; the quasi-static shape control problem can be defined, in the context of optimization formulation (Gallagher and Zienkiewicz, 1973), as follows:

Find $\mathbf{V}=[\mathbf{X}, \boldsymbol{\phi}]^T$ to

Minimise f($\mathbf{V}$) (4.1)

Subject to $g(\mathbf{V}) = 0 \Rightarrow [\mathbf{u}_g(\mathbf{X},\boldsymbol{\phi})] = [\mathbf{K}_{uu}(\mathbf{X})]^{-1}[-\mathbf{K}_{u\phi}(\mathbf{X})][\boldsymbol{\phi}_g]$ (4.2)

$\mathbf{V}_L \le \mathbf{V} \le \mathbf{V}_U \Rightarrow \mathbf{X}_L \le \mathbf{X} \le \mathbf{X}_U$ and $\boldsymbol{\phi}_L \le \boldsymbol{\phi} \le \boldsymbol{\phi}_U$ (4.3)

Where, in the context of general optimisation formulation, V is the design variable vector; f($\mathbf{V}$) is the objective function; g($\mathbf{V}$) is the performance constraint; and $\mathbf{V}_L$ and $\mathbf{V}_U$ are the lower and upper bounds of the design variable vectors. The subscripts L and U denote lower and upper bounds respectively. Considering the PADO problem, the design variable vector V has two components, namely, the geometric variable vector (**X**) and the applied voltage variable vector ($\boldsymbol{\phi}$). In this chapter, the geometric variables in vector **X** are chosen to be the coordinates of the selected design nodes, whereas the voltage variables in vector $\boldsymbol{\phi}$ are the electrical potentials applied across the thickness direction of each actuator. The constraint equations in Equation (4.2) are the equilibrium equations that govern the structural behaviour when the structure is only subjected to electrical loading and are formulated using the finite element method. $[\boldsymbol{\phi}_g]$ is global vector of nodal voltages. $[\mathbf{K}_{uu}(\mathbf{X})]$ and $[\mathbf{K}_{u\phi}(\mathbf{X})]$ are the global stiffness matrix and the global piezoelectric linearly coupling the matrix respectively (refer to Chapter 2 for more details). As described by Equations (4.1-4.3), the PADO is an inverse problem and the optimum applied voltages and geometry parameters of piezoelectric actuators can be obtained simultaneously.

Beyond the structural behaviour constraint in Equation (4.2), additional constraint $h_l(V)$ is stated in the general form as shown in Equation (4.4), which then is used to limit the performance of structure within a given constraint condition. The additional constraint can be energy constraint or error function constraint. B subscripts c and a are the allowable and actual value of the additional constraints, respectively. (l=*1*,…,M), where M is the number of constraint condition.

$$h_l(\mathbf{V}) \le 0 \Rightarrow Ba_l \le Bc_l \tag{4.4}$$

In order to handle the constraint violation fairly and to maintain the magnitudes, the constraints can be normalised. Usually in the optimisation process, an error tolerance τ (say $\tau \sim 10^{-5 \sim -6}$) needs to be prescribed to check the convergence of the constraints as follow:

$$\left| \frac{Ba_l - Bc_l}{Bc_l} \right| \le \tau \tag{4.5}$$

In this chapter, the objective function f(**V**) can be categorised into two types. One is known as the error function (Lnm), which is minimised subjected to the energy consumption constraint. The other is the total energy consumption that can be optimised subjected to the error function constraint. Each type is respectively described with more details in sections 4.4 and 4.5.

4.3 GA Method

This section describes the procedure of GA, which is employed to optimise the voltage distribution in piezoelectric actuators and the geometry of actuators to achieve the desired structural shapes subject to a given additional constraints. When in the presence of an additional constraint, the simplest approach for solving the shape control of smart structures with constraints handling, using the GA algorithm, is to transform the constrained problem into a non-constrained problem by adding a penalty term of constraints to the objective function. Hajela and Woo (1996) derived the expression strategies to handle constraints. Initially developed by Hajela and Lee (1996), Hajela et.

al (1997) employed an immune system into the application of structural optimisation. Tang et. al (in press) introduced the maximum entropy theory in which the surrogate function (proposed by Li, 1994) is also employed to merge the multiple constraints into a single constraint. In this chapter, the technique used to deal with constraints, in the shape control of a smart structure, is based on the same concept proposed by Tang et. al (in press). The basic idea of this technique is that the differential function is used to approach a non-differential function.

The constraint as shown in Equation (4.4) is the non-differential equation. Based on maximum entropy theory, it has an equivalent form shown below:

$$\gamma(\mathbf{V}) = \max_{1 \le l \le M} \{h_l(\mathbf{V})\} \le 0 \tag{4.6}$$

By the meaning of the maximum entropy theory and surrogate function F_p in (Tang et. al, in press), the Equation (4.6) can be rewritten as follow:

$$F_p = \frac{1}{p} \ln \left[\sum_{l=1}^{M} e^{p \times h_l(\mathbf{V})} \right] \tag{4.7}$$

By adding the constraint $h_l(\mathbf{V}) = 0$ to Equation (4.7), it becomes

$$F_p = \frac{1}{p} \ln \left[1 + \sum_{l=1}^{M} e^{p \times h_l(\mathbf{V})} \right] \tag{4.8}$$

The penalty function $\Phi(\mathbf{V},\alpha)$ of the optimisation problem in Equation (4.1) is stated in Equation (4.9).

$$\Phi(\mathbf{V}, \alpha) = f(\mathbf{V}) \times \left\{ 1 + \frac{\alpha}{p} \ln \left[1 + \sum_{l=1}^{M} e^{p \times h_l(\mathbf{V})} \right] \right\} \tag{4.9}$$

where α is the penalty coefficient. The optimal solution of Equation (4.9) is also the optimal solution of Equation (4.1) when the penalty coefficient α is greater than α^0,

where α^0 is the sum of Lagrange multipliers (Tang et. al, in press), and the constant p is approaching infinity. In the actual optimisation process, a constant p (say $p \sim 10^{4 \sim 5}$) needs to be prescribed in order to ensure that the solution is approaching a feasible domain. (Tang et. al, in press) noted that the surrogate penalty is exerted on all constraints instead of individual constraint. Therefore, it is easy to choose a penalty coefficient, which is equivalent to the magnitude of objective function.

Optimisation process has the same a procedure as described in Section 3.3.2 and an additional step for additional constraint checking. The purpose of this additional step is to search for the optimal solution such that the problem performance is within a given condition limitation. The performance (to compute the constraint values) of this additional step is based on the maximum entropy theory and surrogate function method, which is described above. These constraint values are then used in the selection operator. The concept of selection operator is based on the method, which is proposed by Tang et. al (in press). Its basic idea is that the design can enter the feasible domain by using a feasible design and potential design with a short distance. The advantage of consideration of constraint values and their tolerances of constraint violation is that the feasible and slight violated designs carry great and promising gene character. The routine of additional constraint checking has the following steps as described below:

Step 1: According to surrogate function to compute the constraint value for each individual design

Step 2: There are two or more of numbers of individual that are randomly chosen from design pool to search for best individual design. In this step, there occur three possible solutions, to be selected for the mating pool. Firstly, the individual design with the smallest constraint value is chosen when all selected individuals without repeating are infeasible designs. Secondly, if they are all feasible designs, the selection is based on the highest value of finest function. Last case includes both feasible and infeasible designs, so the feasible deigns are chosen.

Step 3: Go back to step 2 if the population in the mating is not filled. Otherwise exit the additional constraint checking routine and go to another routine for continuing of optimisation process.

Tang et. al (in press) noted that there are two advantages of using this surrogate selection operator. It firstly speeds up the convergence. This is because the potential individuals are preserved and best gene has a great chance to be passed onto the mating pool. Secondly, it can prevent the premature convergence by maintaining certain selective pressure.

The whole procedures of GA based algorithm for static shape control of smart structures with constraints handling is defined below. The flowchart of this process is shown in Figure 4.1

Step 1: Obtain the structural and GA input parameters

Step 2: Select boundaries for design variables. The maximum and minimum values of the design variable mapped to the maximum and minimum of chromosome or binary string in the GA

Step 3: Generate the initial design value randomly for piezoelectric actuators and voltage distribution, known as population string chromosomes.

Step 4: Decode one of the string chromosomes of the population to boundary movement.

Step 5: Using the FEA solver to calculate the nodal transverse displacement of the structure of designs.

Step 6: Compute fitness value of individual designs.

Step 7: Repeat step 4 through 6 until all members of the population have been evaluated.

Step 8: Perform additional constraint checking. It then goes through selection, crossover and mutation operators

Step 9: Perform and check the relative error of average fitness of continuous generation. If it is very small then the population is deemed to have converged. If so, create a new set of design variable based on the fittest chromosome. Create a new random parent population.

Step 10: If a set number in Step 9 is converged then go to 13; otherwise go on to step 11.

Step 11: If the fittest chromosome has not been reproduced then randomly replace one offspring through selection, crossover and mutation. Repeat until a new population of offspring has been created.

Step 12: If the number of generation has been reached then go on to step 13, otherwise return to step 4.

Step 13: Replace design variable by movement vector of the fittest chromosome of the last population. The final set of design variable defines the optimum solution.

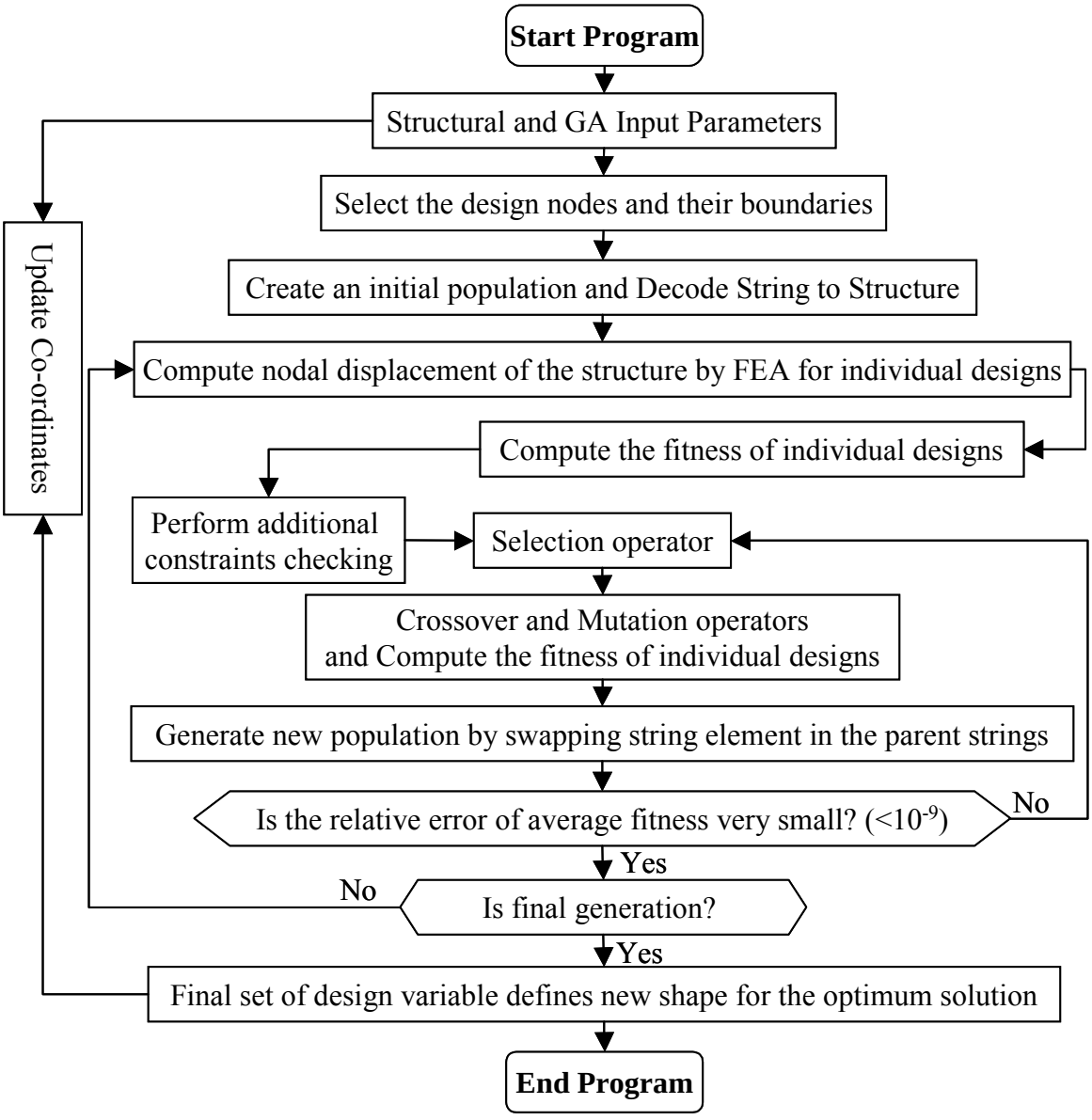

Figure 4.1: Schematic representation of the GA methodology

4.4 Static Shape Control Problem with Energy Constraints

4.4.1 Objective function

The objective function f(**V**) in Equation (4.1) is defined as the estimated error function Lnm($\mathbf{X},\phi$), which is a weighted sum of all square differences in displacements at selected nodes between the desired and calculated structural shapes as shown in Equation (4.10). Where w_i^d and $w_i^c(\mathbf{X},\phi)$ are the desired and actuated (or calculated) displacements of the i^{th} node respectively, and w_{max}^d is the maximum displacement in the desired structural shape and N is the total number of nodes considered. In the case of plates considered in this chapter, w_i^d and $w_i^c(\mathbf{X},\phi)$ are the transverse displacements which is the $[(i-1)*11+3]^{th}$ displacement component in the global displacement vector $\mathbf{u}_g(\mathbf{X},\phi)$.

$$f(\mathbf{V}) = \text{Lnm}(\mathbf{X},\phi) = \frac{\sum_{i=1}^{N} \frac{\left(w_i^d - w_i^c(\mathbf{X},\phi)\right)^2}{(w_{max}^d)^2}}{4 \times N} \tag{4.10}$$

4.4.2 Constraint Treatment

Three types of energy constraints are considered in this section; the total energy constraint, the single applied voltage constraint and the multiple applied voltage constraint are defined as follows (refer to Equations 4.4 and 4.5)

a) Total energy constraint $\quad Ea \le Ec$ (4.11)

b) Single voltage constraint $\quad \left|\phi_a^k\right| \le \left|\phi_c\right|, \quad (k=1,\ldots,Np)$ (4.12)

c) Multiple voltage constraint $\quad \left|\phi_a^k\right| \le \left|\phi_c^k\right|, \quad (k=1,\ldots,Np)$ (4.13)

Where E is the electrical energy consumed, subscripts c and a are the allowable and actual total energy consumption. The total energy consumption is defined in terms of the applied electrical voltages (ϕ) and conductors (R) (k=*1*,…,Np) as shown below:

$$E = \sum_{k=1}^{Np} \frac{\phi_k^2}{R_k} \tag{4.14}$$

where N_p is the total number of active piezoelectric actuator patches. ϕ_c, ϕ_a is the allowable and actual applied voltage

Due to the constraint violation as discussed in Section 4.2, the convergence of the constraint is stated as follow:

a) Total energy constraint $$\left|\frac{Ea - Ec}{Ec}\right| \leq \tau \tag{4.15}$$

b) Single voltage constraint $$\left|\frac{\left|\phi_a^k\right| - \left|\phi_c\right|}{\left|\phi_c\right|}\right| \leq \tau \tag{4.16}$$

c) Multiple voltage constraint $$\left|\frac{\left|\phi_a^k\right| - \left|\phi_c^k\right|}{\left|\phi_c^k\right|}\right| \leq \tau \tag{4.17}$$

4.4.3 Numerical Examples

Two typical examples are presented to demonstrate the structural shape control problem of smart plates with and without energy constraints using the GA method. In the first example, only the applied voltages on fixed piezoelectric actuator patches shape are considered as design variables. In the second example, the voltage and actuator configuration are optimised simultaneously. All the allowable values of constraints are considered that relate to optimal values obtained without constraint handling such as Lnm^n, En, $\phi_n{}^k$.

4.4.3.1 Model Description

Consider a cantilever plate, which is clamped at its left edge and subject to non-applied mechanical load. The plate has a length of 0.15 m, width of 0.06m and consists of two layers of 0.01m thickness each. Six piezoelectric actuators are attached at the top and bottom surface of the plate, which have thickness of 0.001m each. Only the top actuator patches are activated. Patches #1 and #3 are bonded at both ends and patch #2 is bonded in the middle of the plate as shown in Figure 4.2. The host plate material has the

following stiffness constants: $c_{11}=c_{22}=c_{33}=82.68$GPa, $c_{12}=c_{13}=c_{23}=27.56$GPa, $c_{44}=c_{55}=c_{66}=26.5$GPa. The actuator patch's properties are: $c_{11}=c_{33}=84.8$GPa, $c_{22}=29.7$GPa, $c_{12}=c_{13}=c_{23}=36.35$GPa, $c_{44}=c_{55}=c_{66}=24.2$GPa; the $\chi_{11}=\chi_{22}=15.3\text{x}10^{-9}$F/M, $\chi_{33}=15.0\text{x}10^{-9}$F/M and $d_{31}=-254$pm/V, $d_{32}=-254$pm/V, $d_{33}=374$pm/V, $d_{24}=584$pm/V, $d_{15}=584$pm/V. For the bending shape control test, the desired shape is defined as $w^d(x,y)=10^{-5}\cos(10x-1)$. The FE model of this plate is composed of 10 elements. Each piezoelectric actuator patch is modelled using two elements. In the GA calculation, the following parameters are used such as the population is taken as 10; the maximum number of generation is 2000; the probability of crossover and mutation are 1 and 0.001, respectively. Each optimisation problem was run several times. The best results are presented here.

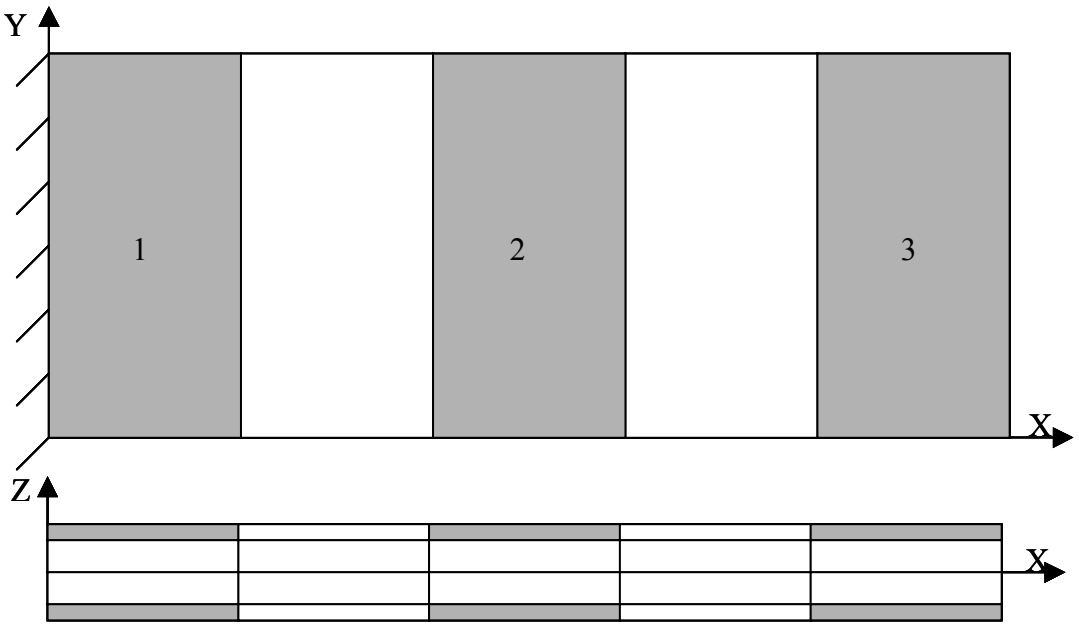

Figure 4.2: Cantilever plate in XY and XZ plane

4.4.3.2 Example 1: Voltage Optimisation

In this example, the applied voltages on fixed piezoelectric actuator patches shape are chosen as the design variables to minimise the error function. The geometrical size of each piezoelectric actuator patch is shown in Figure 4.2. Each of them has length of 0.06 m and width of 0.03m. In this case, the applied voltages are set as design variables (3 design variables in total) and their lower bound and upper bound are –500 volts and 500 volts, respectively. The final voltages required for each patch to achieve the desired

shape were obtained by the GA algorithm. A set of tests were performed here to illustrate the performance of using the electric energy in term of applied voltages as constraint handling. The non-constrained optimal solutions are $Lnm^n = 2.12x10^{-5}$ En = $450x10^3$ (volts^2/R), $\phi_n^1 = 393.28$ volts, $\phi_n^2 = 477.51$ volts and $\phi_n^3 = 135.97$ volts.

4.4.3.2.1 Total Energy Consumption Constraint

The first test investigates the effects of varying the total given energy consumption constraint optimal on the resulting of error function. The convergence curve for the six different cases with allowable energy Ec = 37%, 20%, 62%, 75%, 87% and ≥100% of En are shown in Figure 4.3. The error function of case #1, #2, #3, #4 and #5 are enlarged 309.9, 134.6, 48.3, 12.3, 1.8 times, respectively, which are normalised versus Lnm^n by $\left(\frac{|Lnm^c - Lnm^n|}{Lnm^n}\right)$. The results show that the optimal error function can be dependant of the allowable energy, namely, the optimal error function increases when Ec decreases. However, when Ec is equal to or greater than En, the optimal solutions are the same as the result obtained without energy constraint.

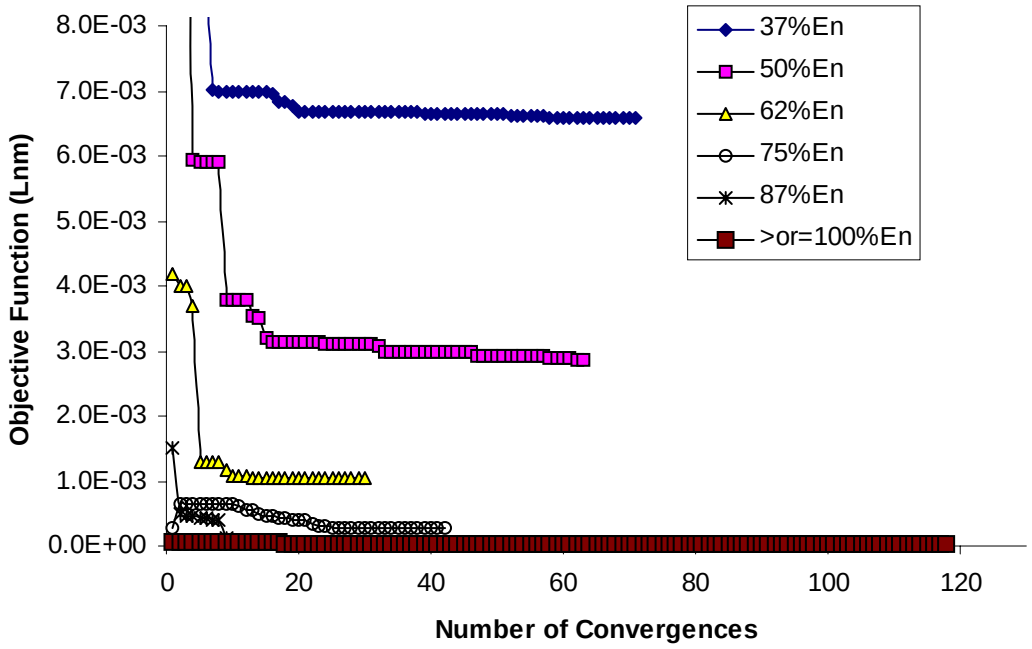

Figure 4.3: Convergence histories with different allowable energy consumptions

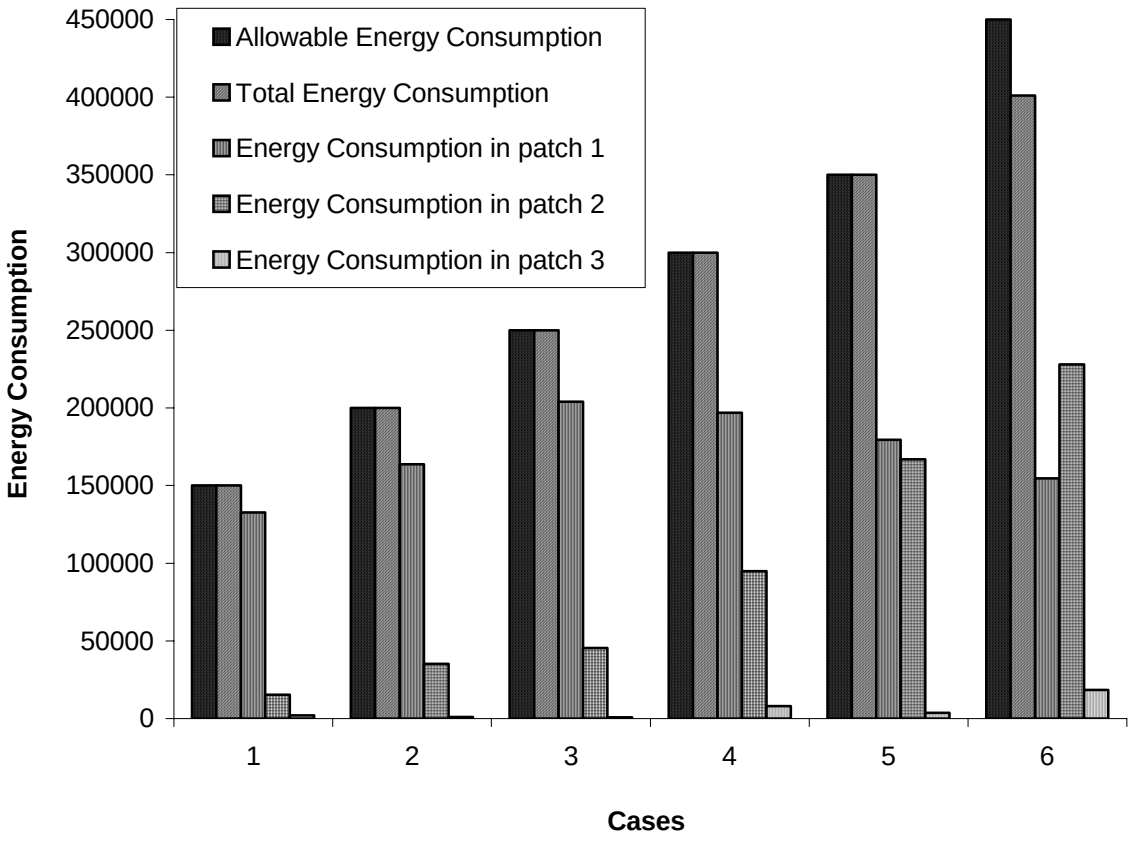

Figure 4.4: Energy distribution for different cases of allowable energy consumption

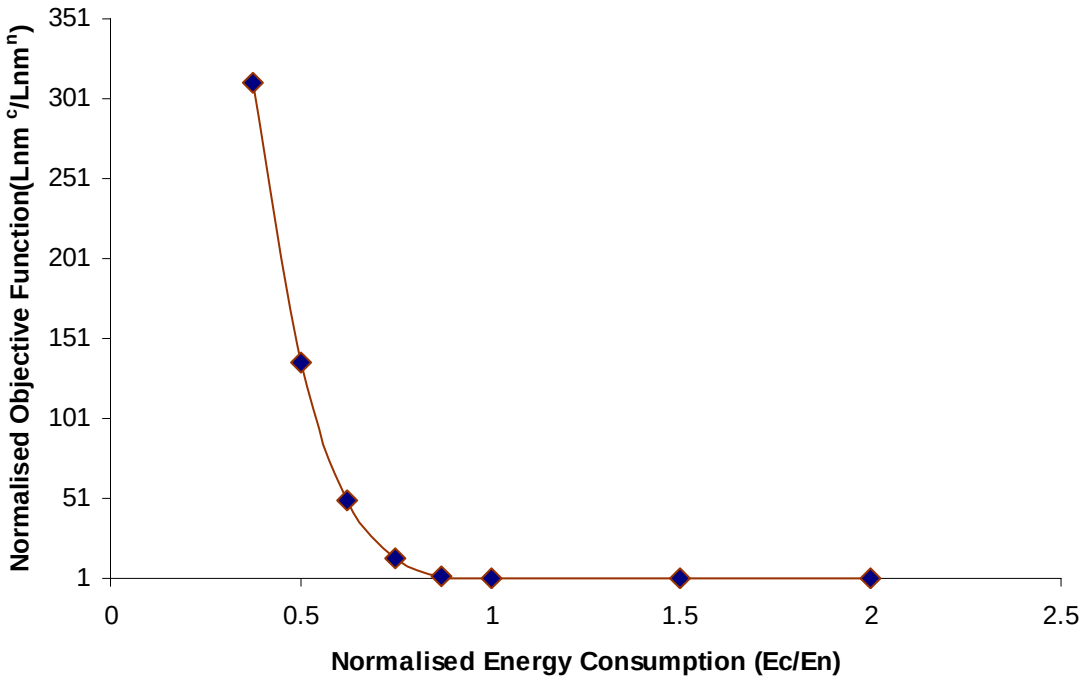

Figure 4.5: Normalised error function versus normalised energy consumption

Figure 4.4 shows the allowable energy (Ec), the actual energy (Ea) and the distribution of energy in the path for six cases. It depicts the variation of the electric potential distribution in the structure. Particularly, when Ec < En, patch #1 consumes higher energy than the other two. When Ec ≥ En, the large amount of energy is consumed by patch #2. The actual energy (Ea) does not attain the allowable energy (Ec) when Ec > En. Figure 4.5 depicts the relationship between the normalised optimal error functions (Lnm^c/Lnm^n) and the normalised energy consumption (Ec/En). It is clearly shown that the error increases more than 300 times at an allowable energy consumption of 37%En.

4.4.3.2.2 Single Applied Voltage Constraint

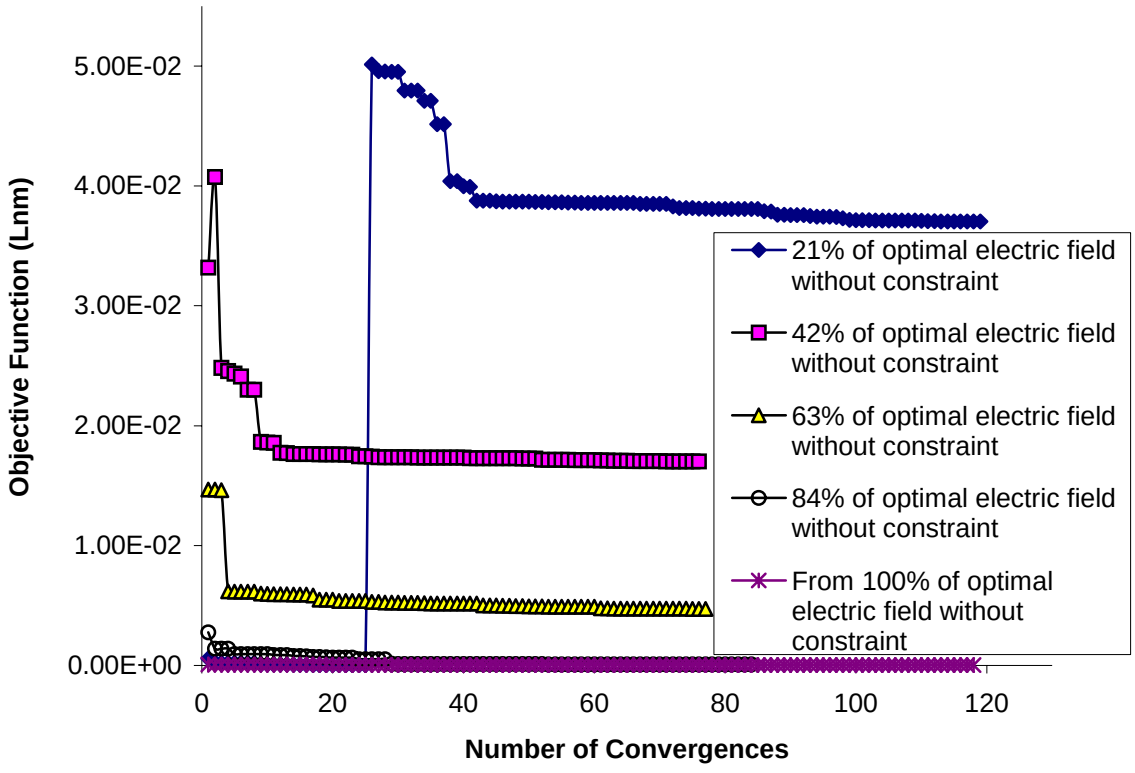

Figure 4.6: Convergence histories with different cases of single applied voltage constraint

The second test is designed to demonstrate the influence of the error function under five different cases of single applied-voltage constraint ($|\phi_a^k| \le |\phi_c|$, k=1…3). The allowable applied voltages $|\phi_c|$ are 21%, 42%, 63%, 84%, and ≥100% of ϕ_n^2. The

convergence histories are shown in Figure 4.6. The corresponding error functions are $3.70x10^{-2}$, $1.70x10^{-2}$, $4.71x10^{-3}$, $8.15x10^{-5}$ and $2.12x10^{-5}$. Figure 4.7 shows the normalised optimal error function versus the normalised applied voltage. These results show the same trend as the results discussed for the cases of total energy constraints.

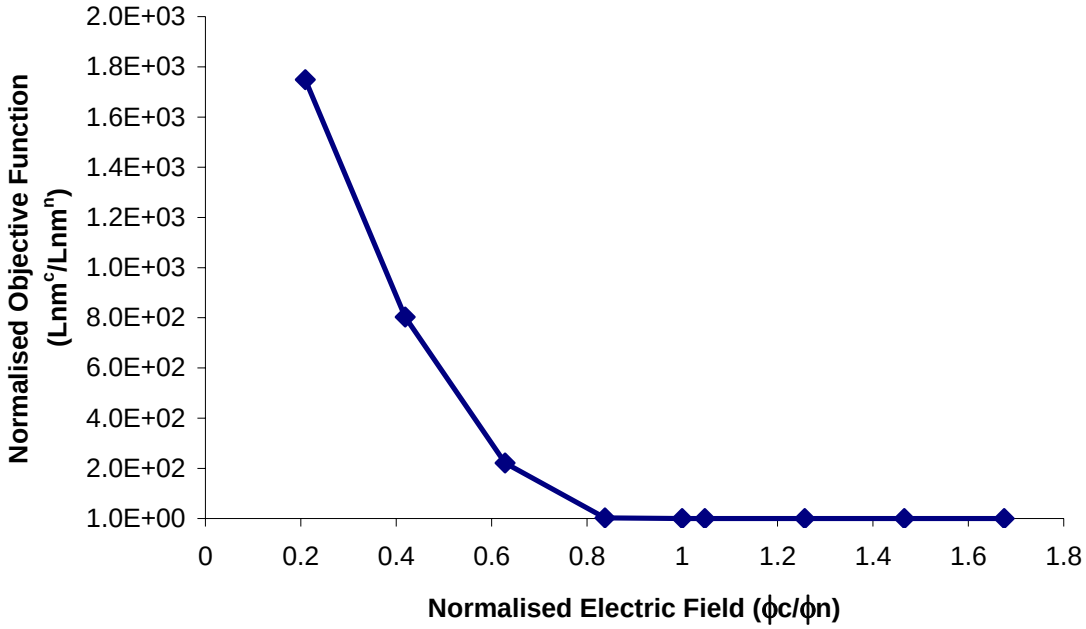

Figure 4.7: Normalised error function versus normalised single applied voltage constraint

Figure 4.8 shows the voltage distribution in actuator patches. It is interesting to note that uniform applied voltages are seen in piezoelectric actuator patches when the allowable applied voltage ($|\phi_c|$) is less than the optimal applied voltage ($|\phi_n|$). However, when $|\phi_c| \geq |\phi_n|$, the applied voltages to the actuator patches are not uniform and are lower than the value of $|\phi_c|$. In addition, comparing the error functions (Lnm) obtained from the results under total energy constraint (test #1) and single-applied voltage constraint (test #2) in terms of the total energy consumption. According to Case #3 in test #1, the error functions (Lnm) at given total of energy consumption of $250x10^3$ (V^2/R) is $1.04x10^{-3}$. While with the same total of energy consumption, Case #3 in test #2 yields the error function (Lnm) of $4.71x10^{-3}$. The results show that the single-applied voltage constraint type yields a larger error about 3.5 times compared to the error function given by the total energy constraint at the same given total energy consumption.

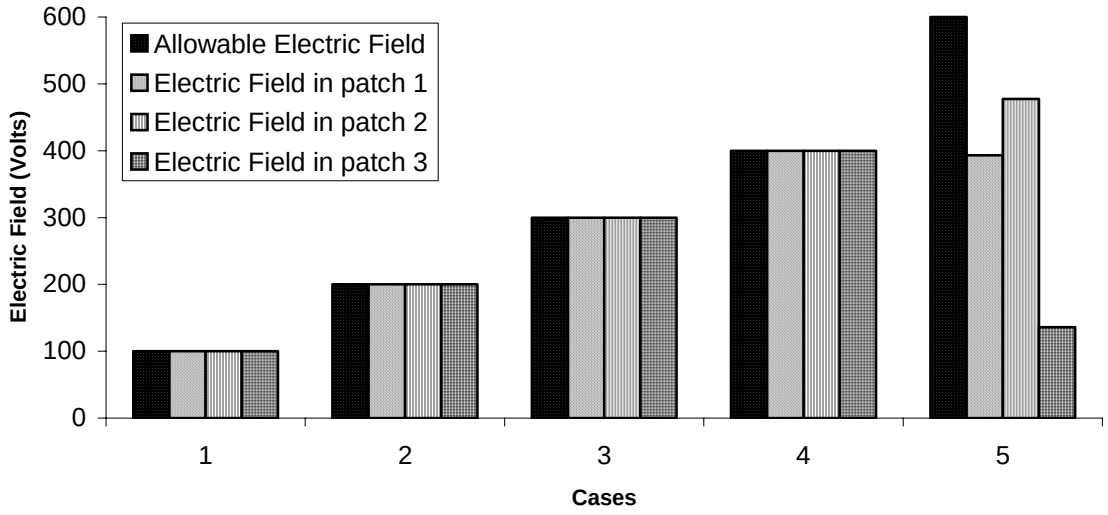

Figure 4.8: Voltage distribution for different cases of single applied voltage constraint

Table 4.1: Limit and actual voltage distribution for different cases

Case	1		2		3		4	
Patch	Limit	Actual	Limit	Actual	Limit	Actual	Limit	Actual
1	200	200	300	300	400	400	300	300
2	300	300	400	400	300	300	700	682
3	400	400	200	200	200	200	100	0

4.4.3.2.3 Multiple Applied Voltage Constraints

The third test is designed to deal with multiple constraints of applied voltages (i.e. $|\phi_a^k| \le |\phi_c^k|$, k= 1,…,3). Four cases are considered. The limit and actual applied voltages for all patches are listed in Table 3.1. The results clearly show that the actual applied voltage ($|\phi_a^k|$) in each patch reaches its allowable value ($|\phi_c^k|$) when $\max(|\phi_c^k|) < \max(|\phi_n^k|)$ for case #1, #2 and #3. The error functions for these 3 cases are $1.17\text{x}10^{-2}$, $2.72\text{x}10^{-3}$ and $9.21\text{x}10^{-4}$, respectively. As already known, patch #2 has the maximum magnitude of applied voltage. In case #4, considering $|\phi_c^1| = 300$ volts, $|\phi_c^2| = 700$volts and $|\phi_c^3|=100$volts, where only $|\phi_c^2| > |\phi_n^2|$, the results in Table 1 show that the electric field in patch #1 attains its allowable value ($|\phi_c^1|$), the electric field in patch #2 exceeds $|\phi_n^2|$ and is close to $|\phi_c^2|$ and the electric field in patch #3 is zero. For this case (#4), the error function is $2.16\text{x}10^{-4}$, which is about 10 times larger than $\text{Lnm}^n = 2.12\text{x}10^{-5}$.

4.4.3.2.4 Summary

The above results show that energy constraint can significantly affect the results of achieving the desired shape based on voltage optimisation. The error function depends on the range of the energy limitation and type of constraint handling. The best fits to desired structural shape can be achieved when a given energy limitation is chosen around an optimal value of energy obtained by the structural shape problem without energy constraint. In other words, there is a larger error function when the smaller energy limitation is considered to compare with the optimal energy obtained by structural shape problem without energy constraint. However, at the same given energy limitation, the desired structural shape can be achieved with the smaller error function by considering multi-criteria optimisation as shown in next example, where the voltage and shape configurations of actuator are optimised simultaneously.

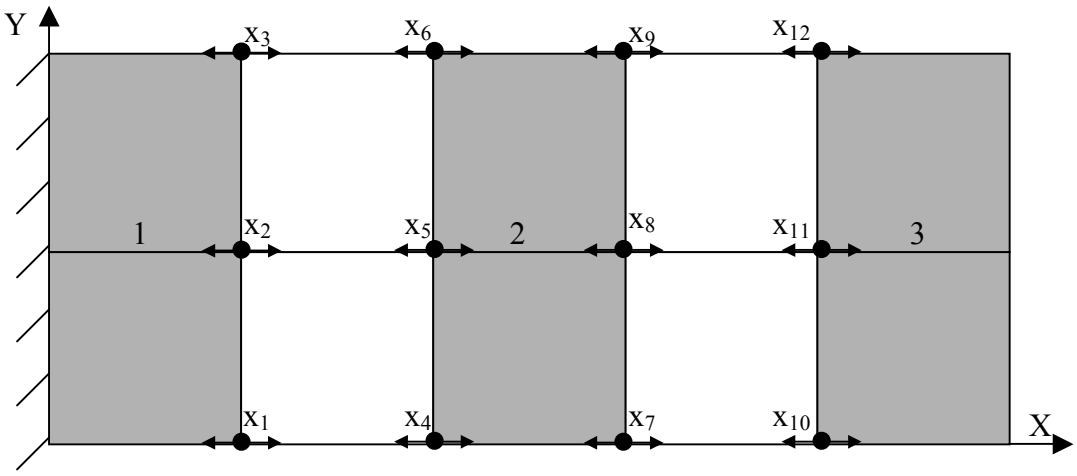

Figure 4.9: Cantilever plate in XY plane and direction of design variables

4.4.3.3 Example 2: Voltage and Piezoelectric Actuator Design Optimisation

For this example, several different types of constraints are investigated. The purpose was to observe the effect of constraints on the results of voltage distribution and actuator configurations. In this case, the voltage and configuration parameters of an actuator are considered as independent design variables to minimise the error function with energy constraint. The structural model, voltage optimisation and GA parameters are chosen to be the same as those in Example 1. Additionally for shape optimisation,

the x-coordinate at 12 points are chosen as design variables. The movement of the selected design points is assumed to be only in the x-direction as shown in Figure 4.9. The bounds for the configuration variables are $0.001 \leq x_1, x_2, x_3 \leq 0.044$; $0.046 \leq x_4, x_5, x_6 \leq 0.074$; $0.076 \leq x_7, x_8, x_9 \leq 0.104$; $0.106 \leq x_{10}, x_{11}, x_{12} \leq 0.149$. The non-constraint optimal solution are $Lnm^n = 9.45x10^{-7}$ $En = 150x10^3$ (volts^2/R), $\phi_n^1 = 300.72$ volts, $\phi_n^2 = 225.59$ volts and $\phi_n^3 = 82.01$ volts. Two types of constraints are considered and their results are presented here.

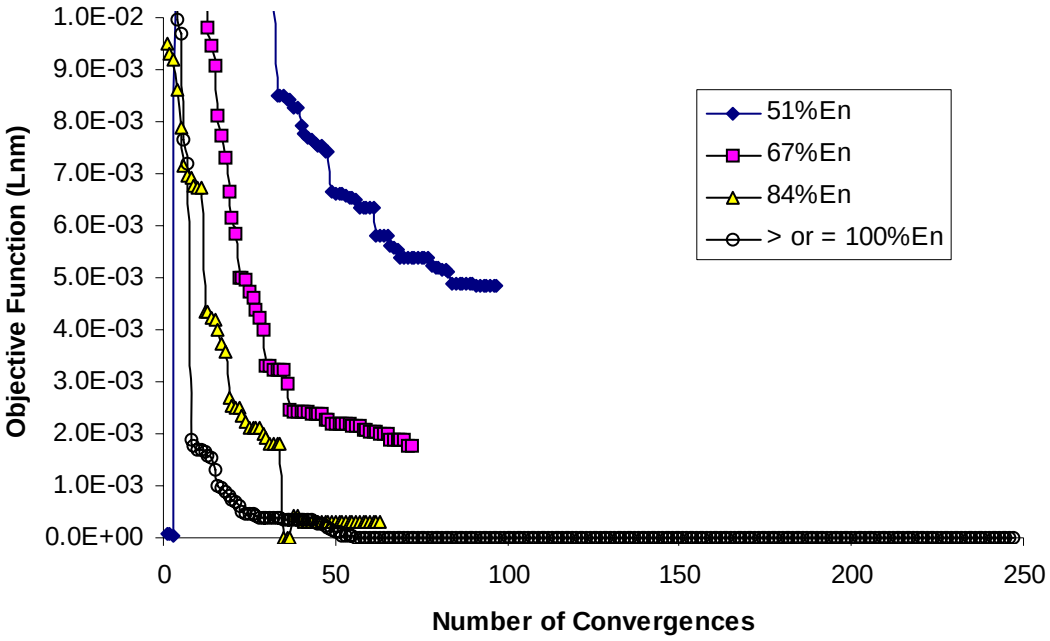

Figure 4.10: Convergence histories for different allowable energy consumption

4.4.3.3.1 Total Energy Consumption Constraint

The effects of four different total of energy consumption constraints on the resulting of voltage and shape configuration is studied, where Ec = 51%, 67%, 84% and ≥100% of En. The minimum error functions for the four cases are $4.85x10^{-3}$, $1.78x10^{-3}$, $3.02x10^{-4}$ and $9.45x10^{-7}$, respectively. Figure 4.10 shows the convergence histories. It can be seen that the error is larger when the total energy (Ec) is smaller than the value (En) and the actual energy consumption Ea is within allowable energy Ec tolerance. Figures 4.11 and 4.12 show the energy distribution in the plate and relation between normalised error functions and normalised total energy, respectively. The energy

distribution in each actuator is increased as Ec increases. Figures 4.13a and 4.13b show the final configuration of actuators when Ec < En and Ec ≥ En, respectively. It can bee seen that the volume of actuator patches are increased to the upper bound as Ec decreases.

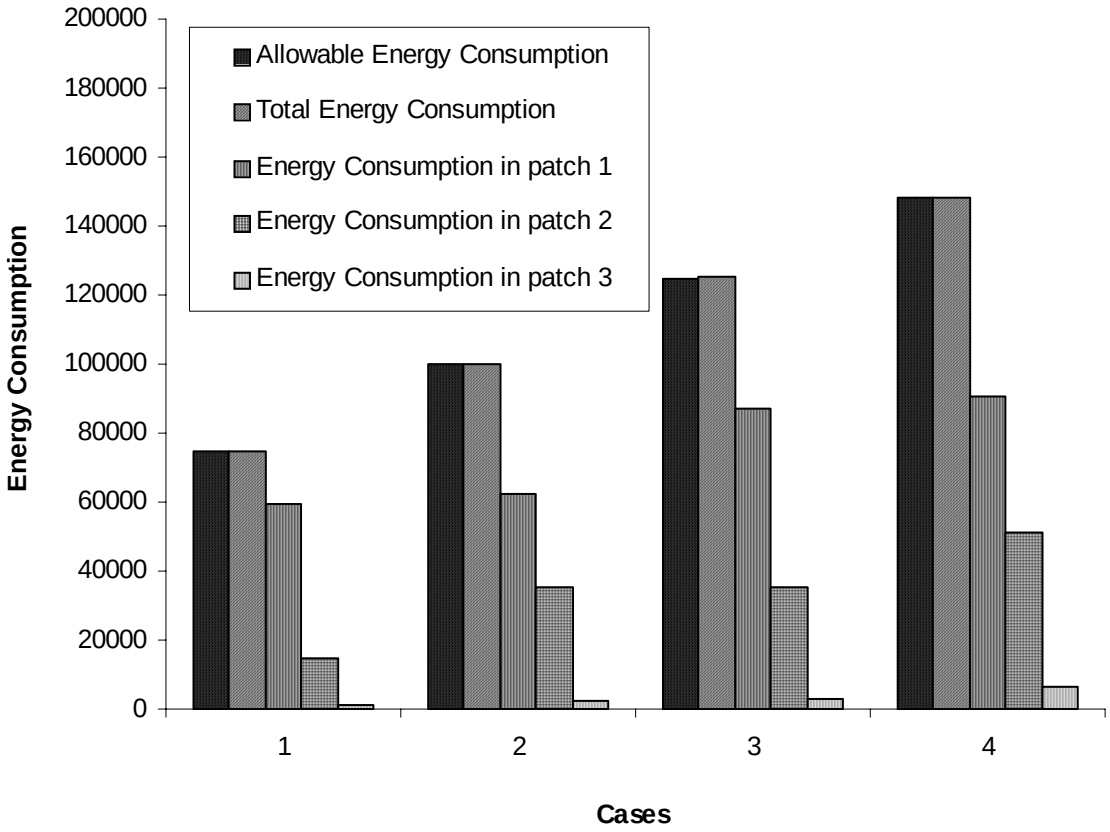

Figure 4.11: Energy distribution for different cases of allowable energy consumption

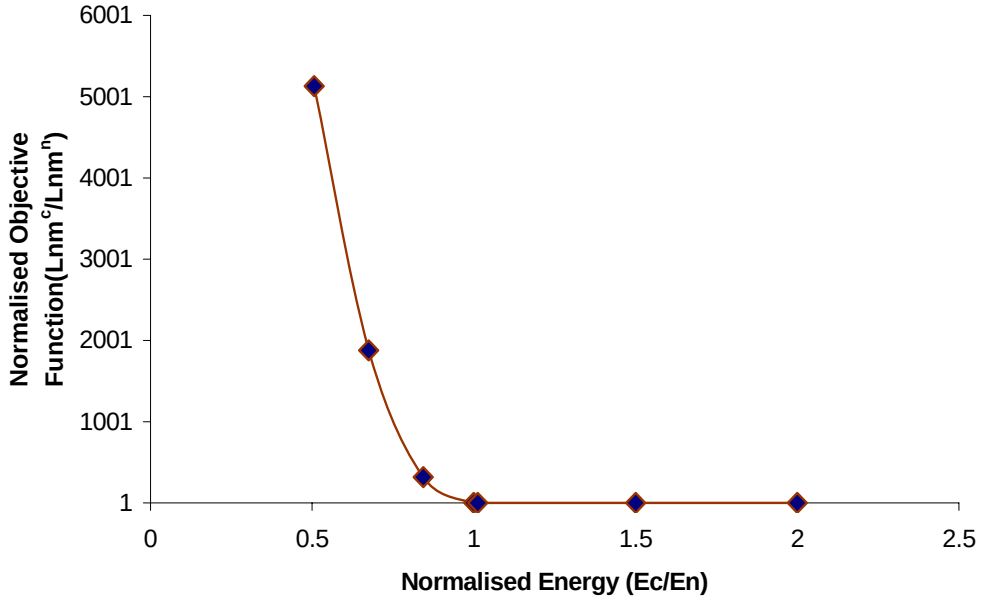

Figure 4.12: Normalised error function versus normalised energy consumption

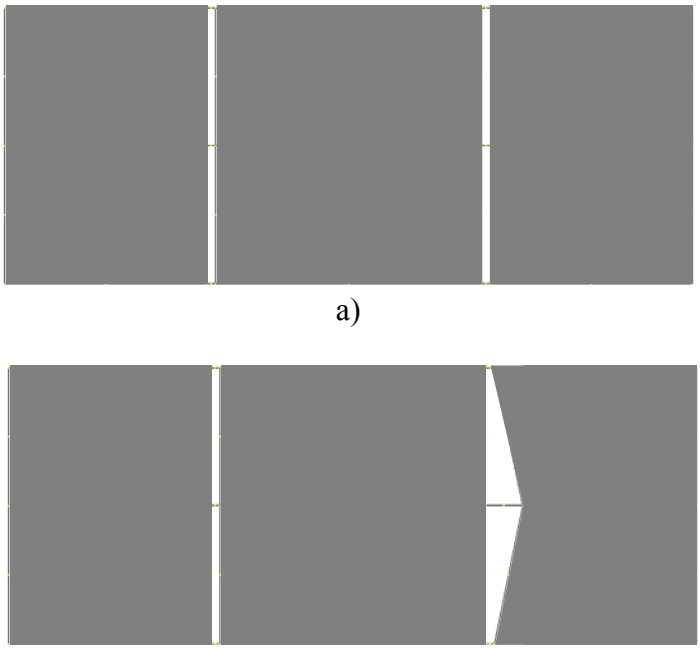

Figure 4.13: Final piezoelectric actuator configuration: a) Case Ec<En; b) Case Ec≥En

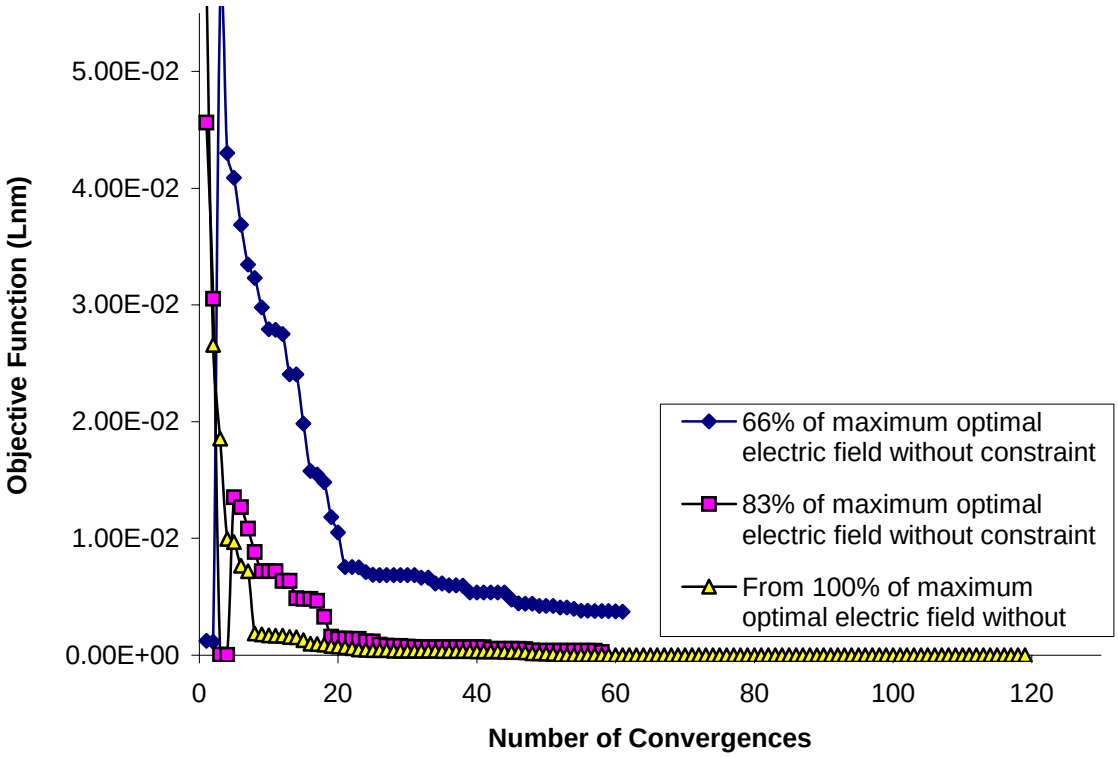

Figure 4.14: Convergence histories for single applied voltage constraint

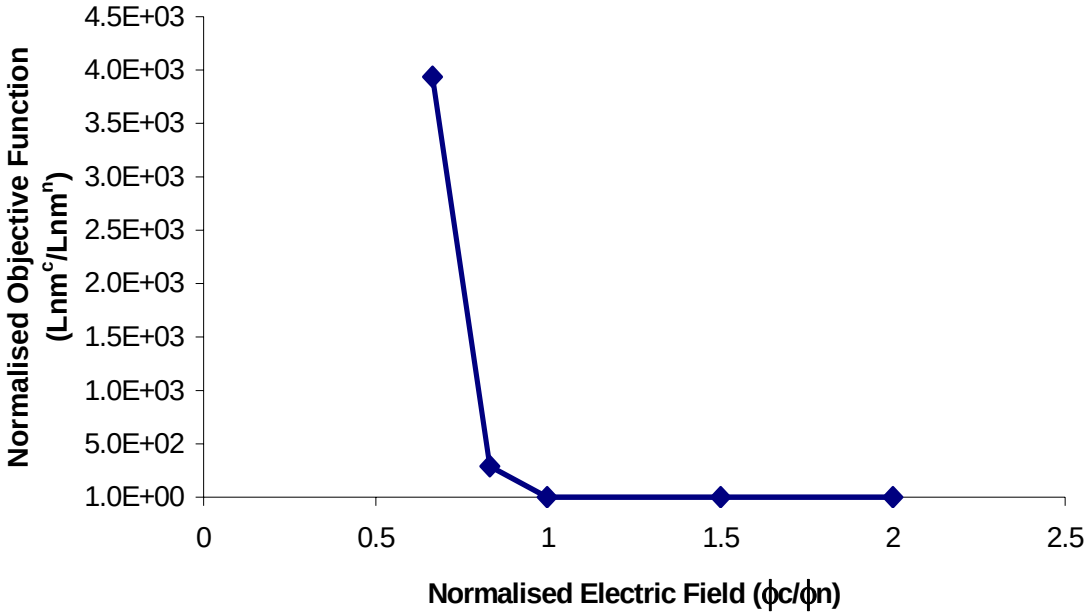

Figure 4.15: Normalised error function versus normalised single applied voltage constraint.

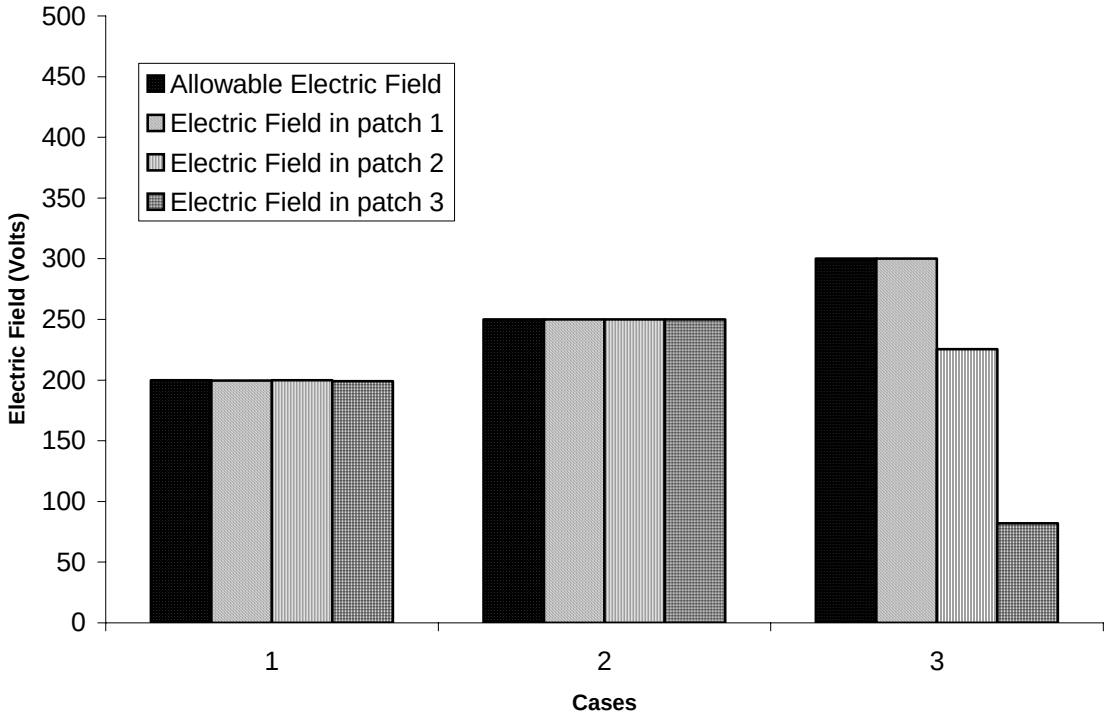

Figure 4.16: Voltage distribution for different cases of single applied voltage constraint

4.4.3.3.2 Single Applied Voltage Constraint

The effect of single applied-voltage constraint on the resulting voltages and shape configuration ($|\phi_a^k| \leq |\phi_c|$, k=1…3) is investigated. Case #1, #2 and #3 are considered with ϕ_c=66%, 83% and ≥100% of ϕ_n, respectively. Convergence histories are shown in Figure 4.14. Figure 4.15 depicts the relation between the normalised error function and the normalised applied voltage. The voltage distributions of each case are shown in Figure 4.16. The uniform voltage distribution can be seen in the cases of $|\phi_c^k| < |\phi_n|$. Figure 4.17a, 4.17b and 4.17c depict the final geometrical shape of actuator, respectively.

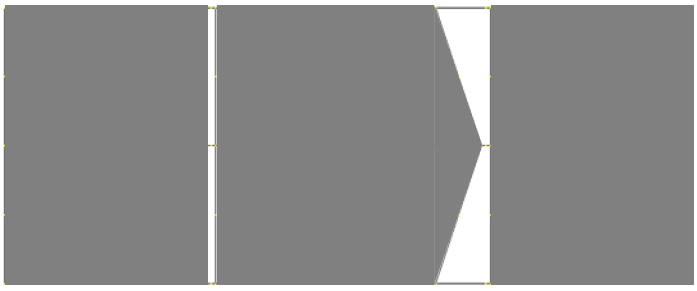

a)

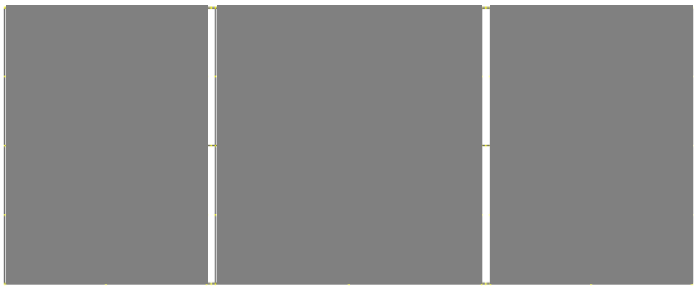

b)

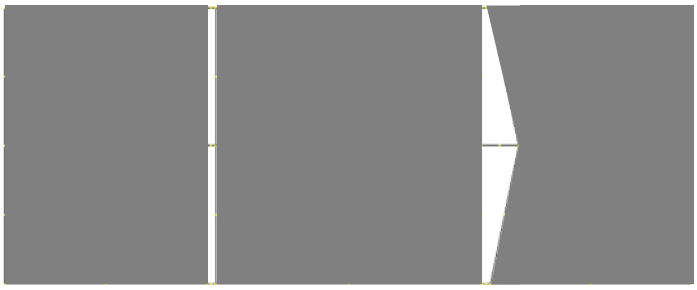

c)

Figure 4.17: Final piezoelectric actuator configuration: a) Case 66% of ϕn_max; b) 83% of ϕn_max ; c) From 100% of ϕn_max.

4.4.3.3.3 Summary

The above results show that the total energy consumption and voltage distribution have the same effects as discussed in previous section (4.4.3.2) except for the geometrical configuration of actuators. Particularly for the case of Ec < En, the final actuator configurations are almost the same, as shown in Figure 4.13a, when the total energy consumption constraint is considered. While Figures 4.17a and 4.17b clearly show that the final actuator configurations are not the same for the problem that considers single constraint of applied voltage when $|\phi_c| < |\phi_n|$. Once again, comparing the error function obtained from these two types of constraints in term of energy consumption, at about the same energy consumption, the single constraint type of applied voltage yields larger error function about 10 times compared to the error function given by the total energy constraint, namely, Lnm are 3.72×10^{-3} and 3.02×10^{-4}, respectively. It clearly shows that the single constraint type of applied voltage does not only affect the results of the error function but also the final actuator configurations.

4.4.3.3.4 Results on the Different FE mesh

A rerun of this example was carried out with different finite element mesh consisting of 20 elements in total, where each actuator patch is modelled by 4 elements. The numbers of design variables are 23 in total including geometrical and voltage variables. Only one case of allowable energy consumption of $Ec=10^5$ is considered in this run. The convergence history and the final actuator configuration are shown in Figure 4.18 and Figure 4.19, respectively. The result was attained after 61 convergences over a total of 884 generations. Table 4.2 shows the numerical results for different FE mesh. Compared with the solution with 2x5 FE coarse meshes, Figures 4.17b and 4.19 show the final actuators configurations, which are almost the same whereas the numerical results are slightly changed. The relative errors of results for the 4x5 FE fine mesh case are normalised against the 2x5 FE mesh case. The relative errors of voltages distribution (ϕ_1, ϕ_2 and ϕ_3) are changed by (+6%, -8%, and -68%). However the actual total of energy consumption is maintained within tolerance (about -0.08×10^{-3} % different). The error function reduces by about -3%. This is because the increase in number of nodal transverse displacements, where the objective function is defined by

summing all the least square differences between the desired and the calculated nodal transverse displacements, and the constraint tolerance (see section 4.4.2) leads to the change in the voltage distribution and the error function.

Table 4.2: Voltages distribution, actual energy consumption and error function for different FE mesh.

Patch (Volts)	2x5 FE mesh	4x5 FE mesh
1	249.97	265.03
2	187.5	171.83
3	48.58	15.35
Actual total energy consumption E_n	100000.85	100000.77
Lnm	1.777×10^{-3}	1.722×10^{-3}

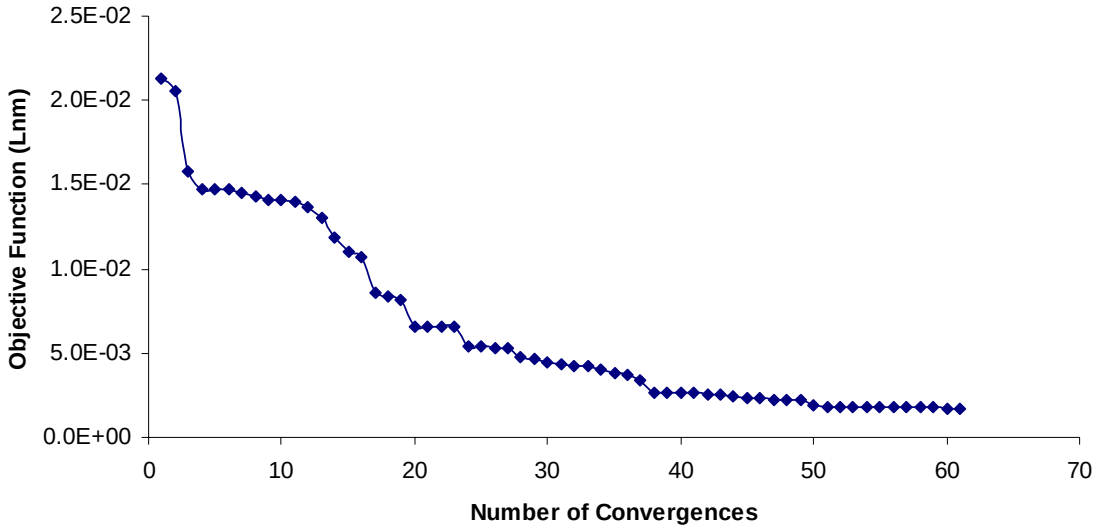

Figure 4.18: Convergence history of model with 4x5 FE mesh.

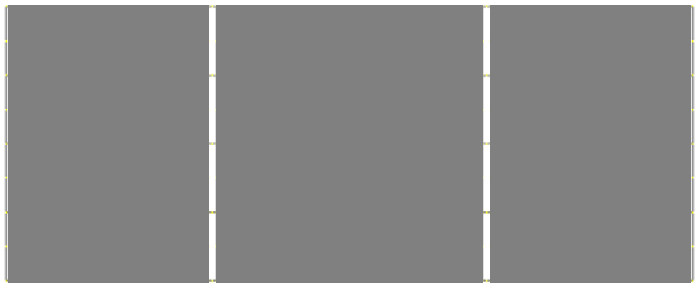

Figure 4.19: Final piezoelectric actuator configurations of model with 4x5 FE mesh.

4.4.3.4 Comparison

This section presents a comparison of the performance between two different optimisation methods with the constraints handling, which considers the single criterion optimisation (voltage optimisation) and multiple criteria optimisation (voltage and actuators configuration optimisation), respectively. The results are shown in Table 4.3. The results show that the multiple criteria optimisation method gives the smaller error function, which means the best fit to the desired structural shape under the same value of energy constraint. For example, with the total energy consumption of $150x10^3(V^2/R)$, the single criterion optimisation method gives the error function of $6.58x10^{-3}$, while $9.45x10^{-7}$ can be obtained from multiple criteria optimisation method. Similarly, for the cases of single constraint on the applied voltages, multiple criteria optimisation method gives a smaller error function of $3.72x10^{-3}$ compared to $1.70x10^{-2}$, and reduces by 78% with respect to results obtained from the single criteria optimisation.

Table 4.3: Voltages distribution and error function for different types of constraint handling and different methods of optimisation.

Type	Total energy consumption E_n		Single constraint of voltage ϕ	
Optimisation Methods	Single	Multiple	Single	Multiple
Allowable	$150x10^3$	$150x10^3$	200	200
Actual	$150x10^3$	$148x10^3$	-	-
Patch	Voltage (Volts)			
1	364.19	300.72	200.00	200.00
2	124.01	225.59	200.00	200.00
3	44.55	82.01	200.00	200.00
Lnm	$6.58x10^{-3}$	$9.45x10^{-7}$	$1.70x10^{-2}$	$3.72x10^{-3}$

4.5 Static Shape Control Problem with Error Function Constraint

The objective of static shape control problem of smart plate structures with an error function (Lnm) constraint is to search for the least total energy consumption E($\mathbf{X}$,$\boldsymbol{\phi}$) for achieving the desired structural shape to satisfy the limitation condition of a given error function. Similarly procedures in Section 4.4, the equation of objective function and constraint treatment are described in follow sections.

4.5.1 Objective function

The objective function in Equation (4.1) can now be written in the form of the total energy consumption as shown in Equation (4.18). As introduced in section 4.4, the total energy consumption is defined in terms of the applied voltages (ϕ) and conductors (R) (k=*1*, …, Np), where N_p is the total number of active piezoelectric actuator patches

$$f(\mathbf{V}) = E(\mathbf{X},\boldsymbol{\phi}) = \sum_{k=1}^{Np} \frac{\boldsymbol{\phi}_k^2}{R_k} \tag{4.18}$$

4.5.2 Error Function Constraint Treatment

For error function constraint, Equation (4.4) becomes

$$Lnm^a \leq Lnm^c \tag{4.19}$$

where Lnm superscripts c and a are the allowable and actual error function. Refer to Equation (4.10) for the definition of the error function (Lnm).

Due to constraint violation as discussed in section 4.2, the convergence of the error function constraint is stated below:

$$\left| \frac{Lnm^a - Lnm^c}{Lnm^c} \right| \leq \tau \tag{4.20}$$

4.5.3 Numerical Examples

The numerical examples are presented here to show that the proposed algorithm is capable to search for the least total energy consumption subjected to a given error function. The work focuses on several aspects such as voltage optimisation (VO), voltage and piezoelectric actuator configuration design optimisation. The same material properties, geometrical data, GA parameters and design variables information as previously described in details in Section 4.4 were used. However, the error function is minimised subjected to a given total of energy consumption. Lnm^n, En and ϕ_n^k are the optimal solutions obtained in the absence of constraint condition.

4.5.3.1 Example 3: Voltage Optimisation

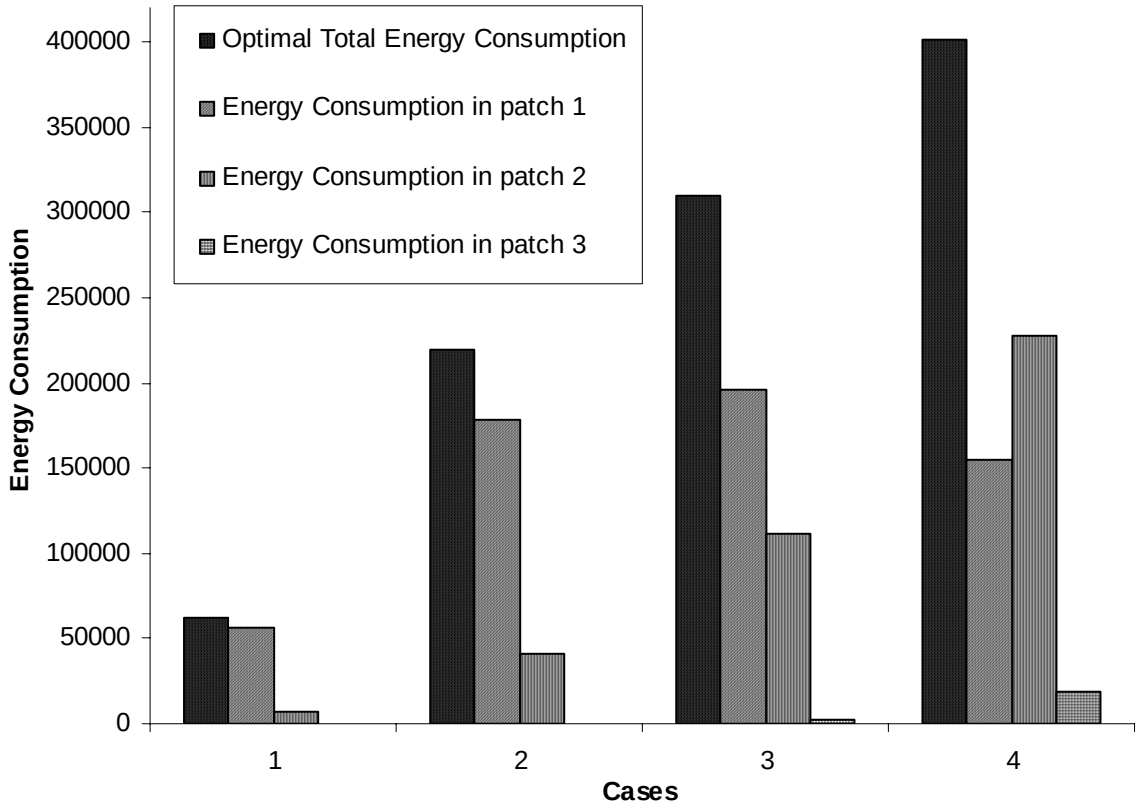

Figure 4.20: Optimal energy consumption and energy distribution for different cases of allowable error function.

In this example, when the error function constraints Lnm^c are equal to $2.0x10^{-2}$, $2.0x10^{-3}$, $2.0x10^{-4}$ and $\geq 2.0x10^{-5}$, the least total energy consumptions Ec are 62.75×10^3, 219.20×10^3, 309.40×10^3, 400.90×10^3 ($Volts^2/R$), respectively. Figure 4.20 depicts the optimal total energy consumption and energy consumption distribution in the piezoelectric actuator patches for the four cases. The convergence histories for four different cases of error function constraint are shown in Figure 4.21 that shows the effect of controlled error function on the results of optimal value of total energy consumption. Figure 4.22 depicts the relationship between the normalised optimal error functions (Lnm^c/Lnm^n) and the normalised total energy consumption (Ec/En). It is clearly shown that the total energy consumption ratio (Ec/En) comes to 1 when the Lnm^c comes to 0. The influence of the error function constraint on the results of energy (or voltage) distribution in the piezoelectric actuator patches has the same trend to that for the problems of minimising the error function subjected to energy constraint. It is also worth noting that the energy distribution gradient becomes steeper when $Lnm^c<Lnm^n$

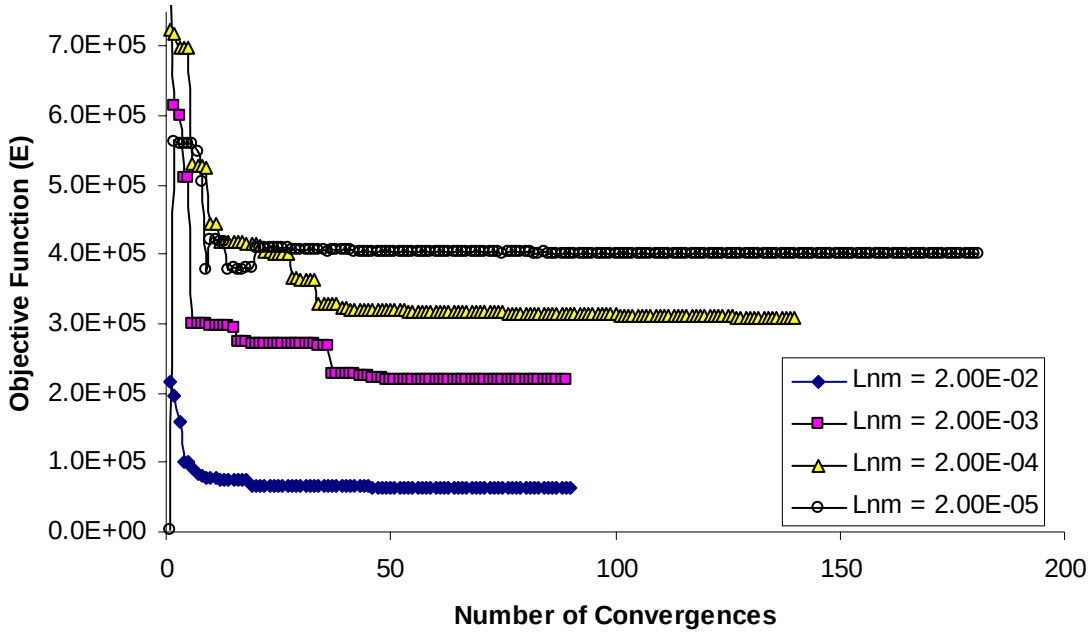

Figure 4.21: Convergence histories for different cases of allowable error function

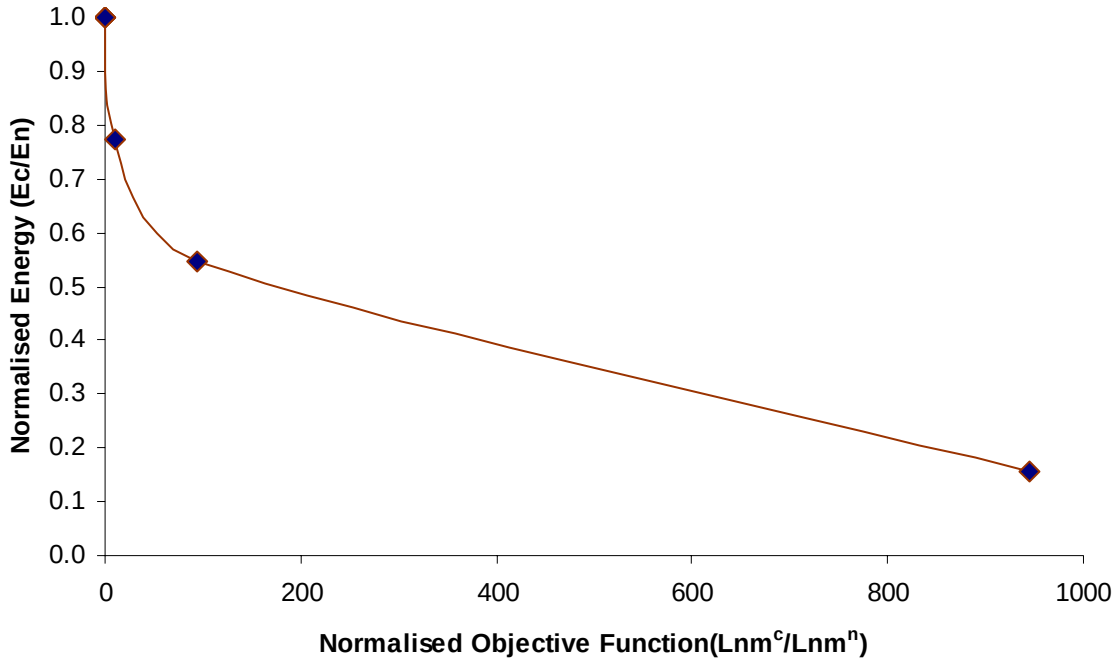

Figure 4.22: Normalised energy consumption versus normalised error function.

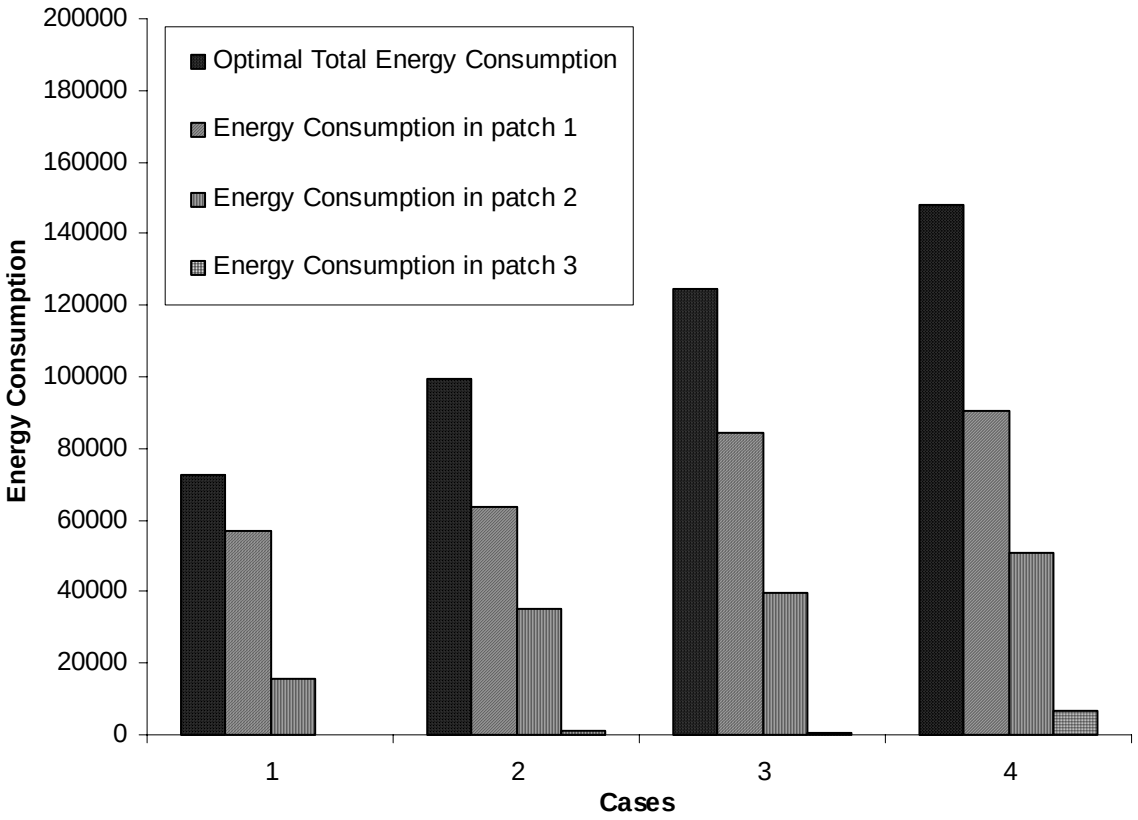

Figure 4.23: Optimal energy consumption and energy distribution for different cases of allowable error function

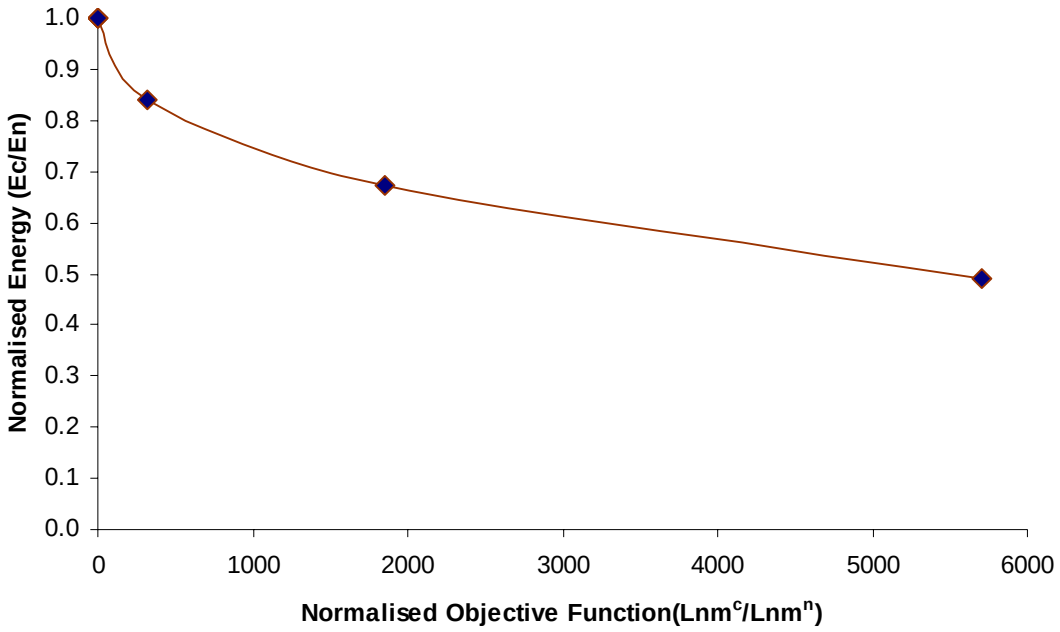

Figure 4.24: Normalised energy consumption versus normalised error function.

4.5.3.2 Example 4: Voltage and Piezoelectric Actuator Design Optimisation

In this example, there are four different cases of the error function constraints that are used to demonstrate the results of minimising the total energy consumption, whereas the applied voltage and piezoelectric actuator configuration are treated as design variables. In the first three cases, the values of error function constraint (Lnm^c) are considered such that $Lnm^c<Lnm^n$. By inspection, the example has the same results for any case with the value of error function constraint (Lnm^c) larger than or equal to the optimal value of error function constraint (Lnm^n). Therefore, case #4 presents the results for the cases of $Lnm^c \geq Lnm^n$. The values of error function constraint (Lnm^c) for these four cases are $5.366x10^{-3}$, $1.747x10^{-3}$, $3.021x10^{-4}$ and $\geq 9.410x10^{-7}$, respectively. The optimal voltage distributions for these cases are shown in Table 4.4. Figure 4.23 shows the optimal total energy consumption and energy consumption in the piezoelectric actuators for different values of the error function constraint. The optimal values of total energy consumption respectively are $72.41x10^3$, $99.66x10^3$, $124.40x10^3$ and $148.10x10^3$ ($Volts^2/R$). Figure 4.24 depicts the relationship between the normalised optimal error functions (Lnm^c/Lnm^n) and the normalised energy consumption (Ec/En). The final piezoelectric actuators configuration is shown in Figure 4.25. The results show that there are only two possible configurations for piezoelectric actuators designs. One is for the cases of $Lnm^c<Lnm^n$ as shown in Figure 4.25a. Figure 4.25b depicts the other when $Lnm^c \geq Lnm^n$.

Table 4.4: Voltage distribution with different cases of error function constraint

Case	1	2	3	4
Patch	Voltages (volts)			
1	238.3	252.0	290.5	300.7
2	125.0	187.6	199.2	225.6
3	0.0	31.3	18.2	82.0

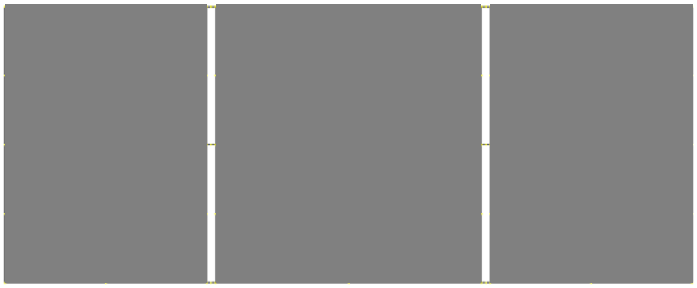

a)

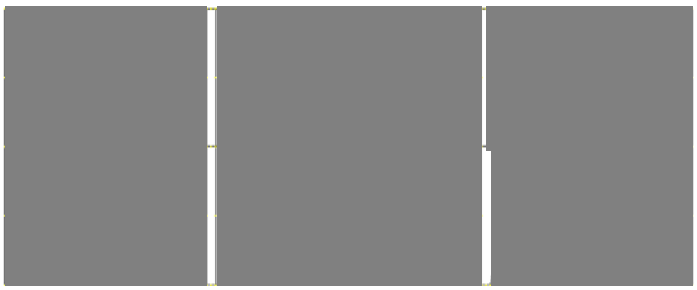

b)

Figure 4.25: Final piezoelectric actuator shape configuration: a) Case $Lnm^c<Lnm^n$; b) Case $Lnm^c \geq Lnm^n$

4.6 Summary

GA based algorithms have been presented for quasi-static shape control of smart composite plate structures subject to additional constraints and with piezoelectric actuators configuration and voltages are being considered as independent design variables. These algorithms are designed to optimise the voltage distribution individually or simultaneously with actuator configuration to minimise the error function (objective function) subject to the energy consumption constraint (additional constraint) or the other way around. For energy consumption constraint, three types of constraint are used; the total energy consumption constraint and single and multiple applied voltage

constraints. Illustrative examples have been presented and discussed. It shows that the proposed algorithms are capable to solve the structural shape control problem under given limitation of additional constraint. It can be clearly seen that the objective function depends on the additional constraint. Particularly, the error function subject to an energy consumption constraint can be greater than the error function obtained from the same problem without constraint. Also, the constraint type of total energy consumption is suitable for shape control problem with constraint handling, which yields lower error function than the single and multiple constraints on the applied voltages. Also presented is a comparison between the results obtained from the single criterion SC (voltage only) and multiple criteria MC (voltage and geometry) optimisation methods subject to the same energy constraint. It shows that the MC optimisation outperforms the SC optimisation. In other words, it is noted that the piezoelectric actuator configuration can enhance the structural shape control at a given energy constraint.

5. Evolutionary Piezoelectric Actuator Design Optimisation for Static Shape Control of Smart Plate Structures

This chapter presents a new evolutionary algorithm to solve various structural shape control problems of smart composite plate structures with active piezoelectric actuators. The Linear Least Square (LLS) method and the features of evolutionary strategies are employed to find the applied voltages and shapes for the active piezoelectric actuators, respectively, in order to achieve the desired structural shapes by gradually removing the active piezoelectric material part of the element based on the error function sensitivity number. In the finite element (FE) analysis, an error function sensitivity number, including electro-mechanical effect, is derived to compute the change in error functions that are defined in terms of the least square difference between calculated and desired structural shapes. The Evolutionary Piezoelectric Actuator Design Optimisation (EPADO) is proposed here to optimise the active piezoelectric actuator shape at a given applied voltage. Finally, several numerical examples are presented to verify that the proposed algorithm improves structural shape control by reducing the error function.

5.1 Introduction

The preceding chapters 3 and 4 presented several piezoelectric actuator design optimisation methods for the quasi-static shape control problems with and without constraint handling. The main objective is to search for the optimal voltage distribution and piezoelectric actuator configuration and location, which is defined based on the geometrical parameters. In other words, the geometrical parameters of piezoelectric actuators and the applied voltages are considered as design variables in these methods. To deal with this problem, the nodal coordinates have to be altered during the optimisation process and then updated after each successful iteration. In the field of structural optimisation, significant progress has been made to avoid alternating the nodal

coordinate or re-meshing the finite element model (Bendsøe, 1995; Rozvany et al, 1995 and Xie and Steven, 1997). The basic concept of the technique is to search for and eliminate any element that is an unnecessary or inefficient portion of the structural performance. Recently this technique has been used widely in structural design optimisation and is known as topology optimisation.

To date, there exists limited work that optimises the actuator shape by removing excessive piezoelectric materials based on selected criterion. Mukherjee and Joshi (2002) presented a gradientless iterative technique to find the actuators shape by gradually removing the piezoelectric material based on the residual voltage of elements for shape control. The residual voltage is calculated by subtraction of normalised voltages of initial and current designs. The elements, which have negative residual voltage, are then moved. But in engineering applications of structural design optimisation, there are many optimisation methods that have been developed based on the removal of material problem (Bendsøe, 1995; Rozvany et. al, 1995; Xie and Steven, 1997; Lee, 1993; and Li et. al, 1999). Evolutionary Structural Optimisation (ESO) is one of the gradientless algorithms proposed by Xie and Steven (1997), which is widely used to find the optimal structural configuration, subjected to various criterion conditions, by removing structural elements based on a selected sensitivity number. Chu et. al (1996) developed an ESO based on FE analysis to minimise the structural weight with stiffness constraint. Li et. al (1999 and 2000) presented an ESO algorithm for problems of variable thickness whilst minimising the maximum stress in a structure. The features of ESO have not been extensively used in structural shape control problems to optimise piezoelectric actuators.

In this chapter, an algorithm for evolutionary piezoelectric actuator design optimisation, for structural shape control problem, is developed by employing the features of ESO. On the basis of FE analysis, where the mechanical deformation is modelled using a 3rd order plate theory, and a layer-wise theory is used to model the electric field, the error function sensitivity number including electro-mechanical effect is derived to compute the change in the error function. The error function is defined in terms of the least square difference between the calculated and desired structural shapes, due to the removal of active piezoelectric materials. An algorithm for Evolutionary Piezoelectric Actuator Design Optimisation (EPADO) is proposed. Numerical results are

presented to demonstrate that the algorithm shows an improvement in terms of reducing the error function and also enhancing the efficiency of piezoelectric material usage for shape control problems.

5.2 Problem Formulation

The shape control problem considered in this chapter focuses on evolutionary piezoelectric actuator design optimization (EPADO) in terms of finding optimum values for applied voltages and actuator geometries. When the geometrical parameter vector of piezoelectric actuators **S** and the applied voltage vector $\boldsymbol{\phi}$ are considered as design variables, the quasi-static shape control problem can be defined, in the context of optimization formulation (Gallagher and Zienkiewicz, 1973), as follows:

Find $\mathbf{V}=[\mathbf{S}, \boldsymbol{\phi}]^T$ to

$$\text{Minimise } f(\mathbf{V}) = \text{Lnm}(\mathbf{S},\boldsymbol{\phi}) = \frac{\sum_{i=1}^{N} \frac{\left(w_i^d - w_i^c(\mathbf{S},\boldsymbol{\phi})\right)^2}{(w_{max}^d)^2}}{4 \times N} \tag{5.1}$$

$$\text{Subject to } g(\mathbf{V}) = 0 \Rightarrow [\mathbf{K}_{uu}(\mathbf{S})][\mathbf{u}_g(\mathbf{S},\boldsymbol{\phi})] = -[\mathbf{K}_{u\phi}(\mathbf{S})][\boldsymbol{\phi}_g] \tag{5.2}$$

Where, in the context of general optimisation formulation, V is the design variable vector; f(**V**) is the objective function; and g(**V**) is the performance constraint vector. Considering the EPADO problem, the design variable vector **V** has two components namely, the geometric variable vector S and the applied voltage variable vector $\boldsymbol{\phi}$. In this chapter, the geometric variables in vector **S** are chosen to be the distribution of selected active piezoelectric actuator material, whereas the voltage variables in vector $\boldsymbol{\phi}$ are the electrical potentials applied across the thickness direction of each actuator. The objective function f(**V**) in Equation (5.1) is defined as the error estimate function Lnm(**S**, $\boldsymbol{\phi}$), which is a weighted sum of all square differences in displacements at selected nodes between the desired and calculated structural shapes. w_i^d and $w_i^c(\mathbf{S}, \boldsymbol{\phi})$ are the desired and actuated (or calculated) displacements of the i^{th} node respectively, and w_{max}^d is the maximum displacement in the desired structural shape and N is the total number of

nodes considered. In the case of plates structure considered in this chapter, w_i^d and $w_i^c(\mathbf{S}, \boldsymbol{\phi})$ are the transverse displacements which is the $[(i-1)*11+3]^{th}$ displacement component in the global displacement vector $\mathbf{u}_g(\mathbf{S}, \boldsymbol{\phi})$. The constraint equations in Equation (5.2) are the equilibrium equations that govern the structural behaviour when the structure is only subjected to an electrical loading and are formulated using the finite element method. $[\boldsymbol{\phi}_g]$ is global vector of nodal voltages. $[\mathbf{K}_{uu}(\mathbf{S})]$ and $[\mathbf{K}_{u\phi}(\mathbf{S})]$ are the global stiffness matrix and the global piezoelectric linearly coupling matrix respectively (see Chapter 2).

5.3 Voltage Optimisation

When actuator configurations are given, the LLS method (Rorres and Anton, 1979) has been used successfully to determine the required optimal voltage distribution to achieve the desired structural shape. The Equations (5.1) and (5.2) become

Find $\boldsymbol{\phi}$ to

$$\text{Minimise } \text{Lnm}(\boldsymbol{\phi}) = \frac{\sum_{i=1}^{N} \frac{\left(w_i^d - w_i^c(\boldsymbol{\phi})\right)^2}{(w_{max}^d)^2}}{4 \times N} \tag{5.3}$$

$$\text{Subject to } [\mathbf{u}_g(\boldsymbol{\phi})] = [\mathbf{K}_{uu}]^{-1}[-\mathbf{K}_{u\phi}][\boldsymbol{\phi}_g] \tag{5.4}$$

For details understanding voltage optimisation, the reader is advised to visit the LLS method in Chapter 3. The solution of optimum voltage can be expressed in terms of the influence coefficient matrix and the desired displacement vector $[\mathbf{w}^d]$ as follow:

$$[\boldsymbol{\phi}] = \left(\left[\mathbf{C}^w\right]^T\left[\mathbf{C}^w\right]\right)^{-1}\left[\mathbf{C}^w\right]^T[\mathbf{w}^d] \tag{5.5}$$

5.4 Sensitivity Analysis

In piezoelectric actuator design, shape of a piezoelectric actuator is an important aspect in improving a desired structural shape. The optimal shape of piezoelectric actuators in terms of piezoelectric material distribution can be found by removing or adding piezoelectric actuator elements that leads to reduction of the error function. The sensitivity analysis approach is employed to evaluate the contribution of a change in volume of piezoelectric actuators to the variation of the error function. This section presents the derivation of the sensitivity equations for the objective function of single and multiple displacement components (error function sensitivity number) including the electro-mechanical effect for a given applied voltage distribution. The applied voltage could be given a specific value or obtained via the LLS solution using Equation (5.5). For sensitivity analysis, Equation (5.1) and (5.2) can be rewritten as

Find **S** to

$$\text{Minimise Lnm}(\mathbf{S}) = \frac{\sum_{i=1}^{N} \frac{\left(w_i^d - w_i^c(\mathbf{S})\right)^2}{(w_{max}^d)^2}}{4 \times N} \tag{5.6}$$

$$\text{Subject to} [\mathbf{K}_{uu}(\mathbf{S})][\mathbf{u}_g(\mathbf{S})] = -[\mathbf{K}_{u\phi}(\mathbf{S})][\phi_g] \tag{5.7}$$

5.4.1 Objective Function of Single Displacement Component

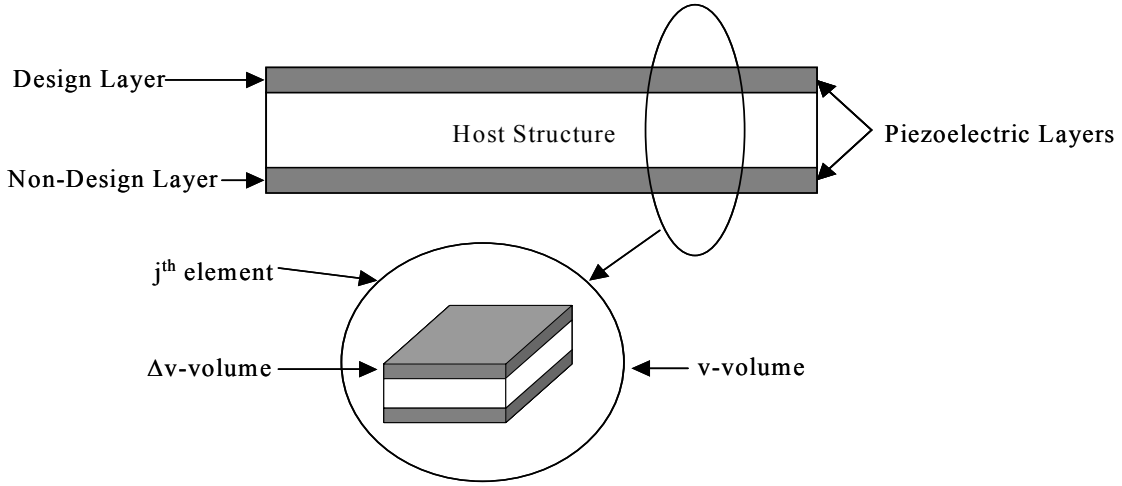

Figure 5.1: Smart structure modelling

For the shape control problem, the j^{th} element consists of a host material and adaptive (piezoelectric) materials. The adaptive materials can be set as active or inactive, known as design or non-design layer, respectively. As an example shown in Figure 5.1, a j^{th} element consists 3 layers, where piezoelectric material patches are bonded at the top and at the bottom of the host structure. Only top piezoelectric layer is chosen to apply electric potential and is allowed to be removed.

When the active piezoelectric material part of the j^{th} element, which has volume of Δv, is removed, the change in the global mechanical and electro-mechanical stiffness matrices are defined as

$$[\Delta\hat{\mathbf{K}}^{j}_{uu}] = [\hat{\mathbf{K}}^{j}_{uu}(v)] - [\hat{\mathbf{K}}^{j}_{uu}(v-\Delta v)] \text{ and } [\Delta\hat{\mathbf{K}}^{j}_{u\phi}] = [\hat{\mathbf{K}}^{j}_{u\phi}(v)] - [\hat{\mathbf{K}}^{j}_{u\phi}(v-\Delta v)] \tag{5.8}$$

Where $\left([\hat{\mathbf{K}}^{j}_{uu}(v)],[\hat{\mathbf{K}}^{j}_{u\phi}(v)]\right)$ and $\left([\hat{\mathbf{K}}^{j}_{uu}(v-\Delta v)],[\hat{\mathbf{K}}^{j}_{u\phi}(v-\Delta v)]\right)$ are the set of global mechanical and electro-mechanical stiffness matrices before and after removal of the active piezoelectric material part of the j^{th} element, respectively. The change in the global displacement vector $[\Delta\mathbf{u}_g]$ can be determined by considering the equilibrium condition before and after removal of the element as given in Equation (5.7) and Equation (5.9), respectively. The reason for a positive $[\Delta\mathbf{u}_g]$ in Equation (5.9) is that the structural stiffness is reduced when active piezoelectric material part is removed.

$$([\mathbf{K}_{uu}(\mathbf{S})]-[\Delta\hat{\mathbf{K}}^{j}_{uu}])([\mathbf{u}_g(\mathbf{S})]+[\Delta\mathbf{u}_g]) = -([\mathbf{K}_{u\phi}(\mathbf{S})]-[\Delta\hat{\mathbf{K}}^{j}_{u\phi}])[\boldsymbol{\phi}_g] \tag{5.9}$$

By expanding Equation (5.9), then subtracting Equation (5.7) and ignoring the higher order terms. The change in the global displacement vector $\Delta\mathbf{u}_g$ can be written as:

$$[\Delta\mathbf{u}_g] = [\mathbf{K}_{uu}(\mathbf{S})]^{-1}([\Delta\hat{\mathbf{K}}^{j}_{uu}][\mathbf{u}_g]+[\Delta\hat{\mathbf{K}}^{j}_{u\phi}][\boldsymbol{\phi}_g]) \tag{5.10}$$

To find the change in the i^{th} nodal transverse displacement for the case of the plate element, which is the $[(i-1)*dof+3]^{th}$ displacement component of $\mathbf{u}_g$, a virtual load vector $\mathbf{f}^i$ is considered where its $[(i-1)*dof+3]^{th}$ component is set equal to 1 and zero for all others. The "dof" term represents the mechanical nodal degree of freedom, which is 11

in FE formulation (Nguyen and Tong, 2004). Multiplying Equation (5.10) by the transpose of $\mathbf{f}^i$, the change $\Delta u_g^{\ i}$ of the i^{th} nodal transverse displacement due to the piezoelectric material volume change in j^{th} element is rewritten as:

$$\Delta w_i^c = \Delta u_g^{\ i} = [\mathbf{f}^i]^T[\mathbf{K}_{uu}(\mathbf{S})]^{-1}([\Delta\hat{\mathbf{K}}_{uu}^j][\mathbf{u}_g]+[\Delta\hat{\mathbf{K}}_{u\phi}^j][\boldsymbol{\phi}_g]) \quad \text{or}$$

$$\Delta u_g^{\ i} = [\mathbf{u}^i]^T([\Delta\hat{\mathbf{K}}_{uu}^j][\mathbf{u}_g]+[\Delta\hat{\mathbf{K}}_{u\phi}^j][\boldsymbol{\phi}_g]) \tag{5.11}$$

Where $[\mathbf{u}^i]^T$ is the displacement vector solution of the virtual system $[\mathbf{K}_{uu}(\mathbf{S})][\mathbf{u}^i] = [\mathbf{f}^i]$. Similarly to Xie and Steven (1997), Equation (5.11) can be conducted at the elemental level as:

$$\Delta w_i^c = [\mathbf{u}^{ji}]^T([\Delta\mathbf{K}_{uu}^j][\mathbf{u}_g^j]+[\Delta\mathbf{K}_{u\phi}^j][\boldsymbol{\phi}_g^j]) \tag{5.12}$$

Where $[\mathbf{u}^{ji}]$, $[\mathbf{u}_g^{\ j}]$ and $\boldsymbol{\phi}_g^j$ are the entries from global solution vectors $[\mathbf{u}_g(\mathbf{S})]$, $\mathbf{u}^i$ and global electrical force vectors $[\boldsymbol{\phi}_g]$, respectively. $[\Delta\mathbf{K}_{uu}^j]$ and $[\Delta\mathbf{K}_{u\phi}^j]$ are the changes in the mechanical and electro-mechanical element stiffness matrices, respectively, due to the removal of active piezoelectric material volume related to the j^{th} element.

In the shape control problem, the term of $[\mathbf{K}_{u\phi}(\mathbf{S})][\boldsymbol{\phi}_g]$ is the representative of an electrical force. Therefore, it is obvious that the removal of active piezoelectric material in the element changes the equivalent applied nodal voltage induced force to the nodes of this element. Equation (5.12) indicates the change of in nodal transverse displacement due to the removal of the active piezoelectric material part in the j^{th} element. It is also defined as the displacement sensitivity number (α_{sc}) of the smart structure. It can be positive or negative, which implies that the transverse displacement may increase or decrease, respectively.

Finally, the displacement sensitivity number for objective function of a single displacement component including electro-mechanical effect can be written as:

$$\alpha_{SC}^i = [\mathbf{u}^{ji}]^T([\Delta\mathbf{K}_{uu}^j][\mathbf{u}_g^j]+[\Delta\mathbf{K}_{u\phi}^j][\boldsymbol{\phi}_g^j]) \tag{5.13}$$

5.4.2 Error Function Sensitivity Number

The above displacement sensitivity number (Equation (5.13)) can be used directly for problems with an objective function with a single displacement. But in the shape control problem, the objective function (error function Lnm) is defined in terms of a sum of the least square errors of all nodal transverse displacements between the calculated and desired shapes. Therefore, to deal with this problem, the effectiveness of the active piezoelectric material volume change of an element needs to be evaluated using this form of error function. The general form for an error function including multiple displacement components is given by

$$\mathrm{Lnm(S)} = \mathrm{h}(\mathrm{w}_1^{\mathrm{c}}, \mathrm{w}_2^{\mathrm{c}}, \cdots, \mathrm{w}_{\mathrm{i}}^{\mathrm{c}}, \cdots, \mathrm{w}_{\mathrm{N}}^{\mathrm{c}}) \tag{5.14}$$

The change in error function due to the removal of an active piezoelectric part of an element is defined in terms of the summation of the products of the change in displacements and the differentiation of the function h with respect to all these displacement components, as given in Equation (5.15). This is known as the error function sensitivity (ΔLnm).

$$\Delta\mathrm{Lnm}^{\mathrm{j}} = \sum_{\mathrm{i}=1}^{\mathrm{N}} \left(\frac{\partial \mathrm{h}}{\partial \mathrm{w}_{\mathrm{i}}^{\mathrm{c}}(\mathbf{S})} \Delta \mathrm{w}_{\mathrm{i}}^{\mathrm{c}} \right) \tag{5.15}$$

Substituting Equation (5.12) into Equation (5.15), it becomes:

$$\Delta\mathrm{Lnm}^{\mathrm{j}} = \nabla \mathrm{h} \times \alpha_{\mathrm{SC}} \tag{5.16}$$

$$\text{where } \nabla \mathrm{h} = \left(\frac{\partial \mathrm{h}}{\partial \mathrm{w}_1^{\mathrm{c}}(\mathbf{S})}, \frac{\partial \mathrm{h}}{\partial \mathrm{w}_2^{\mathrm{c}}(\mathbf{S})}, \cdots, \frac{\partial \mathrm{h}}{\partial \mathrm{w}_{\mathrm{i}}^{\mathrm{c}}(\mathbf{S})}, \cdots, \frac{\partial \mathrm{h}}{\partial \mathrm{w}_{\mathrm{N}}^{\mathrm{c}}(\mathbf{S})} \right)$$

$$\alpha_{\mathrm{SC}} = \left(\Delta \mathrm{w}_{\mathrm{i}}^{\mathrm{c}}, \Delta \mathrm{w}_2^{\mathrm{c}}, \cdots, \Delta \mathrm{w}_{\mathrm{i}}^{\mathrm{c}}, \cdots, \Delta \mathrm{w}_{\mathrm{N}}^{\mathrm{c}} \right) = \left(\alpha_{\mathrm{SC}}^1, \alpha_{\mathrm{SC}}^2, \cdots, \alpha_{\mathrm{SC}}^{\mathrm{i}}, \cdots, \alpha_{\mathrm{SC}}^{\mathrm{N}} \right)^{\mathrm{T}}$$

Then refer to Equation (5.6) and Appendix G, Equation (5.17) gives the error function differentiation with respect to i^{th} displacement components.

$$\frac{\partial h}{\partial w_i^c} = \frac{\left(w_i^c(\mathbf{S}) - w_i^d\right)}{\left(2 \times N \times w_{max}^d\right)} \tag{5.17}$$

Finally, the displacement sensitivity number for the error function including multiple displacement components, known as error function sensitivity number, can be written as:

$$\Delta Lnm^j = \sum_{i=1}^{N} \left(\frac{\partial h}{\partial w_i^c(\mathbf{S})} \left([\mathbf{u}^{ji}]^T ([\Delta \mathbf{K}_{uu}^j][\mathbf{u}_g^j] + [\Delta \mathbf{K}_{u\phi}^j][\boldsymbol{\phi}_g^j]) \right) \right)$$

or

$$\Delta Lnm^j = \sum_{i=1}^{N} \left(\frac{\partial h}{\partial w_i^c(\mathbf{S})} [\mathbf{u}^{ji}]^T \right) ([\Delta \mathbf{K}_{uu}^j][\mathbf{u}_g^j] + [\Delta \mathbf{K}_{u\phi}^j][\boldsymbol{\phi}_g^j]) \tag{5.18}$$

In addition, an alternative form for finding the change in error function including multiple displacement components is employed by Haftka and Gurdal (1992; and Li et. al, (1999). This takes advantage of one virtual system instead of multiple virtual systems, which correspond to the number of displacement components. This significantly reduces the computational cost. Hence the error function sensitivity number due to removal active piezoelectric material of the j^{th} element can be rewritten as (refer to Appendix H).

$$\Delta Lnm^j = [\bar{\mathbf{u}}^j]^T ([\Delta \mathbf{K}_{uu}^j][\mathbf{u}_g^j] + [\Delta \mathbf{K}_{u\phi}^j][\boldsymbol{\phi}_g^j]) \tag{5.19}$$

Where $\bar{\mathbf{u}}^j$ are the entries from solution vectors $\bar{\mathbf{u}} = [\mathbf{K}_{uu}(\mathbf{S})]^{-1}\bar{\mathbf{f}}$ and $\bar{\mathbf{f}} = \sum_{i=1}^{N} \frac{\partial h}{\partial w_i^c(\mathbf{S})} \mathbf{f}^i$

5.5 Evolutionary Piezoelectric Actuator Design Optimisation (EPADO)

This section presents a new optimisation scheme that employs evolutionary structural optimisation strategies (Xie and Steven, 1997) in the application of shape control of smart composite plate structures. This is referred to as the Evolutionary

Piezoelectric Actuator Design Optimisation (EPADO), i.e, to optimise the active piezoelectric actuator distribution at a given applied voltage. The method aims to minimise the error function by achieving a desired structural shape. The method is based on the proposed evolutionary criterion of error function sensitivity number. At the end of each iteration, a selected number of active piezoelectric material parts of the elements is gradually removed from the initial design for the active actuator patch. To achieve the goal of reducing the error function, removal of an active piezoelectric material element must have the lowest value of ΔLnm such that $Lnm^1 > Lnm^2 > \ldots > Lnm^{iter}$ (iter is the number of iterations). The selected number is referred to as the removal material rate (RMR), which is defined in terms of the ratio e^s/e^r, the number of removal piezoelectric material pieces (e^s) and the number of active piezoelectric material pieces in the current design (e^r). RMR should be small to ensure a smooth change (see Xie and Steven, 1997). This is because the error function sensitivity is formulated by neglecting the higher order term, which is only valid when the changes in both stiffness and displacement vectors are small. Furthermore, RMR can not be too small since the computational cost will increase. Setting RMR to zero (RMR=0) is equivalent to an active piezoelectric part of a single element being selected for removal during the iteration. If there is more than one element that has the same smallest error function sensitivity number then they will be removed simultaneously. The evolutionary iteration procedure, EPADO, is given below:

Step 1: Obtain input parameter RMR and applied voltage ϕ

Step 2: Define the initial active piezoelectric actuator shape using a dense Finite Element (FE) mesh.

Step 3: Perform FEA to calculate the nodal transverse displacement of the structure and find out gradient vector ∇h of the objective displacement function.

Step 4: Calculate the error function Lnm^b and introduce a virtual system.

Step 5: Perform FEA for the virtual system to obtain virtual nodal transverse displacement.

Step 6: Compute the error function sensitivity number ΔLnm for all elements.

Step 7: Remove active piezoelectric material part for element that have lowest value of ΔLnm and calculate the error function Lnm^a.

Step 8: Perform error functions check, which are calculated before (Lnm^b) and after (Lnm^a) removing the piezoelectric material part of an element. If (Lnm^a<Lnm^b) then update the active piezoelectric actuator configuration and error function by making Lnm^b = Lnm^a and return to step 3 to continue optimisation process. Otherwise proceed to step 9.

Step 9: Terminate the optimisation process. The results of last iteration are considered as an optimal solution.

And the flowchart for EPADO process is shown in Figure 5.2.

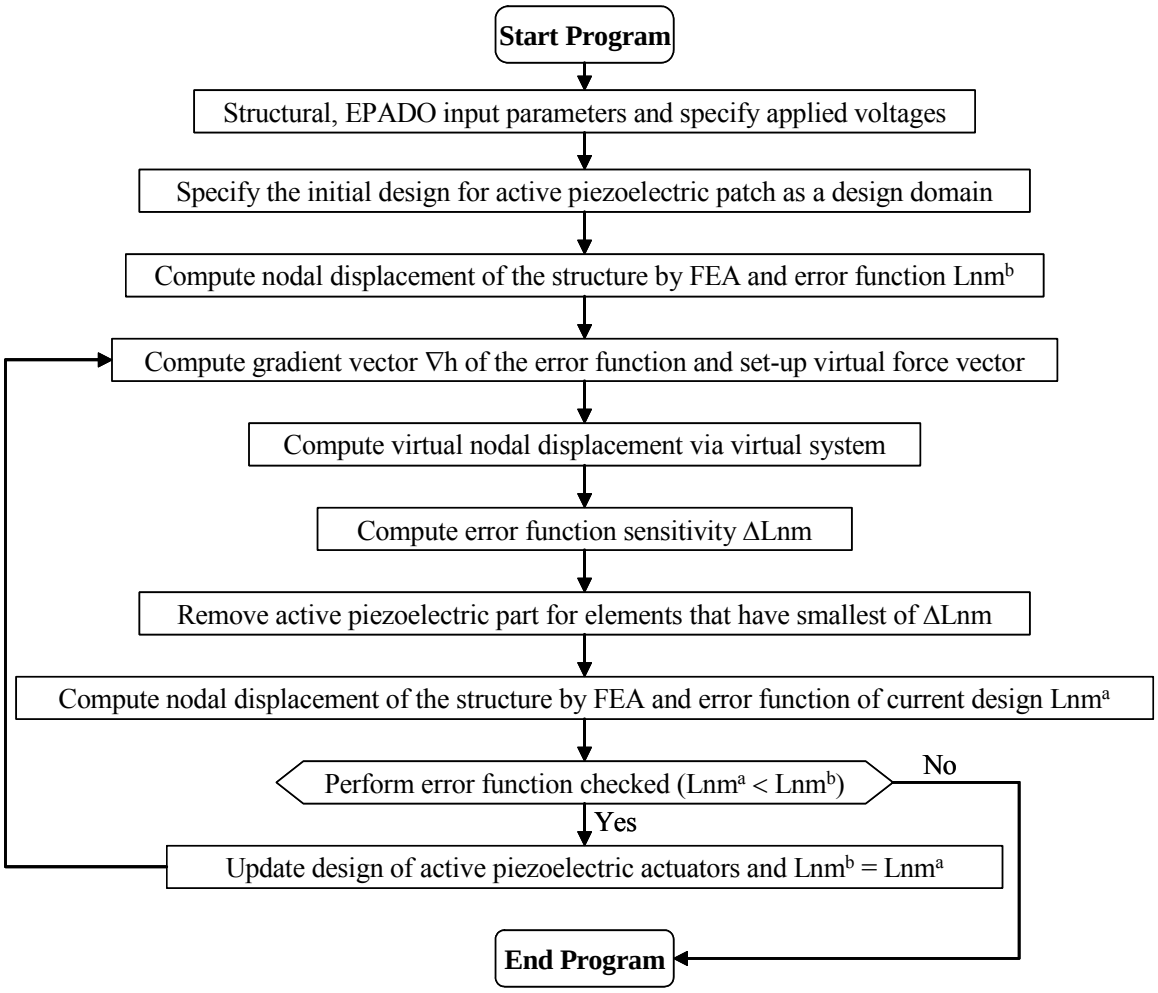

Figure 5.2: Flowchart for EPADO algorithm

5.6 Numerical Examples

The examples are presented to demonstrate the features of the EPADO method based on the proposed evolutionary criterion for error function sensitivity number including electro-mechanical effect for the shape control problem of smart plates. The results are then compared with the results obtained from the LLS method to show the improvement in achieving the desired structural shape in terms of the reduction in the value of the error function.

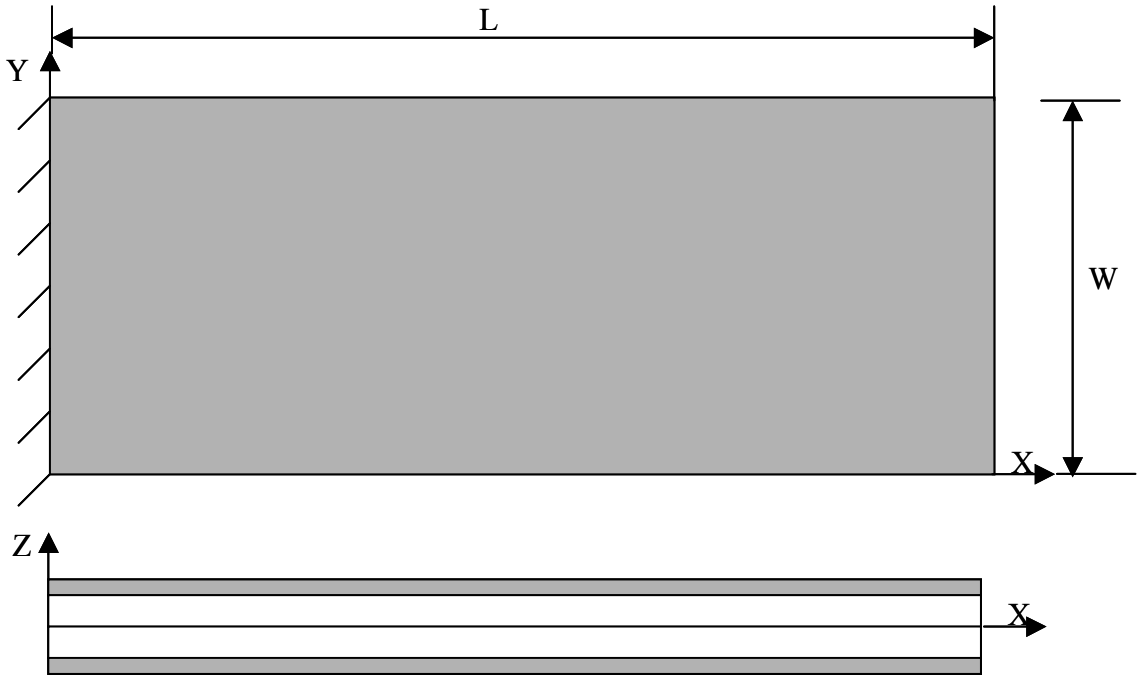

Figure 5.3: Cantilever plate in XY and XZ plane.

5.6.1 Model Description

Consider a cantilever plate, which is clamped at its left edge and subject to non-applied mechanical load. The plate has a length of L meters; width of W meters and consists of two layers of 0.01m thickness each. The piezoelectric actuators are attached on at the top and bottom surfaces of the plate, which have a thickness of 0.001m each. Only the top actuator patches are activated, which is chosen as a design domain where the piezoelectric material can be removed as shown in Figure 5.3. The plate material has the following stiffness constants: $c_{11}=c_{22}=c_{33}=92.9$GPa, $c_{12}=c_{13}=c_{23}=39.8$GPa, $c_{44}=c_{55}=c_{66}=26.5$GPa. The patch properties are: $c_{11}=c_{22}=c_{33}=113.0$GPa,

$c_{12}=c_{13}=c_{23}=55.5$GPa, $c_{44}=c_{55}=c_{66}=28.6$GPa; the $\chi_{11}=\chi_{22}=15.3\text{x}10^{-9}$F/M, $\chi_{33}=15.0\text{x}10^{-9}$F/M and $d_{31}=-254$pm/V, $d_{32}=-254$pm/V, $d_{33}=374$pm/V, $d_{24}=584$pm/V, $d_{15}=584$pm/V. The above properties were used in all calculations.

5.6.2 Example 1

This section will examine the performance of shape control in terms of the error function using EPADO algorithm, where the active piezoelectric actuator shape is optimised at a given applied voltage. A plate has dimensions L=0.15m and W=0.06m. Initially, the active piezoelectric actuator was assumed to be distributed over the entire plate as shown in Figure 5.3. In this section, only the bending structural shape will be tested for all test cases. The bending desired structural shape is defined as $w^d(x,y)=10^{-5}\cos(10x-1)$, where $0 \le x \le 0.15$.

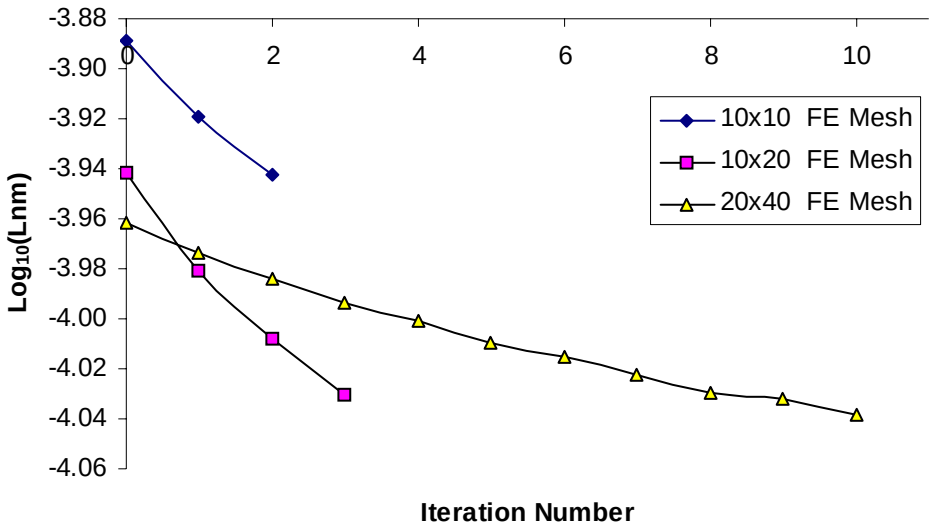

Figure 5.4: Convergence histories for different FE mesh variations at $\phi = \phi_{LLS}$

The first test case investigates the improvement on the resulting of error function and piezoelectric material usage of the EPADO algorithm compared to the LLS method using several FE mesh sizes of 10x10, 10x20 and 20x40 finite elements. Considering RMR = 0 which is equivalent to an active piezoelectric part of single element being selected to be removed at a time during the EPADO iteration. It should be noted that there could be more than one of these elements having identical smallest value of error function sensitivity number. Furthermore, the voltage distribution ($\phi=\phi_{LLS}$) obtained

from the LLS method is used as a given applied voltage for the EPADO procedure. The applied voltage for the 10x10, 10x20 and 20x40 FE mesh are $\phi = \phi_{LLS} = 253.43$ volts, 255.24 volts and 255.96 volts, respectively. The convergence histories and final piezoelectric actuator designs are shown in Figure 5.4 and Figure 5.5, respectively. Figure 5.5 depicts similar locations of unused active piezoelectric material. The numerical results obtained from LLS and EPADO, which respectively optimise the voltage distribution and the number of active piezoelectric actuator elements, are shown in Table 5.1. The 3rd row of Table 5.1 shows the number of active piezoelectric elements. There are reductions in both the error function and the volume of active piezoelectric material. It is noted that all error functions have reduced by from 12% to 19% and the reduction in volume of active piezoelectric material has reduced by from 2.5% to 4%. The effect of the result due to the different FE mesh sizes cannot be clearly seen here. This is because the voltage distribution obtained from LLS method are different. The results show that there is not much change in reduction of error function and volume of active piezoelectric material when ϕ_{LLS} was considered as an applied voltage for EPADO. This test case is further examined with different applied voltages, which are less than the voltage distribution obtained by the LLS method ($\phi<\phi_{LLS}$). The results show that there are no active piezoelectric actuator elements removed when $\phi<\phi_{LLS}$. From all the results in this test case, it can be understood that the optimal voltage distribution obtained by the LLS method (ϕ_{LLS}) could be used as the desired voltage to find the optimal shape of piezoelectric actuators using error function minimisation via EPADO. In other words, the applied voltage must be higher than the voltage distribution obtained by the LLS method ($\phi\geq\phi_{LLS}$) to yield improvement in error function and reduction in piezoelectric material usage.

Table 5.1: Voltage and error function when using LLS and EPADO at $\phi=\phi_{LLS}$

FE Mesh	10x10			10x20			20x40		
	LLS	EPADO	Error (%)	LLS	EPADO	Error (%)	LLS	EPADO	Error (%)
Voltages	253.43	-	-	255.24	-	-	255.96	-	-
Lnm	$1.29\text{x}10^{-4}$	$1.14\text{x}10^{-4}$	-11.58	$1.14\text{x}10^{-4}$	$9.32\text{x}10^{-5}$	-18.50	$1.09\text{x}10^{-4}$	$9.15\text{x}10^{-5}$	-16.16
No of Elements	100	96	-4	200	194	-3	800	780	-2.5
No of Iterations	-	2	-	-	3	-	-	10	-

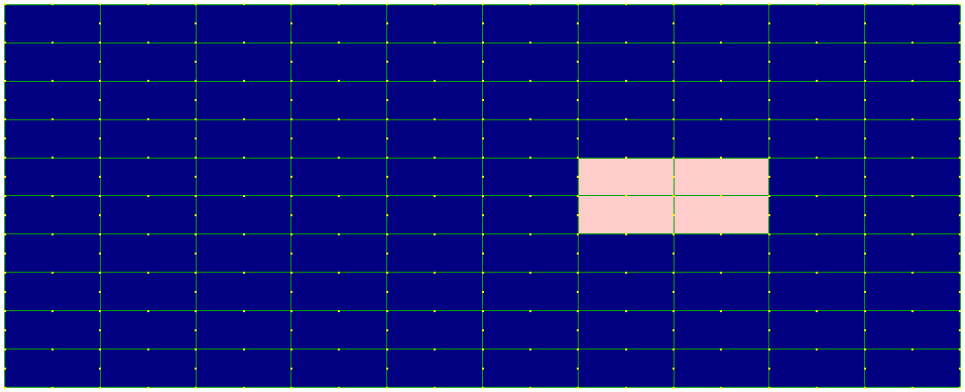

a) 10x10 FE mesh

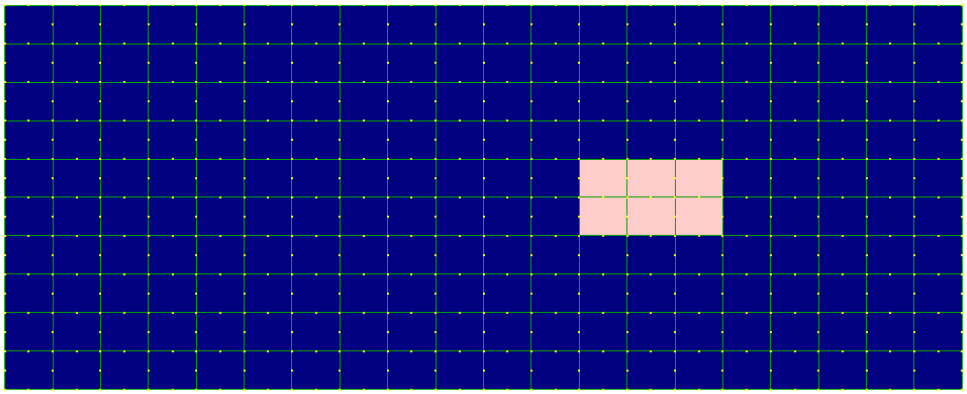

b) 10x20 FE mesh

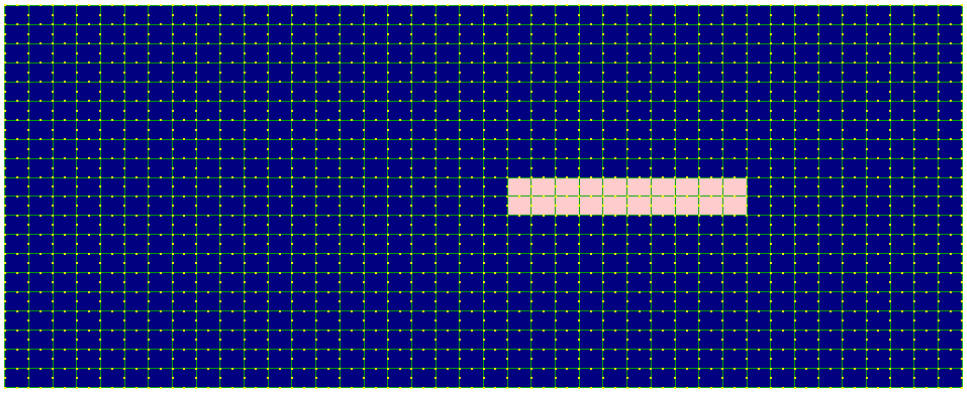

c) 20x40 FE mesh

Figure 5.5: Effect of FE mesh variations on the piezoelectric actuator design at $\phi = \phi_{LLS}$

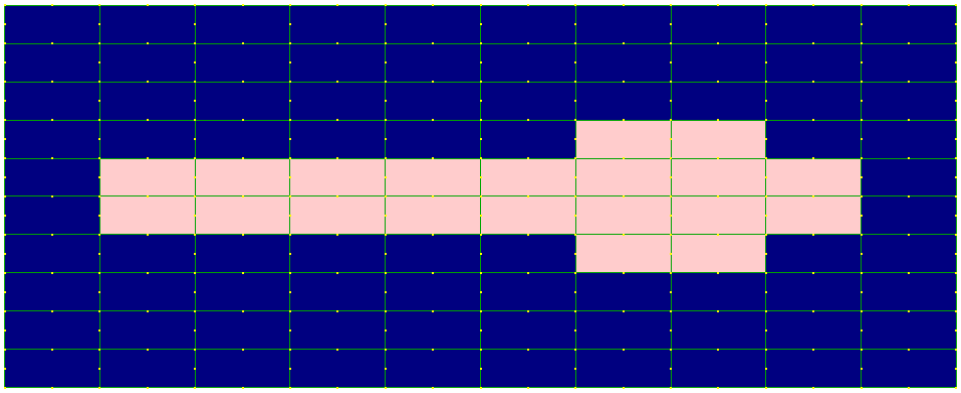

a) 10x10 FE mesh

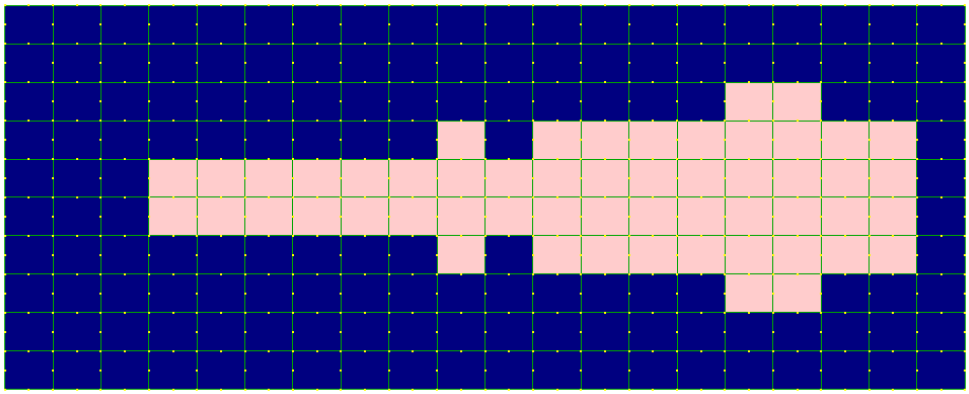

b) 10x20 FE mesh

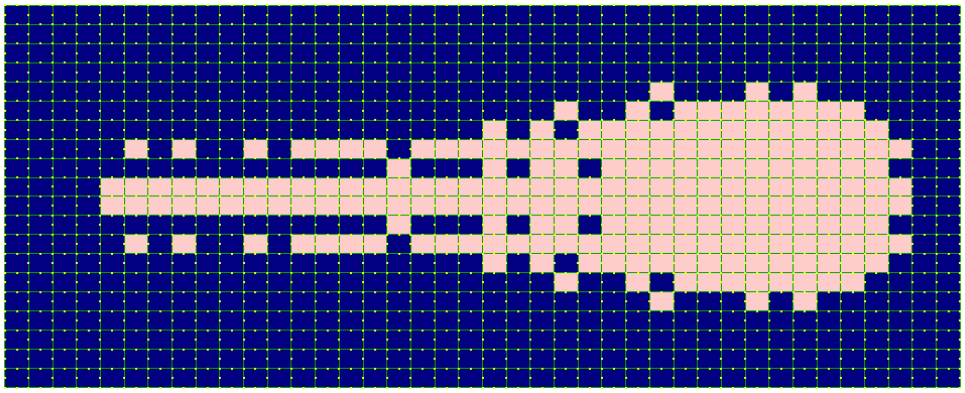

c) 20x40 FE mesh

Figure 5.6: Effect of FE mesh variations on the piezoelectric actuator design at $\phi = 300$ volts

The second test case is designed to demonstrate the influence of FE mesh sizes on the error function and the evolutionary piezoelectric actuator design by running the first test case again with an applied voltage of ϕ=300 volts and RMR=0. The numerical results are given in Table 5.2. It can be observed that there is a remarkable reduction in both error function and volume of piezoelectric material due to an increase in the applied voltage by about 25% of ϕ_{LLS}. The 10x10 FE mesh model yields more than a 66% reduction in the error function and a 20% reduction in the active piezoelectric material volume. The 10x20 and 20x40 FE mesh models have similar results, namely, with a 90% reduction in the error function and 27% reduction in the active piezoelectric material volume. Figure 5.6 shows the effects of FE mesh size on the piezoelectric actuator design. In Figures 5.6b and 5.6c, it can be observed that the final shapes of piezoelectric actuator patches are similar. The curve in piezoelectric actuator design can be seen in Figure 5.6c. The convergence histories of the error function for different FE meshes are shown in Figure 5.7. The test results show that the optimised shapes of piezoelectric actuators have a smooth boundary and an optimal error function when the finest mesh is considered. In addition, an investigation into the evolutionary histories of active piezoelectric actuator design for the 20x40 FE mesh model, as shown in Figure 5.8, shows that there were two pieces of piezoelectric material that were removed at each iteration. This is because the transverse displacements (z-displacement) are symmetrical about the centre horizontal line (x-direction) and due to the setting of RMR=0. The optimal solution is reached after 106 iterations, and 212 elements of active piezoelectric material were removed.

Table 5.2: Voltage and error function when using LLS and EPADO at ϕ=300volts

FE Mesh	10x10			10x20			20x40		
	LLS	EPADO	Error (%)	LLS	EPADO	Error (%)	LLS	EPADO	Error (%)
Voltages	253.43	300	18.38	255.24	300	17.54	255.96	300	17.21
Lnm	$1.29\text{x}10^{-4}$	$4.35\text{x}10^{-5}$	-66.35	$1.14\text{x}10^{-4}$	$1.28\text{x}10^{-5}$	-88.83	$1.09\text{x}10^{-4}$	$1.04\text{x}10^{-5}$	-90.46
No of Elements	100	80	-20	200	146	-27	800	588	-26.5
No of Iterations	-	10	-	-	27	-	-	106	-

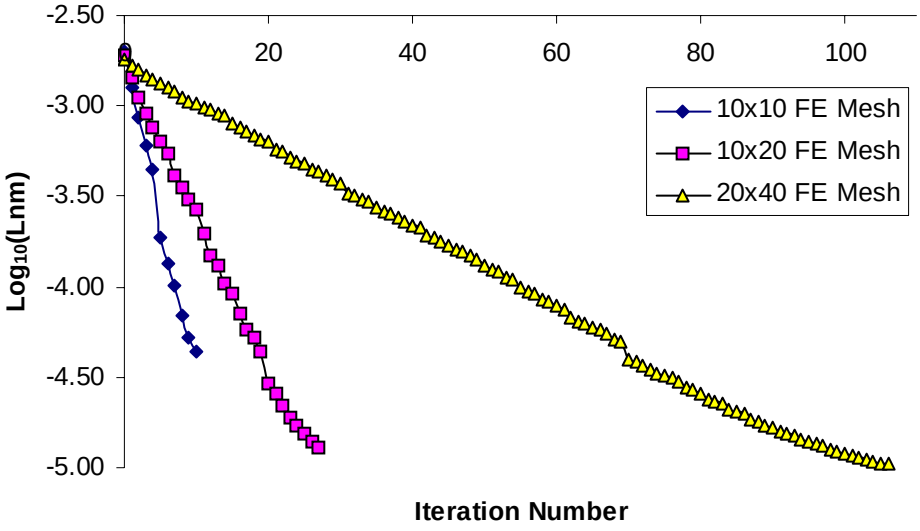

Figure 5.7: Convergence histories for different FE mesh variations at ϕ = 300 volts

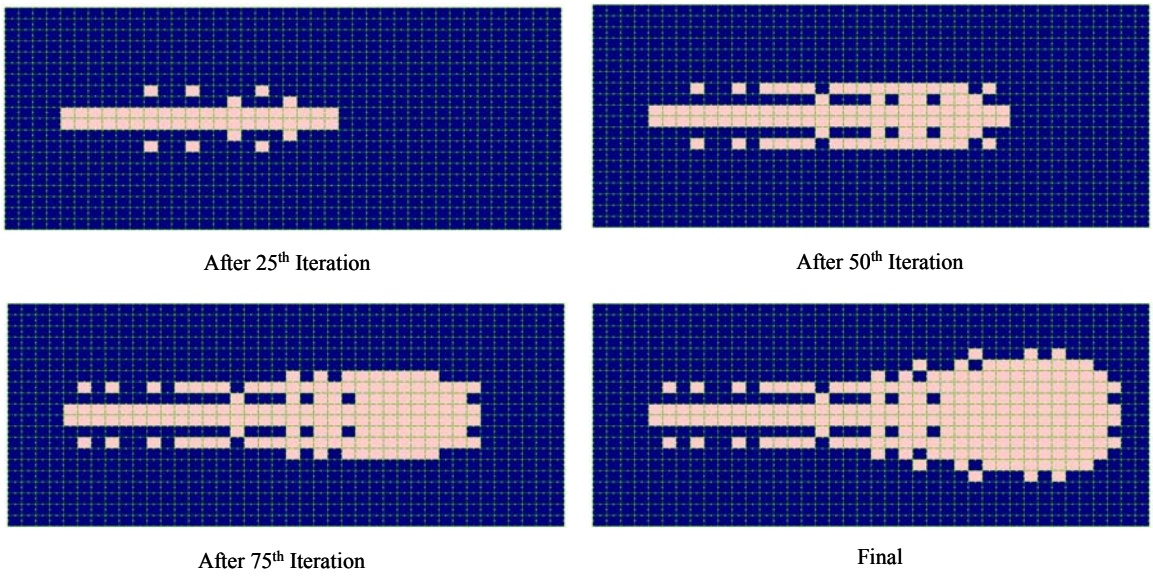

Figure 5.8: Evolution histories of piezoelectric actuator design for 20x40 FE mesh model at ϕ = 300 volts

Table 5.3: Performance with different RMR variations for 10x20 FE mesh model at ϕ=300 volts

RMR	0	0.02499	0.03499	0.04499	0.05499
Initial	$1.91\text{x}10^{-3}$	$1.91\text{x}10^{-3}$	$1.91\text{x}10^{-3}$	$1.91\text{x}10^{-3}$	$1.91\text{x}10^{-3}$
Final	$1.28\text{x}10^{-5}$	$3.17\text{x}10^{-5}$	$9.08\text{x}10^{-6}$	$2.72\text{x}10^{-5}$	$5.96\text{x}10^{-5}$
Error (%)	-99.33	-98.33	-99.52	-98.57	-96.87
Error (%)	-	148.37	-28.86	113.03	366.59
No of iteration	27	13	14	9	4

Third test case investigates the effect of varying RMR on the improvement of error function. As given in Table 5.3, the 10x20 FE mesh model with an applied voltage of ϕ=300 volts was considered for 5 cases of RMR (0.0, 0.02499, 0.03499, 0.04499 and 0.05499). The numbers of element of piezoelectric materials removed are respectively 2, 4, 6, 8 and 10 at each iteration. The 3rd row of Table 5.3 shows the relative errors of the final error functions with respect to their initial values for each case of RMR. It can be seen that they all yield more than 96% improvement in the error function. The 4th row of Table 5.3 shows the relative errors of the final error functions with respect to the final error functions for the case of RMR=0. Amongst all four non-zero RMR cases, only the case of RMR = 0.03499 yields a 29% improvement in error function, 33% reduction in active piezoelectric material usage and about 50% reduction in computational cost. Figure 5.9 shows the convergence histories for the cases with different RMR variations. The effect of RMR variations on the piezoelectric actuator design is also shown in Figure 5.10. The results show that the performance and effectiveness of the optimisation procedure is affected by RMR variation. Therefore, it is important to choose reasonable value of RMR to expedite the optimisation process to converge to the optimal solution that best fits the desired structural shape.

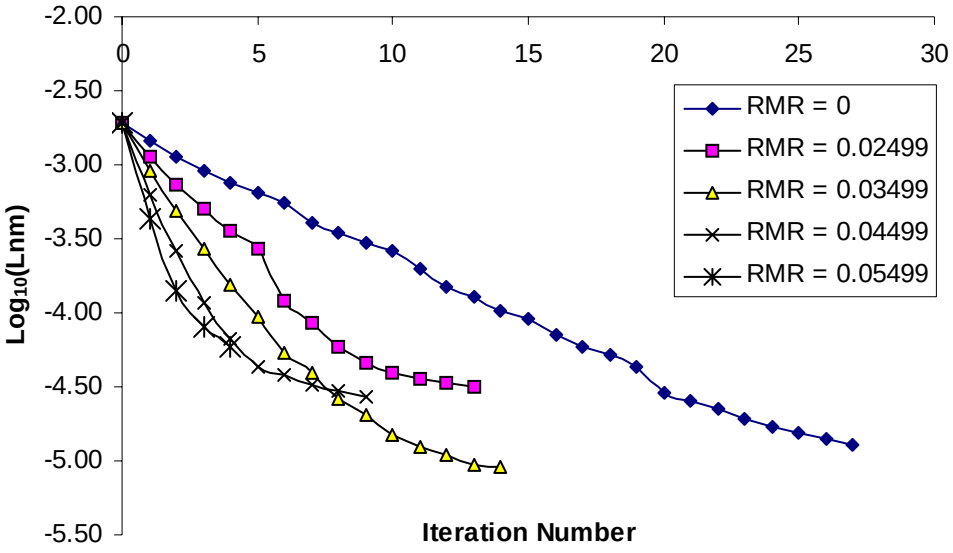

Figure 5.9: Evolution histories for 10x20 FE mesh model with different RMR at ϕ=300 volts.

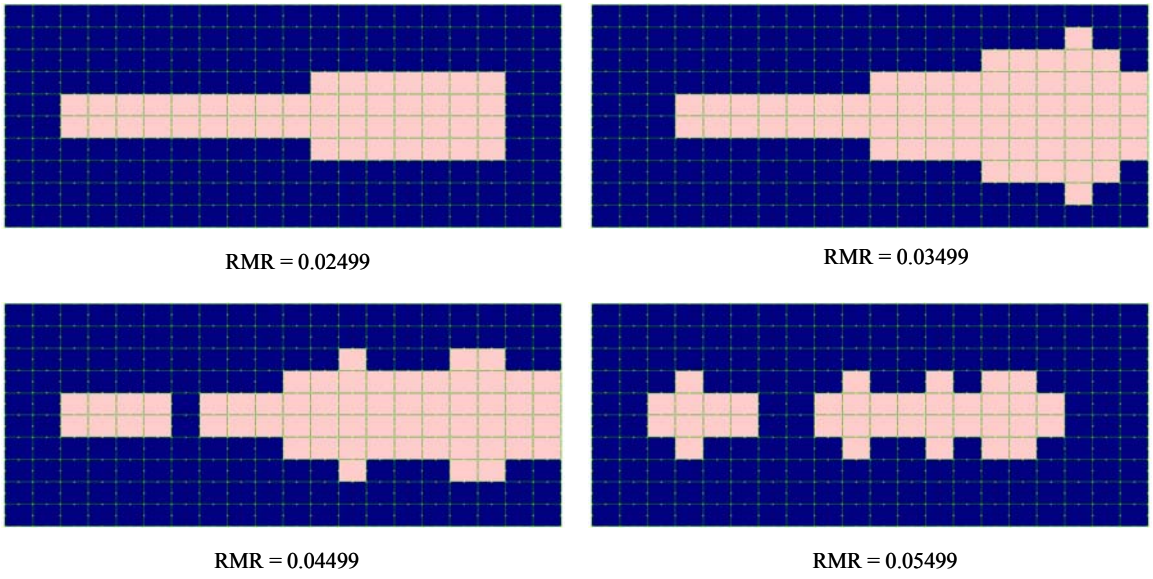

Figure 5.10: Effect of RMR variations on the piezoelectric actuators design for 10x20 FE mesh model at ϕ = 300 volts

The purpose of the fourth test case is to observe the effect of applied voltage on the resulting piezoelectric material distribution and error function by using the 10x20 FE mesh model. Twelve different applied voltages, ranging from 255.24 to 650 volts, are investigated. Figure 5.11 shows the relationship between the error function and applied voltage using the EPADO. As the evolution progresses, it can be seen that the error functions for different applied voltages reduce by approximately 20% to 90%. It is shown that there does not exist a linear relationship between the error function and the applied voltage. Figure 5.11 shows that the lowest error function happens at an applied voltage of 300 volts. Figure 5.12 shows the final piezoelectric actuator design for the four different applied voltage variations, and also depicts the effect of electric field on the results of the piezoelectric actuator design. As the electric field increases, less piezoelectric material is used. The results show that the lowest error function could be obtained when the correct applied voltage is chosen. The results in this example demonstrate that the EPADO algorithm is capable of optimising the piezoelectric actuator distribution for best achieving the desired structural shape with the smallest error function at a given applied voltage.

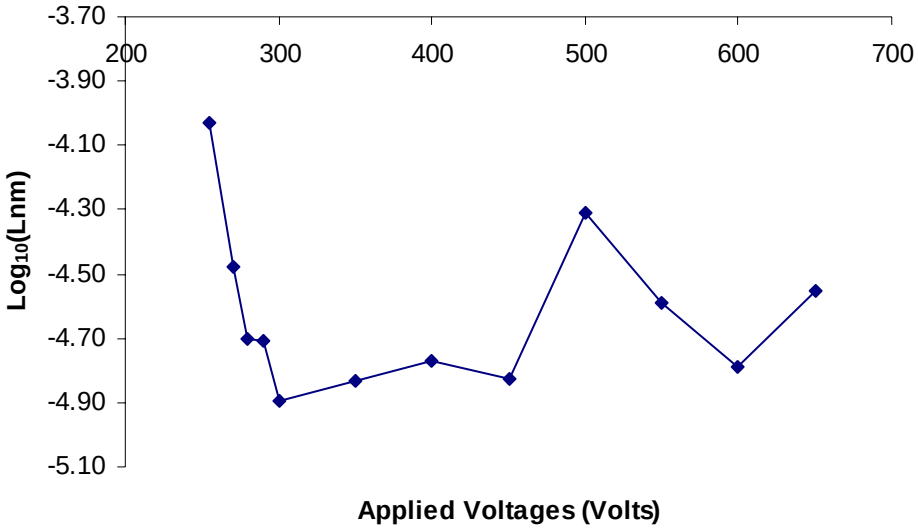

Figure 5.11: Effect of applied voltage variations on the final error function for 10x20 FE mesh model.

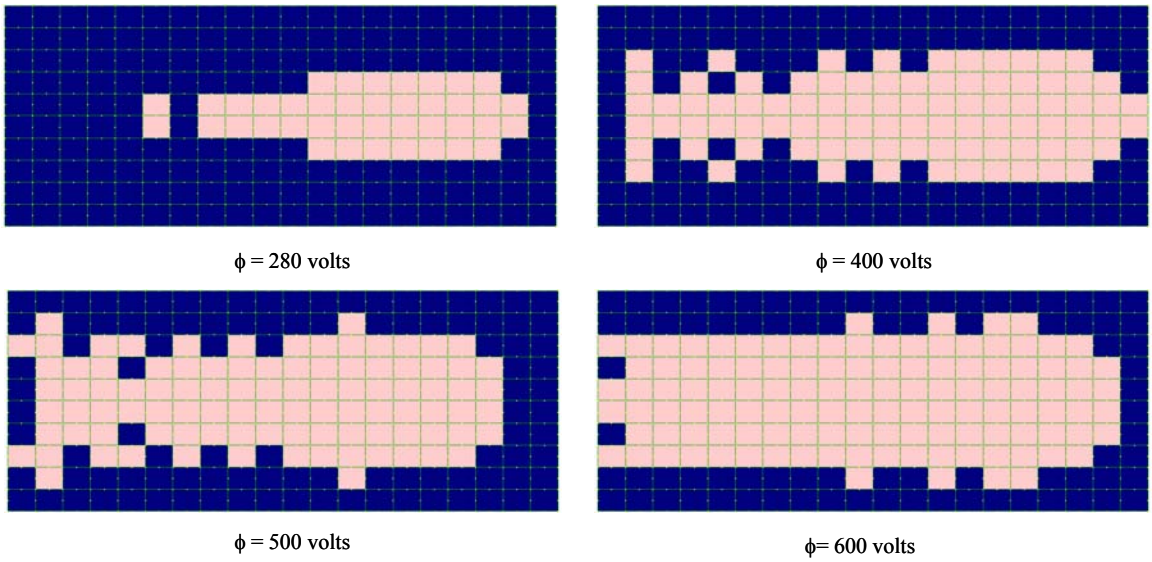

Figure 5.12: Effect of applied voltage variations on the piezoelectric actuators design for 10x20 FE mesh model

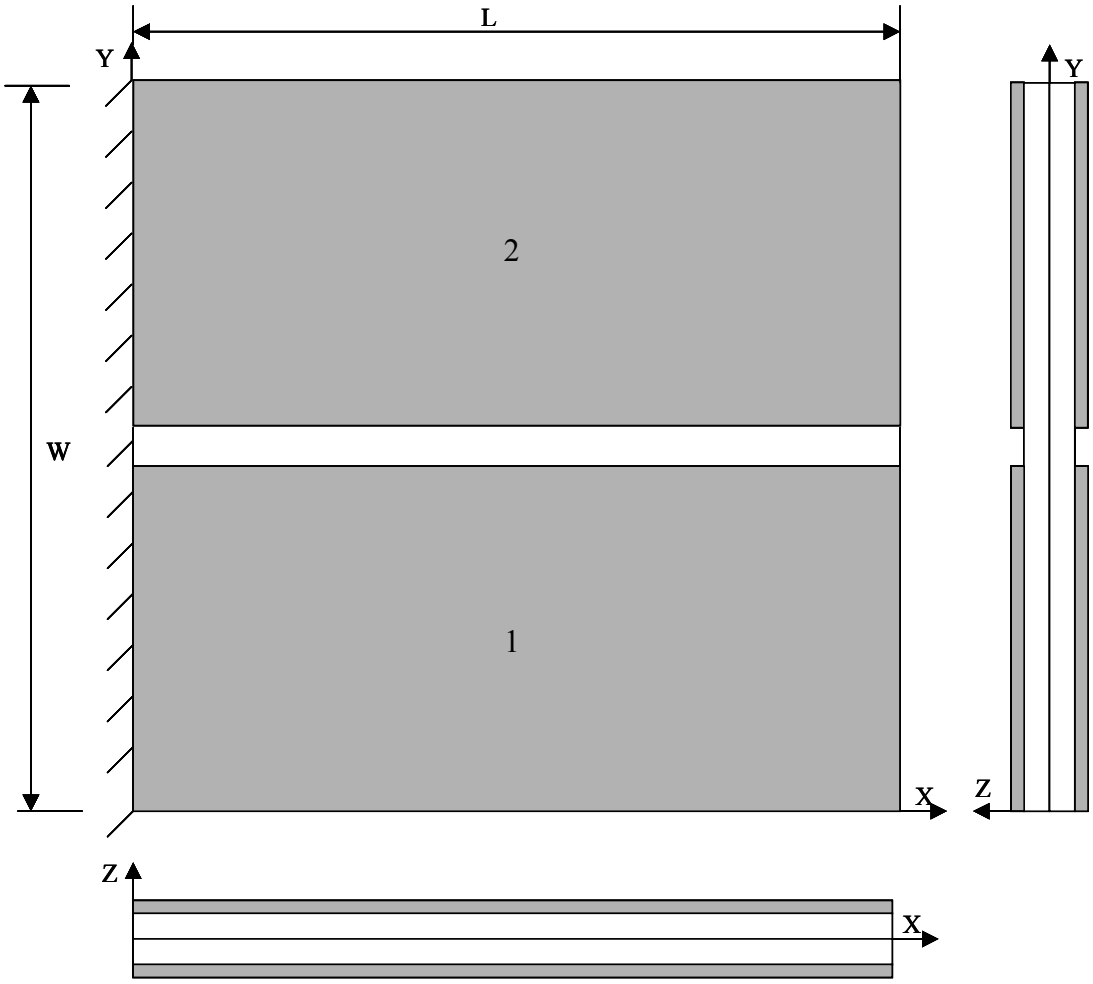

Figure 5.13: Square cantilever plate in XY, YZ and XZ plane

5.6.3 Example 2

This section will examine the performance of shape control in terms of error function using the EPADO algorithm for several desired structural shapes such as bending and twisting. The bending and twisting desired shapes are defined as $w^d(x,y)=10^{-5}\cos(10x-1)$ and $w^d(x,y)=10^{-5}(\cosh(x)-1)*\sin(y)$, respectively. There are two types of twisting structural shapes. One is anti-symmetrical twisting ($0 \le x \le 0.15$ and $0 \le y \le 0.15$). Another is symmetrical twisting ($0 \le x \le 0.15$ and $-0.075 \le y \le 0.075$). A square plate is assumed to have dimensions L=0.15m and W=0.15m. Initially, the active piezoelectric actuators are assumingly distributed over the entire plate. Both top and bottom actuators are subdivided into two separate actuators as shown in Figure 5.13. Only top actuator patches are activated. The lower and upper patches are specified as patch number 1 and 2, respectively. In the EPADO calculation, the parameter RMR is taken as 0.021.

For the bending case, the desired structural shape is shown in Figure 5.14a. The calculated structural shape using LLS – voltage optimisation only, is shown in Figure 5.14b. The applied voltage distribution and error function are $\phi_1=\phi_2=243.24$ volts and $Lnm=5.15x10^{-4}$, respectively. When using EPADO with applied voltages of $\phi_1=\phi_2=243.24$ volts, the optimal solution is obtained after 11 iterations and the minimum value of the error function (Lnm) is $2.09x10^{-4}$. It is shown that the EPADO algorithm yields a remarkable 59% reduction in the minimum value of the error function and a 19% decrease in the volume of active piezoelectric materials compared to the LLS solutions. In addition, for further tests with applied voltages of $\phi_1=\phi_2=300$volts, Figure 5.15 shows the initial and final calculated structural shapes. The initial piezoelectric actuator design is shown in Figure 5.15a and the error function is $3.66x10^{-3}$. The final piezoelectric material distribution, which is the shaded area in Figure 5.15b, was achieved after 25 iterations with a minimal error function of $5.18x10^{-5}$. By comparing this with the LLS results, the error function has been improved by approximately 90% in conjunction with an increase in the electric field in each actuator by about 20%. It should also be noted that the active piezoelectric material usage is 37% less than the LLS method without performing the piezoelectric actuator optimisation

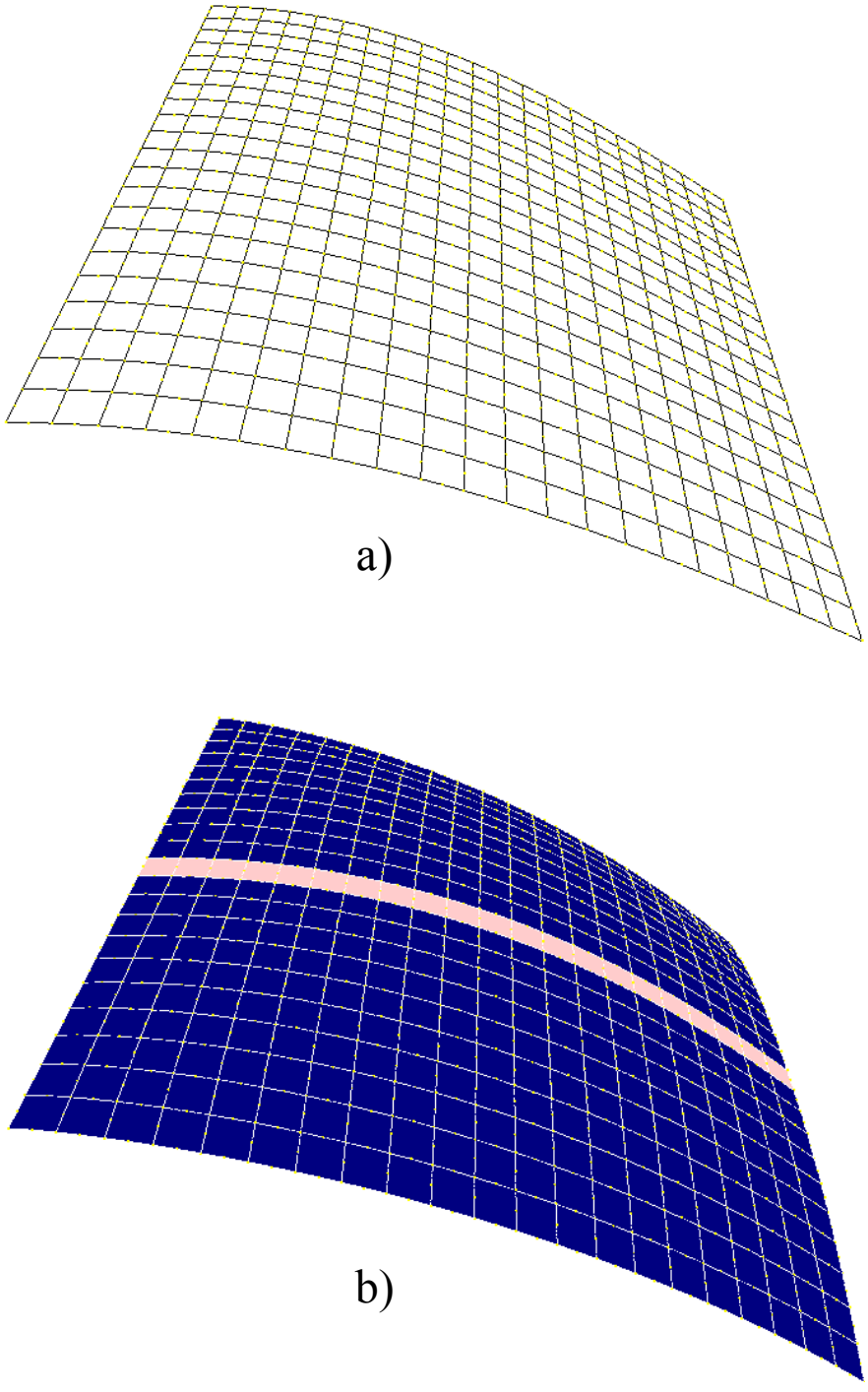

Figure 5.14: Bending case: a) Desired Structural Shape; b) Calculated Structural Shape using LLS Method-Voltage Optimisation Only

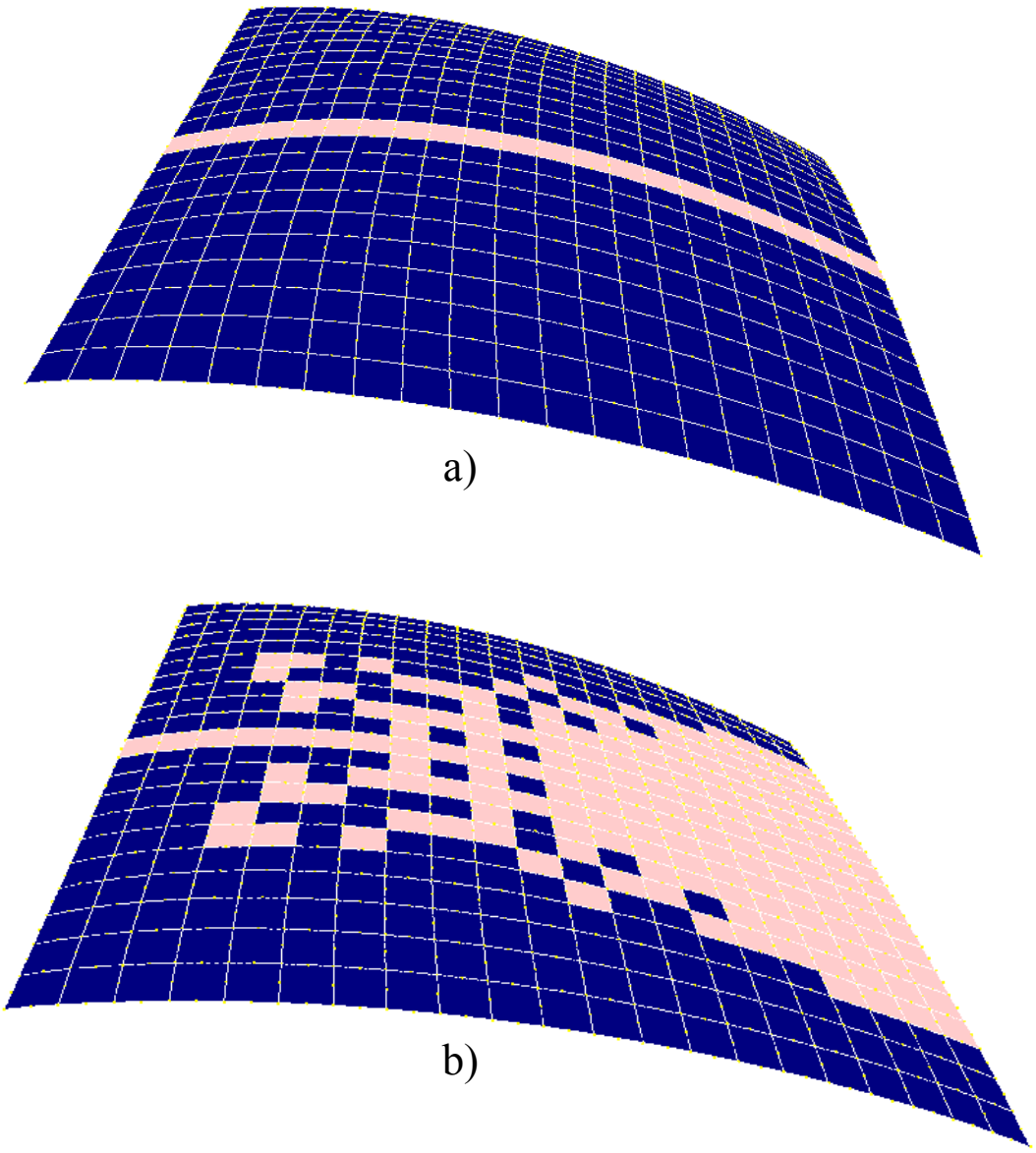

Figure 5.15: Bending Case using EPADO: a) Calculated Structural Shape with Initial Actuators Design; b) Calculated Structural Shape with Final Actuators Design

For the anti-symmetrical twisting test case, the desired structural shape is shown in Figure 5.16a. The calculated structural shape using LLS – voltage optimisation only, is shown in Figure 5.16b. The voltages distribution (ϕ_{LLS}) and error function are ϕ_1=0.71 volts, ϕ_2=-1.13 volts and Lnm=1.53x10^{-3}, respectively. When the considered applied voltages (ϕ_1=0.71 volts, ϕ_2=-1.13 volts), obtained by the LLS method, are used in the EPADO algorithm the optimal solution is obtained after 5 iterations and the minimum value of the error function (Lnm) is 9.37x10^{-4}.

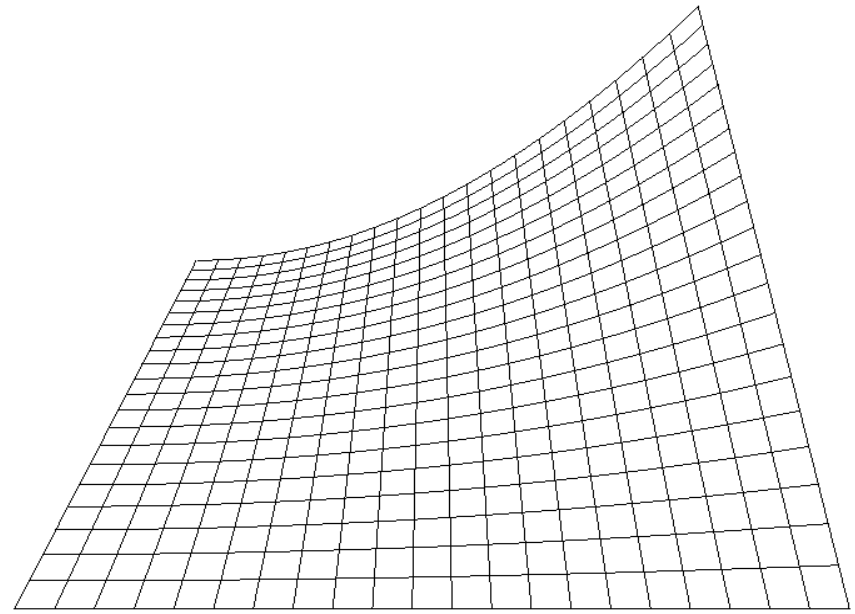

a)

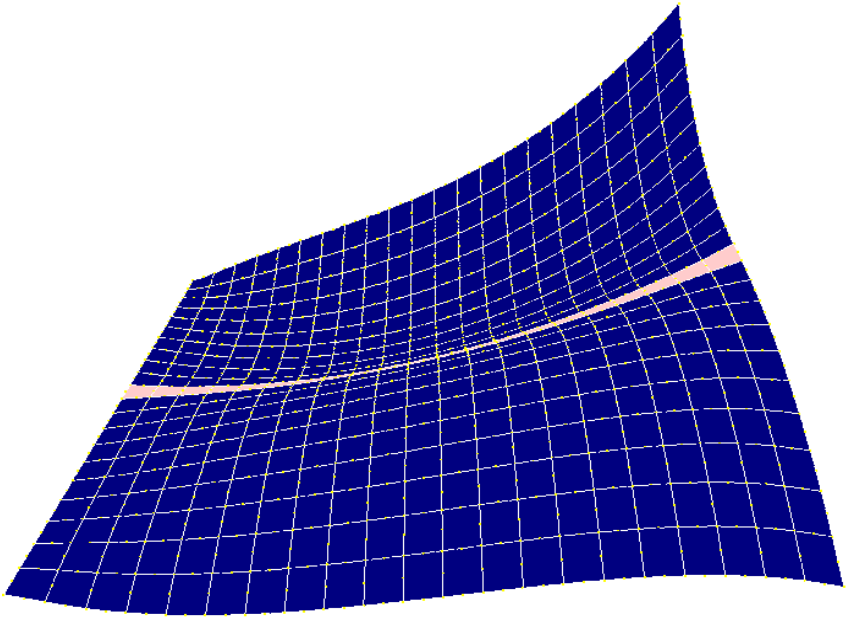

b)

Figure 5.16: Anti-Symmetrical Twisting: a) Desired Structural Shape; b) Calculated Structural Shape using LLS Method-Voltage Optimisation Only

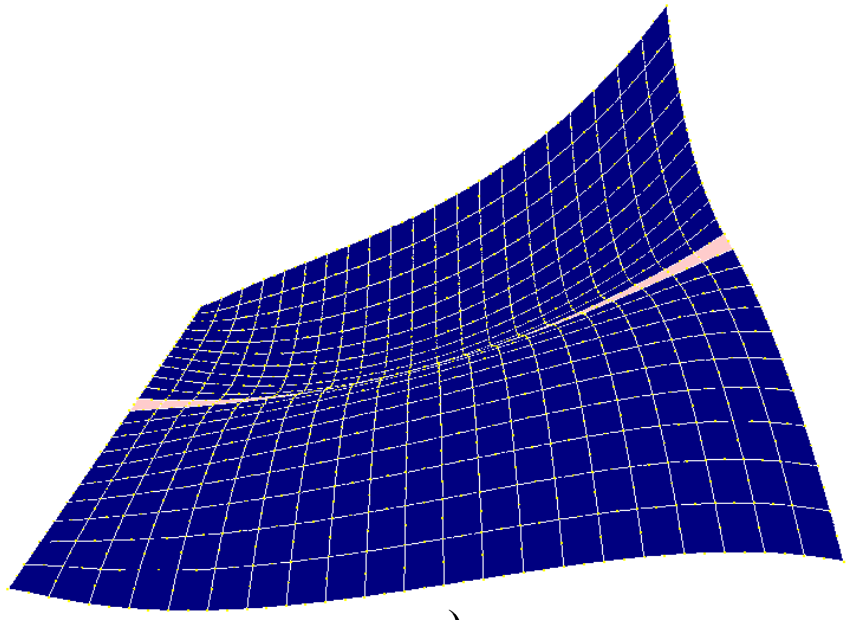

a)

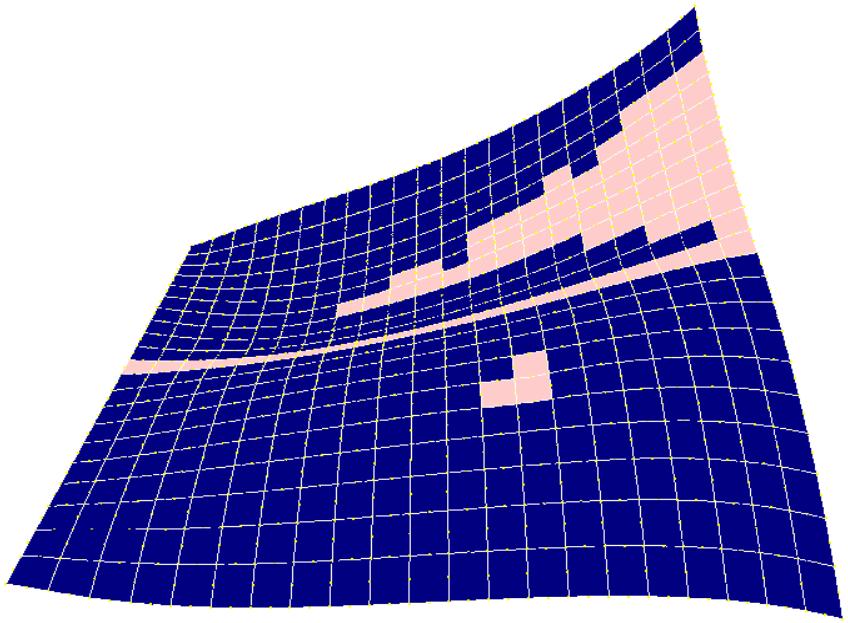

b)

Figure 5.17: Anti-Symmetrical Twisting using EPADO: a) Calculated Structural Shape with Initial Actuators Design; b) Calculated Structural Shape with Final Actuators Design.

The error function predicted the active piezoelectric material volume, required by the EPADO algorithm, is less than that required by the LLS method by about 39% and 10%, respectively for applied voltages. Further investigation in the case of ϕ_1=0.72 volts and ϕ_2=-1.19 volts, where the applied voltages in patch 1 and 2 are increased by about 1.4% and 5.3% with compared to ϕ_{LLS} values, the initial and final calculated structural shapes are shown in Figure 5.17. The initial and final values of the error functions (Lnm) are $1.73x10^{-3}$ and $7.33x10^{-4}$, respectively. The shaded region in Figure 5.17b shows the optimal piezoelectric actuator design. The solution converged after 7 iterations. By comparing this with the LLS results, the error function has been improved by about 52% in conjunction with a decreased active piezoelectric material usage of approximately 13%. In Figure 5.17, it can be observed that the EPADO provides a better calculated structural shape compared to that in Figure 5.16b obtained using the LLS method.

For the symmetrical twisting test case, the desired structural shape is shown in Figure 5.18a. The calculated structural shape using LLS – voltage optimisation only, is shown in Figure 5.18b. The voltage distribution and error function are ϕ_1=0.92, ϕ_2=-0.92 volts and Lnm=$5.71x10^{-3}$, respectively. When the EPADO algorithm is used with the considered applied voltages of ϕ_1=0.92, ϕ_2=-0.92, the optimal solution is reached after 28 iterations and the minimum value of the error function (Lnm) is $6.39x10^{-4}$. The error function predicted by EPADO decreases by about 89% in addition to a reduction in active piezoelectric material usage of about 40%. Figure 5.19 depicts the initial and final calculated structural shapes for applied voltages of ϕ_1=1.10 volts and ϕ_2=-1.10 volts, where the applied voltage in both patches are increased by about 20% compared to ϕ_{LLS}, using the EPADO algorithm. Figure 5.19a shows the initial piezoelectric actuator design with Lnm = $6.18x10^{-3}$. The optimal solution was reached after 32 iterations. The shaded region in Figure 5.19b shows the optimal piezoelectric actuator design. The final error function is $5.06x10^{-4}$, which represents an improvement of about 91% in the error function and a 44% reduction in the active piezoelectric material usage compared to the LLS solution. In particular, Figure 5.19b shows that the piezoelectric material distribution populates around the edges of the host plate except along the tip loci. In other words, a large number of bumps will occur in the middle of the host plate when such a distribution of unused piezoelectric material occurs as shown in Figure 5.19a.

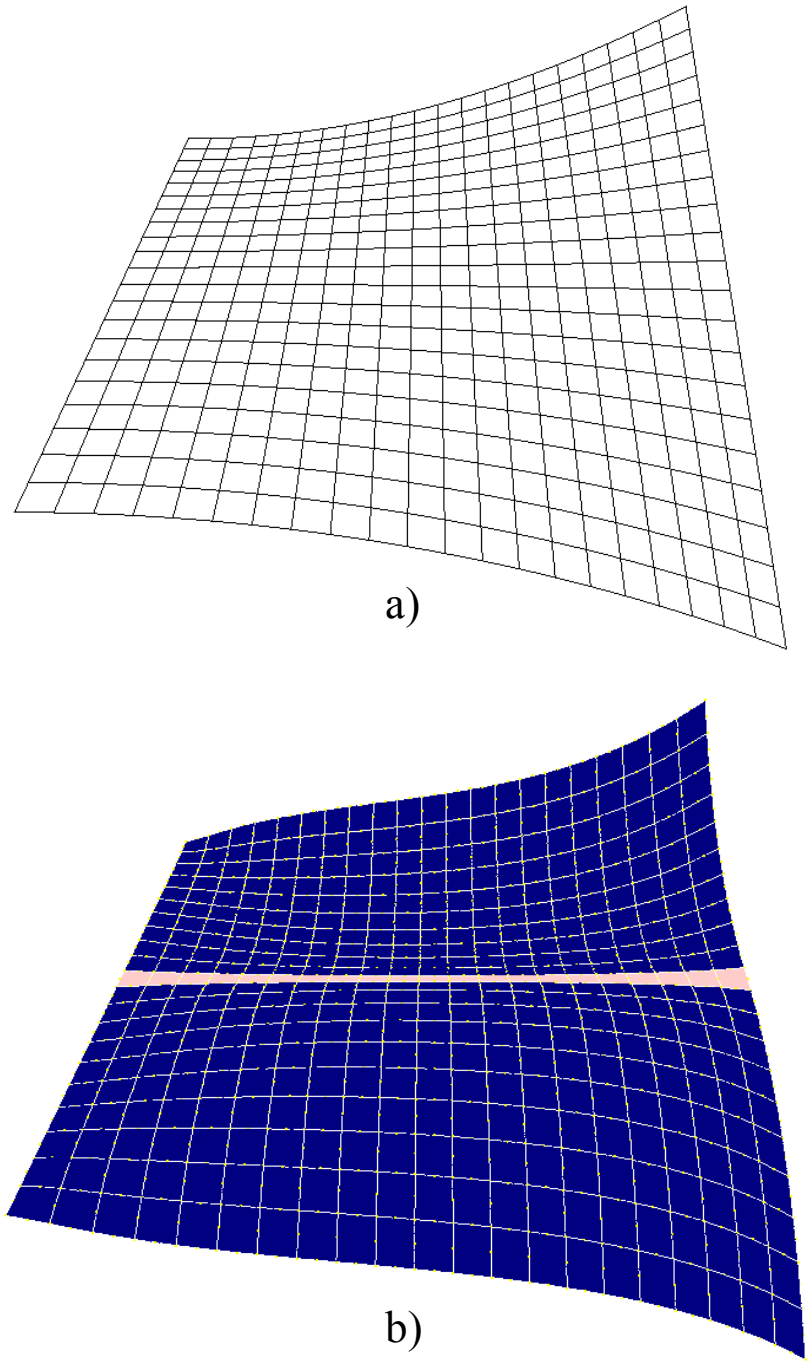

Figure 5.18: Symmetrical Twisting: a) Desired Structural Shape; b) Calculated Structural Shape using LLS Method-Voltage Optimisation Only

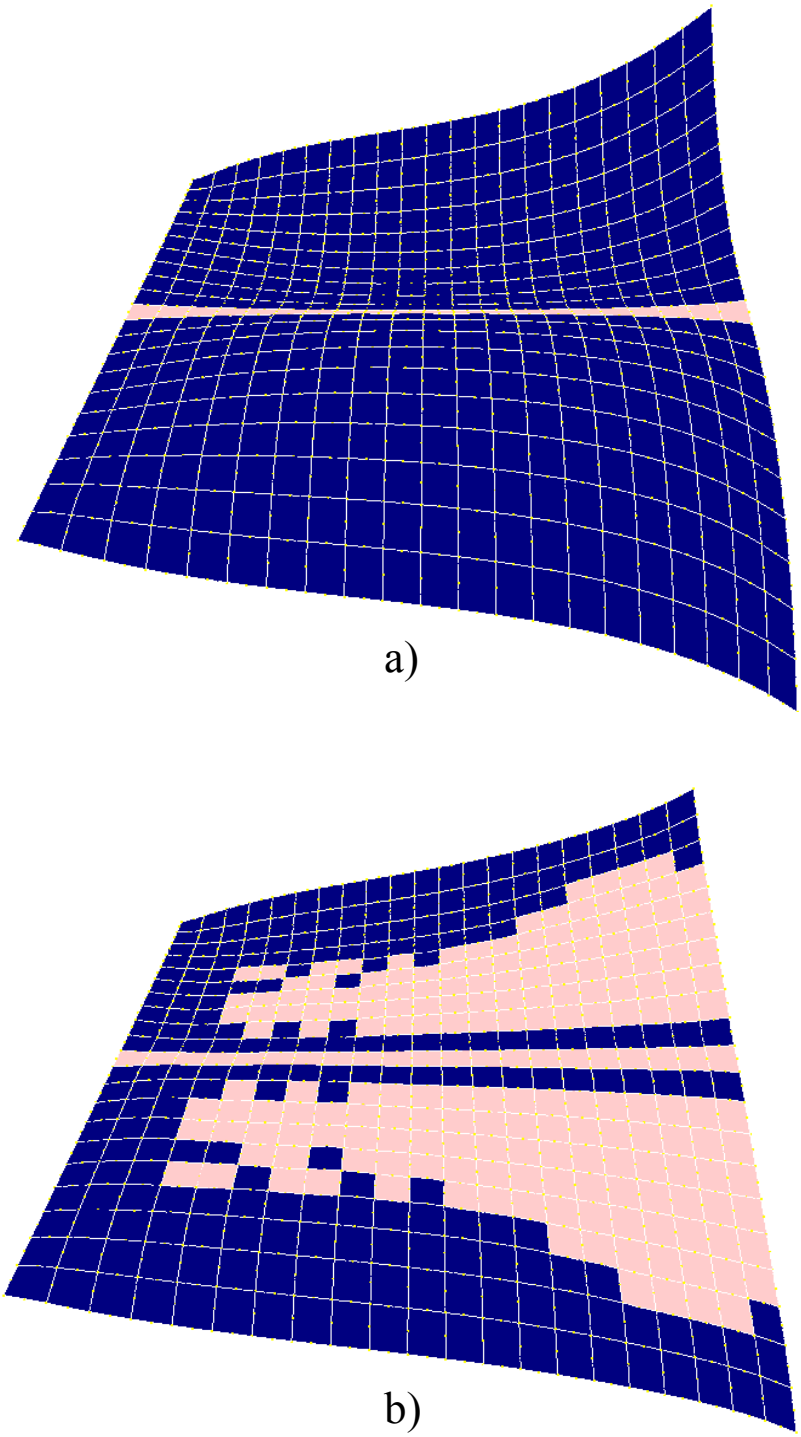

Figure 5.19: Symmetrical Twisting using EPADO: a) Calculated Structural Shape with Initial Actuators Design; b) Calculated Structural Shape with Final Actuators Design

Finally, the results demonstrate that the EPADO algorithm is capable of finding optimal piezoelectric actuator shapes to achieve the desired structural shape, whether it is simple or complex. Bruce et. al (2000) mentioned that more actuators are required if the desired structural shape is more complex. In this section, the twisting case example shows that EPADO can reduce the number of actuators for a complex shape. As Bruce et. al (2000) noticed actuators must be subdivided into several pieces (more than two) to reduce the waves in the resultant structural shape using the LLS method for the twisting case above. In engineering design applications, it can be difficult to apply a voltage from multiple power sources due to non-uniform voltage distributions when there are many actuators.

5.7 Summary

For the shape control problem of minimising the error function between the actuated and desired structural shapes of smart structures, an evolutionary piezoelectric actuator design optimisation (EPADO) algorithm at a given applied voltage has been developed. Based on a sensitivity analysis with respect to discrete piezoelectric material layer, an error function sensitivity number is presented to estimate the effect of the piezoelectric material layer distribution on the error function. The approach of this algorithm is to gradually remove the active piezoelectric material layer in elements to optimise the piezoelectric actuator shape by minimising of the error function. Illustrative examples are presented and discussed. It is clear that the error functions obtained by the proposed algorithm have been improved compared to the results obtained by the LLS (voltage optimisation only). In other words, the lowest error function can be achieved in combination with reduced piezoelectric material usage. The removal material rate (RMR) and finite element mesh are found to be effective in influencing the error function and computational cost. The shape of the piezoelectric actuator can be refined when finer finite element meshes are considered. Finally, EPADO is capable of solving for a variety of desired structural shapes from simple (bending) cases to complex (either anti-symmetrical twisting or symmetrical twisting) cases with less number of actuator patches than the LLS methods.

6. Voltage and Evolutionary Piezoelectric Actuator Design Optimisation for Static Shape Control of Smart Plate Structures

A design of piezoelectric actuator and applied voltage with an optimal error function is a greater practical significance in structural shape control application. Following Chapter 5, this chapter further extends the piezoelectric actuator design based on the Evolutionary Piezoelectric Actuator Design Optimisation (EPADO) procedure to multi-criteria design problems, which consist of voltage and piezoelectric actuator criteria designs, whereas the optimum value for the applied voltage to actuator can be determined using the Linear Least Square (LLS) method. The criterion identifies the overall effects of the error function on these two components of design criteria due to removing active piezoelectric materials. Two algorithms are proposed. One is the Alternative Voltage and Evolutionary Piezoelectric Actuator Design Optimisation (AVEPADO). Another is Voltage and Evolutionary Piezoelectric Actuator Design Optimisation (VEPADO). Both algorithms aim to simultaneously optimise the active piezoelectric actuator configuration and the applied voltages. Numerical results are presented to show that the proposed algorithms are capable to determine both voltage distribution and piezoelectric actuators configuration in structural shape control problems.

6.1 Introduction

In Chapter 5, Evolutionary Piezoelectric Actuator Design Optimisation (EPADO), has been developed to optimise the active piezoelectric actuators shape at given applied voltages. The criterion is used to determine the distribution of active piezoelectric actuator to achieve the desired structural shapes, subjected to removing of the active piezoelectric material part of the element based on the error function sensitivity number. The error function sensitivity number was derived to include the electro-mechanical effect, in which the third order displacement field had been used for mechanical

deformation and a linear layer-wise formulation had been used to model electrical field. The optimisation procedure was based on the features of evolutionary strategies, which were proposed by Xie and Steven (1997). The numerical examples were also presented to validate the EPADO. The results have shown that the EPADO is capable of being used in the application of static shape control problems. The investigations of the effect of applied voltage variations on the error function were discussed and have generated the results that the lowest error function could be obtained when the optimal value of an applied voltage is known. Therefore, this chapter further extends the piezoelectric actuator design based on the EPADO procedure to multi-criteria design problems, which consist of voltage and piezoelectric actuator criteria designs. Two algorithms are developed here based on the same concepts, which have been proposed in Chapter 3, for voltage and piezoelectric actuator design optimisation. One is the Alternative Voltage and Evolutionary Piezoelectric Actuator Design Optimisation (AVEPADO) and the other is referred to as Voltage and Evolutionary Piezoelectric Actuator Design Optimisation (VEPADO). Both algorithms optimise the active piezoelectric actuator shape and applied voltages simultaneously by employing the Linear Least Square (LLS) technique and EPADO. Numerical results are presented to illustrate the capabilities of the proposed algorithms to determine the voltage and piezoelectric actuator distribution in the application of shape control problem, in terms of the improvement of error function and the efficiency of piezoelectric material usage. In addition, they are also used to compare the performance between AVEPADO and VEPADO algorithms.

6.2 Model Description

Consider a cantilever plate, which is clamped at its left edge and subjected to a non-applied mechanical load. The plate has a length of L; width of W and consists of two layers of 0.01m thickness each. The piezoelectric actuators are attached to the top and bottom surfaces of the plate, which have a thickness of 0.001m each. Only the top piezoelectric actuator patches are applied with electric voltage, which are chosen as a design domain where the piezoelectric material can be removed as shown in Figure 6.1. The plate material has the following stiffness constants: $c_{11}=c_{22}=c_{33}=92.9$GPa, $c_{12}=c_{13}=c_{23}=39.8$GPa, $c_{44}=c_{55}=c_{66}=26.5$GPa. The patch properties are:

$c_{11}=c_{22}=c_{33}=113.0$GPa, $c_{12}=c_{13}=c_{23}=55.5$GPa, $c_{44}=c_{55}=c_{66}=28.6$GPa; the $\chi_{11}=\chi_{22}=15.3\text{x}10^{-9}$F/M, $\chi_{33}=15.0\text{x}10^{-9}$F/M and $d_{31}=-254$pm/V, $d_{32}=-254$pm/V, $d_{33}=374$pm/V, $d_{24}=584$pm/V, $d_{15}=584$pm/V. The above properties were used in all examples in this chapter.

Figure 6.1: Cantilever plate in XY and XZ plane

6.3 Alternative Voltage and Evolutionary Piezoelectric Actuator Design Optimisation (AVEPADO)

In this section, EPADO has been developed further, including voltage optimisation. The new algorithm is called Alternative Voltage and Evolutionary Piezoelectric Actuator Design Optimisation (AVEPADO) based on the CAA concept in Chapter 3. In this algorithm, the active piezoelectric actuator configuration and the applied voltage are optimised alternatively, where voltage distribution is obtained via the LLS method. The AVEPADO procedure can be separated in two stages for each iterative loop. In the p^{th} iterative loop, the first stage uses the LLS method to determine the optimal voltage distribution (ϕ^p) to attain the desired structural shape at a given piezoelectric actuator configuration; then at stage 2, the optimal voltage distribution (ϕ^p),

which was previously calculated from the first stage, is used to search for the piezoelectric configuration to minimise the error function by using the EPADO algorithm. The piezoelectric actuator configuration at the end of the second stage is used in the first stage of $(p+1)^{th}$ iterative loop to seek the voltage configuration and so on. At the end of each iterative loop, a convergence condition defined in terms of the objective error function is checked as shown in Figure 6.2. Such iteration process continues until the selected convergence criterion is satisfied.

6.3.1 Algorithm Procedures

The iterative algorithm procedure of AVEPADO is given below. And the flowchart for the AVEPADO process is shown in Figure 6.2.

Step 1: Obtain input parameter RMR.

Step 2: Define the initial active piezoelectric actuator configuration using a dense Finite Element (FE) mesh.

Step 3: Perform LLS to find the voltage distribution ϕ and calculate the error function Lnm^b.

Step 4: Initialise the value of the error function by making $Lnm^c = Lnm^b$ for EPADO

Step 5: Perform FEA to calculate the nodal transverse displacement of the structure and find out gradient vector ∇h of the objective displacement function.

Step 6: Introduce a virtual system.

Step 7: Perform FEA for the virtual system to obtain virtual nodal transverse displacement

Step 8: Compute the error function sensitivity number ΔLnm for all elements.

Step 9: Remove active piezoelectric material part for elements that have the lowest value of ΔLnm.

Step 10: Compute the error function Lnm^d.

Step 11: Perform error function checks, which are calculated before (Lnm^c) and after (Lnm^d) removing the piezoelectric material part of an element. If ($Lnm^d < Lnm^c$) then update the active piezoelectric actuator configuration

and the error function by making $Lnm^c = Lnm^d$ and return to step 5 to continue the optimisation process. Otherwise proceed to step 12.

Step 12: Perform LLS to find the voltage distribution ϕ and compute the error function Lnm^a for the current active piezoelectric actuator configuration.

Step 13: Perform error function checks again. If ($Lnm^a < Lnm^c$) then update the error function by making $Lnm^b = Lnm^a$ and return to step 4 to continue optimisation process. Otherwise proceed to step 14.

Step 14: Terminate the optimisation process. The current results are considered as an optimal solution.

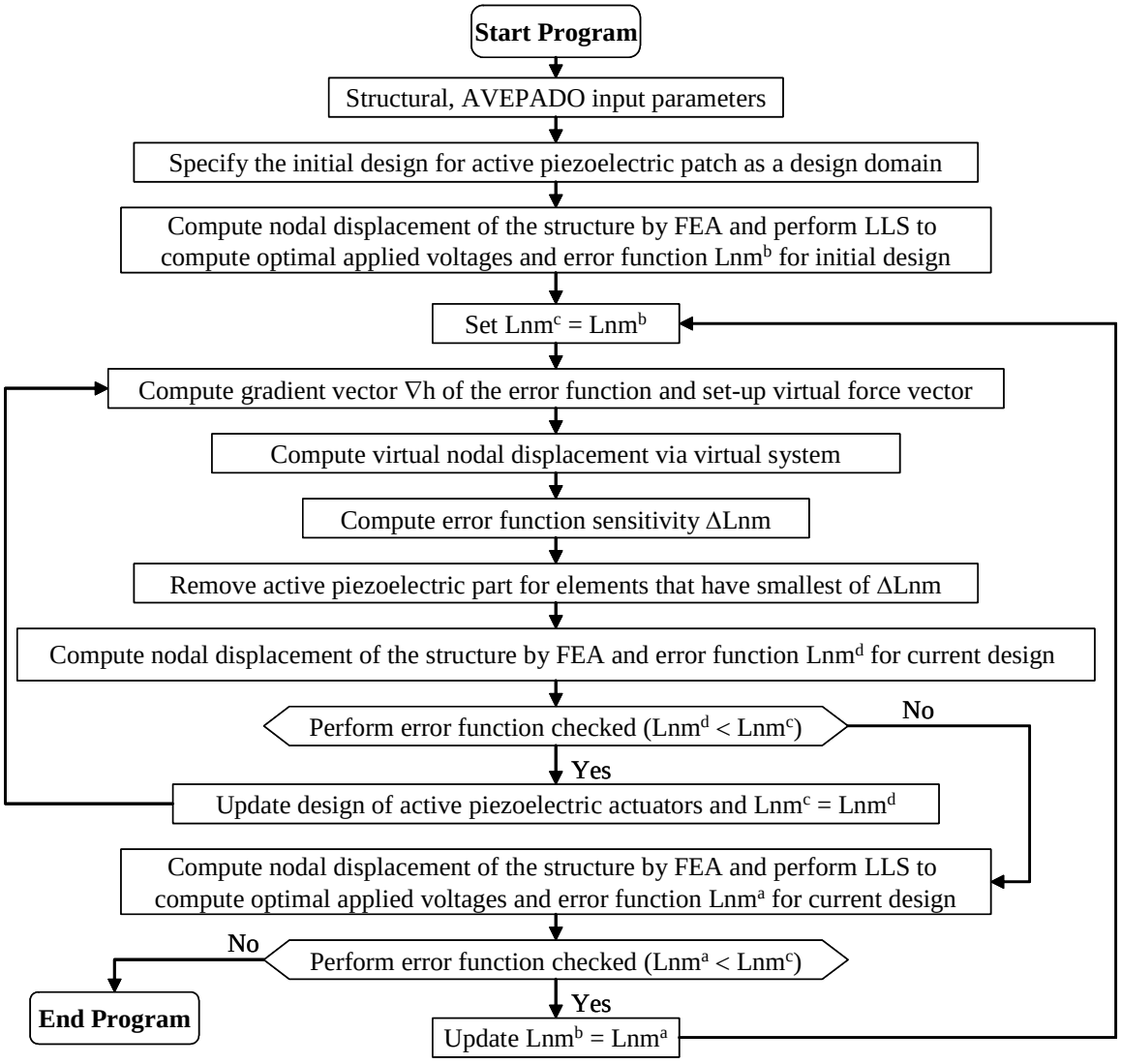

Figure 6.2: Flowchart for AVEPADO algorithm.

6.3.2 Numerical Examples

Numerical examples are presented to demonstrate the features of the AVEPADO algorithm based on the proposed evolutionary criterion of error function sensitivity number including the electro-mechanical effect for shape control problems of smart plates. The results are then compared with results obtained from the LLS method to show the improvement in achieving the desired structural shape by reducing the error function. The following test cases will examine the performance of shape control in terms of the error function using AVEPADO algorithm, where the active piezoelectric actuator configuration and voltage distribution are alternatively optimised to achieve the best-fit of a desired structural shape. A plate has dimensions of L=0.15m and W=0.06m. Initially, the active piezoelectric actuator was assumed to be distributed over the entire host plate as shown in Figure 6.1. In this section, only the bending structural shape will be tested for all test cases. The bending desired structural shape is defined as $w^d(x,y)=10^{-5}\cos(10x-1)$. The structure is sub-divided into 10x20 FE mesh.

The first test case considers RMR=0. The convergence history is shown in Figure 6.3. In Figure 6.4, the shaded areas show the evolution of piezoelectric actuator design using the AVEPADO algorithm. It depicts that the optimal solution can be attained after 5 loops, where each loop consists of voltage optimisation and evolutionary piezoelectric actuator design optimisation. For example, in Loop 1, the LLS method is used to find the optimal voltage distribution (ϕ^1_{LLS}=255.24 volts) for initial piezoelectric actuator design (Figure 6.1). ϕ_{LLS} is then used as an applied voltage ($\phi^1=\phi^1_{LLS}$) to minimise the active piezoelectric actuator configuration using EPADO, where the solution is converged after 3 iterations. The LLS method now is re-performed to compute the voltage distribution (ϕ^2_{LLS}=258.30 volts) for the current piezoelectric actuator design (shown in Figure 6.4a) at stage 1 in Loop 2. The ϕ^2_{LLS} and piezoelectric actuator design (as shown in Figure 6.4a) are respectively used as the applied voltage and the initial actuator design for optimisation process at stage 2 in Loop 2. The process repeats until the selected convergence condition is met. In this particular example, there are total of 11 iterations for the evolutionary piezoelectric actuator design optimisation and 5 calculations for the voltage optimisation in 5 loops of the AVEPADO algorithm. The optimal applied voltage and the error function (Lnm) obtained by the AVEAPDO algorithm are 266.06 volts and $3.99\text{x}10^{-5}$, respectively. The final error function reduces by 65% (from

$1.14x10^{-4}$ to $3.99x10^{-5}$) compared with about 11% reduction in the active piezoelectric material usage compared with the results obtained by LLS method. The final actuator configuration is shown in Figure 6.4d.

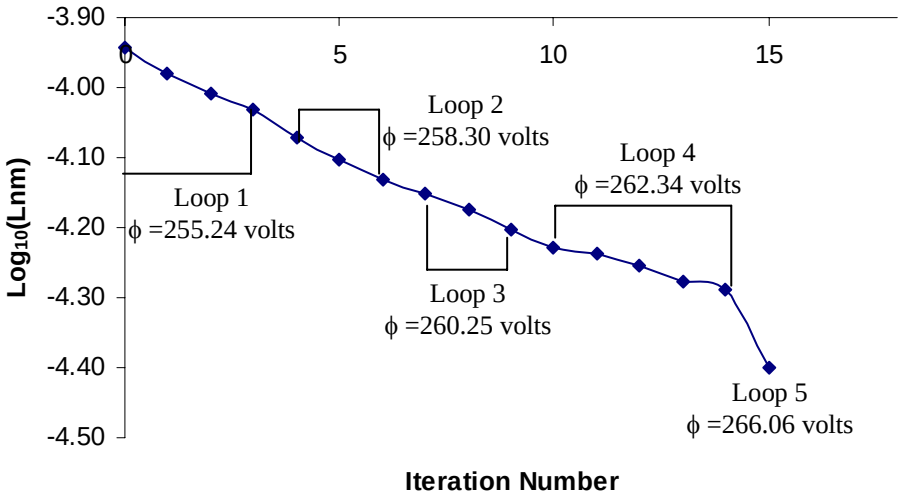

Figure 6.3: Convergence history for 10x20 FE mesh model using AVEPADO.

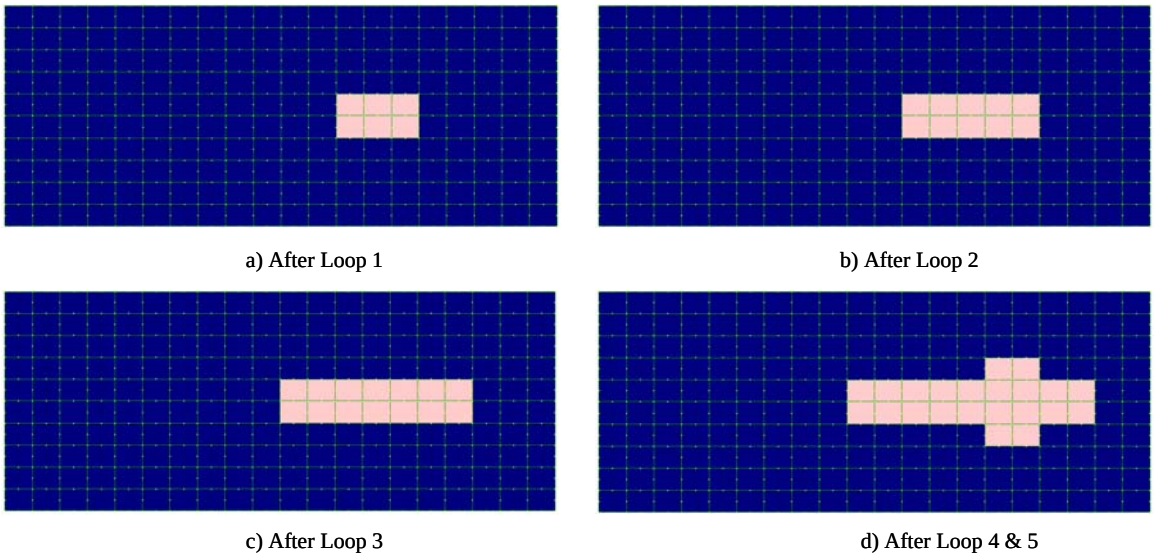

Figure 6.4: Evolutionary histories of piezoelectric actuator design using AVEPADO algorithm

The second test case investigates the effect of varying RMR on the improvement of error function using the AVEPADO algorithm. Five cases of RMR (0.0, 0.02499, 0.03499, 0.04499 and 0.05499) are considered. The number of elements of piezoelectric materials removed is respectively 2, 4, 6, 8 and 10 at each iteration. The results are given in Table 6.1 and there is no solution for case of RMR=0.05499. The 3rd row of Table 6.1 shows the relative error of the final error functions with respect to their initial values for each case of RMR. It can be seen that they all yield more than 50% improvement in the error function. The 4th row of Table 6.1 shows the relative error of the final error functions with respect to the final error function for the case of RMR=0. Amongst all four non-zero RMR cases, only the case of RMR = 0.04499 yields a 9.57% improvement in error function, 9% in reduction in active piezoelectric material usage and 2 loops with 8 iterations less in computational cost and not much change in the optimal applied voltage. The effect of RMR variations on the piezoelectric actuator design is also shown in Figure 6.5. The results show that the performance and effectiveness of optimisation is affected by RMR variations. Therefore, it is important to choose a reasonable value of RMR to expedite the optimisation process to attain the optimal solution that best fits to the desired structural shape when using AVEPADO. This work does not show how to find the reasonable value of RMR. More examples need to be carried out to find the relationship between RMR and FE mesh.

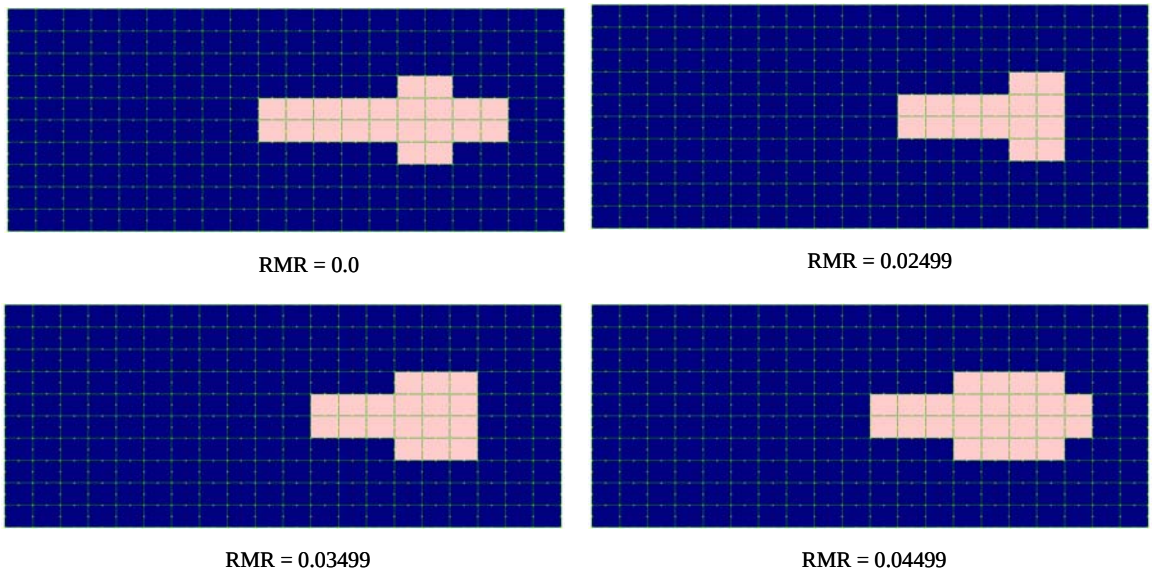

Figure 6.5: Effect of RMR variations on the piezoelectric actuators design using AVEPADO algorithm.

Table 6.1: Performance using AVEPADO for 10x20 FE mesh model

RMR	0	0.02499	0.03499	0.04499
Initial	$1.14x10^{-4}$	$1.14x10^{-4}$	$1.14x10^{-4}$	$1.14x10^{-4}$
Final	$3.99x10^{-5}$	$5.50x10^{-5}$	$4.93x10^{-5}$	$3.61x10^{-5}$
Error (%)	-65.08	-51.86	-56.84	-68.42
Error (%)	-	37.84	23.60	-9.57
No of iteration	11	4	3	3
No of Loop	5	2	2	3
Final Voltage	266.06	261.39	262.17	265.16

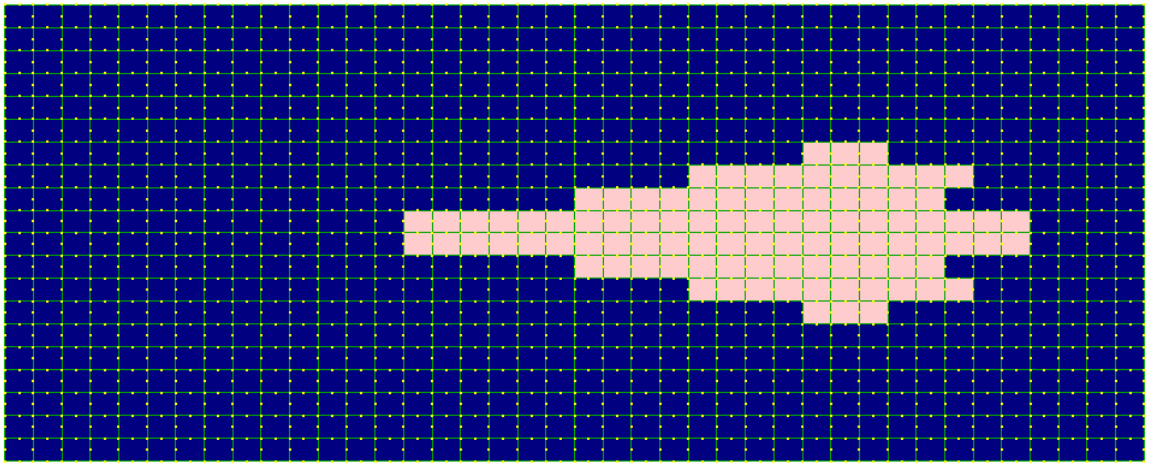

Figure 6.6: Final piezoelectric actuator design for 20x40 FE mesh model using AVEPADO algorithm

As shown in Figure 6.6, the shaded area is the final piezoelectric actuator configuration when considering the finest FE mesh (20x40) with RMR=0. The convergence history is shown in Figure 6.7. The optimal solution converges after 7 loops. There were a total of 54 iterations in EPADO process. The optimal applied voltage and the error function are 269.11volts and $3.22x10^{-5}$, respectively. The achieved minimum error function reduces about 71% and a 12% reduction in active piezoelectric actuator martial usage compared to the LLS solution. The test results show that the optimised shapes of piezoelectric actuators have a smooth boundary and an optimal error function when the finest mesh is considered.

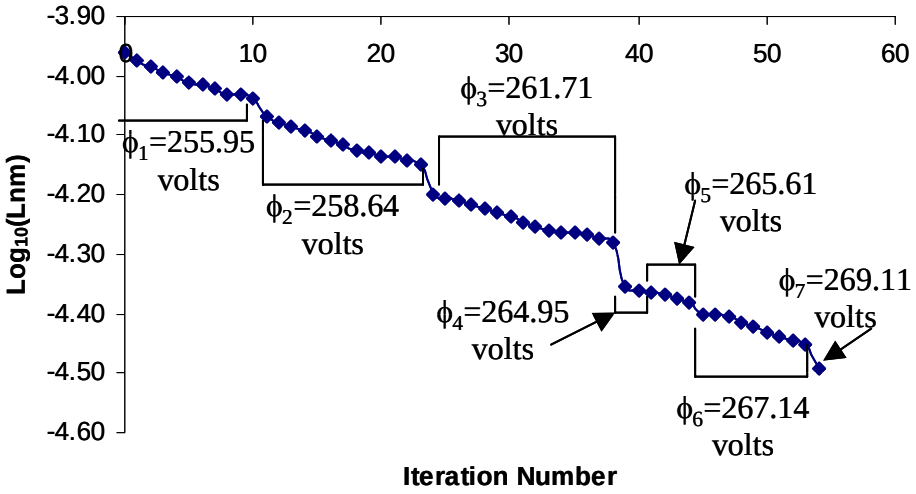

Figure 6.7: Convergence history for 20x40 FE mesh model using AVEPADO

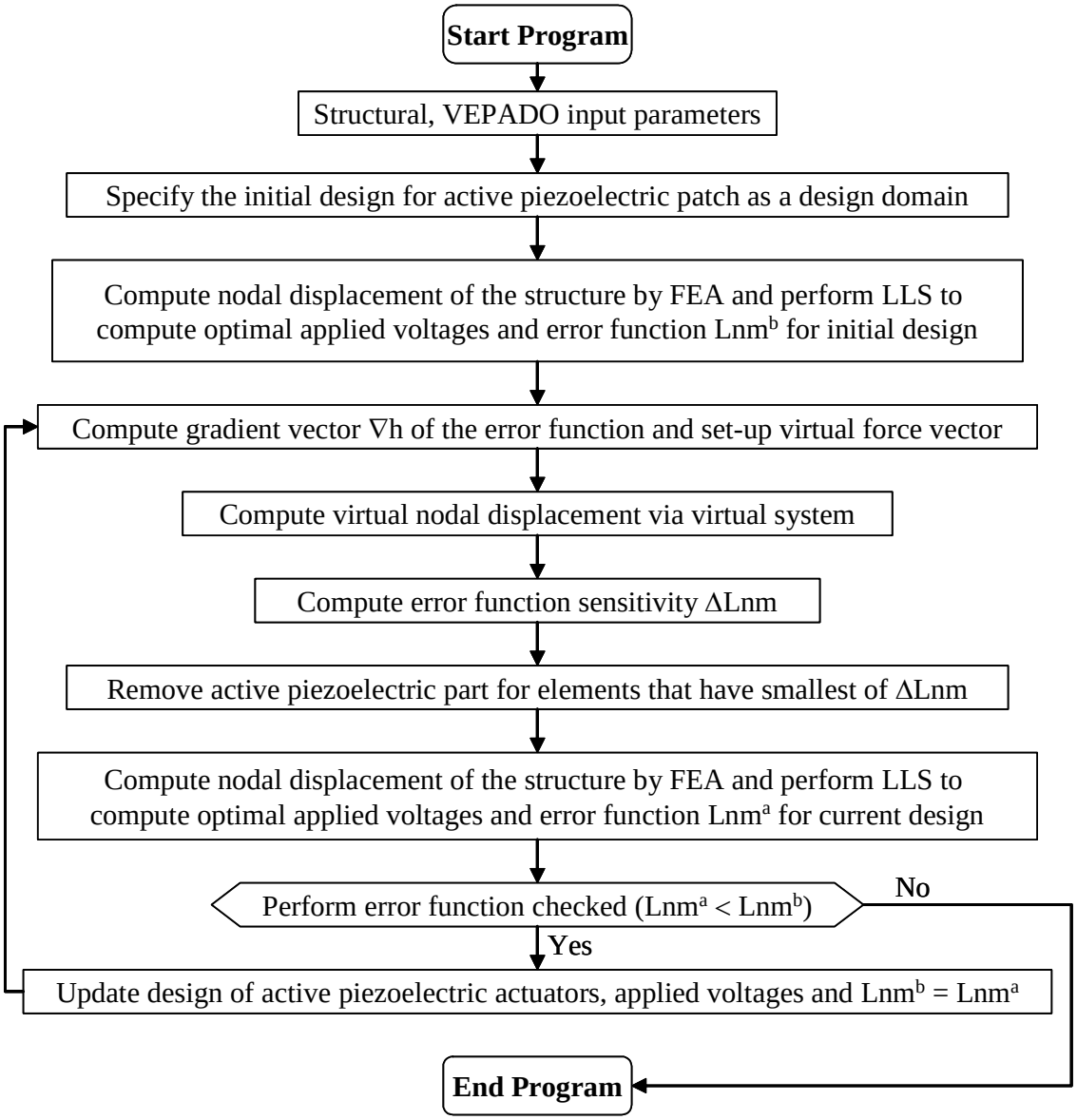

Figure 6.8: Flowchart for VEPADO algorithm

6.4 Voltage and Evolutionary Piezoelectric Actuator Design Optimisation (VEPADO)

In VEPADO algorithm, the active piezoelectric actuator configuration and the applied voltages are optimised simultaneously based on the coupled LLS method and EPADO algorithm. Unlike AVEPADO algorithm, the LLS method is mapped into the EPADO algorithm. The VEPADO algorithm has the same procedure as the EPADO algorithm except that there is an additional step in which the LLS method determines the optimal applied voltage for the current piezoelectric actuator configuration to compute the error function sensitivity number for each element due to removing the active piezoelectric actuator part. In other words, the applied voltage to the piezoelectric actuator is updated after each EPADO iteration. At the end of each iteration, a convergence condition defined in terms of the objective error function is checked, as shown in Figure 6.8, such that the iteration process continues until the selected convergence criterion is satisfied.

6.4.1 Algorithm Procedures

The flowchart for VEPADO process is shown in Figure 6.8. The evolutionary iteration procedure of VEPADO is given below:

Step 1: Obtain input parameter RMR.

Step 2: Define the initial active piezoelectric actuator configuration using a dense Finite Element (FE) mesh.

Step 3: Perform LLS to find the voltage distribution ϕ and calculate the error function Lnm^b.

Step 4: Perform FEA to calculate the nodal transverse displacement of the structure and find out the gradient vector ∇h of the objective displacement function.

Step 5: Introduce a virtual system.

Step 6: Perform FEA for the virtual system to obtain virtual nodal transverse displacement

Step 7: Compute the error function sensitivity number ΔLnm for all elements.

Step 8: Remove active piezoelectric material part for elements that have lowest value of ΔLnm.

Step 9: Re-perform LLS to find the voltage distribution ϕ and calculate the error function Lnm^a for the new piezoelectric actuator configuration.

Step 10: Perform error function checks, which are calculated before (Lnm^b) and after (Lnm^a) removing the piezoelectric material part of an element. If (Lnm^a<Lnm^b) then update the active piezoelectric actuator configuration, the voltage distribution, the error function by making Lnm^b = Lnm^a and return to step 4 to continue optimisation process. Otherwise proceed to step 11.

Step 11: Terminate the optimisation process. The result of the last iteration is considered as an optimal solution.

6.4.2 Numerical Examples

This section will examine the performance of structural shape control in terms of the error function using VEPADO algorithm, where the active piezoelectric actuator configuration and the voltage distribution are optimised simultaneously. The results are then compared with the results obtained by the LLS method to show the improvement in achieving the desired structural shape by reducing the error function. This section re-examines with the same number of test cases together with all the same information as described in Section 6.3.

The first test case considers RMR=0 and 10x20 FE mesh model. The convergence history is shown in Figure 6.9. Figure 6.10 shows the evolution of piezoelectric actuator design using VEPADO algorithm. The optimal solution converges after 18 iterations. The optimal applied voltage and the error function is 278.53volts and 2.13×10^{-5}, respectively. The final error function reduces 81% (from 1.14×10^{-4} to 2.13×10^{-5}) compared to its initial value. The lowest error function was achieved in conjunction with an 18% reduction in the active piezoelectric material usage. The optimal piezoelectric actuator configuration is shown as the shaded area in Figure 6.10d. The error function obtained by the LLS method is 1.14×10^{-4}. The results show that there is more than 81%

improvement in the error function compared with results obtained by the LLS method-voltage optimisation only.

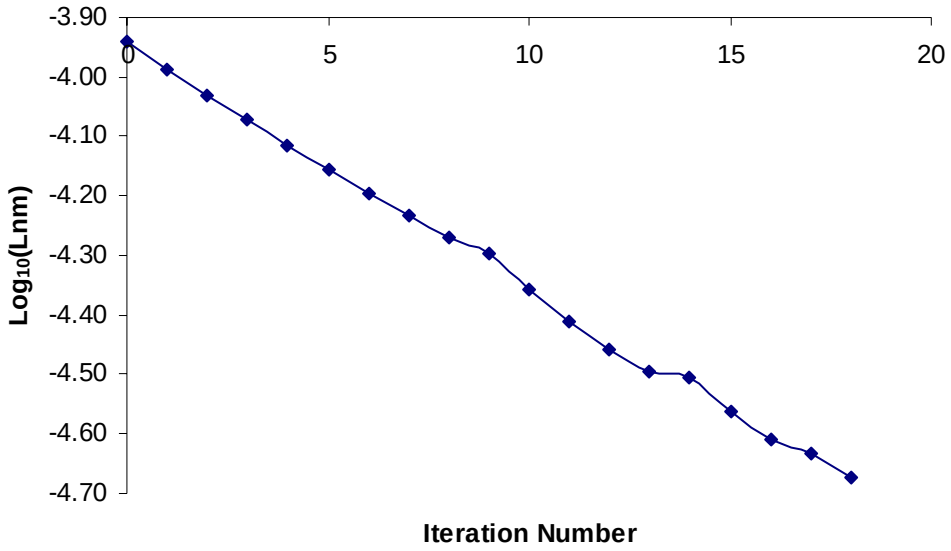

Figure 6.9: Evolutionary histories for 10x20 FE mesh model using VEPADO

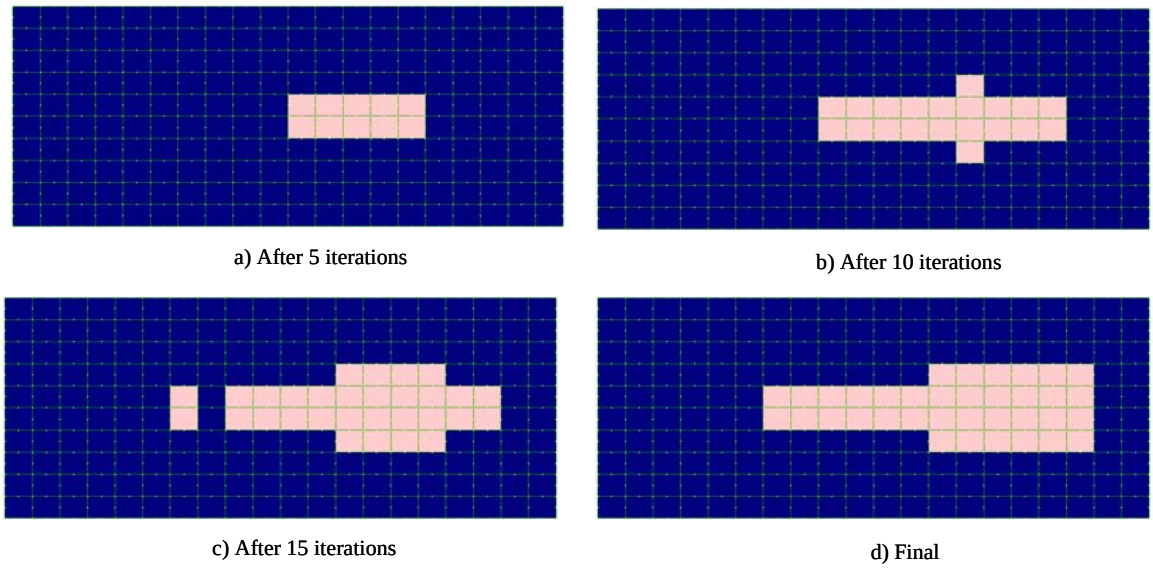

Figure 6.10: Evolutionary histories of piezoelectric actuator design for 10x20 FE mesh model using VEPADO algorithm.

The second test case investigates the effect of varying RMR on the improvement of error function using VEPADO algorithm. Five cases of RMR (0.0, 0.02499, 0.03499, 0.04499 and 0.05499) are considered. This test considers a full model, which is symmetrical about x-axis. It means that there are two elements, which have identical error function sensitivity number. Therefore, values of RMR are chosen how it is that the even number of elements is removed at each iteration to maintain the symmetrical model. The number of elements of piezoelectric materials removed is respectively 2, 4, 6, 8 and 10 at each iteration. The results are given in Table 6.2. The 3rd row of Table 6.2 shows the relative error of the final error functions with respect to their initial values for each case of RMR. It is noted that they all have relative errors from 81% up to 89% improvement in the error function. The 4th row of Table 6.2 shows the relative error of the final error functions with respect to the final error function for the case of RMR=0. Amongst all four non-zero RMR cases, only the case of RMR=0.05499 yields a 45% improvement in error function, a 10% in reduction in active piezoelectric material usage, a 65% decease in computational cost and about 3% increase in the final applied voltage. The effect of RMR variations on the piezoelectric actuator design is also shown in Figure 6.11. The results show that the performance and effectiveness of optimisation is affected by RMR variations. Therefore, it is important to choose a reasonable value of RMR to expedite the optimisation process to attain the optimal solution that best fits to desired structural shape when using VEPADO.

Table 6.2: Performance using VEPADO for 10x20 FE mesh model

RMR	0	0.02499	0.03499	0.04499	0.05499
Initial	$1.14\text{x}10^{-4}$	$1.14\text{x}10^{-4}$	$1.14\text{x}10^{-4}$	$1.14\text{x}10^{-4}$	$1.14\text{x}10^{-4}$
Final	$2.13\text{x}10^{-5}$	$1.73\text{x}10^{-5}$	$1.62\text{x}10^{-5}$	$1.64\text{x}10^{-5}$	$1.25\text{x}10^{-5}$
Error (%)	-81.41	-84.90	-85.82	-85.68	-89.04
Error (%)	-	-18.79	-23.74	-23.00	-41.05
No of iteration	18	10	8	6	6
Final Voltage	278.53	279.56	282.30	282.01	285.63

As shown in Figure 6.12, the shaded area is the final piezoelectric actuator configuration when considering the finest FE mesh (20x40) with RMR=0. The optimal solution converges after 58 iterations. The optimal applied voltage and the error function is 274.43 volts and $2.54\text{x}10^{-5}$, respectively. There are reductions in both error function

and volume of active piezoelectric material compared with the LLS solution. It is noted that the improvement in error function is reduced by 77% and the reduction in volume of active piezoelectric material is reduced by 14.5%.

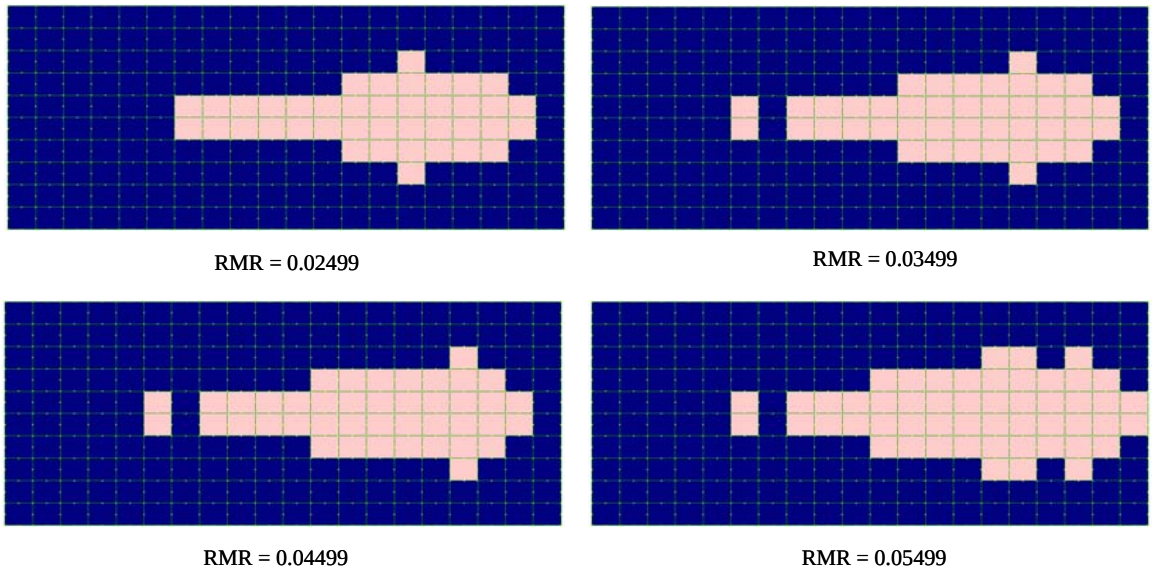

Figure 6.11: Effect of RMR variations on the piezoelectric actuators design using VEPADO algorithm

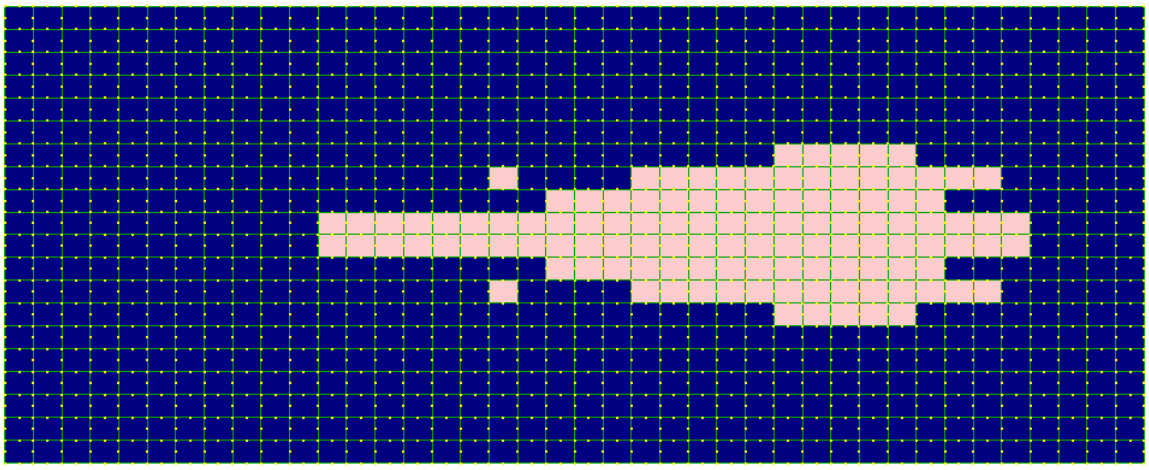

Figure 6.12: Final piezoelectric actuator design for 20x40 FE mesh model using VEPADO algorithm

6.5 Comparison of Algorithms Performances

This section shows the comparison of results between two different proposed algorithms AVEPADO and VEPADO, where the applied voltage to piezoelectric actuator and piezoelectric actuator configuration are optimised simultaneously by coupled the LLS method and the EPADO algorithm. Considering the results in Chapter 5 (see Section 5.6.2) as references for this particular cantilever plate structure example for case of RMR=0. As discussed, the results of the error function rely on the applied voltage variation as shown in Figure 5.11. The smallest error function ($1.27x10^{-5}$) is predicted at an applied voltage of 300 volts, which is assumed and used as an optimal solution as the optimal error function (Lnm_{opt}) and the optimal voltage (ϕ_{opt}), respectively. Table 6.3 compares the numerical results obtained using the proposed AVEPADO and VEPADO algorithms with those based on the optimal voltage (ϕ_{opt}) and the optimal error function (Lnm_{opt}). It can be observed that the proposed VEPADO algorithm shows a good performance in finding the applied voltage to piezoelectric actuator and piezoelectric actuator configuration. As shown in Table 6.3, it is evident that the VEPADO algorithm yields the applied voltage of 278.53 volts and error function of $2.13x10^{-5}$, which is closer to ϕ_{opt} and Lnm_{opt} than the results obtained by the AVEPADO algorithm. There are improvements in both the error function (47%) and the applied voltage (5%) when compared to the AVEPADO solution.

Similarly for the finer 20x40 FE mesh model, the results are summarised and compared as shown in Table 6.4. At an applied voltage of ϕ=300 volts, the EPADO algorithm yields $Lnm=1.04x10^{-5}$. The VEPADO algorithm predicts the voltage of 274.43 volts and error function of $2.54x10^{-5}$. The VEPADO algorithm shows that there are 2% and 21% improvement in finding applied voltage and the error function when compared to AVEPADO algorithm, respectively. The shaded area in Figures 6.6 and 6.12 obtained by the AVEPADO and the VEPADO algorithms depict similar final piezoelectric actuator configuration. Finally, all the above results are evident that the VEPADO algorithm has a better performance in searching for the applied voltage and piezoelectric actuator configuration to minimise the error function either for coarse or fine FE mesh models.

Table 6.3: Comparison of VEPADO with respect to AVEPADO for 10x20 FE mesh

	Optimal Solution	AVEPADO	VEPADO	Error (%)
Lnm	1.28×10^{-5}	3.99×10^{-5}	2.13×10^{-5}	-46.73
Voltage	300.00	266.06	278.53	5.00

Table 6.4: Comparison of VEPADO with respect to AVEPADO for 20x40 FE mesh

	Optimal Solution	AVEPADO	VEPADO	Error (%)
Lnm	1.04×10^{-5}	3.22×10^{-5}	2.54×10^{-5}	-21.11
Voltage	300.00	269.11	274.43	2.00

The last columns in Tables 6.3 and 6.4 show the relative percentage error of VEPADO solution with respect to AVEPADO solution.

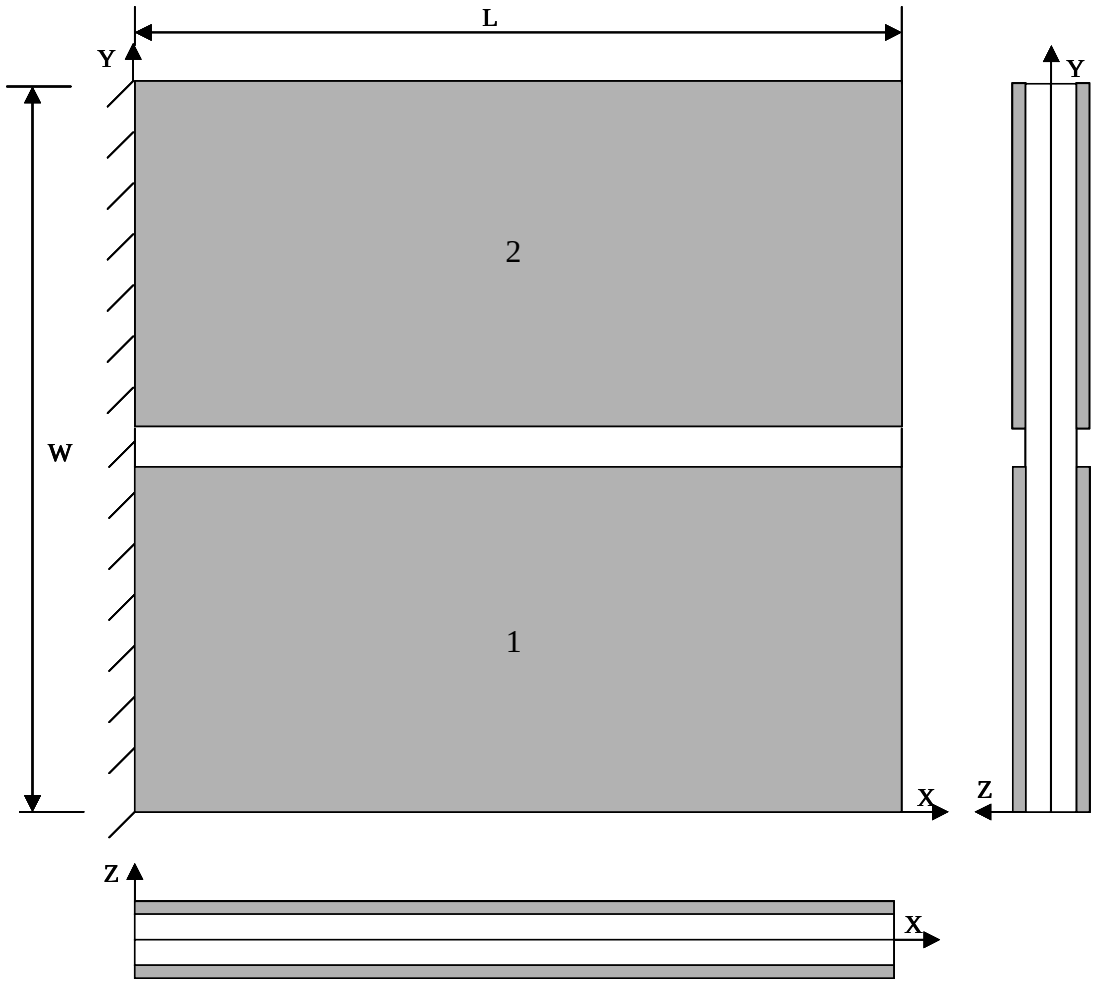

Figure 6.13: Square cantilever plate in XY, YZ and XZ planes.

6.6 Additional Examples

In the previous sections, the numerical examples were presented to validate the proposed AVEPADO and VEPADO algorithms for finding the applied voltage and the piezoelectric actuator configuration with an optimal error function. This section will present more examples to prove that the proposed algorithms are capable of dealing with the range of desired structural shapes from simple (bending) case to complex (twisting) case. The bending and twisting desired shapes are defined as $w^d(x,y)=10^{-5}\cos(10x-1)$ and $w^d(x,y)=10^{-5}(\cosh(x)-1)*\sin(y)$, respectively. There are two types of twisting structural shapes. One is anti-symmetrical twisting ($0 \le x \le 0.15$ and $0 \le y \le 0.15$), the other is symmetrical twisting ($0 \le x \le 0.15$ and $-0.075 \le y \le 0.075$). A square plate is assumed to have dimensions L=0.15m and W=0.15m. Initially, the active piezoelectric actuator patches are assumed to be distributed over the entire host plate. Both top and bottom actuators are subdivided into two separate actuators as shown in Figure 6.13. Only top actuator patches are applied electric voltage. The lower and upper patches are specified as patch number 1 and 2, respectively. A plate structure is subdivided into 21x21 FE mesh.

6.6.1 Performance using VEPADO Algorithm

For the bending case, the desired structural shape is shown in Figure 6.14a. The calculated structural shape using LLS – voltage optimisation only, is shown in Figure 6.14b. The voltage distribution and the error function are $\phi_1=\phi_2=243.24$ volts and $Lnm=5.15x10^{-4}$, respectively. When using VEPADO algorithm with a random RMR=0.04, the calculated structural shape is shown in Figure 6.14c. The shaded region in Figure 6.14c shows the optimal piezoelectric actuator configuration. The solution converges after 12 iterations. The voltage distribution and the error function are $\phi_1=\phi_2=294.11$ volts and $Lnm=5.11x10^{-5}$, respectively. By comparing with the LLS results, the error function has been improved by approximately 90% in conjunction with an increase in the electric field in each actuator by about 21%. It is also noted that the active piezoelectric material usage is 36% less than the LLS method without performing the piezoelectric actuator design optimisation.

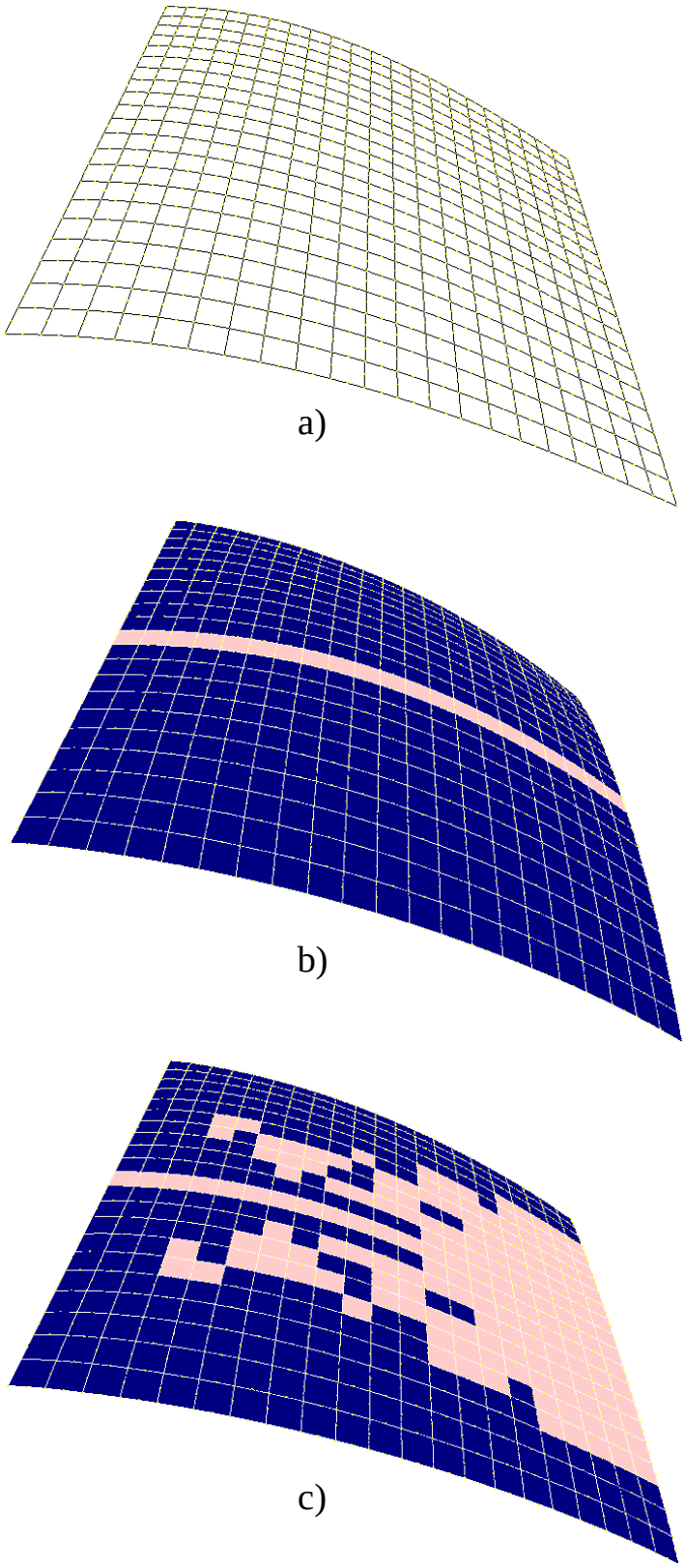

Figure 6.14: Bending case: a) Desired Structural Shape; b) Calculated Structural Shape using LLS-voltage optimisation only; c) Calculated Structural Shape using VEPADO

For the anti-symmetrical twisting case, the desired structural shape is shown in Figure 6.15a. The calculated structural shape using LLS–voltage optimisation only, is shown in Figure 6.15b. The applied voltage distribution and error function are ϕ_1=0.71 volts, ϕ_2=-1.13 volts and Lnm=1.53x10^{-3}, respectively. When using VEPADO algorithm with a random RMR=0.02, the calculated structural shape is shown in Figure 6.15c. The shaded region in Figure 6.15c shows the optimal piezoelectric actuator design. The solution converges after 26 iterations. The applied voltage distribution and error function are ϕ_1=0.72 volts, ϕ_2=-1.33 volts and Lnm=2.13x10^{-4}, respectively. By comparing with the LLS results, the error function has been improved by approximately 86% in conjunction with the increase of electric field in patch 1 and 2 about 1% and 17%, respectively. There is a 36% reduction in active piezoelectric material usage.

For the symmetrical twisting case, the desired structural shape is shown in Figure 6.16a. The calculated structural shape using LLS–voltage optimisation only, is shown in Figure 6.16b. The applied voltage distribution and error function are ϕ_1=0.92 volts, ϕ_2=-0.92 volts and Lnm=5.71x10^{-3}, respectively. When using VEPADO algorithm with a random RMR=0.02, the calculated structural shape is shown in Figure 6.16c. The shaded area in Figure 6.16c shows the final piezoelectric actuator configuration. The solution is attained after 44 iterations. The applied voltage distribution and error function are ϕ_1=1.08 volts, ϕ_2=-1.08 volts and Lnm=3.83x10^{-4}, respectively. By comparing with LLS results, there are reductions in both the error function and the volume of active piezoelectric material. It is noted that the error functions are reduced by 93% and the reduction in active piezoelectric material usage is 55% with an increase of electric field in patch 1 and 2 by approximately 17%.

As shown in Figures 6.14, 6.15 and 6.16, it can be observed that the VEPADO algorithm gives the better-calculated structural shape (Figures 6.14c, 6.15c and 6.16c) compared to the shape (Figures 6.14b, 6.15b and 6.16b) by using the LLS method. As an initial piezoelectric actuator design as shown in Figures 6.14b, 6.15b and 6.16b, there is larger bumpiness compared to the desired structural shape. The calculated structural shape is smoother and reduces bumpiness in the presence of the piezoelectric actuator design optimisation.

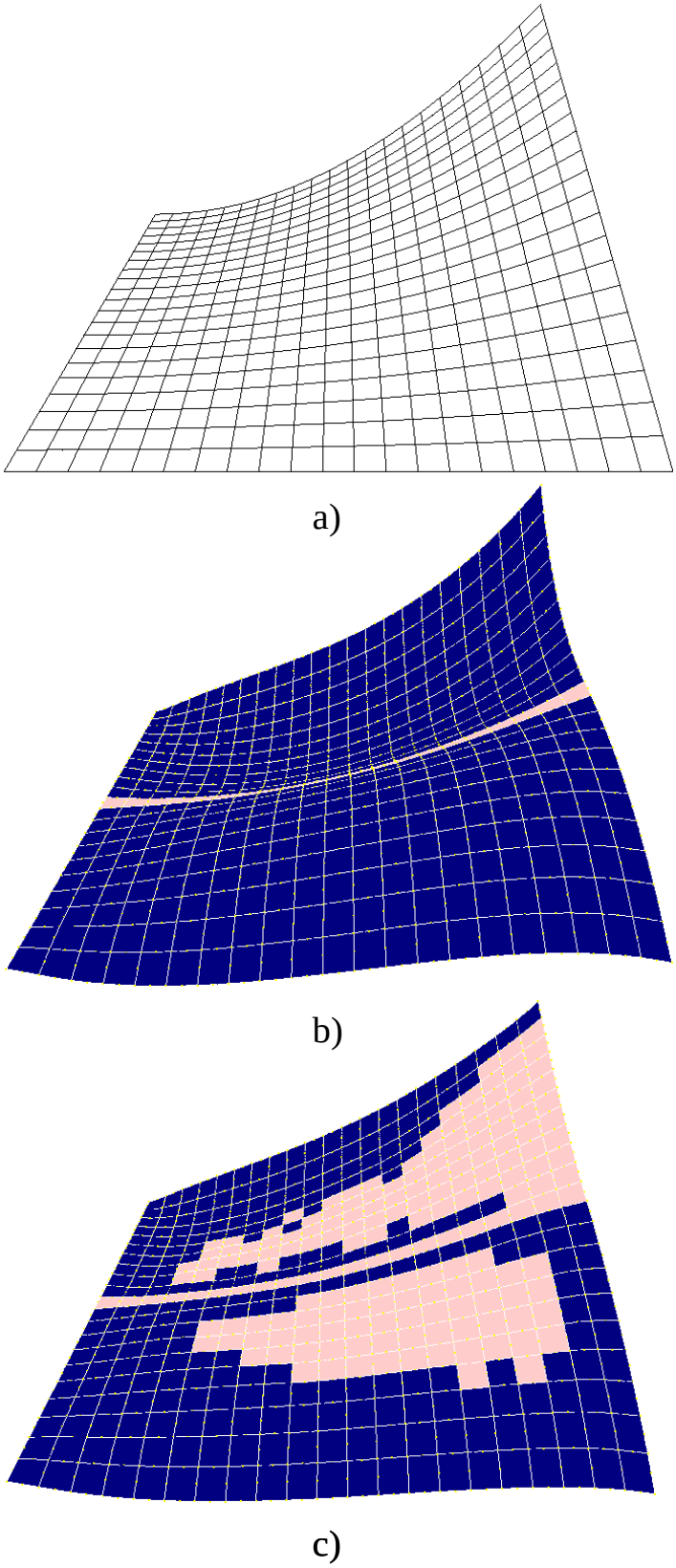

Figure 6.15: Anti-Symmetrical Twisting case: a) Desired Structural Shape; b) Calculated Structural Shape using LLS-voltage optimisation only; c) Calculated Structural Shape using VEPADO.

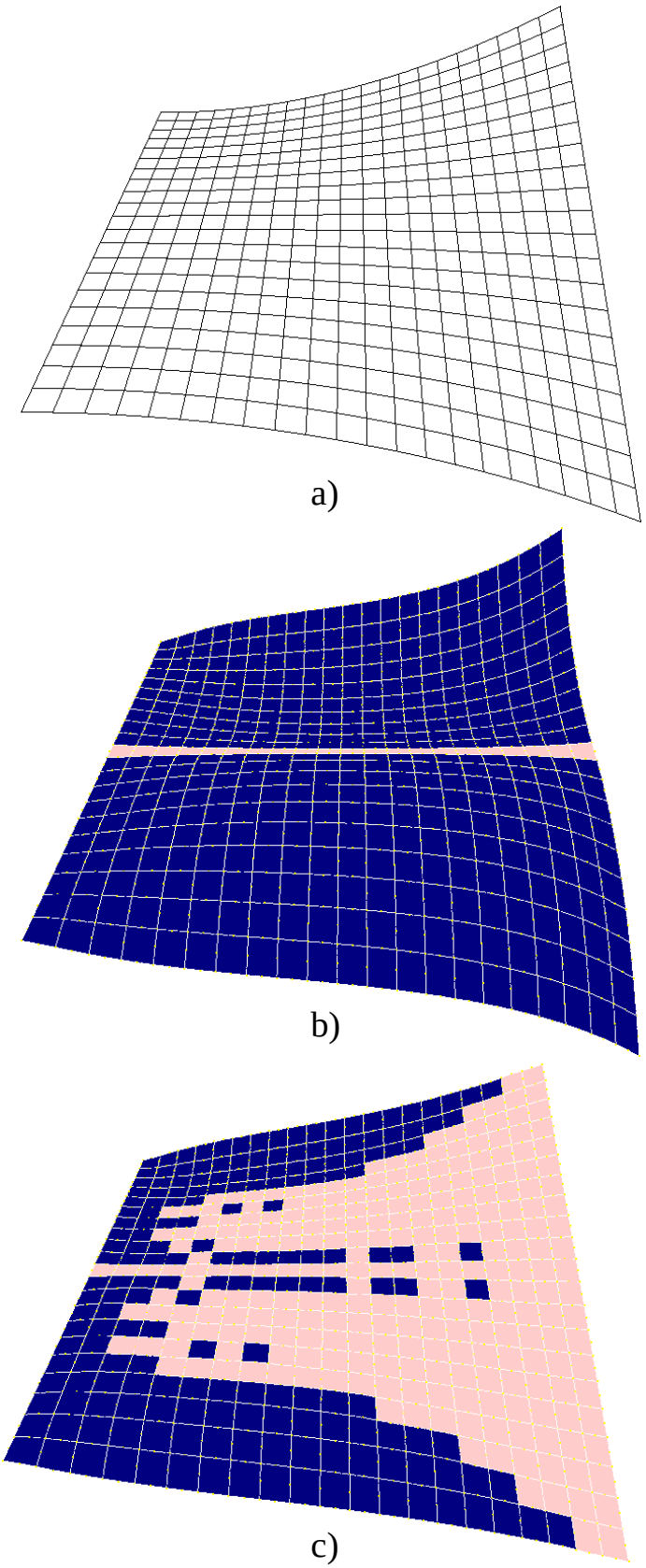

Figure 6.16: Symmetrical Twisting case: a) Desired Structural Shape; b) Calculated Structural Shape using LLS-voltage optimisation only; c) Calculated Structural Shape using VEPADO.

-

6.6.2 Performance using AVEPADO Algorithm

In this section, all the results predicted by the AVEPADO algorithm are used to compare with the LLS results (refer to Section 6.6.1). The parameter RMR is taken as 0.02.

Figure 6.17 depicts the calculated structural shape for the bending test case. The final piezoelectric actuator design is indicated by shaded region in Figure 6.17. The solution converges after a total of 17 iterations over 4 loops. The applied voltage distribution and error function are $\phi_1=\phi_2=261.30$ volts and $Lnm=8.06x10^{-5}$, respectively. The error function is reduced by 84% and the active piezoelectric material volume is reduced by 26% when compared to the associated LLS results.

Figure 6.18 shows the calculated structural shape for the case of anti-symmetrical twisting. The shaded region in Figure 6.18 is the final piezoelectric actuator design. The solution is attained after a total of 6 iterations over 2 loops. The voltage distribution and error function are $\phi_1=0.70$ volts $\phi_2=-1.16$ volts and $Lnm=8.39x10^{-4}$, respectively. The error function is improved by about 45% in conjunction with 10% reduction in active piezoelectric material usage comparing to the associated LLS results.

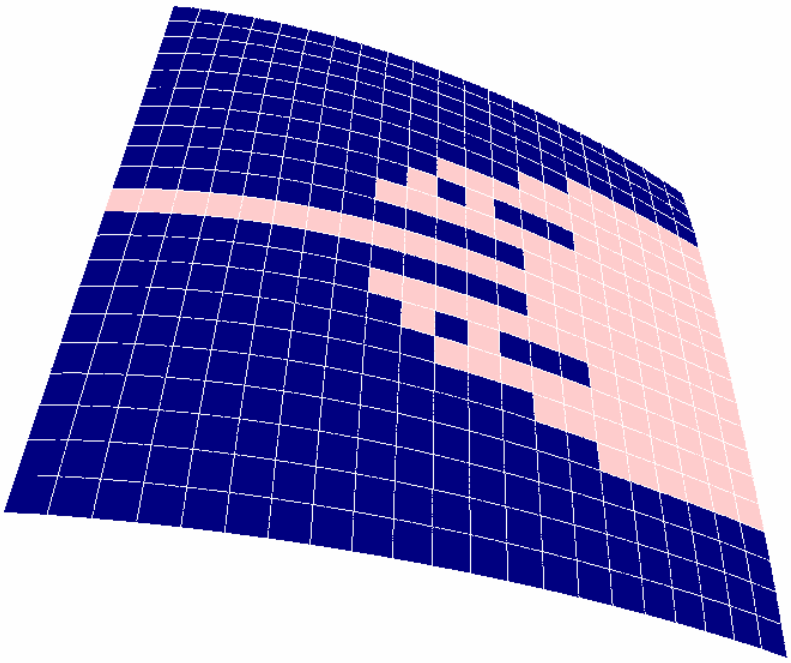

Figure 6.17: Calculated Bending Structural Shape using AVEPADO.

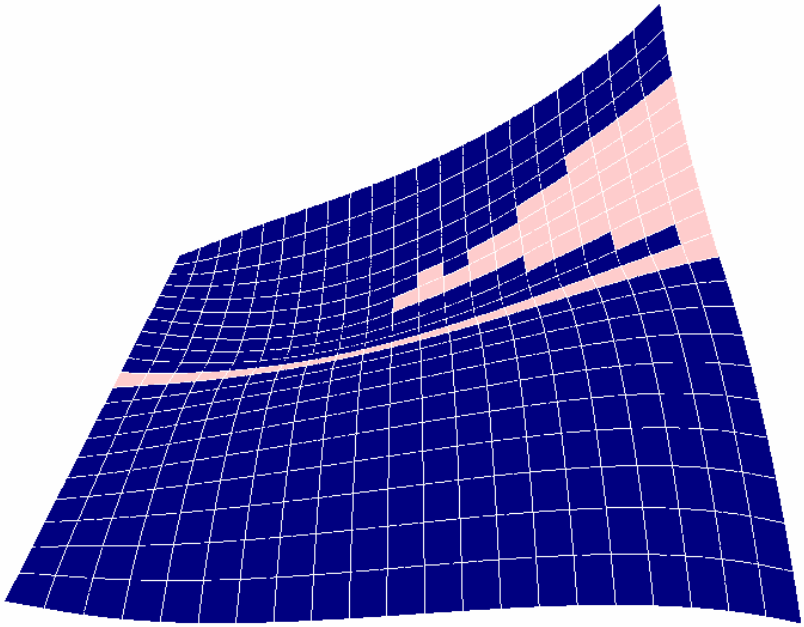

Figure 6.18: Calculated Anti-Symmetrical Twisting Structural Shape using AVEPADO.

For the symmetrical twisting case, Figure 6.19 shows calculated structural shape and the final piezoelectric actuator configuration by shaded area. The optimal solution converges after a total of 37 iterations over 4 loops with a 92% reduction in error function and a 48% reduction in active piezoelectric material usage. The voltage distribution and error function are ϕ_1=1.02 volts ϕ_2=-1.02 volts and Lnm=4.64x10^{-4}.

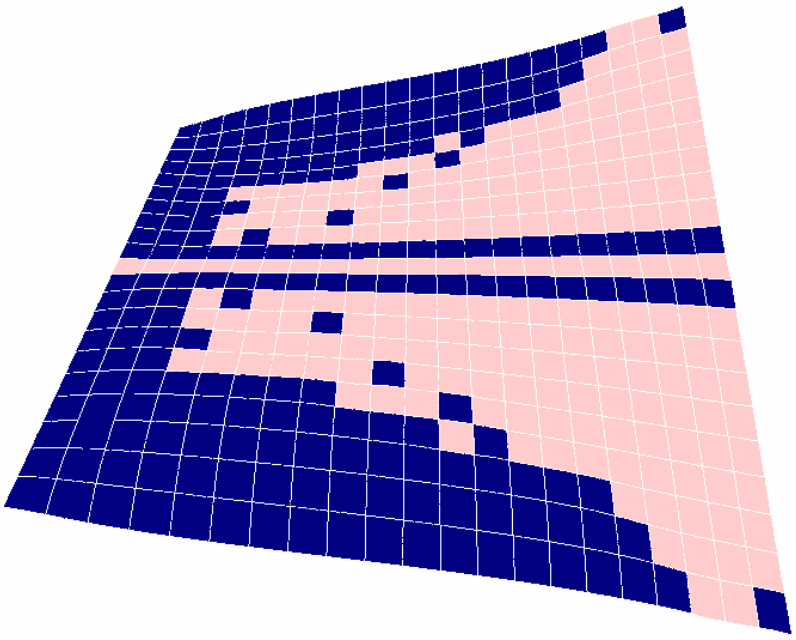

Figure 6.19: Calculated Symmetrical Twisting Structural Shape using AVEPADO.

6.7 Summary

This chapter further extends the evolutionary piezoelectric design optimisation (EPADO) with the searching for the optimal applied voltage distribution instead of using a given applied voltage distribution. Two algorithms, AVEPADO and VEPADO, have been developed based on the coupling of the LLS method and the EPADO algorithm. Illustrative examples have been presented and discussed to verify that the proposed algorithms are capable of optimising the voltage and piezoelectric materials distribution to achieve the best-fit of a desired structural shape with a smallest error function. The influence of removal material rate (RMR) and finite element mesh is found to be effective on the error function and computational cost (This chapter introduced the effect of RMR on the optimal solution, but it did not show how to choose the reasonable value of RMR to expedite the optimisation process). The shape of the piezoelectric actuator can be refined when a finer finite element mesh is considered. In addition, the comparison of performance between AVEPADO and VEPADO algorithms shows that the VEPADO algorithm yields much better results in achieving the goal of searching for global optimal solution for shape control of smart structures. The additional examples demonstrate that both proposed algorithms are capable of solving for any type of desired structural shape from simple (bending) cases to complex (twisting) cases.

7. Controlled Resonant Vibration of Smart Composite Plates using Piezoelectric Actuators

This chapter presents controlled resonant vibration of smart composite plates using piezoelectric actuators. A dynamic finite element (FE) formulation was developed on the basis of the static (FE) formulation by including the structural mass. FE formulation has been developed in Chapter 2 using the third order displacement field for mechanical deformation and a linear layer-wise electric potential for an electrical field. Modal analysis and Linear Least Square technique are also employed to optimise the applied electric fields in actuators to achieve the modal shapes. The Newmark direct time integration method is used to study harmonic excitation of smart structures. Numerical results are presented to show the optimal values of electrical fields in the actuator to achieve modal shape and to induce harmonic vibration of structure with controlled magnitude via adjusting the damping.

7.1 Introduction

A design of the piezoelectric actuators with loci, shapes and sizes criteria is usually of greater practical significance in shape control. Shape control can be categorised as either static or dynamic shape control. Whether it is transient or gradual change, static or dynamic shape control, both aim to determine the size of piezoelectric actuators, their applied electric fields and loci such that the desired shape is achieved effectively. Dynamic control for smart composite structures have drawn significant attention in the past decades, which is rather broad, including vibration control or suppression, dynamic position tracking, etc. Piezoelectric actuators are used to exert forces to structures, such as beams, plates and shells to induce desired deformations. For example, in vibration suppression, electrical fields are applied to the bonded actuators in the structure to minimise the effect of disturbance on its deformation. Previous work

focused on optimisation of the size, number and location of piezoelectric actuators to control structural vibration in smart composite structure. Tzou and Tseng (1990 and 1991) developed an algorithm to determine the distribution of piezoelectric sensor/actuator for dynamic measurement and active vibration control for the smart structures. Mackiewicz et. al (1996) and Kang et. al (1996) optimised the sizes, number and locations of the piezoelectric sensors/actuators to control vibration of smart composite beams. Librescu et. al (1997) integrated structural tailoring and piezoelectric materials to control the dynamic response of cantilever beams subject to external excitations. Kang et. al (1998) presented a gradient-based numerical scheme based on the damping characteristics to optimise the sensor and actuator placement for vibration control of plates. Rizet et. al (2000) developed an active control system to control the vibration of a smart flexural beam. Lim et. al (2001) studied the three-dimensional responses for parallel piezoelectric bimorphs. Mukherjee et. al (2002) employed a gradient-less iterative technique for optimal distribution of piezoelectric material to control the shape of a plate under the influence of external excitation. Irschik et. al (2003) designed the piezoelectric actuation to obtain a displacement field that coincides with a selected dynamic displacement field induced by external forces. Luo and Tong (2003a and 2003b) formulated the analytical dynamic solutions for smart beams using of piezoelectric, which includes peel stresses and the shear lag models.

Based on the developed dynamic FE formulation for analysing and controlling dynamic deformation of smart composite plate structures using piezoelectric actuators in Chapter 2, the work presented in this chapter focuses on the several aspects such as modal shape control and controlled resonant vibration. The modal shapes and their corresponding natural frequencies for selected structures are determined using an inverse iteration method (Chandrupatla and Belegundu, 2001). Using the Linear Least Square algorithm (Rorres and Anton, 1979), the optimum values of the electric fields in actuators are determined to achieve the selected modal shape. Controlled resonant harmonic vibration is investigated using the Newmark method (Rao, 2004) to study the effect of controlled damping due to applied electric fields to actuators.

7.2 Mathematical Formulation

7.2.1 Dynamic Equation

On the basis of dynamic FE formulation of a laminated composite plate structure with piezoelectric actuator derived in Chapter 2, the general dynamic equation of the system without damping can be seen in Equation (7.1). When damping is considered, it can be rewritten as Equation (7.2).

$$\begin{bmatrix} \mathbf{M}_{uu} & 0 \\ 0 & 0 \end{bmatrix} \begin{bmatrix} \ddot{\mathbf{u}}_g \\ \ddot{\boldsymbol{\phi}}_g \end{bmatrix} + \begin{bmatrix} \mathbf{K}_{uu} & \mathbf{K}_{u\phi} \\ \mathbf{K}_{\phi u} & \mathbf{K}_{\phi\phi} \end{bmatrix} \begin{bmatrix} \mathbf{u}_g \\ \boldsymbol{\phi}_g \end{bmatrix} = \begin{bmatrix} \mathbf{F}_g \\ -\mathbf{Q}_g \end{bmatrix} \tag{7.1}$$

$$\begin{bmatrix} \mathbf{M}_{uu} & 0 \\ 0 & 0 \end{bmatrix} \begin{bmatrix} \ddot{\mathbf{u}}_g \\ \ddot{\boldsymbol{\phi}}_g \end{bmatrix} + \begin{bmatrix} \mathbf{C}_{uu} & 0 \\ 0 & 0 \end{bmatrix} \begin{bmatrix} \dot{\mathbf{u}}_g \\ \dot{\boldsymbol{\phi}}_g \end{bmatrix} + \begin{bmatrix} \mathbf{K}_{uu} & \mathbf{K}_{u\phi} \\ \mathbf{K}_{\phi u} & \mathbf{K}_{\phi\phi} \end{bmatrix} \begin{bmatrix} \mathbf{u}_g \\ \boldsymbol{\phi}_g \end{bmatrix} = \begin{bmatrix} \mathbf{F}_g \\ -\mathbf{Q}_g \end{bmatrix} \tag{7.2}$$

For a vibrating structure, the damping term ($\mathbf{C}_{uu}$) represents the loss of the total system energy. Due to the hysteresis in the material and the slip in the connections, all structures are under the effect of damping. However, the exact mechanisms of damping are not fully understood and it is normal to approximate this with viscous damping. Viscous damping is introduced by specifying some fraction of critical damping. Critical damping for a structure marks the transition between oscillatory and non-oscillatory response. In the proposed FE formulation, damping can be modelled through viscous damping, known as Rayleigh damping or proportional damping, which is one of the most common models of damping in FE formulation. The general form of Rayleigh damping is expressed in a linear combination of stiffness and mass matrices as $[\mathbf{C}_{uu}] = \alpha[\mathbf{M}_{uu}] + \beta[\mathbf{K}_{uu}]$ and α & β are Rayleigh's damping coefficients.

When piezoelectric actuator is used Equation (7.2) can be rewritten as follow:

$$[\mathbf{M}_{uu}][\ddot{\mathbf{u}}_g] + [\mathbf{C}_{uu}][\dot{\mathbf{u}}_g] + [\mathbf{K}_{uu}][\mathbf{u}_g] = [\mathbf{F}_g] - [\mathbf{K}_{u\phi}][\boldsymbol{\phi}_g] \tag{7.3}$$

From now on, all the derivations are based on the Equation (7.3).

7.2.2 Eigenvalues and Eigenvectors Analysis

For free vibration, there is no mechanical and electrical force. Hence Equation (7.3) becomes:

$$[\mathbf{M}_{uu}][\ddot{\mathbf{u}}_g] + [\mathbf{K}_{uu}][\mathbf{u}_g] = 0 \tag{7.4}$$

The generalised problem in free vibration is that evaluating an Eigenvalue problem. Eigen-analysis was performed on Equation (7.3) by solving Equation (7.4). The solution consists of Eigenvalues ($\lambda=\omega^2$), mechanical natural frequencies (ω) and eigenvectors (**V**). For steady state condition, the Equation (7.5) is solution of Equation (7.4)

$$[\mathbf{u}_g] = [\mathbf{V}]\sin(\omega t) \tag{7.5}$$

$$\Rightarrow [\ddot{\mathbf{u}}_g] = -\omega^2[\mathbf{V}]\sin(\omega t) \tag{7.6}$$

Hence Equation (7.4) becomes

$$[\mathbf{K}_{uu}][\mathbf{V}] - \omega^2[\mathbf{M}_{uu}][\mathbf{V}] = 0 \tag{7.7}$$

The generalised Eigenvalue problem

$$[\mathbf{K}_{uu}][\mathbf{V}] - \lambda[\mathbf{M}_{uu}][\mathbf{V}] = 0 \tag{7.8}$$

Finally, Equation (7.8) is used to analyse the frequency of vibration together with the corresponding eigenvector indicating the mode shape. $\mathbf{K}_{uu}$ and $\mathbf{M}_{uu}$ are symmetric matrices. $\mathbf{K}_{uu}$ is positive definite. The required condition for nontrivial eigenvector is $\det([\mathbf{K}_{uu}] - \lambda[\mathbf{M}_{uu}]) = 0$, which presents the characteristic polynomial in term of λ. For the implementation of the characteristic polynomial, inverse iteration method (Chandrupatla and Belegundu, 2001) is used.

7.2.3 Modal Shape Control

The objective of this section is to find the optimum distribution of the electric fields in actuators, which are determined to achieve the selected modal structural shape using LLS method (Rorres and Anton, 1979). The concept of this work is similar to the quasi-static shape control problem. The main difference in modal shape control is that the structural shape is defined based on the i^{th} mode shape (eigenvector) $\mathbf{V}_i$ and scalar factor G as $\mathbf{w}^d = G^* \mathbf{V}_i$.

When the actuator configurations are fixed, the LLS method (Rorres and Anton, 1979) has been used successfully to determine the optimal voltage distribution to achieve the modal structural shape. Similarly in previous sections, the modal shape control problem can be formulated as

Find $\boldsymbol{\phi}$ to

$$\text{Minimise } \text{Lnm}(\boldsymbol{\phi}) = \frac{\sum_{i=1}^{N} \frac{\left(w_i^d - w_i^c(\boldsymbol{\phi})\right)^2}{(w_{max}^d)^2}}{4 \times N} \tag{7.9}$$

$$\text{Subject to } [u_g(\boldsymbol{\phi})] = [\mathbf{K}_{uu}]^{-1}[-\mathbf{K}_{u\phi}][\boldsymbol{\phi}_g] \tag{7.10}$$

Equation (7.10) is the simplified version of Equation (7.3) in the absence of the mass, damping and mechanical force matrices. The solution of optimum voltage distribution of the i^{th} modal shape can be expressed in terms of Influence Coefficient Matrices and desired displacement as shown in Equation (7.11).

$$[\boldsymbol{\phi}]_i = \left(\left[\mathbf{C}^w\right]^T \left[\mathbf{C}^w\right]\right)^{-1} \left[\mathbf{C}^w\right]^T [\mathbf{w}^d] \tag{7.11}$$

7.2.4 Controlled Resonant Vibration

To investigate the controlled harmonic excitation of the i^{th} vibration mode of a smart structure using applied electric fields in actuators, the solution of "f" factor can be derived in terms of Rayleigh's coefficients, frequency input and natural frequency of the i^{th} mode as followed.

Assume $[\boldsymbol{\phi}_g] = f \times [\boldsymbol{\phi}^0]_i \sin(\Omega_i t)$ is control input of electric field of the i^{th} mode. Equation (7.3) then can be rewritten as follow:

$$[\mathbf{M}_{uu}][\ddot{\mathbf{u}}_g] + [\mathbf{C}_{uu}][\dot{\mathbf{u}}_g] + [\mathbf{K}_{uu}][\mathbf{u}_g] = [\mathbf{F}_g] - f \times [\mathbf{K}_{u\phi}][\boldsymbol{\phi}^0]_i \sin(\Omega_i t) \qquad (7.12)$$

Where f is a constant factor and Ω_i is the frequency input of the i^{th} mode. Factor "f" is determined to change the natural damping of a smart structure. The nodal applied voltage vector ($[\boldsymbol{\phi}^0]_i$) is calculated based on quasi-statically achieving the i^{th} mode shape with a given displacement at a selected point. The problem is to minimise 'f' factor to achieve harmonic vibration of the structures with controlled amplitude via counteracting structural damping, namely.

$$\text{Minimise f, subject to: } [\mathbf{C}_{uu}][\dot{\mathbf{u}}_g] + f \times [\mathbf{K}_{u\phi}][\boldsymbol{\phi}^0]_i \sin(\Omega_i t) = 0 \qquad (7.13)$$

Thus the solution of harmonic excitation of smart structures is assumed to have the following form:

$$[\mathbf{u}_g] = [\mathbf{u}^0]_i \cos(\Omega_i t) \Rightarrow [\dot{\mathbf{u}}_g] = -\Omega_i [\mathbf{u}^0]_i \sin(\Omega_i t) \qquad (7.14)$$

By substituting the velocity into Equation (7.13), it then becomes:

$$\text{Minimise f, subject to: } f \times [\mathbf{K}_{u\phi}][\boldsymbol{\phi}^0]_i - \Omega_i [\mathbf{C}_{uu}][\mathbf{u}^0]_i = 0 \qquad (7.15)$$

where: $[\mathbf{u}^0]_i$ is the initial displacement vector (modal shape) of the i^{th} mode.

The eigenvalue solution is shown in Equation (7.16) (see Section 7.2.2).

$$[\mathbf{K}_{uu}][\mathbf{u}^0]_i - \omega_i^2[\mathbf{M}_{uu}][\mathbf{u}^0]_i = 0 \tag{7.16}$$

where: ω_i is natural frequency.

By solving Equation (7.15) and (7.16) simultaneously, Equation (7.15) now is rewritten in terms of Rayleigh's coefficients as follow:

$$f \times [\mathbf{K}_{u\phi}][\boldsymbol{\phi}^0]_i - \Omega_i(\alpha\mathbf{M}_{uu}] + \beta[\mathbf{K}_{uu}])[\mathbf{u}^0]_i = 0 \tag{7.17}$$

From Equation (7.16), $[\mathbf{M}_{uu}] = \frac{1}{\omega_i^2}[\mathbf{K}_{uu}]$ and it is substituted in to Equation (7.17), yielding Equation (7.18).

$$f \times [\mathbf{K}_{u\phi}][\boldsymbol{\phi}^0]_i - \Omega_i\left(\frac{\alpha}{\omega_i^2} + \beta\right)[\mathbf{K}_{uu}][\mathbf{u}^0]_i = 0 \tag{7.18}$$

Hence, the solution of "f" factor can be written in terms of Rayleigh's coefficients, frequency input and natural frequency of the i^{th} mode as shown in Equation (7.19).

$$f = \Omega_i\left(\frac{\alpha}{\omega_i^2} + \beta\right) \tag{7.19}$$

When the structural response is considered at the natural frequency (it means that the frequency input is the same as natural frequency), the solution of Equation (7.19) can be simplified as follow:

$$f = \frac{\alpha}{\omega_i} + \beta\omega_i \tag{7.20}$$

Meaning of f is a scalar factor that scales the required voltage for a static modal shape to the required voltage for a dynamic modal shape control.

7.2.5 Newmark Direct Time Integration Method

Newmark direct time integration method is used to study harmonic excitation of smart structures (Rao, 2004). The method is based on the assumption that the acceleration varies linearly between each time step. This section describes in details the procedure for dynamic response of the system under harmonic excitation. At a given initial position $[\mathbf{u}_g]_{t_0}$ and velocity $[\dot{\mathbf{u}}_g]_{t_0}$ the initial acceleration $[\ddot{\mathbf{u}}_g]_{t_0}$ can be computed via Equation (7.12) as in Equation (7.21).

$$\left[\ddot{\mathbf{u}}_g\right]_{t_0} = \left[\mathbf{M}_{uu}\right]^{-1}\left(\left[\mathbf{F}_g\right]_{t_0} - f \times \left[\mathbf{K}_{u\phi}\right]\left[\boldsymbol{\phi}^0\right]_i \sin\left(\Omega_i t_0\right) - \left[\mathbf{C}_{uu}\right]\left[\dot{\mathbf{u}}_g\right]_{t_0} - \left[\mathbf{K}_{uu}\right]\left[\mathbf{u}_g\right]_{t_0}\right) \tag{7.21}$$

By using Newmark method (Rao, 2004), the velocity and displacement at time t_{j+1} can be written in the form of velocity and displacement at time t_j, acceleration at time t_{j+1} and Newmark's parameters α^* and β^* as shown in Equation (7.22) and Equation (7.23), respectively. Where j=*0* and $t_{j+1} = t_j + \Delta t$.

$$\left[\dot{\mathbf{u}}_g\right]_{t_{j+1}} = \left[\dot{\mathbf{u}}_g\right]_{t_j} + \left\{\left(1-\beta^*\right)\left[\ddot{\mathbf{u}}_g\right]_{t_j} + \beta^*\left[\ddot{\mathbf{u}}_g\right]_{t_{j+1}}\right\}\Delta t \tag{7.22}$$

$$\left[\mathbf{u}_g\right]_{t_{j+1}} = \left[\mathbf{u}_g\right]_{t_j} + \Delta t\left[\dot{\mathbf{u}}_g\right]_{t_j} + \left\{\left(0.5-\alpha^*\right)\left[\ddot{\mathbf{u}}_g\right]_{t_j} + \alpha^*\left[\ddot{\mathbf{u}}_g\right]_{t_{j+1}}\right\}\left(\Delta t\right)^2 \tag{7.23}$$

Newmark's parameters α^* and β^* indicate how much the acceleration at the end of the interval substitutes to the velocity and displacement equation at the end of the interval Δt. The values of these parameters are commonly used in equations (7.22) and (7.23) as α^*=*1/6* and β^*=*1/2* for the case of linear acceleration; α^*=*1/4* and β^*=*1/2* for the case of constant acceleration. The method is unconditionally stable for $\alpha^* \geq \frac{1}{4}\left(\beta^* + \frac{1}{2}\right)^2$ and $\beta^* \geq$*1/2*.

The velocity and the acceleration at time $t = t_{j+1}$ can be expressed in term of displacement at time $t = t_{j+1}$ using Equation (7.22) and Equation (7.23). The resulting

expression can be substituted into the equation of motion Equation (7.24) at time $t = t_{j+1}$. Finally, equations (7.25), (7.26) and (7.27) respectively show the relation for finding the displacement, velocity and acceleration of system at time $t = t_{j+1}$.

$$\left[\mathbf{M}_{uu}\right]\left[\ddot{\mathbf{u}}_g\right]_{t_{j+1}} + \left[\mathbf{C}_{uu}\right]\left[\dot{\mathbf{u}}_g\right]_{t_{j+1}} + \left[\mathbf{K}_{uu}\right]\left[\mathbf{u}_g\right]_{t_{j+1}} = \left[\mathbf{F}_g\right]_{t_{j+1}} - f \times \left[\mathbf{K}_{u\phi}\right]\left[\boldsymbol{\phi}^0\right]_i \sin\left(\Omega_i t_{j+1}\right) \tag{7.24}$$

$$\left[\mathbf{u}_g\right]_{t_{j+1}} = \left[\frac{1}{\alpha^*(\Delta t)^2}\left[\mathbf{M}_{uu}\right] + \frac{\beta^*}{\alpha^*\Delta t}\left[\mathbf{C}_{uu}\right] + \left[\mathbf{K}_{uu}\right]\right]^{-1} \times \left(\mathbf{A} + \mathbf{B} + \mathbf{C}\right) \tag{7.25}$$

Where:

$$\mathbf{A} = \left[\mathbf{F}_g\right]_{t_{j+1}} - f \times \left[\mathbf{K}_{u\phi}\right]\left[\boldsymbol{\phi}^0\right]_i \sin\left(\Omega_i t_{j+1}\right)$$

$$\mathbf{B} = \left[\mathbf{M}_{uu}\right]\left(\frac{1}{\alpha^*(\Delta t)^2}\left[\mathbf{u}_g\right]_{t_j} + \frac{1}{\alpha^*\Delta t}\left[\dot{\mathbf{u}}_g\right]_{t_j} + \left(\frac{1}{2\alpha^*} - 1\right)\left[\ddot{\mathbf{u}}_g\right]_{t_j}\right)$$

$$\mathbf{C} = \left[\mathbf{C}_{uu}\right]\left(\frac{\beta^*}{\alpha^*\Delta t}\left[\mathbf{u}_g\right]_{t_j} + \left(\frac{\beta^*}{\alpha^*} - 1\right)\left[\dot{\mathbf{u}}_g\right]_{t_j} + \left(\frac{\beta^*}{\alpha^*} - 2\right)\frac{\Delta t}{2}\left[\ddot{\mathbf{u}}_g\right]_{t_j}\right)$$

$$\left[\ddot{\mathbf{u}}_g\right]_{t_{j+1}} = \frac{1}{\alpha^*(\Delta t)^2}\left(\left[\mathbf{u}_g\right]_{t_{j+1}} - \left[\mathbf{u}_g\right]_{t_j}\right) - \frac{1}{\alpha^*\Delta t}\left[\dot{\mathbf{u}}_g\right]_{t_j} - \left(\frac{1}{2\alpha^*} - 1\right)\left[\ddot{\mathbf{u}}_g\right]_{t_j} \tag{7.26}$$

$$\left[\dot{\mathbf{u}}_g\right]_{t_{j+1}} = \left[\dot{\mathbf{u}}_g\right]_{t_j} + \left(1 - \beta^*\right)\Delta t\left[\ddot{\mathbf{u}}_g\right]_{t_j} + \beta^*\Delta t\left[\ddot{\mathbf{u}}_g\right]_{t_{j+1}} \tag{7.27}$$

7.3 Numerical Examples

Numerical examples are used, as in Chapter 2, to verify results for free vibration based on the developed FE formulation by comparing the numerical results with the numerical results obtained from commercial FEA software Strand7. In this section, the examples are presented to focus on modal shape control of a smart structure, which can

be obtained through optimising the applied electric field in actuators to achieve the modal shapes using recent Linear Least Square technique and the resonant vibration control of a smart composite structure and the effect of frequency input and energy consumption.

7.3.1 Modal Shape Control

Consider a cantilevered plate that has a length of 0.292 m, width of 0.152 m and a total thickness of 0.83 mm. There is no mechanical load in structure. The plate has the following material constants: $c_{11}=c_{22}=c_{33}=82.68GPa$, $c_{12}=c_{13}=c_{23}=27.56GPa$, $c_{44}=c_{55}=c_{66}=27.6GPa$, density $\rho=2780kg/m^3$. Fifteen piezoelectric ceramic patches of 0.25 mm thick are attached to top and bottom of the structure and have been indicated as shown in Figure 7.1. Patch #1, #6 and #11, each consist of 2 elements. The properties of the patches include the elastic constants: $c_{11}=c_{22}=c_{33}=84.8GPa$, $c_{12}=c_{13}=c_{23}=36.35GPa$, $c_{44}=c_{55}=c_{66}=24.2GPa$; density $\rho=8000kg/m^3$; electric permittivity: $\chi_{11}=\chi_{22}=15.3x10^{-9}F/M$, $\chi_{33}=15.0x10^{-9}F/M$; piezoelectric strain constant $d_{31}=-254pm/V$, $d_{32}=-204pm/V$, $d_{33}=374pm/V$, $d_{15}=584pm/V$, $d_{24}=484pm/V$. The piezoelectric patch #1, #2, #3, #4, #5, #11, #12, #13, #14 and #15 have an area of $1950.75mm^2$, patch #6 has area of $637.5mm^2$, and patch #7, #8, #9 and #10 have area of $1275mm^2$. The finite element mesh has 84 elements and total of 3 layers as shown in Figure 7.1. The left end of all models has been clamped. Scalar factor of modal shape is $G=10^{-5}$.

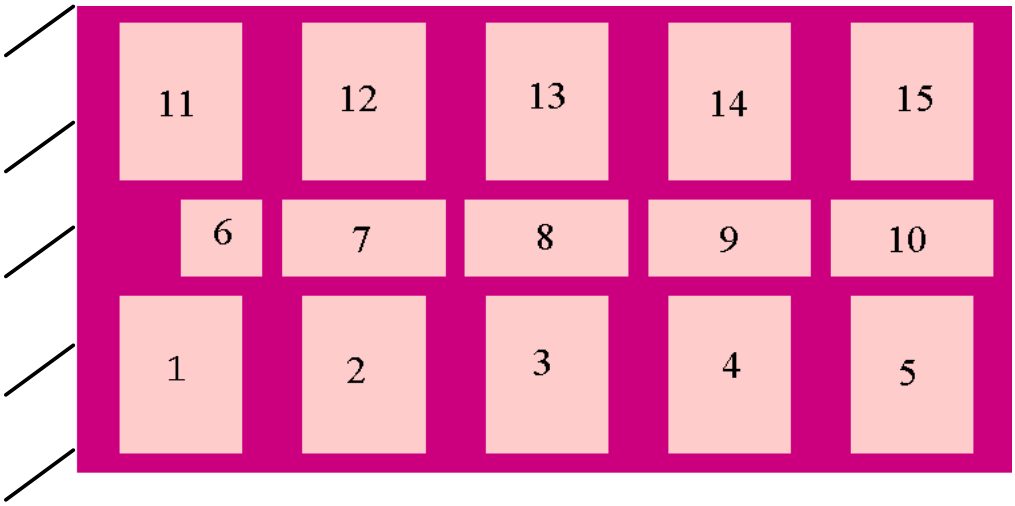

Figure 7.1: Cantilever plate in XY plane

By modal analysis and using the LLS method, the natural frequencies and the optimum values of voltages applied to each patch are obtained and listed in Table 7.1. In the first 4 modes, the natural frequencies are 8.29 Hz, 38.85 Hz, 53.9 Hz and 154 Hz, the highest magnitude of voltages are 4.18V, 66.3V, 27.63 and 65.87V and the error functions are 5.077×10^{-6}, 0.001304, 0.00385 and 0.002824, respectively. Figure 7.2 shows the desired modal shape and the calculated shape in each mode. The graphs also show that the plate vibration could perform either bending or twisting deformation or both at the same time. In this example, modes 1 and 3 have bending deformation, whereas mode 2 shows clearly twisting deformation. Then there are bending deformations along the plate and slight twisting deformation at the tip. The results in Table 7.1 shows that it is easily to achieve the modal shape of modes 1 and 3 with low applied voltages, whilst modal shapes of modes 2 and 4 require very high energy to achieve. Values of the error function show that it is hard to achieve twisting modal shape.

Table 7.1: Voltage distribution for cantilever plates in different modal shape

Mode	**1**	**2**	**3**	**4**
Frequencies (Hz)	8.29	38.85	53.09	154.00
Patches/Voltages(volts)				
1	-3.36	66.30	-14.98	-28.59
2	-2.57	12.82	20.72	65.78
3	-2.21	17.63	19.22	-23.36
4	-0.99	-2.35	21.73	-61.46
5	-0.30	-9.61	3.23	-30.33
6	4.17	0.00	8.49	65.87
7	3.43	0.00	-21.78	-33.81
8	4.18	0.00	-35.49	46.14
9	1.80	0.00	-21.83	36.51
10	1.68	0.00	-27.63	114.58
11	-3.36	-66.30	-14.98	-28.59
12	-2.57	-12.82	20.72	65.78
13	-2.21	-17.63	19.22	-23.36
14	-0.99	2.35	21.73	-61.46
15	-0.30	9.61	3.23	-30.33
Lnm	5.08×10^{-6}	1.30×10^{-3}	3.85×10^{-4}	2.82×10^{-3}

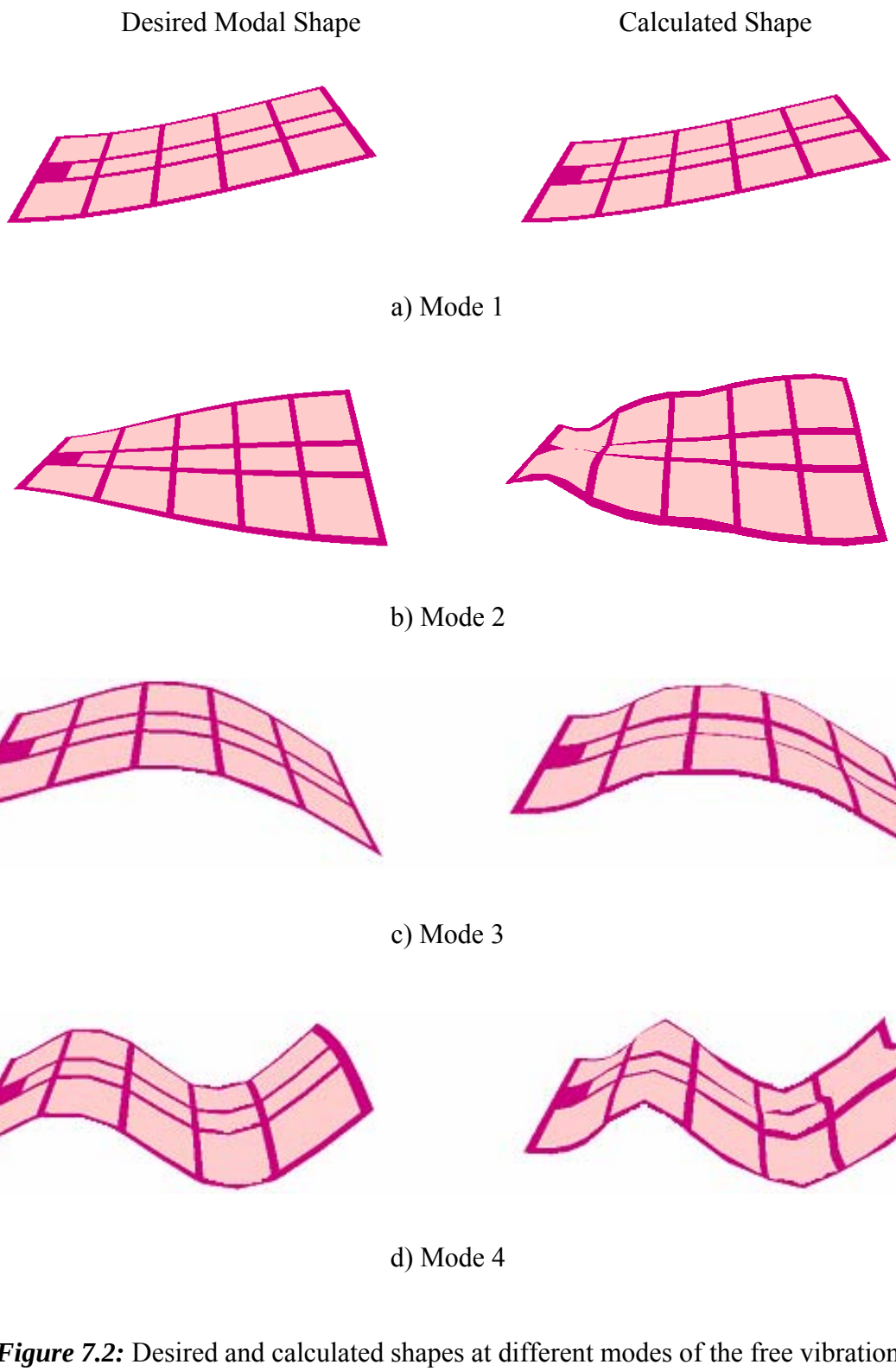

Figure 7.2: Desired and calculated shapes at different modes of the free vibration

7.3.2 Controlled Resonant Vibration

7.3.2.1 Example 1

Consider a long cantilever plate clamped at the left end and subject to non-applied mechanical load. It has a length of 0.15 m, width of 0.06 m and consists of 4 layers of thickness of 0.0005m each. The material of the plate has the following stiffness constants: $c_{11}=c_{22}=c_{33}=92.9$GPa, $c_{12}=c_{13}=c_{23}=39.8$GPa, $c_{44}=c_{55}=c_{66}=26.5$GPa; density $\rho=2780$kg/m^3. Three pairs of piezoelectric actuator are bonded on the top and bottom of the plate. Only the top sets of the actuators are activated, which are modelled using six elements. Patch #1 and #3 are bonded at both ends and patch #2 is bonded at middle of the plate as numbered in Figure 7.3. The properties of the patches include the stiffness constants: $c_{11}=c_{22}=c_{33}=112.6$GPa, $c_{12}=c_{13}=c_{23}=55.5$GPa, $c_{44}=c_{55}=c_{66}=28.6$GPa, density $\rho=8000$kg/m^3; the electric permittivity: $\chi_{11}=\chi_{22}=15.3\text{x}10^{-9}$F/M, $\chi_{33}=15.0\text{x}10^{-9}$F/M; and piezoelectric strain constants $d_{31}=-254$pm/V, $d_{32}=-254$pm/V, $d_{33}=374$pm/V, $d_{24}=584$pm/V, $d_{15}=584$pm/V. As mention in chapter 2, the present FE formulation was not included the adhesive layer. Therefore, the bonds between the host structure and piezoelectric actuator patches are assumed as a perfect-bond.

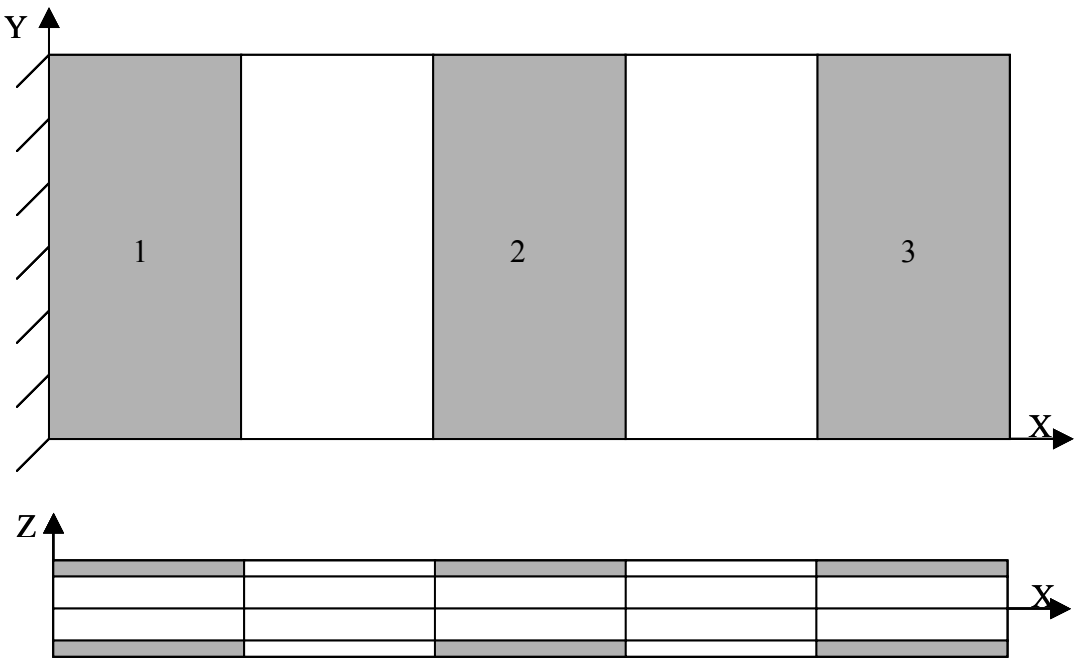

Figure 7.3: Cantilever plate in XY and XZ plane

In this example, the resonant vibration control of the smart composite structures is studied. It demonstrates the damping effect of the first modal vibration of the cantilever plate due to electrical fields in piezoelectric actuator. In this simulation, the plate is subjected to a non-mechanical force and considers a first modal shape as initial displacement of 0.6mm at the centre of the free end of the clamped plate, which has coordinates of (0.15m, 0.03m), and the first natural frequency ω_1=379.1 rad/s (60Hz). The required electrical fields (ϕ_0^l) to achieve the best first modal shape for patch 1, 2 & 3 are -322.1V, -367.2 V and 28.6 V, respectively. The Newmark direct method of time integration is used to obtain the solution of Equation (7.12). The Newmark method parameters α^* and β^* are set to be 0.25 and 0.5, respectively. The values of Rayleigh's coefficients α, β are taken as 10^2 rad.s^{-2} and 10^{-6}rad.s^{-1}, respectively for damping case and zeros for non-damping case. A time step of Δt=8.29x10^{-4} s is used. The first test is designed to demonstrate the effect of structural damping in terms of identifying the changes of 'f' factor caused by an applied electrical field to the actuator.

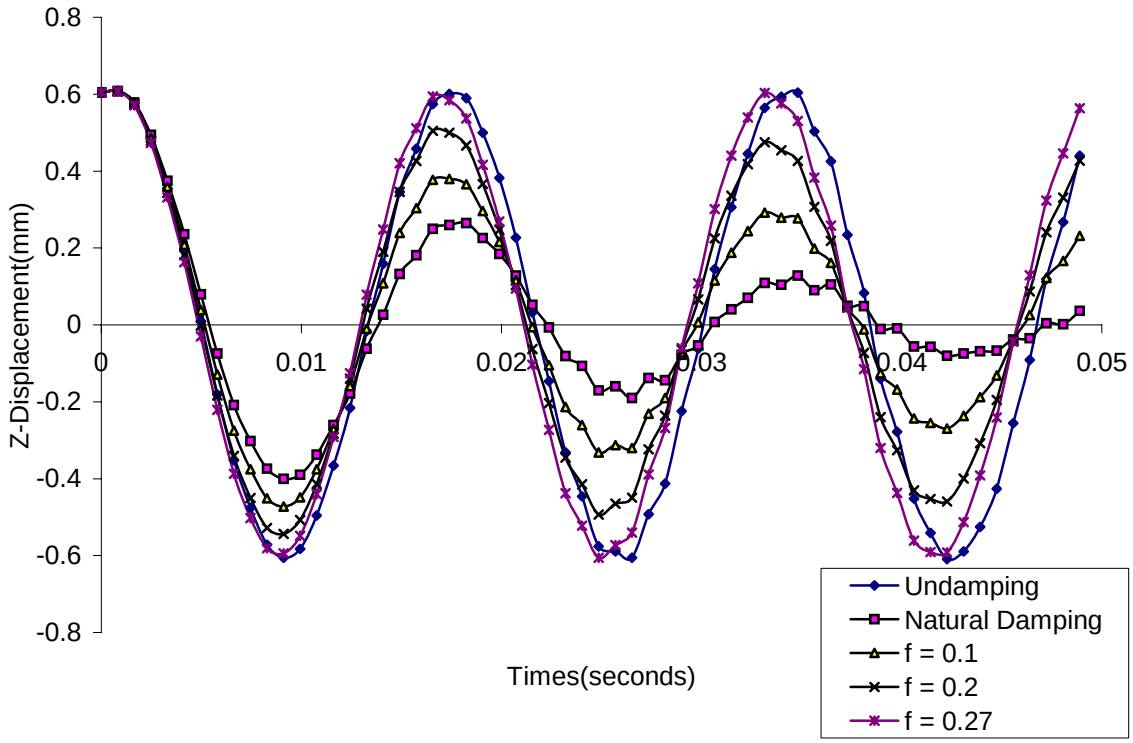

Figure 7.4: Structure response with different 'f' factor

Figure 7.4 presents the response of the plate under electrical fields with different 'f' factors and the same frequency. The results show that the transverse displacement at the point (0.15m, 0.03m) increases as the 'f' factor increases, and the amplitude of the non-damping case is approximately achieved when 'f' factor is about 0.27. It diverges when the 'f' factor is greater than 0.27. It can be seen that about 27% of voltage used in static shape control are required to maintain amplitude or to minimize the natural structural damping in the controlled resonant vibration. The results show a good agreement with the results obtained by Equation (7.20), where f is 0.264 when the frequency input is the same as natural frequency ($\Omega_1=\omega_1$). The plate has identical response to that of the non-damping case.

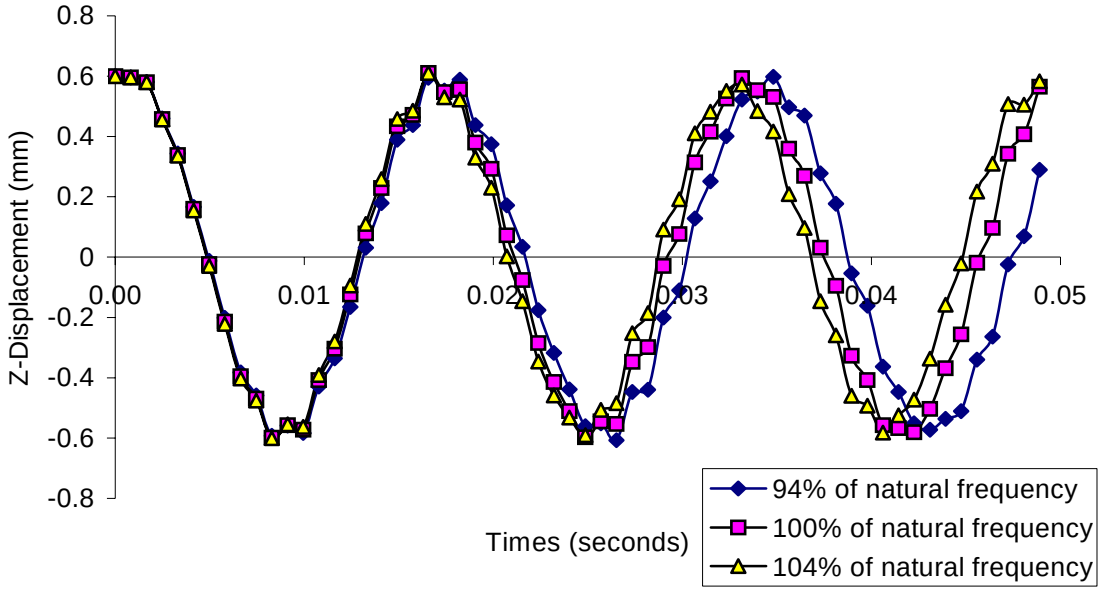

Figure 7.5: Structure response with different frequency input (Ω)

The second test is designed to demonstrate the effect of structural damping in terms of identifying the frequency changes caused by an applied electrical field to an actuator. A value for the 'f' factor of 0.264 is considered as an optimum factor to maintain the amplitude of resonant vibration at natural frequency (ω_1). Figure 7.5 depicts the response of the plate at point of (0.15m, 0.03m) under the electrical fields with slightly different frequency input (Ω_1). The results show that the structural damping is enlarged as the frequency is increased or decreased. It can be seen that it quickly converges as the frequency input (Ω_1) changes compared to the natural frequency (ω_1).

Therefore, the energy consumption must be increased by increasing the 'f' factor to reduce the structural damping caused by the frequency changing. The results also show that the amplitude of resonant vibration can be maintained with the frequency input in the range of $0.94\omega_1 \leq \Omega_1 \leq 1.04\omega_1$.

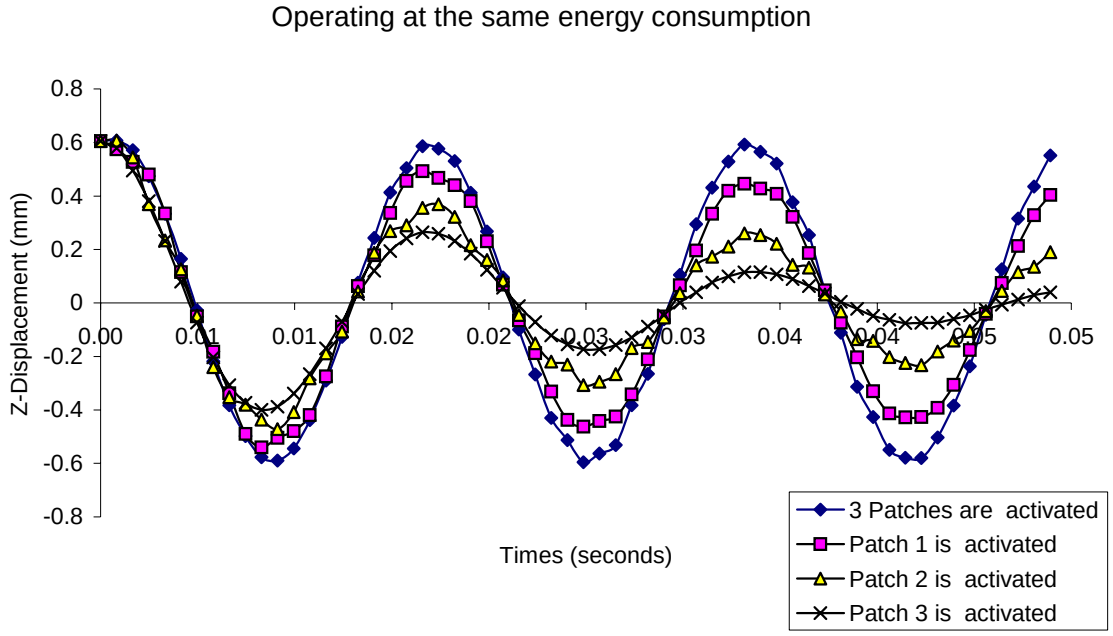

Figure 7.6: Structural response with different number and location of actuators

The third test is designed to investigate the effect of structural damping and energy consumption in terms of identifying the number and location of piezoelectric actuators. As known, the energy consumption is defined by the ratio of applied voltage (V) square and conductor (R) (V^2/R). According to the results from the first test of this example, where three piezoelectric actuator patches have been applied with an electric field, the total energy consumption of these actuator patches are considered as an optimal energy (V_o^2/R) to maintain the resonant vibration. Now considering that the plate performs with a single active actuator patch with the same amount of optimal energy consumption at a time. Particular, structural response with the root actuator can be observed by applying voltage to the patch 1, $\phi_1 = V_o$ Volts and 0.0 Volts on all other patches and repeating this for patches 2 and 3. The structural response with different active actuator patches at the selection node is shown in Figure 7.6. In this figure, the required minimum energy consumption to maintain amplitude can be clearly seen in the case with three active

piezoelectric actuator patches. The required energy consumption is more for cases with single active piezoelectric actuator patches. Particularly, the case which has active piezoelectric actuators located at the tip of the plate, requires much more energy than other cases to control the amplitude of resonant vibration. The case of three active actuators is also having the best performance in term of the error function. The result points out that the more active piezoelectric actuator patches that are considered, the less energy consumption is required and the best modal shapes can be achieved. Secondly, the effect of the location of the active piezoelectric actuator patches on the energy consumption.

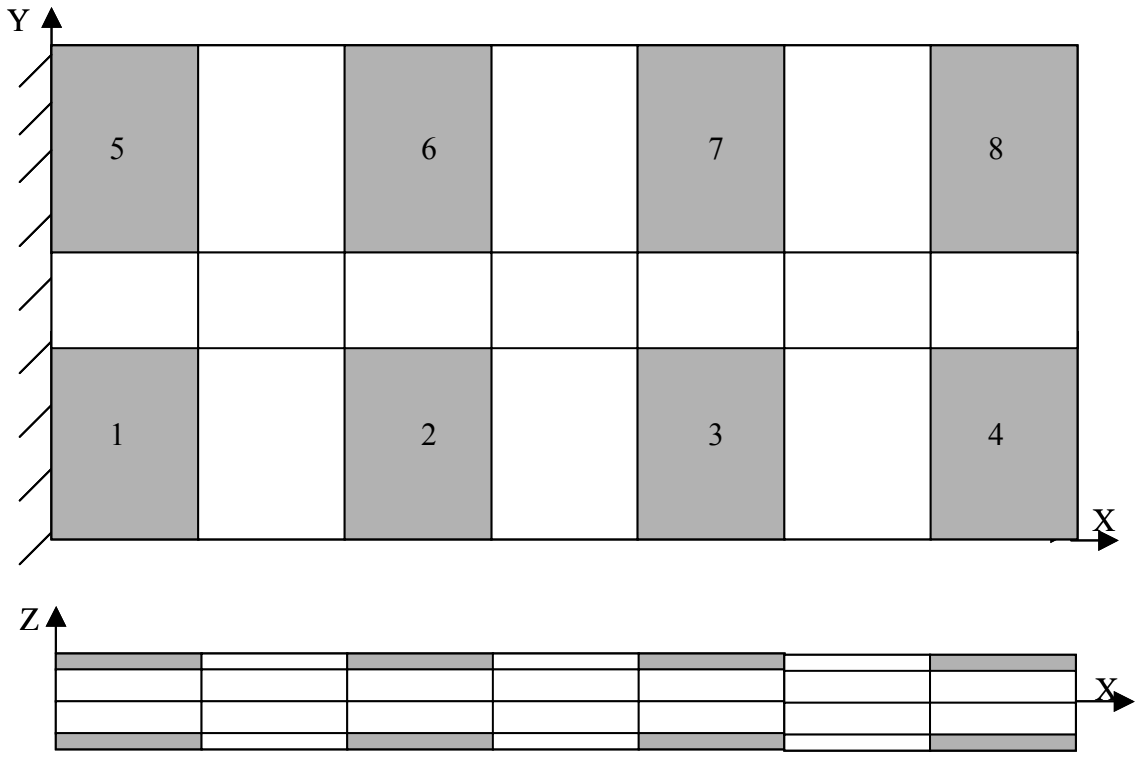

Figure 7.7: Cantilever plate in XY and XZ plane

7.3.2.2 Example 2

In the last example, only the first mode is considered. So this example demonstrates the applicability and performance of the present model in controlled resonant vibration of different mode. Consider a long cantilever plate, which is clamped at its left end, subjected to non-applied mechanical load. It has a length of 0.3 m, width of 0.15m and consists of 4 layers of thickness of 0.004 m in total. The material of the

plate has the following stiffness constants: $c_{11}=c_{22}=c_{33}=82.7$GPa, $c_{12}=c_{13}=c_{23}=27.6$GPa, $c_{44}=c_{55}=c_{66}=27.6$GPa; density $\rho=2780$kg/m^3. Eight pairs of piezoelectric actuators are bonded on the top and bottom of the plate. Only the top sets of actuator are activated and modelled using single elements as shown in Figure 7.7. The properties of the patches including the stiffness constants are: $c_{11}=c_{22}=c_{33}=84.8$GPa, $c_{12}=c_{13}=c_{23}=36.4$GPa, $c_{44}=c_{55}=c_{66}=24.2$GPa, density $\rho=8000$kg/m^3; the electric permittivity: $\chi_{11}=\chi_{22}=15.3\text{x}10^{-9}$F/M, $\chi_{33}=15.0\text{x}10^{-9}$F/M; and piezoelectric strain constants $d_{31}=-254$pm/V, $d_{32}=-204$pm/V, $d_{33}=374$pm/V, $d_{24}=484$pm/V, $d_{15}=584$pm/V. The Newmark method parameters α^* and β^* are set to be 0.25 and 0.5, respectively. The values of Rayleigh's coefficients α, β are taken as 10^2 rad.s^{-2} and 10^{-6}rad.s^{-1}, respectively for the damping case and zeros for the non-damping case. A time step of $\Delta t=8.29\text{x}10^{-4}$ s and $\Delta t=8.29\text{x}10^{-6}$ s is used for mode 1 and mode 4, respectively. Mode 2 and mode 3 considers time step of $\Delta t=8.29\text{x}10^{-5}$ seconds.

Table 7.2: Voltage distribution and electrical factor for cantilever plates in different modal shape

Mode	**1**	**2**	**3**	**4**
Frequencies (Hz)	29.80	127.10	189.80	412.90
Patches/Voltages(volts)				
1	-453.67	-4387.15	-3164.19	1440.93
2	-561.25	-4464.63	3379.16	16049.00
3	-196.49	-318.45	6695.12	10100.80
4	122.19	1769.82	-2324.72	-6754.74
5	-453.67	4386.30	-3177.73	-1443.40
6	-561.25	4465.52	3365.38	-16041.60
7	-196.49	320.23	6694.13	-10109.10
8	122.19	-1770.44	-2319.26	6755.34
Lnm	$2.59 \text{ x } 10^{-5}$	$1.08\text{x } 10^{-3}$	$1.54\text{x } 10^{-3}$	$7.92\text{x } 10^{-3}$
f - factors	0.53	0.13	0.09	0.04

Table 7.2 gives the natural frequencies and the optimum values of voltages applied to each patch, obtained from modal analysis and LLS method. In the first 4 modes, the natural frequencies are 29.8 Hz, 127.1 Hz, 189.8 Hz and 412.9 Hz, the values of the electrical field factors are 0.53, 0.13, 0.09 and 0.04 at an electric frequency input the same as the natural frequency, and the error functions are 2.59×10^{-5}, 1.08×10^{-3}, 1.54×10^{-3} and 7.92×10^{-3}, respectively. The maximum magnitudes of applied voltage for achieving the first four static modal shapes are 454 volts, 4465 volts, 6695 volts and 16049 volts, respectively. For the first four dynamic modal shapes, the maximum magnitudes of applied voltage are required to be 241 volts, 580 volts, 603 volts and 642 volts, respectively. It can be seen that the less applied voltage compared to voltage used in static modal shape control are required to maintain amplitude or to minimize the natural structural damping in the controlled resonant vibration. Table 7.2 shows that the magnitude of the applied voltage is high to achieve modal shape and the electric factor "f" is low for higher order mode. Figure 7.8, 7.9, 7.10, and 7.11 show the structural responses corresponding to the mode 1, 2, 3 and 4, respectively. The amplitude of resonant vibration is maintained with the frequency input within about ±5% tolerance of the natural frequency of i^{th} mode. The structural damping can be enlarged or reduced when the frequency input is considered out of that range.

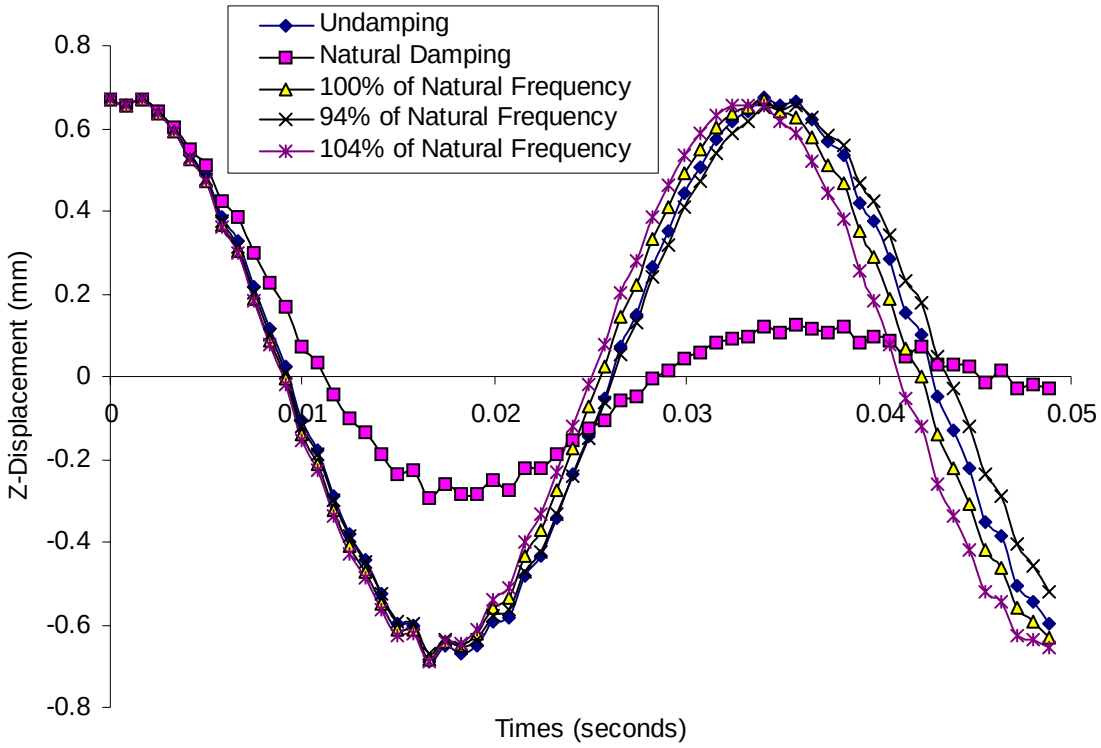

Figure 7.8: Mode 1

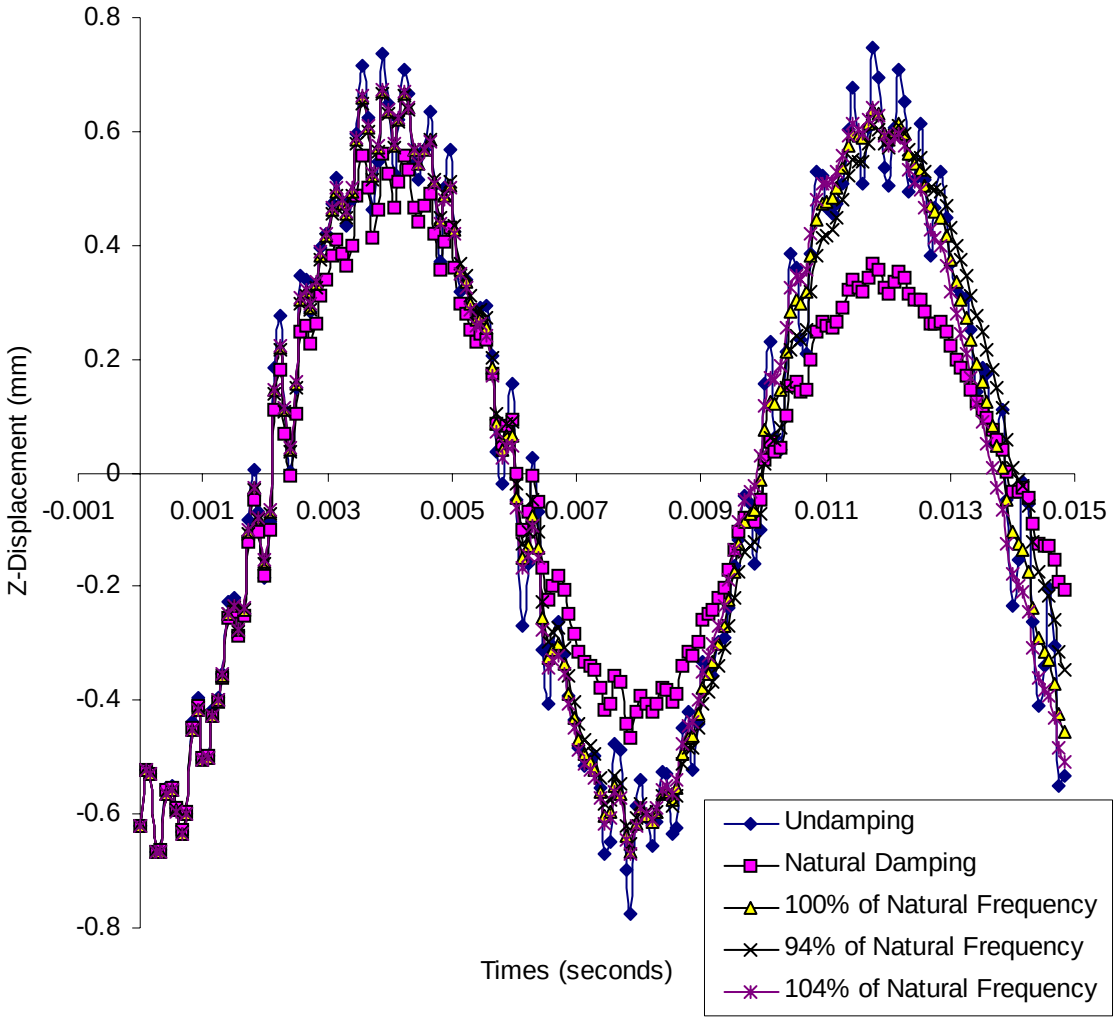

Figure 7.9: Mode 2

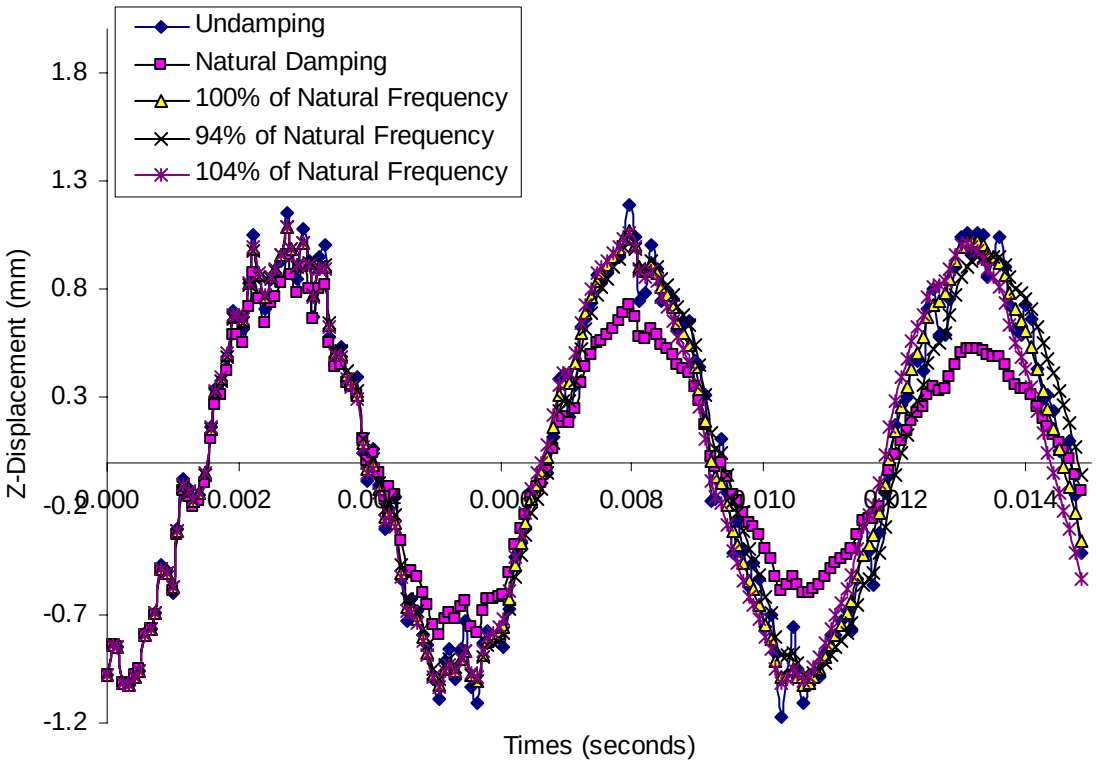

Figure 7.10: Mode 3

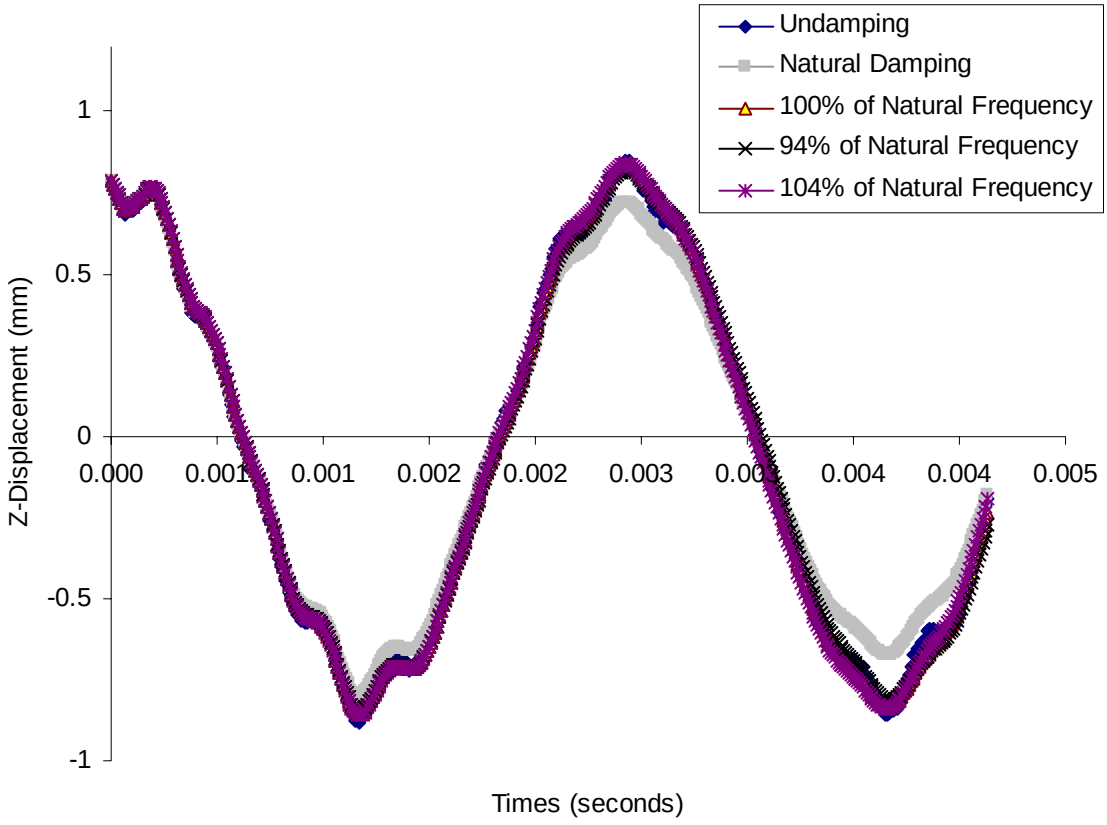

Figure 7.11: Mode 4

7.4 Summary

Code to implement the finite element formulation for static and dynamic analysis and control of smart composite plate structures has been developed. The program can be potentially used for optimal voltage distribution in piezoelectric actuators to control the modal shape and control the resonant vibration of smart composite plate structure. The illustrative examples have been presented and discussed. Firstly, for modal shape control, the numerical results show that high-energy consumption is required and it is hard to achieve the desired shape for the twisting problem. Finally, the electrical field can be applied to dynamic applications to minimise the natural structural damping and maintain a controlled resonant vibration. Based on the presented numerical study, the following salient points can be drawn: 1) the optimal voltage distributions for achieving modal shape can be rescaled by the electrical factor "f" to control the amplitude of harmonic excitation. For controlled resonant vibration of modal shapes, the required applied electrical fields are less than results from static modal shape analysis. 2) for controlled resonant vibration, the electrical forcing frequency input must be in the range of ±5% tolerance of the natural frequency. 3) the effects of the error function and energy consumption are caused by the number and location of the active piezoelectric actuator patches in the structure. Particularly, the more active piezoelectric actuators are used, the less energy consumption is required and the best modal shape can be achieved.

8. Conclusions

The main concluding remark of the present work has been summarised at the end of each chapter. This chapter presents an overview of the work done and achievements of this thesis. Following is a summary of some thoughts on some future directions for current research.

8.1 Overview

The main aim of the work in this thesis was to provide FE formulation, which uses third order plate theory to model the mechanical behaviour and layer wise method to model electric field, for laminated composite plate structures with irregular/non-rectangular elements. It is also a development of new shape control algorithms for the voltage and piezoelectric actuator design optimisation in the application of a quasi-static shape control of smart composite plate structures. These shape control algorithms were developed based on the techniques and features of existing methods such as LLS, GA and ESO, which were incorporated with the present FE formulation. This has been successfully achieved through the creation and application of the GA, CAA, GALLS (CCA), EPADO, AVEPADO and VEPADO algorithms. These algorithms can be used as tools for shape, location and evolutionary piezoelectric actuator design optimisation, where the applied voltage can be set as fixed variables or design variables. Beside static shape control, a controlled resonant vibration was also introduced. The complete body of work in this thesis comprises of the creation and development of these algorithms in the form of concepts, source code, testing and analysis. The most salient results are summarised below:

Firstly, the FE formulation using third order plate theory and layer wise concept for laminated composite plate structures with irregular/non-rectangular elements was successfully developed. It is capable to analyse the structure behaviour under influence of electric fields in the presence of piezoelectric materials. The transverse deflections are measured from experimental and numerical results obtained from different software

packages for smart cantilever plates and are used to validate the present formulation, which has shown a good correlation between the measured and predicted results. The additional numerical examples clearly showed the effect of the difference in piezoelectric actuators pattern on the results of error function and applied voltage for achieving of the desired structural shape.

Secondly, several algorithms for voltage and piezoelectric actuator design optimisation have been developed. Piezoelectric actuator design variables can be shape or location. These algorithms incorporate an iterative process of linear least square (LLS) method and genetic algorithm (GA) into finite element analysis, known as coupled alternating algorithm (CAA) and coupled concurrent algorithm (CCA or GALLS), which are the combination of voltage and piezoelectric actuator configuration optimisation. The presented numerical results showed that the proposed algorithms, GA, CAA and GALLS, are capable of finding the piezoelectric actuator configuration and voltage simultaneously. The local optimisation can be seen in CAA algorithm, while GA and GALLS algorithms give global optimal solution. The GALLS algorithm showed a reduction in total computational speed. The results obtained by these algorithms show that there is an improvement in the error function with the presence of design variables that define the shape and location of a piezoelectric actuator.

Thirdly, providing a framework for the use of the GA as a tool for quasi-static shape control of smart composite plate structures with additional constraints handling based on piezoelectric actuator configuration design and voltages optimisation. This has been successfully achieved through the creation and application of the quasi-static shape control of smart composite plate structures subjected to energy and error function constraints. For the constraint energy, a range of problems (including those with total energy consumption constraint, single applied voltage constraint and multiple applied voltage constraint) is considered to minimise the error function. On the other hand, the total energy consumption is optimised due to a given error function tolerance for the problems with the constraint of error function. The numerical results had shown that there was a relationship between the error function and the total energy consumption, that one can be used as a constraint to optimise the other. There was an effect of the additional constraint on the results of the objective function. Particularly, the error

function subject to an energy consumption constraint can be greater than the error function obtained from the same problem without constraint.

Fourthly, the LLS and ESO were successfully applied to quasi-static shape control of smart composite plate structure problems including the searching for applied voltage and active piezoelectric material distribution. The finite element (FE) formulation of the principle was derived using a third order displacement field theory for mechanical deformation and the linear layer-wise electric potential for electrical field. On the basis of FE analysis, the error function sensitivity number including electro-mechanical effect was derived to compute the change in error functions, which are defined in terms of the least squares difference between calculated and desired structural shapes. The active piezoelectric material part of the element which has the lowest value of error function sensitivity number, is gradually removed from the initial design of active actuator patch. EPADO (in Chapter 5), AVEPADO and VEPADO (in Chapter 6) algorithms were developed. In EPADO, the design variable of applied voltage was set as fixed and its value must be higher than or equal to voltage distribution obtained via LLS with initial piezoelectric actuator configuration. In the other two algorithms, the applied voltage was treated as design variable. VEPADO was performed with results that are qualitatively close to the optimal solution. It shows to be significantly better than AVEPADO. The presented numerical results obtained via these algorithms have shown that there is much improvement in error function in conjunction with the reduction of piezoelectric material usage. They are also capable to solve for any varied structural shape from simple (bended) to complex (twisted) structural shape.

Finally, controlled resonant vibration of smart composite plates using piezoelectric actuators was introduced. Numerical results were demonstrated to show the optimal values of electrical fields in the actuator to achieve modal shape and to induce harmonic vibration of the structure with controlled magnitude via adjusting the damping. The optimal voltage distributions for achieving modal shape can be rescaled by electrical factor “f” to control amplitude of harmonic excitation. For controlled resonant vibration of modal shape, the required applied electrical fields are less than results from static modal shape analysis. For controlled resonant vibration, the electrical forcing frequency input must be in the range of ±5% tolerance of natural frequency.

8.2 Future Work

As for future developments, a few issues have been identified

As seen in Chapter 2, in the numerical results, the deflection increases linearly with an increasing electrical field, whilst a non-linear curve is observed in the experimental results. The presented FE formulation did not consider non-linear terms in the constitutive equation. In this thesis, all demonstrated numerical examples are considered with a perfect bond between host plates and piezoelectric actuator patches. Therefore, the FE formulation for smart composite plate structure discussed in Chapter 2 can be used to extend further by adding an adhesive layer and the non-linear terms into the constitutive equation, and then to be verified by comparing with presented experimental results.

A framework of GA based for quasi-static shape control of smart composite plate structure with constraint handling was developed in Chapter 4 in which only the constraint of energy consumption, applied voltage and error function were considered. Future work will look at expanding the methods to include the consideration of stress and stiffness constraints as well as multiple objectives.

The EPADO, AVEPADO and VEPADO algorithms were restricted to one directional optimisation, which means that the completed block of active piezoelectric material in an element is gradually removed from initial design only. Future work will include extension to EPADO, AVEPADO and VEPADO algorithms, where the completed block of active piezoelectric material in an element can be regenerated or thinned (piezoelectric material thickness distribution) as well as the consideration of constraints.

Appendix A: Electric Potential Linearising

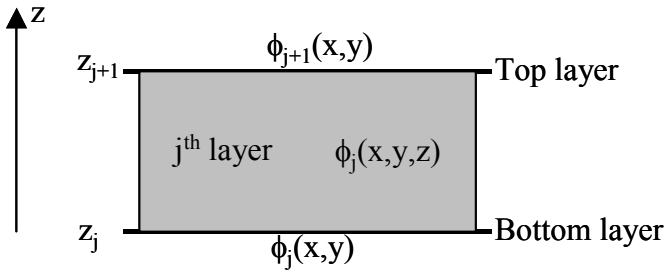

Figure A.1: Electric potential of j^{th} layer

The electric potential within the j^{th} layer has general linear form as shown

$$\phi_j(x,y,z) = mz + b$$

From the boundary condition

$$z = z_j \qquad \phi_j(x,y,z) = \phi_j(x,y)$$

$$z = z_{j+1} \qquad \phi_j(x,y,z) = \phi_{j+1}(x,y)$$

Hence

$$m = \frac{\phi_{j+1}(x,y) - \phi_j(x,y)}{z_{j+1} - z_j} \qquad b = \frac{z_{j+1}\phi_j(x,y) - z_j\phi_{j+1}(x,y)}{z_{j+1} - z_j}$$

And

$$\phi_j(x,y,z) = \frac{\phi_{j+1}(x,y) - \phi_j(x,y)}{z_{j+1} - z_j} z + \frac{z_{j+1}\phi_j(x,y) - z_j\phi_{j+1}(x,y)}{z_{j+1} - z_j}$$

Final equation for electric potential in j^{th} layer is:

$$\phi_j(x,y,z) = \frac{z - z_{j+1}}{z_j - z_{j+1}}\phi_j(x,y) + \frac{z - z_j}{z_{j+1} - z_j}\phi_{j+1}(x,y)$$

Appendix B: Shape Functions

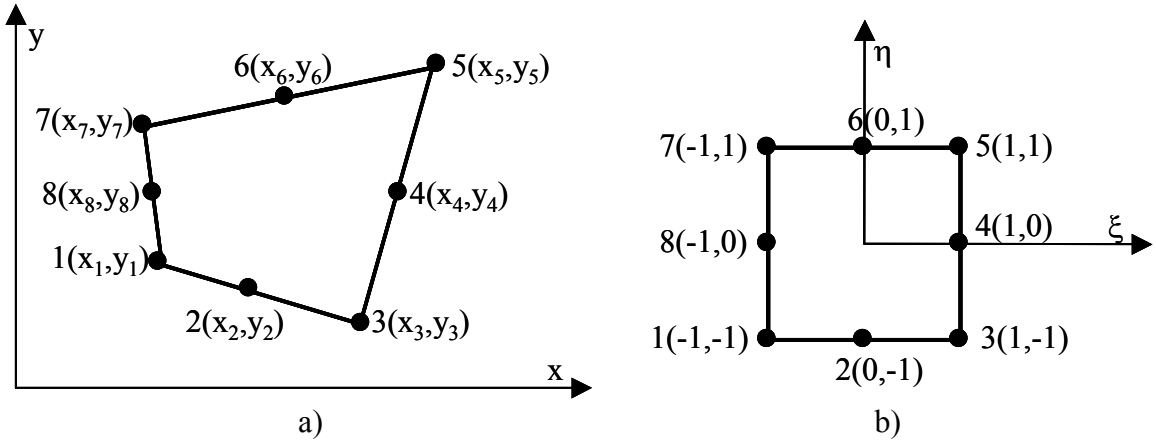

Figure B.1: a) 8-node non-rectangular element in global coordinates
b) 8-node square element in local coordinates

Figure B.1b shows the 8 node square element in local coordinates. The shape functions in terms local coordinates is represented in Equation (B.1)

$$N_1(\xi,\eta) = -\frac{1}{4}(1-\xi)(1-\eta)(1+\xi+\eta) \;; \qquad N_2(\xi,\eta) = \frac{1}{2}(1-\xi^2)(1-\eta)$$

$$N_3(\xi,\eta) = -\frac{1}{4}(1+\xi)(1-\eta)(1-\xi+\eta) \;; \qquad N_4(\xi,\eta) = \frac{1}{2}(1+\xi)(1-\eta^2) \qquad \text{(B.1)}$$

$$N_5(\xi,\eta) = -\frac{1}{4}(1+\xi)(1+\eta)(1-\xi-\eta) \;; \qquad N_6(\xi,\eta) = \frac{1}{2}(1-\xi^2)(1+\eta)$$

$$N_7(\xi,\eta) = -\frac{1}{4}(1-\xi)(1+\eta)(1+\xi-\eta) \;; \qquad N_8(\xi,\eta) = \frac{1}{2}(1-\xi)(1-\eta^2)$$

Equation (B.2) shows the differentiations of the shape functions with respect to ξ

$$N_{1,\xi}(\xi,\eta) = \frac{1}{4}(1-\eta)(2\xi+\eta) \quad ; \quad N_{2,\xi}(\xi,\eta) = -\xi(1-\eta)$$

$$N_{3,\xi}(\xi,\eta) = \frac{1}{4}(1-\eta)(2\xi-\eta) \quad ; \quad N_{4,\xi}(\xi,\eta) = \frac{1}{2}(1-\eta^2) \qquad \text{(B.2)}$$

$$N_{5,\xi}(\xi,\eta) = \frac{1}{4}(1+\eta)(2\xi+\eta) \quad ; \quad N_{6,\xi}(\xi,\eta) = -\xi(1+\eta)$$

$$N_{7,\xi}(\xi,\eta) = \frac{1}{4}(1+\eta)(2\xi-\eta) \quad ; \quad N_{8,\xi}(\xi,\eta) = -\frac{1}{2}(1-\eta^2)$$

The differentiations of the shape functions with respect to η is shown Equation (B.3)

$$\begin{aligned}
N_{1,\eta}(\xi,\eta) &= \frac{1}{4}(1-\xi)(2\eta+\xi) \quad ; \quad N_{2,\eta}(\xi,\eta) = -\frac{1}{2}(1-\xi^2) \\
N_{3,\eta}(\xi,\eta) &= \frac{1}{4}(1+\xi)(2\eta-\xi) \quad ; \quad N_{4,\eta}(\xi,\eta) = -\eta(1+\xi) \\
N_{5,\eta}(\xi,\eta) &= \frac{1}{4}(1+\xi)(2\eta+\xi) \quad ; \quad N_{6,\eta}(\xi,\eta) = \frac{1}{2}(1-\xi^2) \\
N_{7,\eta}(\xi,\eta) &= \frac{1}{4}(1-\xi)(2\eta-\xi) \quad ; \quad N_{8,\eta}(\xi,\eta) = -\eta(1-\xi)
\end{aligned} \tag{B.3}$$

By the chain rule, the differentiation of the shape functions with respect to x and y can be written in matrix form as shown in Equation (B.4)

$$\begin{bmatrix} \frac{\partial N_1(\xi,\eta)}{\partial x} & \frac{\partial N_1(\xi,\eta)}{\partial y} \\ \vdots & \vdots \\ \frac{\partial N_8(\xi,\eta)}{\partial x} & \frac{\partial N_8(\xi,\eta)}{\partial y} \end{bmatrix} = \begin{bmatrix} \frac{\partial N_1(\xi,\eta)}{\partial \xi} & \frac{\partial N_1(\xi,\eta)}{\partial \eta} \\ \vdots & \vdots \\ \frac{\partial N_8(\xi,\eta)}{\partial \xi} & \frac{\partial N_8(\xi,\eta)}{\partial \eta} \end{bmatrix} [\mathbf{J}]^{-1} \tag{B.4}$$

Where: $[\mathbf{J}] = \left|\frac{\partial(x,y)}{\partial(\xi,\eta)}\right| = \begin{bmatrix} \frac{\partial x}{\partial \xi} & \frac{\partial x}{\partial \eta} \\ \frac{\partial y}{\partial \xi} & \frac{\partial y}{\partial \eta} \end{bmatrix}$

J is called as Jacobian matrix. For numerical integration, the Jacobian can be defined as in Equation (B.5)

$$[\mathbf{J}] = \begin{bmatrix} \frac{\partial N_1(\xi,\eta)}{\partial \xi} & \cdots & \frac{\partial N_8(\xi,\eta)}{\partial \xi} \\ \frac{\partial N_1(\xi,\eta)}{\partial \eta} & \cdots & \frac{\partial N_8(\xi,\eta)}{\partial \eta} \end{bmatrix} \begin{bmatrix} x_1 & y_1 \\ \vdots & \vdots \\ x_8 & y_8 \end{bmatrix} \tag{B.5}$$

Appendix C: 3-D Transformation Matrix

Rotation about Z-Axis

$$\mathbf{T}_{3D} = \begin{bmatrix} \cos^2(\theta) & \sin^2(\theta) & 0 & 0 & 0 & 2\sin(\theta)\cos(\theta) \\ \sin^2(\theta) & \cos^2(\theta) & 0 & 0 & 0 & -2\sin(\theta)\cos(\theta) \\ 0 & 0 & 1 & 0 & 0 & 0 \\ 0 & 0 & 0 & \cos(\theta) & -\sin(\theta) & 0 \\ 0 & 0 & 0 & \sin(\theta) & \cos(\theta) & 0 \\ -\sin(\theta)\cos(\theta) & \sin(\theta)\cos(\theta) & 0 & 0 & 0 & \cos^2(\theta)-\sin^2(\theta) \end{bmatrix}$$

$$\mathbf{T}_{3D}^{-1} = \begin{bmatrix} \cos^2(\theta) & \sin^2(\theta) & 0 & 0 & 0 & -2\sin(\theta)\cos(\theta) \\ \sin^2(\theta) & \cos^2(\theta) & 0 & 0 & 0 & 2\sin(\theta)\cos(\theta) \\ 0 & 0 & 1 & 0 & 0 & 0 \\ 0 & 0 & 0 & \cos(\theta) & \sin(\theta) & 0 \\ 0 & 0 & 0 & -\sin(\theta) & \cos(\theta) & 0 \\ \sin(\theta)\cos(\theta) & -\sin(\theta)\cos(\theta) & 0 & 0 & 0 & \cos^2(\theta)-\sin^2(\theta) \end{bmatrix}$$

$$\mathbf{R} = \begin{bmatrix} 1 & 0 & 0 & 0 & 0 & 0 \\ 0 & 1 & 0 & 0 & 0 & 0 \\ 0 & 0 & 1 & 0 & 0 & 0 \\ 0 & 0 & 0 & 2 & 0 & 0 \\ 0 & 0 & 0 & 0 & 2 & 0 \\ 0 & 0 & 0 & 0 & 0 & 2 \end{bmatrix} \qquad \mathbf{R}^{-1} = \begin{bmatrix} 1 & 0 & 0 & 0 & 0 & 0 \\ 0 & 1 & 0 & 0 & 0 & 0 \\ 0 & 0 & 1 & 0 & 0 & 0 \\ 0 & 0 & 0 & 0.5 & 0 & 0 \\ 0 & 0 & 0 & 0 & 0.5 & 0 \\ 0 & 0 & 0 & 0 & 0 & 0.5 \end{bmatrix}$$

$$\mathbf{R}\mathbf{T}_{3D}\mathbf{R}^{-1} = \begin{bmatrix} \cos^2(\theta) & \sin^2(\theta) & 0 & 0 & 0 & \sin(\theta)\cos(\theta) \\ \sin^2(\theta) & \cos^2(\theta) & 0 & 0 & 0 & -\sin(\theta)\cos(\theta) \\ 0 & 0 & 1 & 0 & 0 & 0 \\ 0 & 0 & 0 & \cos(\theta) & -\sin(\theta) & 0 \\ 0 & 0 & 0 & \sin(\theta) & \cos(\theta) & 0 \\ -2\sin(\theta)\cos(\theta) & 2\sin(\theta)\cos(\theta) & 0 & 0 & 0 & \cos^2(\theta)-\sin^2(\theta) \end{bmatrix}$$

$$\mathbf{Q} = \begin{bmatrix} \cos(\theta) & \sin(\theta) & 0 \\ -\sin(\theta) & \cos(\theta) & 0 \\ 0 & 0 & 1 \end{bmatrix} \qquad \mathbf{Q}^{-1} = \begin{bmatrix} \cos(\theta) & -\sin(\theta) & 0 \\ \sin(\theta) & \cos(\theta) & 0 \\ 0 & 0 & 1 \end{bmatrix}$$

Appendix D: Local and Global Matrix

The local and global matrices are given below, note that the global property matrices in general contain more non-zero terms than their corresponding local orthotropic matrices. It is this set of global material matrices that will be used in the constitutive equation to model the structure.

Local Stiffness Matrix

$$\mathbf{c}_{\text{local}} = \begin{bmatrix} c'_{11} & c'_{12} & c'_{13} & 0 & 0 & 0 \\ c'_{12} & c'_{22} & c'_{23} & 0 & 0 & 0 \\ c'_{13} & c'_{23} & c'_{33} & 0 & 0 & 0 \\ 0 & 0 & 0 & c'_{44} & 0 & 0 \\ 0 & 0 & 0 & 0 & c'_{55} & 0 \\ 0 & 0 & 0 & 0 & 0 & c'_{66} \end{bmatrix}$$

Global Stiffness Matrix

$$\mathbf{c}_{\text{global}} = \begin{bmatrix} c_{11} & c_{12} & c_{13} & 0 & 0 & c_{16} \\ c_{12} & c_{22} & c_{23} & 0 & 0 & c_{26} \\ c_{13} & c_{23} & c_{33} & 0 & 0 & c_{36} \\ 0 & 0 & 0 & c_{44} & c_{45} & 0 \\ 0 & 0 & 0 & c_{45} & c_{55} & 0 \\ c_{16} & c_{26} & c_{36} & 0 & 0 & c_{66} \end{bmatrix}$$

Local Piezoelectric Stress Constant Matrix

$$\mathbf{e}_{\text{local}} = \begin{bmatrix} 0 & 0 & 0 & 0 & e'_{15} & 0 \\ 0 & 0 & 0 & e'_{24} & 0 & 0 \\ e'_{31} & e'_{32} & e'_{33} & 0 & 0 & 0 \end{bmatrix}$$

Global Piezoelectric Stress Constant Matrix

$$\mathbf{e}_{\text{global}} = \begin{bmatrix} 0 & 0 & e'_{31}\cos^2(\theta) + e'_{32}\sin^2(\theta) \\ 0 & 0 & e'_{32}\cos^2(\theta) + e'_{31}\sin^2(\theta) \\ 0 & 0 & e'_{33} \\ (e'_{15} - e'_{24})\cos(\theta)\sin(\theta) & e'_{24}\cos^2(\theta) + e'_{15}\sin^2(\theta) & 0 \\ e'_{15}\cos^2(\theta) + e'_{24}\sin^2(\theta) & (e'_{15} - e'_{24})\cos(\theta)\sin(\theta) & 0 \\ 0 & 0 & (e'_{31} - e'_{32})\cos(\theta)\sin(\theta) \end{bmatrix}$$

Local Piezoelectric Strain Constant Matrix

$$\mathbf{d}_{\text{local}} = \begin{bmatrix} 0 & 0 & 0 & 0 & d'_{15} & 0 \\ 0 & 0 & 0 & d'_{24} & 0 & 0 \\ d'_{31} & d'_{32} & d'_{33} & 0 & 0 & 0 \end{bmatrix}$$

Local Electrical Permittivity Matrix

$$\boldsymbol{\chi}_{\text{local}} = \begin{bmatrix} \chi'_{11} & 0 & 0 \\ 0 & \chi'_{22} & 0 \\ 0 & 0 & \chi'_{33} \end{bmatrix}$$

Global Electrical Permittivity Matrix

$$\boldsymbol{\chi}_{\text{global}} = \begin{bmatrix} \chi'_{11}\cos^2(\theta) + \chi'_{22}\sin^2(\theta) & (\chi'_{11} - \chi'_{22})\sin(\theta)\cos(\theta) & 0 \\ (\chi'_{11} - \chi'_{22})\sin(\theta)\cos(\theta) & \chi'_{22}\cos^2(\theta) + \chi'_{11}\sin^2(\theta) & 0 \\ 0 & 0 & \chi'_{33} \end{bmatrix}$$

Appendix E: 3x3 Gaussian Numerical Integration

The *3x3* Gaussian numerical integration operates by evaluating the function at the specific points, multiplying the resulting number by an appropriate weighting factor, and adding the results. It is applied to the integration of stiffness matrix to be integrated over the element area.

For a plane element, the area can be defined as in Equation E.1

$$A = \int_{y_1}^{y_2}\int_{x_1}^{x_2} dxdy \tag{E.1}$$

An area of an element having limits of $x_1 \le x \le x_2$ and $y_1 \le y \le y_2$ (element in global coordinates) can be transformed into an area of an element having $-1 \le \xi \le 1$ and $-1 \le \eta \le 1$ (element in local coordinates) by using isopametric shape function (see Appendix B) which is for 8 nodes plate element. The isoparmetric formulation incorporates the limit change. Thus Equation E.1 becomes

$$A = \int_{-1}^{1}\int_{-1}^{1}\left|\frac{\partial(x,y)}{\partial(\xi,\eta)}\right| d\xi d\eta \tag{E.2}$$

By Gauss rules, the area can be expressed in term of Gauss-Legendre coefficients

$$A = \sum_{i=1}^{3}\sum_{j=1}^{3}\left|\frac{\partial(x,y)}{\partial(\xi_i,\eta_j)}\right| W_i W_j \tag{E.3}$$

Where:

$$[\xi_1 \quad \xi_2 \quad \xi_3] = \left[-\sqrt{0.6} \quad 0 \quad \sqrt{0.6}\right]$$

$$[\eta_1 \quad \eta_2 \quad \eta_3] = \left[-\sqrt{0.6} \quad 0 \quad \sqrt{0.6}\right]$$

$$[W_1 \quad W_2 \quad W_3] = \left[\frac{8}{9} \quad \frac{8}{9} \quad \frac{8}{9}\right]$$

Appendix F: Auto Mesh Generation

The aim of this section is to describe the capability and the limitation of the auto mesh generation routines. It can help users to understand how to use the developed software can to correctly model a structure. There was no attempt to design the auto mesh generation routines to emulate existing auto mesh generation routines and the simple auto mesh generation routines are sufficient for the current research purposes

Capability

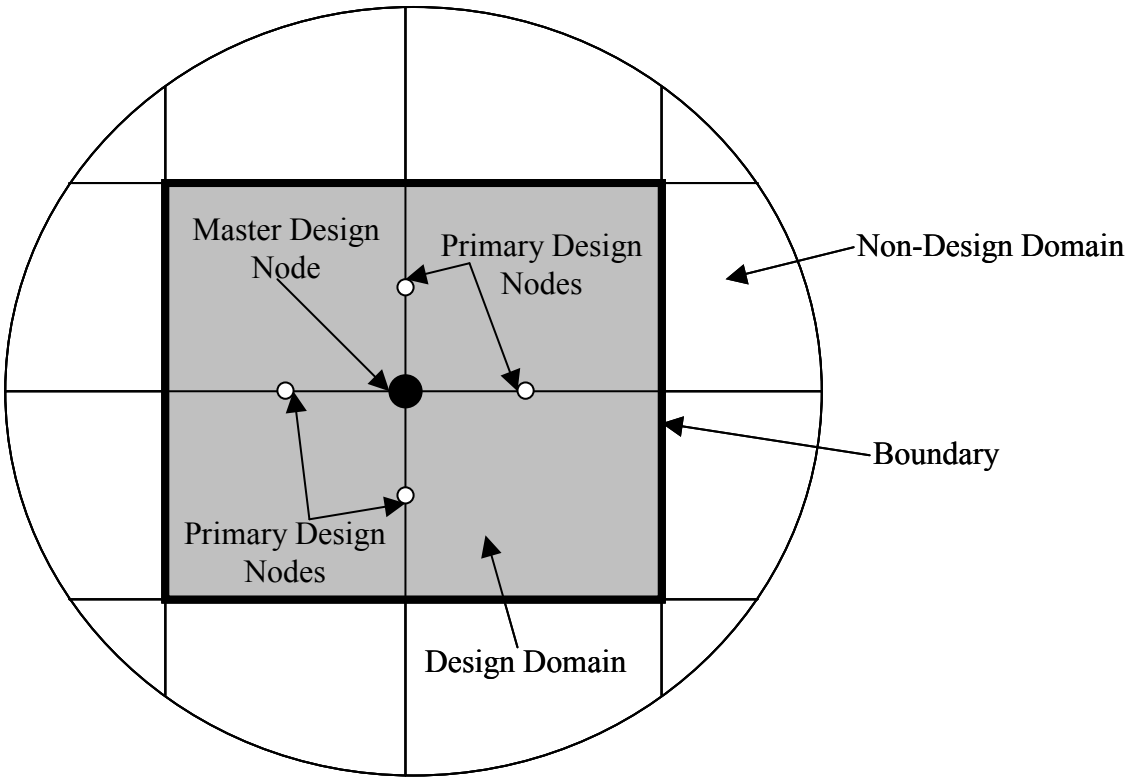

Figure F.1: FE Mesh Model

As the 8 nodes non-rectangular element using in the developed FEA software, only the comer nodes can be used as design variables for piezoelectric actuator shape optimisation in this thesis. Refer to Figure F.1; the shaded region is identified as a design domain in which there are 1 master design node, 5 primary design nodes and 4 elements. The primary design nodes are automatic recalculated based on the movement of master design node (main design variable).

Limitation and Possibility Results

1) Master design node is allowed to move within the design domain (shaded region as shown in Figure F.1 exclude the boundary line) to avoid overlap mesh.
2) Due to the capability in FEA software that the general structure is modelled as laminated composite (in other word, the element identification in each layer through thickness is identical). There is few possible results occur during auto mesh generation on the resulting of structure modelling.

   Example: Model has 3 layers as shown in Figure F.2. Due to change in the master design node, Figure F.2a and F.2b show the geometrical of structure before and after.

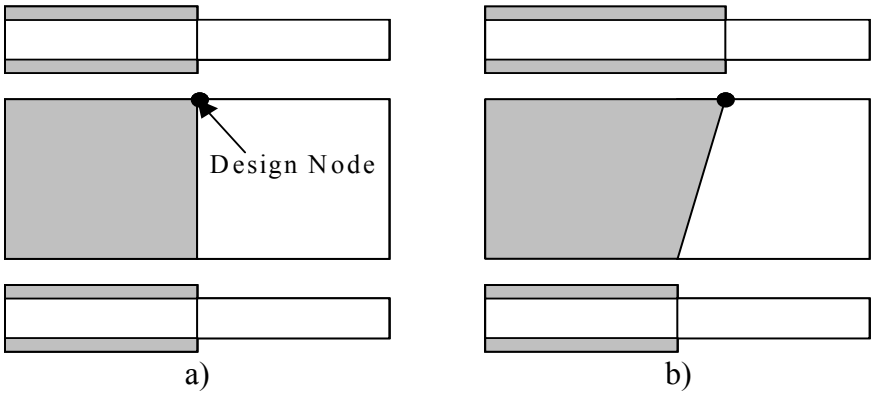

Figure F.2: Model in XY, YZ plane

3) If all elements within each layer have the same material identity then there is no effect in materials due to change in FE mesh. Otherwise, it happens as shown in Figure F.3. In particular, Figure F.3a shows the initial volume of material 1 and 2. When design node is shifted to left then the volume of material 1 is decreased in conjunction of increasing in volume of material 2 as shown in Figure F.3b.

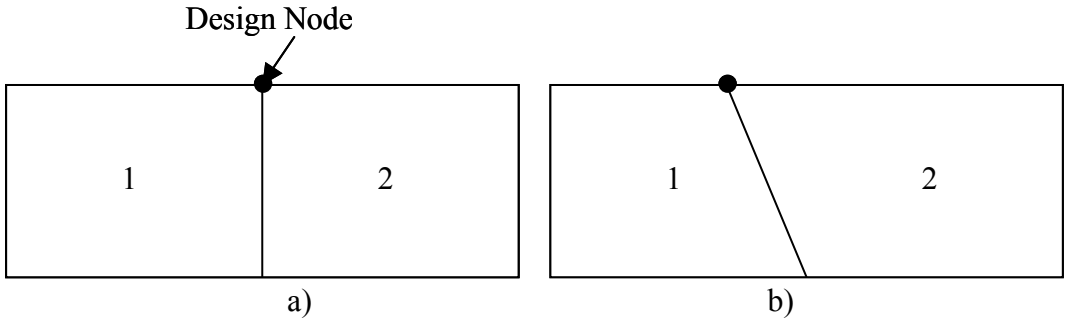

Figure F.3: FE Mesh in XY plane

Appendix G: Partial Differentiation of Error Function

Error function differentiation with respect to i^{th} displacement components

$$\mathrm{Lnm}(\mathbf{S}) = \frac{\sum_{i=1}^{N} \frac{\left(w_i^d - w_i^c(\mathbf{S})\right)^2}{\left(w_{max}^d\right)^2}}{4 \times N} \tag{G.1}$$

$$\Leftrightarrow \mathrm{Lnm}(\mathbf{S}) = \frac{\left(w_1^d - w_1^c(\mathbf{S})\right)^2 + \left(w_2^d - w_2^c(\mathbf{S})\right)^2 + \cdots + \left(w_i^d - w_i^c(\mathbf{S})\right)^2 + + \left(w_N^d - w_N^c(\mathbf{S})\right)^2}{4 \times N \times \left(w_{max}^d\right)^2} \tag{G.2}$$

Then

$$\left(w_i^c(\mathbf{S}) - w_i^d\right)^2 = \left((w_i^c(\mathbf{S}))^2 - 2w_i^c(\mathbf{S})w_i^d + (w_i^d)^2\right) \tag{G.3}$$

By differentiation with respect to w_i^c, Equation G.3 becomes

$$\frac{\partial\left(w_i^c(\mathbf{S}) - w_i^d\right)^2}{\partial w_i^c(\mathbf{S})} = \frac{\left(2w_i^c(\mathbf{S}) - 2w_i^d\right)}{\left(4 \times N \times (w_{max}^d)^2\right)} = \frac{\left(w_i^c(\mathbf{S}) - w_i^d\right)}{\left(2 \times N \times (w_{max}^d)^2\right)} \tag{G.4}$$

$$\therefore \frac{\partial h}{\partial w_i^c(\mathbf{S})} = \frac{\left(w_i^c(\mathbf{S}) - w_i^d\right)}{\left(2 \times N \times (w_{max}^d)^2\right)} \tag{G.5}$$

Appendix H: Multiple Virtual Systems

The solution for i^{th} virtual system

$$[\mathbf{K}_{uu}(\mathbf{S})][\mathbf{u}^{ji}] = [\mathbf{f}^{i}] \tag{H.1}$$

Multiply the gradient component $\frac{\partial h}{\partial w_i^c(\mathbf{S})}$ with the Equation H.1 above yields

$$[\mathbf{K}_{uu}(\mathbf{S})]\frac{\partial h}{\partial w_i^c(\mathbf{S})}[\mathbf{u}^{ji}] = \frac{\partial h}{\partial w_i^c(\mathbf{S})}[\mathbf{f}^{i}] \tag{H.2}$$

Adding all such N virtual equilibrium equations as given above. Hence

$$[\mathbf{K}_{uu}(\mathbf{S})]\sum_{i=1}^{N}\frac{\partial h}{\partial w_i^c(\mathbf{S})}[\mathbf{u}^{ji}] = \sum_{i=1}^{N}\frac{\partial h}{\partial w_i^c(\mathbf{S})}[\mathbf{f}^{i}] \tag{H.3}$$

Then

$$[\mathbf{K}_{uu}(\mathbf{S})][\bar{\mathbf{u}}] = [\bar{\mathbf{f}}] \tag{H.4}$$

$$\text{where } [\bar{\mathbf{u}}] = \sum_{i=1}^{N}\frac{\partial h}{\partial w_i^c(\mathbf{S})}[\mathbf{u}^{ji}] \text{ and } [\bar{\mathbf{f}}] = \sum_{i=1}^{N}\frac{\partial h}{\partial w_i^c(\mathbf{S})}[\mathbf{f}^{i}]$$

$$\therefore [\bar{\mathbf{u}}] = [\mathbf{K}_{uu}(\mathbf{S})]^{-1}[\bar{\mathbf{f}}] = [\mathbf{K}_{uu}(\mathbf{S})]^{-1}\sum_{i=1}^{N}\frac{\partial h}{\partial w_i^c(\mathbf{S})}[\mathbf{f}^{i}] \tag{H.5}$$

Hence the error function sensitivity number due to removing active piezoelectric part of the j^{th} element is

$$\Delta Lnm^{j} = [\bar{\mathbf{u}}^{j}]^{T}([\Delta\mathbf{K}_{uu}^{j}][\mathbf{u}_{g}^{j}] + [\Delta\mathbf{K}_{u\phi}^{j}][\boldsymbol{\phi}_{g}^{j}]) \tag{H.6}$$

References

Austin F., Rossi M. J., Vannostrand W., Knowles G. and Jameson A., 1994, "Static Shape Control for Adaptive Wings", *AIAA Journal*, Vol. 32 (9), pp. 1895-1901.

Agrawal S. K., Tong D. Q. and Nagaraja K., 1994, "Modeling and Shape Control of Piezoelectric Actuator Embedded Elastic Plates", *Journal of Intelligent Material Systems and Structures*, Vol. 5 (4), pp. 514-521.

Akella P., Cheng X., Hughes D. and Wen J. T., 1994, "Modelling and Shape Control of Smart Structures with Bonded Piezoelectric Sensors and Actuators", *Smart Materials and Structures*, Vol. 3 (3), pp. 344-353.

Allik H. and Hughes T. J. R., 1970, "Finite Element Method for Piezoelectric Vibration", *International Journal for Numerical Methods in Engineering*, Vol. 2, pp. 151-157.

Balas M. J., 1985, "Optimal Quasi-static Shape Control for a Large Space Antenna", *Journal of Optimisation Theory and Applications*, Vol. 46 (2), pp. 153-170.

Bendsøe M. P. and Kikuchi N., 1988, "Generating Optimal Topologies in Structural Design using Homogenisation Methods", *Computer Methods in Applied Mechanics and Engineering*, Vol. 71, pp. 197-224.

Bendsøe M. P., 1995, "Optimisation of Structural: Topology, Shape and Material", *Springer-Verlage*, Berlin.

Bhavikatti S. S. and Ramakrishnan C. V., 1977, "Optimum Design of Fillets in Flat and Round Tension Bars", ASME-77-DET-45.

Botkin M. E. and Bennett J. A., 1985, "Optimisation of Three Dimensional Folded Plate Structures", *AIAA Journal*, Vol. 23 (11), pp. 1804-1810.

Braibant V. and Fleury C., 1984, "Shape Optimal Design using B-spline", *Computer Methods in Applied Mechanics and Engineering*, Vol. 44 (3), pp. 247-267.

Bruch J. C. J., Sloss J. M., Adali S. and Sadek I. S., 2000, "Optimal Piezoelectric-Actuator Locations/Lengths and Applied Voltage for Shape Control of Beams", *Smart Materials and Structures*, Vol. 9, pp. 205-211.

Chaudhry Z. and Roger C. A., 1994, "Performance and Opimisation Induced Strain Actuated Structures under External Loading", *AIAA Journal*, Vol. 32 (6), pp. 1289-1294.

Chandrashekhara K. and Varadarajan S., 1997, "Adaptive Control of Composite Beams with Piezoelectric Actuators", *Journal of Intelligent Material System and Structures*, Vol. 8 (2), pp. 112-124.

Chandrupatla T. R. and Belegundu A. D., 2001, "Introduction to Finite Elements in Engineering", Upper Saddle River, N. J.: Prentice Hall, 3rd Edition.

Chee C., Tong L. and Steven G., 1999, "A Mixed Model for Composite Plates with Piezoelectric Actuator and Sensor", *The Second Australasian On Applied Mechanics*, pp. 421-426, *Computers and Structures*, Vol. 9 (1), pp. 3-19.

Chee C., Tong L. and Steven G., 2000a, "A Mixed Model for Adaptive Composite Plates with Piezoelectric for Anisotropic Actuation", *Computers and Structures*, Vol. 77 (3), pp. 253-268.

Chee C., Tong L. and Steven G., 2000b, "A Buildup Voltage Distribution (BVD) Algorithm for Shape Control of Smart Plate Structures", C*omputational Mechanics*, Vol. 26, pp. 115-128.

Chee C. Y. K., 2000c, "Static Shape Control of Laminated Composite Plate Smart Structures using Piezoelectric Actuators", PHD Thesis, Department of Aeronautical Engineering, The University of Sydney, Australia.

Chee C., Tong L. and Steven G., 2001, “Static Shape Control of Composite Plates using a Curvature–Displacement based Algorithm”, *International Journal of Solids and Structures*, Vol. 38, pp. 6381-6403.

Chee C., Tong L. and Steven G., 2002a, “Piezoelectric Actuator Orientation Optimisation for Static Shape Control of Composite Plates”, *Composite Structures*, Vol. 55, pp. 169-184.

Chee C., Tong L. and Steven G., 2002b, “Shape Control of Composite Plates using a Slope-Displacement-based Algorithm”, *AIAA Journal*, Vol. 40, pp. 1611-1618.

Chen W. M., Wang D. J. and Li M., 2004, “Static Shape Control Employing Displacement-Stress Dual Criteria”, *Smart Materials and Structures*, Vol. 13 (3), pp. 468-472.

Cheng T. Y., 1998, “A Comprehensive Solution for Enhancing the Efficiency and the Robustness of the SLP Algorithm”, *Computers and Structures*, Vol. 66, pp. 373-384.

Chopra I., 2002, “Review State of Art of Smart Structures and Integrated Systems”, *AIAA Journal*, Vol. 40 (11), pp. 2145-2187.

Chu D. N., Xie Y. M., Hira A. and Steven G. P., 1996, “Evolutionary Structure Optimisation for Problem with Stiffness Constraints”, *Finite Elements in Analysis and Design*, Vol. 21, pp. 239-251.

Cook R. D., Malkus D. S. and Plestia M. E., 1989, *Concepts and application of finite elements analysis*, 3rd Edition, Chapter 6, pp. 163-176.

Crawley E. F, and Deluis J., 1987, “Use of Piezoelectric Actuators as an Elements of Intelligent Structures”, *AIAA Journal*, Vol. 25 (10), pp. 1373-1384.

Crawley E. F, Deluis J., Hagod N. W. and Anderson E. H., 1988, “Development of Piezoelectric Technology for Application in Control of Intelligent Structures”, *Proceeding of the 1988 American Control Conference, Atlanta,* Georgia, USA, pp. 1890-1896.

Crawley E. F. and Lazarus K. B., 1991, “Induced Strain Actuation of Isotropic and Anisotropic Plates”, *AIAA Journal*, Vol. 29 (6), pp. 944-951.

Dantzig G., 1948-1963, “Linear Programming and Extensions”, *Princeton University Press*, USA.

Della Santa A., De Rossi D. and Mazzoldi A., 1997, “Characterisation and Modelling of a Conducting Polymer Muscle Like Linear Actuator”, *Smart Materials and Structures*, Vol. 6, pp. 23-34.

Ding Y., 1986, “Shape Optimisation of Structure”, A Literatures Survey, *Computers and Structures*, pp. 985-1004.

Donthireddy P. and Chandrashekhara K., 1996, “Modelling and Shape Control of Composite Beams with Embedded Piezoelectric Actuator”, *Composite Structures*, Vol. 35 (2), pp. 237-244.

Eisenberger M. and Abramovich H., 1997, “Shape Control of Non-Symmetric Piezolaminated Composite Beams”, *Composite Structures*, Vol. 38 (1-4), pp. 565-571.

Furuya H. and Haftka R., 1996, “Combining Genetic and Deterministic Algorithm for locating Actuator on Space Structures”, *Journal of Spacecraft and Rockets*, Vol. 33 (3), pp. 422-427.

Gallagher R. H. and Zienkiewicz O. C., “Optimum Structural Design”, *Theory and Applications*, Chapter 7, London, New York, Wiley 1973.

Gandhi M. V. and Thompson B. S., 1992, “Smart Materials and Structures”, London, UK Chapman and Hall, Chapters 3-7.

Ghosh K. G. and Batra R. C., 1995, “Shape Control of Plates using Piezoceramic Elements”, *AIAA Journal*, Vol. 33 (7), pp. 1354-1357.

Goldberg D. E., 1989, “Genetic Algorithm in Search, Optimisation and Machine Learning”, *Addison-Wesley Publishing Company*.

Gopinathan S. V., Varadan V. V. and Varadan V. K., 2000, “A Review and Critique of Theories for Piezoelectric Laminates”, *Smart Materials and Structures*, Vol. 9, pp. 24-48.

Gornandt A. and Gabbert U., 2002, “Finite Element Analysis of Thermopiezoelectric Smart Structures”, *ACTA Mechanic*, Vol. 154 (1-4), 129-140.

Griffithand R. E. and Stewart R. A., 1961, “A Nonlinear Programming Technique for the Optimisation of Continuous Processing Systems”, *Management Science*, Vol. 7, pp. 379-392.

Gu H., Chattopadhyay A., Li J. and Zhou X., 2000, “A High Order Temperature Theory for Coupled Thermo-Piezoelectric-Mechanical Modelling of Smart Composite”, *International Journal of Solids and Structures*, Vol. 37, pp. 6479-6497.

Ha S. K., Keilers C. and Chang F. K., 1992, “Finite Element Analysis of Composite Structures Containing Distributed Piezoceramic Sensors and Actuators”, *AIAA Journal*, Vol. 30 (3), pp. 772-780.

Hac A. and Lui L., 1993, “Sensor and Actuator Location in Motion Control of Flexible Structures”, *Journal of Sound Vibration*, Vol. 167, pp. 239-261.

Hadley G., 1964, “Non-Linear and Dynamic Programming”, *Addison-Wesley, Reading, Mass*.

Haftka R. T. and Grandhi R. V., 1986, “Structural Shape Optimisation – a Survey”, *Computer Methods in Applied Mechanics and Engineering*, Vol. 57, pp. 91-106.

Haftka R. T. and Gurdal Z., 1992, "Element of Structural Optimisation", 3rd Edition, Kluwer, Academic, Netherlands.

Hajela P. and Woo J., 1996, "Constraint Handling in Genetic Search using Expression Strategies", *AIAA Journal*, Vol. 34 (12), pp. 2414-2420.

Hajela P. and Lee J., 1996, "Constrained Genetic Search via Schema Adaptation: An Immune Network Solution", *Proceeding of the First World Congress of Structural and Multidisciplinary Optimisation*, Goslar, Germany, Eds. Olhoff N. and GIN Rozvany, Pergamon Press, pp. 914-920.

Hajela P., Woo J. and Lee J., 1997, "GA Based Simulation of Immune Network Application in Structural Optimisation", *Engineering Opt*, Vol. 29, pp. 131-149.

Hall D. L. and Flatau A. B., 1998, "On Analog Feedback Control for Magnetostrictive Transducer Linearisation", *Journal of Sound and Vibration*, Vol. 211 (3), pp. 481-494.

Han J. H. and Lee I., 1999, "Optimal Placement of Piezoelectric Sensors and Actuators for Vibration Control of Composite Plate using Genetic Algorithm", *Smart Materials and Structures*, Vol. 8 (2), pp. 257-267.

Hassani B. and Hinton E., 1998, "A Review of Homogenisation and Topology Optimisation III - Topology Optimisation using Optimality Criteria", *Computers and Structures*, Vol. 69, pp. 739-756.

Heyliger P., 1994, "Static Behaviour of Laminated Elastic/Piezoelectric Plates", *AIAA Journal*, Vol. 32 (12), pp. 2481-2484.

Heyliger P. and Saravanos D. A., 1995, "Exact Free Vibration Analysis of Laminated Plates with Embedded Piezoelectric Layer", *Journal of Acoustical Society of America*, Vol. 98 (3), pp. 1547-1557.

Heyliger P. and Brooks S., 1996, “Exact Solutions for Laminated piezoelectric Plates in Cylindrical Bending”, *Transactions of the ASME: Journal of Applied Mechanics*, Vol. 63, pp. 903-910.

Heyliger P., 1997, “Exact Solutions for Simply Supported Laminated Piezoelectric Plates”, *Transactions of the ASME*: *Journal of Applied Mechanics*, Vol. 64, pp. 299-306.

Hodgson D. E., Wu M. H., and Biermann R. J., 1996, Shape Memory Alloys, MiTi smart sheet, Shape Memory Applications Homepage.

Holland J. H., 1975, “Adaptations in Natural and Artificial System”, *MIT Press*, London England.

Im S. and Atluri S. N., 1989, “Effects of a Piezo-Actuator on a Finitely Deformed Beam Subjected to General Loading”, *AIAA Journal*, Vol. 27 (12), pp. 549-564.

Imam M. H., 1982, “Three Dimensional Shape Optimisation”, *International Journal of Numerical Methods in Engineering*, Vol. 18, pp. 661-673.

Irschik H., 2002, “A Review on Static and Dynamic Shape Control of Structures by Piezoelectric Actuation”, *Engineering Structures*, Vol. 24, pp. 5-11.

Irschik H., Krommer M. and Pichler U., 2003, “Dynamic Shape Control of Beam Type Structures by Piezoelectric Actuation and Sensing”, *International Journal of Applied Eclectromagnetics and Mechanics*, Vol. 17, pp. 251-258.

Kabir H. R. H., 1995, “A Shear Locking Free Robust Isoparametric Three-Nodes Triangular Finite Element for Moderately-Thick and Thin Arbitrarily Laminated Plates”, *Computers and Structures*, Vol. 57 (4), pp. 589-597.

Kang Y. K., Park H. C., Hwang W. and Han K. S., 1996, “Optimum Placement of Piezoelectric Sensor/Actuator for Vibration Control of Laminate Beams”, *AIAA Journal*, Vol. 34, pp. 1921-1926.

Kang Y. K., Park H. C. and Agrawal B., 1998, “Optimisation of Piezoelectric Sensor/Actuator Placement for Vibration Control of Laminate Plate”, *AIAA Journal*, Vol. 36, pp. 1763-1765.

Kapuria S., Sengupta S. and Dumir P. C., 1997, “Three Dimensional Piezothermoelastic Solution for Shape Control of Cylindrical Panel”, *Journal of Thermal Stresses*, Vol. 20 (1), pp. 67-85.

Karczmarzyk S., 1996, “An Exact Elastodynamic Solution to Vibration Problems of a Composite Structure in the Plane Stress State”, *Journal of Sound and Vibration*, Vol. 196 (1), pp. 85-96.

Kelley J. E., 1960, “The Cutting Plane Method for Solving Convex Programs”, *Journal of the Society for Industrial and Applied Mathematic*, pp. 703-713.

Khot N. S., Berke L. and Venkaya V. B., 1979, “Comparison of Optimality Criteria Algorithms for Minimum Weight Design of Structures”, *AIAA Journal*, Vol. 17, pp. 182-190.

Koconis D. B., Kollar L. P and Springer G. S., 1994, “Shape Control of Composite Plates and Shells with Embedded Actuators. II Desired Shape Specified”, *Journal of Composite Materials*, Vol. 28 (3), pp. 262-285.

Kohn R. V. and Strang G., 1983, “Optimal Design for Torsional Rigidity”, In (Gallagher R. H. and Zienkiewicz O. C.), *Hybrid and Mixed Finite Element Methods*, Wiley & Son, pp. 281-288.

Kristensen E. S. and Madsen N. F., 1976, “On The Optimum Shape of Fillets in Plates Subjected To Multiple In-Plane Loading Cases”, *International Journal for Numerical Methods in Engineering*, Vol. 10, pp. 1007-1019.

Lage R., Garcia C. M., Mota S. C. A. and Reddy J. N., 2004, “Analysis of Adaptive Plate Structures by Mixed Layerwise Finite Elements”, *Composite Structures*, Vol. 66 (1-4), pp. 269-276.

Lage R., Garcia, C. M., Mota S. C. A. and Reddy J. N., 2004, "Layerwise Partial Mixed Finite Element Analysis of Magneto-Electro-Elastic Plates", *Computers and Structures*, Vol. 82 (17-19), pp. 1293-1301.

Lamberti L. and Pappalettere C., 2000, "Comparison of the Numerical Efficiency of Different SLP based Algorithms for Structural Optimisation Problems", *Computers and Structures*, Vol. 76, pp. 713-728.

Lee B. Y, 1993, "Shape Sensitivity Formulation for an Axisymmetric Thermal Conducting Solid", *Proceedings of Institution of Mechanical Engineers Part C: Journal of Mechanical Engineering Science*, Vol. 207 (C3), pp. 209-216.

Li X. S., 1994, "An Efficient Solution to Non-Differentiable Optimisation Problem", *China Science*, Vol. 24 (4), pp. 371-377.

Li Q., Xie Y. M. and Steven G. P., 1999, "Displacement Minimisation of Thermoelastic Structure by Evolutionary Thickness Design", *Computer methods in Applied Mechanics and Engineering*, Vol. 179, pp. 361-378.

Librescu L., Meirovitch L. and Na S. S., 1997, "Control of Cantilever Vibration via Structural Tailoring and Adaptive Materials", *AIAA Journal*, Vol. 35, pp. 1309-1315.

Lim K. B., 1992, "Method for Optimal Actuator and Sensor Placement for Large Flexible Structures", *Journal of Guidance Control Dynamics*, Vol. 15, pp. 49-57.

Lim Y., Varadan V. V. and Varadan V. K., 1996, "Finite Element Modelling of the Transient Response of Smart Structures", *Proceeding of SPIE – The International Society for Optical Engineering Smart Structures and Materials 1996: Mathematic and Control in Smart Structures*, San Diego, CA, USA, Vol. 27 (15), pp. 233-242.

Lim C. W., He L. H. and Soh A. K., 2001, "Three-dimensional Electric Responses of a Parallel Piezoelectric Bimorph", *International Journal of Solids and Structures*, Vol. 38, pp. 2833-2849.

Lin C. C. and Hsu C. Y., 1996, "Finite Element Analysis on Deflection Control of Plates With Piezoelectric Actuators", *Journal of Composite Structures*, Vol. 35, pp. 423-433.

Lo K. H., Christensen R. M. and Wu E. M., 1977, "A High Order Theory of Plate Deformation –Part 1 & 2: Homogenous Plates", *Journal of Applied Mechanics*, Vol. 44, pp. 663-676.

Loewy R., 1997, "Recent Developments in Smart Structures with Aeronautical Applications", *Smart Materials and Structures*, Vol. 6, pp. R11-R42.

Luo Q. and Tong L., 2002a, "Exact Static Solutions to Piezoelectric Smart Beams Including Peel Stresses – I: Theoretical Formulation", *International Journal Solids and Structures*, Vol. 39 (18), pp. 4677-4695.

Luo Q. and Tong L., 2002b, "Exact Static Solutions to Piezoelectric Smart Beams Including Peel Stresses – II: Numerical Results, Comparison and Discussion", *International Journal of Solids and Structures*, Vol. 39 (18), pp. 4697-4722.

Luo Q. and Tong L., 2002c, "A Finite Element Analysis for Piezoelectric Smart Plates Including Peel Stresses", *Proceedings of International Conference of Scientific and Engineering Computation*, Singapore, pp. 897-900.

Luo Q. and Tong L, 2003a, "Exact Dynamic Solutions to Piezoelectric Smart Beams Including Peel Stresses – I: Theory and Application", *International Journal of Solids and Structures*, Vol. 40 (18), pp. 4789-4812.

Luo Q. and Tong L., 2003b, "Exact Dynamic Solutions to Piezoelectric Smart Beams Including Peel Stresses – II: Numerical Results, Comparison and Approximate Solutions", *International Journal of Solids and Structures* Vol. 40 (18), pp. 4813-4836.

Lurie K. A. and Cherkaev A. V., 1984, "G-Closure of Some Particular Sets of Admissible Material Characteristics for The Problem of Bending of Thin Plate", *Journal of Optimisation Theory in Application*, Vol. 42, pp. 305-315.

Mackiewicz A., Holnicki-Szulc J. and Lopez-Almansa F., 1996, "Optimal Sensor Location in Active Control of Flexible Vibration", *AIAA Journal*, Vol. 34, pp. 857-859.

Maute K. and Ramm E., 1994, "Topology Optimisation of Plate and Shell Structures", *Proceeding of the IASS-ASCE International Symposium*, Atlanta, Georgia.

Michell A. G. M., 1904, "The Limit of Economy of Material in Frame Structure", *Phil Mag*, Vol. 8, pp. 589-597.

Miller S. E. and Abramovich H., 1995, "A Self-Sensing Piezolaminated Actuator Model for Shells using a First Order Shear Deformation Theory", *Journal of Intelligent Material System and Structures*, Vol. 6, pp. 624-638.

Mukherjee A. and Joshi S. P., 2001, "Design Actuator Profiles for Minimum Power Consumption", *Smart Materials and Structures*, Vol. 10 (2), pp. 305-313.

Mukherjee A. and Joshi S. P., 2002, "Piezoelectric Sensor and Actuator Spatial Design for Shape Control of Piezolaminated Plates", *AIAA Journal*, Vol. 40 (6), pp. 1204-1210.

Nagaya K. and Ryu H., 1996, "Deflection Shape Control of a Flexible Beam by using Shape Memory Alloy Wires under the Genetic Algorithm Control", *Journal of Intelligent Material Systems and Structures*, Vol. 7 (3), pp. 336-341.

Nava R., Ponce M. A., Rejon L., Viquez S. and Castano V. M., 1997, "Response Time and Viscosity of Electrorheological Fluids", *Smart Materials and Structures*, Vol. 6 (1), pp. 67-75.

Nguyen Q. and Tong L., 2002a, "Shape Control of Smart Composite Plate Structures with Non-Rectangular Shaped PZT Actuator", *Proceeding of the Third Australasian Congress on Applied Mechanics*, Sydney, Australia, February 20th-22nd, pp. 421-426.

Nguyen, Q. and Tong, L., 2002b, “Shape Control of Smart Composite Plates Structures Based on Actuator Shape Optimisation”, *Recent Advances in Computational Sciences and Engineering-Proceeding of the International Conference on Scientific and Engineering Computation*, Singapore, December 3rd-5th, Ed. H.P. Lee and K. Kumar, Imperial College Press, London, pp.434-437.

Nguyen Q. and Tong L., 2004, “Modal Shape Control of Smart Composite Plates Using Piezoelectric Actuators”, Proceeding of *The Sixth World Congress on Computation Mechanics in conjunction with The Second Asian Pacific Congress on Computational Mechanics*, Beijing, China, September 5th-10th, Tsinghua University Press & Springer-Verlag.

Nguyen Q. and Tong L., 2004, “Shape Control of Smart Composite Plate Structures with Non-Rectangular Piezoelectric Actuator”, *Composite Structures*, Vol. 66. (1-4), pp. 207-214.

Oda J. and Yamazaki K., 1981, “Pattern Transformation Method for Shape Optimisation and Its Application to Spoked Rotatory Disks”, *Proceeding of the International Symposium on Optimum Structural Design*, Tucson, Arizona, USA, pp. 4.29-4.35.

Odetayo M. O. and McGregor D. R., 1989, “Genetic Algorithm for Inducing Control Rules for a Dynamic System”, *Proceeding of the Third International Conference on Genetic Algorithm*, Morgan Kaufmann Publisher Inc, pp. 177-182.

Onada J. and Hanawa Y., 1992, “Optimal Location of Actuator for Statistical Static Shape Control of Large Space Structure: A comparison of Approach”, *Proceeding of 31st AIAA/ASME/ASCE/ASC Structures, Structural Dynamics and materials Conference*, Washington DC, pp. 2788-2795.

Onada J. and Hanawa Y., 1998, “Actuator Placement Optimisation by Genetic and Improved Simulated Annealing Algorithms”, *AIAA Journal*, Vol. 31 (6), pp. 156-162.

Pan E. and Heyliger P. R., 2003, “Exact Solutions for Magneto-electro-elastic Laminates in Cylindrical Bending”, *International Journal of Solids and Structures*, Vol. 40 (24), pp. 6859-6876.

Paradies R., Hertwig M. and Elspass W. J., 1996, “Shape Control of Adaptive Mirror at Different Angles of Inclination”, *Journal of Intelligent Materials Systems and Structures*, Vol. 7 (2), pp. 203-210.

Phan N. D. and Reddy J. N., 1985, “Analysis of Laminated Composite Plates using a Higher-order Shear Deformation Theory”, *International Journal of Numerical Methods Engineering*, Vol. 21, pp. 2201-2219.

Pletner B. and Abramovich H., 1997, “Consistent Methodology for the Modelling of Piezoelectric Shells”, *AIAA Journal*, Vol. 35 (8), pp. 1316-1326.

Powell M. J. D., 1978, “Algorithm for Non-Linear Constraints that use Lagrangian Function”, *Mathematical Programming*, Vol. 14 (2), pp. 224-248.

Prager W. and Sield R. T., 1967, “A General Theory of Optimal Design”, *Journal of Applied Mechanics*, Vol. 34, pp. 184-186.

Prahbu M. R. and Dhanaraj R., 1994, “Thermal Buckling of Laminated Composite Plates”, *Computers and Structures*, Vol. 53 (5), pp. 1193-1204.

Proos K., Steven G. P., Querin O. M. and Xie Y. M., 2000, “Multicriteria Evolutionary Structural Optimisation using the Weighting and Global Criterion Methods”, *AIAA/NASA/USAF/ISSMO Symposium on MDO*, Long Beach, CA.

Putcha, N. S. and Reddy J. N., 1986a, “A Refined Mixed Shear Flexible Finite Element for the Non-Linear Analysis of Laminated Plates”, *Computers and Structures*, Vol. 22 (4), pp. 529-538.

Putcha N. S. and Reddy J. N., 1986b, “Stability and Natural Vibration Analysis of Laminated Plates by using a Mixed Element based on a Refined Plate Theory”, *Journal of Sound and Vibration*, Vol. 104 (2), pp. 285-300.

Querin O. M., 1997, “Evolutionary Structure Optimisation: Stress based Formulation and Implementation”, PHD Thesis, Department of Aeronautical Engineering, The University of Sydney, Australia.

Querin O. M., Steven G. P. and Xie Y. M., 1998, “Evolutionary Structure Optimisation using a Bidirectional Algorithm”, *Engineering Computations*, Vol. 15, pp. 1031-1048.

Rao S. S., 2004, “Mechanical Vibrations”, Upper Saddle River, N. J.: Pearson Prentice Hall, 4th Edition.

Ray M. C. and Mallik N., 2004, “Finite Element Analysis of Smart Structures Containing Piezoelectric Fiber-Reinforced Composite Actuator”, *AIAA Journal*, Vol. 42 (7), pp. 1398-1405.

Reddy J. N., 1984, “A Simple Higher Order Theory for Laminated Composite Plates”, *Journal of Applied Mechanics*, Vol. 51, pp. 745-752.

Reddy J. N., 1987, “A Generalisation of Two-Dimensional Theories of Laminated Composite Plates”, *R-10 Communications in Applied Numerical Methods*, Vol.3 (3), pp. 173-180.

Reddy J. N., 1989a, “On the Generalisation of Displacement-Based Laminate Theories”, *Applied Mechanics Reviews*, Vol. 42 (11), pp. S213-S222, Part 2.

Reddy J. N., 1989b, “A General Non-Linear Third Order Theory of Plates with Moderate Thickness”, *International Journal of Non-linear Mechanics*, Vol. 25 (6), pp. 677-686.

Reddy J. N., 1989c, “A Review of Refined Theories of Laminated Composite Plates”, *Shock and Vibration Digest*, Vol. 22, pp. 3-17.

Reddy J. N. and Phan N. D, 1985, “Stability and Vibration of Isotropic, Orthotropic and Laminated Plates According to Higher-order Shear Deformation Theory”, *Journal of Sound Vibration*, Vol. 98 (2), pp. 157-170.

Richard J. S. and Cudney H. H., 1993, “Modelling Multiple Layer Piezoelectric Actuators in Active Structural Control”, *Proceeding of SPIE*, Vol. 19 (16), pp. 231-243.

Rizet N., Brissaud M., Gonnard P., Bera J. C. and Sunyach M., 2000, “Modal Control of Beam Flexural Vibration”, *Journal of the Acoustic Society of America*, Vol. 107 (4), pp. 2061-2067.

Redmond J. and Barney P., 1997, “Vibration Control of Stiff Beams and Plates using Structurally Integrated PZT Stack Actuators”, *Journal of Intelligent Material Systems and Structures*, Vol. 8 (6), pp. 525-535.

Robbins D. H. and Reddy J. N., 1991, “Analysis of Piezoelectrically Actuated Beams using a Layer-wise Displacement Theory”, *Computers and Structures*, Vol. 41, pp. 265-279.

Rorres C. and Anton H., *Application for Linear Algebra*, New York, Wiley 1979.

Rozvany G. I. N., 1989, “Structural Design via Optimality Criteria”, Kluwer, Dordreccht, The Netherlands.

Rozvany G. I. N. and Zhou M., 1991, “The COC Algorithm, Part I: Cross-Section Optimisation or Sizing Homogenisation”, *Computer Methods in Applied Mechanics and Engineering*, Vol. 89, pp. 281-308.

Rozvany G. I. N, Zhou M. and Birker T., 1992, “Generalised Shape Optimisation without Homogenisation”, *Structure Optimisation*, Vol. 4, pp. 250-252.

Rozvany G. and Zhou M., 1994, “Optimal Criteria Methods for Large Discretized System”, *In: Adeli H, Editor, Advances in Design Optimisation,* Chapman & Hall, London, pp. 41-108.

Rozvany G. I. N., Bendsøe M. P. and Kirsch U., 1995, “Layout Optimisation of Structures”, *Applied Mechanics Review,* Vol. 48 (2), pp. 41-119.

Saravanos D. A. and Heyliger P. R., 1995, “Coupled Layerwise Analysis of Composite Beams with Embedded Piezoelectric Sensors and Actuators”, *Journal of Intelligent Material Systems and Structures,* Vol. 6, pp. 350-363.

Saravanos D. A., 1996, “Coupled Mixed-Field Laminated Theory and Finite Element for Smart Piezoelectric Composite Shell Structures”, *NASA Contractor Report 198490,* Prepared for Lewis Research Centre Under Contract NCC3-391, pp. 1-38.

Saravanos D. A., 1997, “Mixed Laminate Theory and Finite Element for Smart Piezoelectric Composite Shell Structures”, *AIAA Journal,* Vol. 35 (8), pp. 1327-1333.

Saravanos D. A., Heyliger P. R. and Hopkins D. A., 1997, “Layerwise Mechanics and Finite Element Formulation for Dynamic Analysis of Piezoelectric Composite Plates”, *International Journal of Solids and Structures*, Vol. 34 (3), pp. 359-378.

Schulz G. and Heimbold G., 1983, “Dislocated Actuator/Sensor Positioning and Feedback Design for Flexible Structures”, *Journal of Guidance Control Dynamics,* Vol. 5, pp. 361-367.

Sloss J. M., Bruch J. C., Adali S. and Sadek I. S., 2001, “Piezoelectric Patch Control using an Integral Equation Approach”, *Thin-Walled Structures*, Vol. 39, pp. 45-63.

Stam M., Wang D. and Carman G., 1995, “Analytically/Experimentally Evaluating the Response of Cylindrical Piezoelectric Material Systems Subjected to Thermal Load”, *Proceeding of SPIE – The International Society for Optical Engineering*, Vol. 24 (43), pp. 434-445.

Steven G. P. and Xie Y. M, 1993, "Evolutionary Structural Optimisation with FEA", *In: Computational Mechanics*, Valliappan S. et al. (Ed), A. A. Balkema Publishers, Rotterdam, Vol. 1, pp. 27-34.

Sun D., Tong L. and Atluri S. N., 2001, "Effects of Piezoelectric Sensor/Actuator Debonding on Vibration Control of Smart Beams", *International Journal of Solids and Structures*, Vol. 38, pp. 9033-9051.

Sun D. and Tong L., 2002, "Modelling and Vibration Control of Beams with Partially Debonded Active Constrained Layer Damping Patch", *Journal of Sound and Vibration*, Vol. 252 (3), pp. 493-507.

Sun D. C. and Tong L. Y., 2003, "Optimum Control Voltage Design for Constrained Static Shape Control of Piezoelectric Structures", *AIAA Journal*, Vol. 41 (12), pp. 2444-2450.

Tang W., Tong L. and Gu Y., "Improved Genetic Algorithm for Design Optimisation of Truss Structures with Size, Shape and Topology Variables", (in press).

Tong L. and Steven G. P., 1999, "Analysis and Design of Structural Bonded Joints", *Kluwer Academic*, Boston.

Tong L., Sun D. and Atluri S. N., 2001, "Sensing and Actuating Behaviours of Piezoelectric Layer in Smart Beams with Debonding", *Smart Materials and Structures*, Vol. 10 (4), pp. 713-723.

Tong L. and Sun X., 2002, "Shape Optimisation of a Bonded Patch to a Cylindrical Shell", *Proceeding of the Third Australasian Congress on Applied Mechanics*, Sydney, Australia, pp. 455-460.

Tzou H. S. and Tseng C. I., 1990, "Distributed Piezoelectric Sensor/Actuator Design for Dynamic Measurement/Control of Distributed Parameter Systems: a Piezoelectric Finite Element Approach", *Journal of Sound and Vibration*, Vol. 138 (1), pp. 17-34.

Tzou H. S. and Tseng C. I., 1991, "Distributed Vibration Control and Identification of Coupled Elastic/Piezoelectric Systems: Finite Element Formulation and Application", *Mechanical System and Signal Processing*, Vol. 5 (3), pp. 215-231.

Varadarajan S. and Chandrashekhara K., 1998, "Adaptive Shape Control of Laminated Composite Plates using Piezoelectric Materials", *AIAA Journal*, Vol. 36 (9), pp. 1694-1698.

Venkaya V. B., 1993, "Introduction: Historical Perspective and Future Direction", (Kamat M. P. Ed) *Structure Optimisation: Status and Promise*, AIAA Inc., pp. 1-10.

Xie Y. M and Steven G. P., 1992, "Shape and Layout Optimisation via an Evolutionary Procedure", *in Proceeding of International Conference on Computational Engineering Science*, Hong Kong University of Science and Technology, Hong Kong, pp. 471.

Xie Y. M and Steven G. P., 1994, "A Simple Approach to Structure Frequency Optimisation", *Computers and Structures*, Vol. 53, pp. 1487-1491.

Xie Y.M. and Steven G.P., 1997, "Evolutionary Structural Optimization", Springer-Verlag, Berlin.

Wang B. T. and Rogers C. A., 1991, "Laminated Plate Theory for Spatially Distributed Induced Strain Actuators", *Journal of Composite Materials*, Vol. 25, pp. 433-452.

Wang X. M., Ehlers C. and Neitzel M., 1996, "Dynamic Analysis of Piezoelectric Actuator Bonded on Beam", *Third International Conference on Intelligent Materials/ Third European Conference on Smart Structures and Materials*, Lyon, France.

Wang Z., Chen S. H. and Han W., 1997, "The Static Shape Control for Intelligent Structures", *Finite Element in Analysis and Design*, Vol. 26, pp. 303-314.

Wang X. D. and Meguid S. A., 2000, "On the Electro-elastic Behaviour of A Thin Piezoelectric Actuator Attached to An Infinite Host Structure", *International Journal of Solids and Structures*, Vol. 37, pp. 3231-3251.

Whitney J. M. and Pagano N. J., 1970, "Shear Deformation in Heterogenous Anisotropic Plates", *Journal of Applied Mechanics*, Vol. 37, pp. 1031-1036.

Woon, S. Y., 2002, "Effective GA based Optimisation of Continuum Structures", PHD Thesis, School of Aerospace, Mechanical and Mechatronic Engineering, The University of Sydney, Australia.

Woon, S. Y., Tong, L., Querin O. M. and Steven G. P., 2003, "Knowledge based Algorithms in Fixed Grid Shape Optimisation", *International Journal for Numerical Methods in Engineering*, Vol. 58 (4), pp. 643-660.

Yang R. J. and Chuang C. H., 1994, "Optimal Design using Linear Programming", *Computers and Structures*, Vol. 52 (2), pp. 265-275.

Yin L. and Wang W., 2001, "Optimal Criteria Method for Topology Optimisation under Multiple Constraints", *Computers and Structures*, Vol. 79, pp. 1839-1850.

Young V., Querin O. M., Steven G. P. and Xie Y. M., 1999, "3D Multiple Load Case Bidirectional Evolutionary Structural Optimisation (BESO)", *Structure Optimisation*, Vol. 18, pp. 183-192.

Zhang H., Lennox B., Goulding P. and Leung A., 2000, "A Float Encoded Genetic Algorithm Technique for Integrated Optimisation of Piezoelectric Actuators and Sensors Placement and Feedback Gain", *Smart Materials and Structures*, Vol. 9 (4), pp. 552-557.

Zhao C., Steven G. P. and Xie Y. M., 1996, "Evolutionary Natural Frequency Optimisation of Thin Plate Bending Vibration Problems", *Structure Optimisation*, Vol. 11, pp. 244-251.

Zienkiewicz O. C. and Campbell J. S., 1973, “Shape Optimisation and Sequential Linear Programming”, *Gallagher R. H. and Zienkiewicz O. C. Ed, Optimum Structural Design*, Wiley, pp. 109-126.

Zhou M. and Rozvany G. I. N., 1991, “The COC Algorithm, Part II: Topological, Geometrical and Generalised Shape Optimisation”, *Computer Methods in Applied Mechanics and Engineering*, Vol. 89, pp. 309-336.